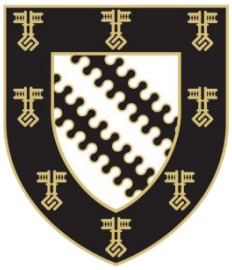
Unravelling the genetic and molecular mechanisms of the left-right patterning genes *Pkd1l1* and *Pkd2*

A thesis presented for the degree of Doctor of Philosophy (DPhil)

Exeter College, University of Oxford



Laura Margaret Dyer

Mammalian Genetics Unit, MRC Harwell Institute

Department of Biochemistry, University of Oxford

Supervisors: Dr Dominic Norris (MGU, MRC Harwell Institute)

Professor Matthew Whitby (Biochemistry, Oxford)

Michaelmas Term 2022

Word Count: 37,623

Abstract

Pkd1 and *Pkd2* encode the polycystin proteins which underlie human ADPKD, a major cause of end stage renal failure. Recently, by analysing the *Pkd2*^{lrm4} mouse, a previous member of the lab provided evidence that loss of ciliary PKD2 underlies kidney cyst formation. Furthermore, the *Pkd2*^{lrm4} mouse highlights a requirement for PKD2 in nodal cilia for correct L-R patterning. However, we are yet to fully understand its cilia-specific role and the mechanisms controlling its ciliary trafficking and entry. PKD1L1 (a PKD1 Paralog) functions with PKD2 in the embryonic node to allow correct L-R patterning and its expression and localisation during this process remain to be fully characterized.

By generating endogenously tagged alleles of PKD1L1 and PKD2, I have investigated their localisation and co-localisation, in the embryonic node during L-R determination. Using these tagged alleles, *Pkd1l1*^{mTFP1} and *Pkd2*^{mNG}, I have been able to evaluate their localisation in *Pkd2*$^{-/-}$ and *Pkd1l1*$^{-/-}$ embryos respectively. Enabling us to further understand the role of their co-localisation, and assess the co-dependent relationship between PKD2 and PKD1L1 for ciliary localisation. Using *Pkd2*$^{lrm4/lrm4}$ samples, I have been able to identify a selection of candidate interacting proteins that may be involved in trafficking to cilia and ciliary entry of PKD2.

The work in this thesis provides a new insight into the genetic and molecular mechanisms involved with the polycystins, and their roles in left-right pattern determination.

Acknowledgements

I would like to begin by thanking my supervisor Dr Dominic Norris. Your support, encouragement, guidance and generous patience have been invaluable to my work. Without this, especially during the writing, I would not have been able to complete this thesis. Even through all of my writing struggles, you did not give up on me and continued to support me until the end, for that I am extremely grateful.

Next, I would like to thank all of the members of the Norris Lab present during my time at Harwell: Jonathan Whitchurch, Wang Twan, Rosie Little, Vrinda Sreekumar, David Asante, Hannah Farley and Dragoş Leordean. I thoroughly enjoyed all of your company, expertise and support over the years. Special thanks go out to Jonathan who shared my lab bay, put up with me until the closure of the lab, and has continued to support me since.

Thank you to all of the core facilities at Harwell, in particular to Lucie Visor and her ward staff for looking after my mice, protein core and genotyping for their teaching and histology for processing and sectioning my kidney samples. I would also like to give a special mention to Jeremy Sanderson, you have taught me so much about microscopy and helped me achieve a lot in the world of Airyscan imaging. You have also been a great source of encouragement and support since the beginning of my DPhil – thank you.

Big thank you to the amazing community of Harwell students, you are all wonderful. We have been through so much together over the last few years, and you have all provided so much moral support– I am very thankful for that. I hope to continue our friendships and wish each of you the best of luck for the future.

I would like to thank my family for all of their support throughout the duration of my DPhil. You have always been there for me when I needed you, and continued to believe that I could do it even when I felt otherwise.

Finally, I would like to thank my two lovely dogs (Bobby & Sally) for providing unconditional love and making me leave the house at least once a day.

Table of Contents

Abstract I
Acknowledgements II
Table of Figures VI
1. Introduction 1
1.1 History of L-R patterning/asymmetry 1
1.1.1. Discovery of the first molecular L-R asymmetries 3
1.2. Left-Right patterning of the mouse embryo 4
1.2.1. The node & nodal cilia 4
1.2.2. Generation of leftward fluid flow 5
1.2.3. Responding to nodal flow 7
1.2.4. Nodal signalling cascade: from the node to the LPM 9
1.3. Polycystins 11
1.3.1. The family of polycystin proteins 12
1.3.2. The polycystins and disease 13
1.3.3. Role of polycystins in L-R pattern determination 14
1.4. Aims 17
2. Materials & Methods 18
2.1. Mouse Strains 18
2.1.1. Background Strains 18
2.1.2. *Pkd2^{lrm4}* 18
2.1.3. *Pkd2^{del}* 18
2.1.4. *Pkd2^{mNG}* 19
2.1.5. *Pkd1l1$^{-/-}$* 19
2.1.6. *Pkd1l1^{mTFP1}* 19
2.2. Dissection 19
2.2.1. Whole Mount Immunofluorescence (7.5-8.5 d.p.c) 19
2.2.2. Whole Mount In Situ Hybridisation 20
2.2.3. Situs and Kidney Phenotyping 21
2.3. Molecular Biology 21
2.3.1. Polymerase Chain Reaction 21
2.3.2. Agarose Gel Electrophoresis 22
2.3.3. Purification of PCR products 22
2.3.4. Restriction Digest 22
2.3.5. Ligation 22
2.3.6. Bacterial Transformation 22
2.3.7. Inoculating bacterial cultures 23
2.3.8. Isolation of plasmid DNA 23
2.3.9. DNA Sequencing 23
2.3.10. In-Situ probe synthesis 23

2.3.11. RNA Extraction 24
2.3.12. cDNA Synthesis 24
2.3.13. RT-PCR 24
2.3.14. 5’ RACE 24
2.3.15. RT-qPCR 24
2.3.16. Genotyping 25
2.3.17. Primers 26
2.4. Protein Biochemistry 27
2.4.1. Protein Extraction 27
2.4.2. Protein Quantification 27
2.4.3. Immunoprecipitation 27
2.4.4. Western Blotting 27
2.4.5. Pilot Protein Induction 28
2.4.6 Large Scale Expression 29
2.4.7 Antibody Affinity Purification 30
2.5. Cell Culture 31
2.5.1. Cell Media 31
2.5.2. Thawing Cells 31
2.5.3. Passaging Cells 31
2.5.4. Freezing Cells 32
2.5.5. Making Mouse Embryonic Fibroblasts (MEFs) 32
2.5.6. Immortalising MEFs 32
2.5.7. Transfecting Cells 33
2.5.8. Immunocytochemistry 33
2.6. Antibodies 34
3. Identifying Novel *Pkd1l1* Transcripts 35
3.1 Introduction 35
3.2 Results 37
3.2.1 Predicting previously un-annotated *Pkd1l1* 5’ exons 37
3.2.2 Validating predicted *Pkd1l1* exons 44
3.2.3 5’ RACE identifies an additional *Pkd1l1* exon and transcript 48
3.2.4 Confirmation of additional 5’ exons in RNA-Seq data 54
3.2.5 Assessing the expression of the two identified *Pkd1l1* 5’ variants 60
3.3 Discussion 64
4. Investigating PKD2 ciliary localisation 66
4.1 Introduction 66
4.2 Results 69
4.2.1 Developing PKD2 antibodies 69
4.2.2 Testing new PKD2 antibodies 78
4.2.3 Novel PKD2 isoform identified 88

4.2.4 Mass spectrometry analysis confirms presence of PKD2 in 75/85 kDa band 97
4.2.5 Interacting partners in adult kidney and lung identified by mass spectrometry 104
4.2.6 Investigating PKD2^{lrm4} interacting partners 123
4.3 Discussion 131
5. Examining PKD2 and PKD1L1 expression during L-R patterning 134
5.1 Introduction 134
5.2 Results 136
5.2.1 Testing PKD1L1 antibodies in B6J WT embryos 136
5.2.2 Testing PKD1L1 antibodies in *Pkd1l1*$^{+/+}$, *Pkd1l1*$^{+/-}$ *and Pkd1l1*$^{-/-}$ embryos 142
5.2.3 *Pkd2*^{mNG} and *Pkd1l1*^{mTFP1} are homozygous viable 155
5.2.4 PKD1L1^{mTFP1} localises to nodal cilia 165
5.2.5 PKD2^{mNG} localises to nodal cilia 169
5.2.6 PKD1L1^{mTFP1} and PKD2^{mNG} co-localise in nodal cilia 174
5.2.7 PKD1L1 and PKD2 are co-dependent for nodal cilia localisation 179
5.3 Discussion 186
6. Discussion 190
6.1. Summary of findings 190
6.1.1. *Pkd1l1* contains an additional seven 5' exons to the Ensembl annotated sequence 190
6.1.2. A lower ~85 kDa isoform of PKD2 is present in multiple tissues and cell lines 191
6.1.3. Mass spectrometry analysis of *Pkd2*$^{lrm4/lrm4}$ kidney and lung samples identified candidate interacting partners for ciliary localisation 191
6.1.4. *Pkd2*^{mNG} and *Pkd1l1*^{mTFP1} are homozygous viable 192
6.1.5. PKD2^{mNG} and PKD1L1^{mTFP1} co-localise within nodal cilia 193
6.1.6. PKD2 and PKD1L1 are co-dependent for ciliary localisation in the embryonic node 193
6.7. Future work 194
6.7.1. Implications of additional *Pkd1l1* 5' exons 194
6.7.2. Further investigation into the smaller ~85 kDa PKD2 isoform 195
6.7.3. *Pkd2*^{mNG} and *Pkd1l1*^{mTFP1} 196
7. Appendix 197
7.1 Supplementary Figures 197
7.2 Mass Spectrometry data tables 199
Bibliography 262

Table of Figures

1. Introduction

1.1 The nodal signalling cascade 10

3. Identifying novel *Pkd1l1* transcripts

3.1 Schematic representation of Human PKD1L1 and predicted Mouse *Pkd1l1* 5' exons 38

3.2 Multiple species alignment of PKD1L1 40

3.3 Sequence alignments of predicted *Pkd1l1* 5' exons 43

3.4 RT-PCR of predicted mouse Pkd1l1 exons 45

3.5 Mouse *Pkd1l1* 5' exons confirmed by Sanger sequencing 47

3.6 5' RACE of mouse *Pkd1l1* 49

3.7 Two 5' sequences identified by 5' RACE 51

3.8 Sequence alignment of mouse 5' long variant and sequence upstream of annotated *PKD1L1* 52

3.9 B6J 1ss RNA-Seq read coverage track with RefSeq track positioned to the 5' end of *Pkd1l1* 55

3.10 B6J 1ss RNA-Seq read coverage track for peaks/exons 1 and 2 56

3.11 B6J 1ss RNA-Seq read coverage for peaks/exons 3, 4 and 5 57

3.12 B6J 1ss RNA-Seq read coverage for peaks/exons 6 and 7 58

3.14 Relative expression and fold change of 5' Short and 5' Long variants 61

3.15 *Pkd1l1* 5' exons are expressed in the node and notochord 63

4. Investigating PKD2 ciliary localisation

4.1 Pilot protein expression of PKD2 (aa689-968) in the pRSETa vector 71

4.2 Pilot protein expression of PKD2 (aa689-968) in the pET-32a vector 72

4.3 Large scale expression of PKD2 (aa689-968) in the pET-32a vector 74

4.4 Final purification of PKD2 in the pET-32a vector for immunisation 77

4.5 Western blots using Rb8 and Rb12 antibodies 80

4.6 Immunoprecipitation using Rb8 and Rb12 antibodies 82

4.7 Immunofluorescence in Pkd2 MEFs using Rb8 and Rb12 antibodies 85

4.8 Immunofluorescence in 8 d.p.c. mouse embryos using Rb8, R12 and H280 antibodies 86

4.9 Additional examples of immunofluorescence in 8 d.p.c. mouse embryos using the Rb8 PKD2 antibody 87

4.10 Immunoprecipitation using 8 d.p.c. B6J embryos 92

4.11 Immunoprecipitation using multiple adult mouse tissues and cell lines 93

4.12 Immunoprecipitation for mass spectrometry analysis 98

4.13 Mapping of PKD2 peptides identified by mass spectrometry 103

4.14 Interacting partners identified by mass spectrometry in kidney IP 1 105

4.15 Interacting partners identified by mass spectrometry in kidney IP 2 106

4.16 Interacting partners identified by mass spectrometry in kidney IP 3 107

4.17 Interacting partners identified by mass spectrometry in kidney IP 4 108

4.18 Interacting partners identified by mass spectrometry in kidney IP 5 109
4.19 Interacting partners identified by mass spectrometry in kidney IP 6 110
4.20 Interacting partners identified by mass spectrometry in kidney IP 7 111
4.21 Interacting partners identified by mass spectrometry in lung IP 1 112
4.22 Interacting partners identified by mass spectrometry in lung IP 2 113
4.23 Interacting partners identified by mass spectrometry in both *Pkd2*$^{+/+}$ adult and 14.5 d.p.c. embryonic kidneys 125

5. Examining PKD2 and PKD1L1 expression during L-R patterning

5.1 Diagrammatic representation of PKD1L1 and PKD2 137
5.2 PKD1L1 mouse monoclonal antibody staining in WT B6J nodes 138
5.3 PKD1L1 rabbit polyclonal antibody staining in WT nodes 139
5.4 PKD1L1 OSP00015W antibody staining in WT nodes 140
5.5 PKD1L1 mouse monoclonal antibody staining in *Pkd1l1*$^{+/+}$ and *Pkd1l1*$^{+/-}$ nodes 143
5.6 PKD1L1 mouse monoclonal antibody staining in *Pkd1l1*$^{+/-}$ nodes 144
5.7 PKD1L1 mouse monoclonal antibody staining in *Pkd1l1*$^{-/-}$ nodes 145
5.8 PKD1L1 rabbit polyclonal antibody staining in *Pkd1l1*$^{+/+}$ and *Pkd1l1*$^{+/-}$ nodes 147
5.9 PKD1L1 rabbit polyclonal antibody staining in *Pkd1l1*$^{+/-}$ nodes 148
5.10 PKD1L1 rabbit polyclonal antibody staining in *Pkd1l1*$^{-/-}$ nodes 149
5.11 PKD1L1 OSP00015W antibody staining in *Pkd1l1*$^{+/+}$ nodes 151
5.12 PKD1L1 OSP00015W antibody staining in *Pkd1l1*$^{+/-}$ nodes 152
5.13 PKD1L1 OSP00015W antibody staining in PKD1L1-/- nodes 153
5.14 *Pkd2*^{mNG} mice are homozygous viable and show no situs defects 156
5.15 *Pkd1l1*^{mTFP1} mice are homozygous viable and show no situs defects 157
5.16 *Pkd2*$^{mNG/mNG}$;*Pkd1l1*$^{mTFP1/mTFP1}$ embryos are viable and show no situs defects 159
5.17 *Pkd2*$^{-/mNG}$ and *Pkd1l1*$^{-/mTFP1}$ embryos and *Pkd2*$^{mNG/mNG}$;*Pkd1l1*$^{mTFP1/mTFP1}$ mice are viable 161
5.18 *Pkd2*^{mNG} kidneys are indistinguishable from *Pkd2*$^{+/+}$ Kidneys 164
5.19 Immunofluorescence in *Pkd1l1*$^{+/+}$ embryos 166
5.20 PKD1L1^{mTFP1} fluorescence in *Pkd1l1*$^{+/mTFP1}$ embryos 167
5.21 PKD1L1^{mTFP1} fluorescence in *Pkd1l1*$^{+/mTFP1}$ embryos cont. 168
5.22 Live imaging of PKD2^{mNG} in 8 d.p.c. embryos 170
5.23 PKD2^{mNG} fluorescence in *Pkd2*$^{+/mNG}$ and *Pkd2*$^{mNG/mNG}$ embryos 171
5.24 Lightsheet imaging of PKD2^{mNG} in an 8 d.p.c. embryo 173
5.25 PKD2^{mNG} and PKD1L1^{mTFP1} fluorescence in 8 d.p.c. embryos 176
5.26 PKD2^{mNG} and PKD1L1^{mTFP1} fluorescence in 8 d.p.c. embryos 177
5.27 PKD2^{mNG} and PKD1L1^{mTFP1} fluorescence in 8 d.p.c. embryos 178
5.28 PKD2^{mNG} fluorescence in *Pkd1l1*$^{-/-}$ 8 d.p.c. embryos 181
5.29 PKD2^{mNG} fluorescence in *Pkd1l1*$^{-/-}$ 8 d.p.c. embryos continued 182
5.30 PKD1L1^{mTFP1} fluorescence in *Pkd2*$^{-/-}$ 8 d.p.c. embryos 184

5.31 PKD1L1^{mTFP1} fluorescence in *Pkd2*$^{-/-}$ 8 d.p.c. embryos 185

7. Appendix

7.1 Glomerular dilation measurements in 14.5 d.p.c. kidney sections 197

7.2 CopyCaller analysis of *Pkd1l1*$^{-/-}$ genotyping 198

1. Introduction

1.1 History of L-R patterning/asymmetry

Evidence of left-right asymmetry can be seen in nature, where some animals show striking external asymmetries; Male Narwhals usually have an erupted canine tusk on the left side (Nweeia et al. 2012), male fiddler crabs have one large claw used for attracting a mate and fighting other males (Swanson et al. 2013). While flatfish begin life bilaterally symmetrical, during larval development one eye migrates to the other side of the head, opposite to the side that will sit on the sea floor (Xing et al. 2019). The New Zealand Wrybill is unique being the only species of bird that's beak is always curved to the right (Pierce 1979). The coiling of snail shells can be either dextral (right-handed) or sinistral (left-handed) and most snail species are dextral, however a few snail species show both forms of chirality (Grande and Patel 2009; Wandelt and Nagy 2004); indeed a species of snail-eating snake (*Pareas iwasakii)* has more teeth on the right mandible than the left, an adaptation to eating the more common dextral rather than the rarer sinistral snails (Hoso et al. 2010). However, most vertebrates are largely left-right mirror symmetrical externally, although internally they show asymmetric positioning and patterning of the organs. In Humans, the heart apex is on the left along with the stomach and spleen, the liver is on the right and lung lobation is asymmetric with two lobes on the left and three on the right (Blum et al. 2014).

Defects in the establishment of sidedness (Situs) have been recognised for many years, being first formally described in the 1600's in reports by Italian anatomists and surgeons Girolamo Fabrizio (around 1600) and Marco Aurelio Severino - who described finding a human heart on the right hand side in 1643 (Cleveland 1926;

Pennekamp et al. 2015). Over a century later, in 1788, the Scottish physician and pathologist Matthew Baillie reported the complete L-R transposition of the thoracic and abdominal organs – what we now describe as *situs inversus totalis* (Baillie 1788). In 1933, Manes Kartagener first recognised an association of bronchiectasis and sinusitis alongside *situs inversus* and this triad was known as Kartagener's syndrome (Kartagener 1933); it is now more commonly referred to as Primary Ciliary Dyskinesia (Sleigh 1981). The name PCD was due to identifying defects in cilia motility as the primary cause of disease; however only ~50% of PCD patients show laterality defects, and the name Kartagener's syndrome is still used to define this subtype of PCD (Bukowy-Bieryllo et al. 2022). Björn Afzelius was the first to publish this finding, describing patients with immotile sperm who had recurring bronchitis and sinusitis; he noticed a lack of dynein arms in spermatozoa and bronchial cilia using electron microscopy (Afzelius 1976). He was also the first to speculate a role for motile cilia in L-R patterning "I postulate that cilia on the embryonic epithelia have a certain position and a fixed beat direction (in normal embryos), and that their beating somehow is instrumental in determining the visceral situs" (Afzelius 1976).

In 1990, Brown and Wolpert proposed a model for developing handed asymmetry, suggesting that a handed molecule "the F molecule" aligns itself in relation to the anteroposterior and dorsoventral axes (Brown and Wolpert 1990). They also suggested there must then be a conversion mechanism to convert the molecular asymmetry to a cellular and multicellular asymmetry (Brown and Wolpert 1990). Although this model was mostly theoretical and lacked specific details about the molecule and mechanisms of the conversion, it was influential and helped drive subsequent thought about the establishment of L-R asymmetry.

1.1.1. Discovery of the first molecular L-R asymmetries

The first L-R asymmetrically expressed genes identified were in the chick embryo, in 1995; Michael Levin described the asymmetric expression of three genes - *activin receptor IIa* (*cAct-RIIa*), *Sonic hedgehog* (*Shh*), and *chicken nodal-related 1* (*cNR-1*) (Levin et al. 1995). These genes were asymmetrically expressed in and around Hensen's node, *cNR-1* was also expressed in the left but not right lateral plate at later stages. Shortly after this, asymmetric mouse *Nodal* expression was described in two letters to nature, along with another letter reporting the asymmetric expression of *Lefty* in mouse – all published in the same volume (Collignon et al. 1996; Lowe et al. 1996; Meno et al. 1996).

These initial identifications lead to the discovery of the nodal signalling cascade, described in further detail in section 1.2.4.

1.2. Left-Right patterning of the mouse embryo

1.2.1. The node & nodal cilia

The term node in mammalian embryology comes from Hensen's node; described by Viktor Hensen in 1875 as an enlargement at the anterior end of the primitive streak (Blum et al. 2007; Leikola 1976; Viebahn 2001). The term "node" is most commonly used to describe the left-right organizer (LRO) in mouse. In other organisms the LRO is often referred to as: Hensen's node in chick, Kupffer's vesicle in zebrafish, and the gastrocoel roof plate in *Xenopus* (Blum et al. 2007; Blum et al. 2014).

In mouse, the node is a tear-drop shaped pit of ciliated cells that sits at the distal end of the notochord (Beddington and Robertson 1999; Little and Norris 2021). Nodal cilia were first identified in 1994, and cells in the node and notochord showed a single cilium in SEM imaging (Sulik et al. 1994). Motility of nodal cilia was described four years later, by Nonaka and colleagues. They were investigating *Kif3B*$^{-/-}$ embryos which showed randomised left-right asymmetry, SEM analysis revealed the complete absence of nodal cilia in *Kif3B*$^{-/-}$ embryos (Nonaka et al. 1998). To assess the functionality of nodal cilia they performed video microscopy, revealing that nodal cilia rotate in a clockwise motion to generate a leftward fluid flow within the node, a phenomenon now called nodal flow (Nonaka et al. 1998). This lead to the suggestion that a molecule or morphogen may be secreted into the node and carried across by leftward fluid flow (Nonaka et al. 1998). Afzelius had hypothesised a role for motile cilia in left right patterning in 1976, this was now revealed to be the case with the observation of motile cilia in the node (Afzelius 1976; Nonaka et al. 1998).

1.2.2. Generation of leftward fluid flow

Since the original observation that nodal cilia generate a leftward fluid flow, many studies have been undertaken to understand the mechanisms underlying this process.

Nodal flow was investigated in two well characterised mouse mutants that exhibit situs defects: *inversus viscerum* (*iv*) and *inversion of embryonic turning* (*inv*), exhibit randomised laterality and situs inversus respectively. In *iv*, nodal cilia were present but immotile leading to no nodal flow and randomised laterality (Okada et al. 1999). In contrast, *inv* embryos had motile nodal cilia and leftward nodal flow, however the flow was much slower than in wild type embryos (Okada et al. 1999).

One experiment was designed to test whether the direction of nodal flow truly controlled sidedness. Nonaka and colleagues developed an artificial flow culture system; with this system they could culture developing embryos with the node exposed to a constant flow of culture medium (Nonaka et al. 2002). They tested the effects of slow and fast fluid flow in a leftward or rightward direction. In wild type embryos exposed to fast leftward, slow leftward or rightward fluid flow most embryos established normal situs (Nonaka et al. 2002). However, when wild type embryos were exposed to fast rightward fluid flow, most of them developed situs inversus (Nonaka et al. 2002). They also performed the same experiments in *iv/iv* embryos, which have immotile cilia. In these embryos, slow or fast leftward flow led mostly to the development of normal situs, whilst slow or fast rightward flow led mostly to the development of situs inversus (Nonaka et al. 2002). This showed that situs could be more completely reversed in the absence of endogenous

leftward nodal flow, and that randomised laterality of *iv/iv* embryos could be rescued with artificial flow. These findings provided direct evidence for the role of fluid flow in L-R pattern determination.

One of the questions left unanswered after this study was how the rotational movement of the nodal cilia generate a leftward fluid flow. Computation analysis provided insight into the fluid dynamics within the node (Cartwright et al. 2004). They calculated that the Reynolds number (reflecting the relative importance of inertial to viscous forces in the flow) of nodal flow is very low, which means that if the cilia were to stop rotating the flow would immediately stop (Cartwright et al. 2004). They further argued that if nodal cilia were posteriorly tilted it would result in a leftward flow similar to the one seen experimentally (Cartwright et al. 2004). Following on from this analysis two papers were published that confirm the posterior tilt of nodal cilia (Nonaka et al. 2005; Okada et al. 2005). Both of these papers also revealed that the nodal cilia localise to the posterior side of the apical plasma membranes of node cells; they both used immunofluorescent imaging to show the basal bodies are positioned posteriorly within the cells (Nonaka et al. 2005; Okada et al. 2005). The posterior tilting of nodal cilia allows for an “effective stroke” leftwards driving leftward fluid flow, where the cilium is extended almost vertically, and a less efficient rightwards “recovery stroke” where the cilia sweeps close to the cell surface (Okada et al. 2005).

1.2.3. Responding to nodal flow

Although it is clear that nodal flow is required for correct left-right patterning, the mechanism by which leftward fluid flow breaks symmetry remains uncertain. Two main hypothesis have been suggested: chemosensation and mechanosensation.

Chemosensation was originally proposed by Nonaka with the identification of nodal flow, where they suggested nodal flow could create a morphogen gradient stronger on the left side of the node (Nonaka et al. 1998). In experimental conditions, nodal flow has been shown capable of generating a concentration gradient (Okada et al. 2005). However, there has been no identification of a left-right morphogen since the initial proposal (Cartwright et al. 2020; Little and Norris 2021).

In 2003, McGrath and colleagues demonstrated that there are two populations of nodal cilia. They were analysing mice expressing GFP-tagged left-right dynein, the gene mutated in *iv* which encodes an outer arm axonemal dynein found in cilia (McGrath et al. 2003; Supp et al. 1997). Immunofluorescent imaging of lrdGFP revealed lrd is mostly found in centrally located nodal cilia, and a second subset of cilia at the peripheries of the node do not contain lrd (McGrath et al. 2003). Video microscopy confirmed the presence of central motile cilia and immotile cilia at the margins of the node, similar to the distribution of lrd (McGrath et al. 2003). They also showed the presence of PKD2 in nodal cilia that do not contain lrd, and suggested they may act as sensory cilia to detect and respond to flow (McGrath et al. 2003). PKD2 is known to act as a cation permeable channel, and had been shown to function as a mechanotransductor in renal epithelium, increasing intracellular calcium in response to fluid flow (Nauli et al.

2003). Based on this information, McGrath examined calcium transients around the embryonic node during development using a calcium binding dye; this revealed asymmetric left-sided calcium signal which was lost in *Ird*$^{GFP\Delta neo/GFP\Delta neo}$ and *Pkd2*$^{-/-}$ embryos (McGrath et al. 2003). They proposed the "two-cilia" model of mechanosensation, the idea that leftward fluid flow generated by the motile nodal cilia bends the immotile cilia on the left initiating a left sided cascade of events (McGrath et al. 2003).

A variation of the morphogen gradient hypothesis was proposed by Tanaka and colleagues; they visualised membrane-sheathed parcels, which they termed "nodal vesicular parcels", being released into the node and carried to the left with nodal flow (Tanaka et al. 2005). Their model suggested that NVPs are released into the node carrying signalling molecules, these get transported by nodal flow to the left and are fragmented close to the left wall through contact with immotile cilia (Tanaka et al. 2005).

These hypotheses rely on the leftward fluid flow generated by motile cilia, and the sensation of the signal by immotile cilia in the crown cells; however the underlying mechanism remains unclear.

1.2.4. Nodal signalling cascade: from the node to the LPM

The first asymmetric gene to be expressed in the node is thought to be *Cerl2* (Marques et al. 2004; Pearce et al. 1999). *Cerl2* was shown to have stronger expression on the right side of the mouse node, showing complementary expression to *Nodal* which is stronger on the left (Collignon et al. 1996; Lowe et al. 1996; Marques et al. 2004). CERL2 acts as a NODAL inhibitor, and prevents the further activation of *Nodal*, *Lefty2* and *Pitx2* in the lateral plate mesoderm (Marques et al. 2004). Initially, *Cerl2* is expressed symmetrically and its mRNA is preferentially decayed on the left side of the node in response to nodal flow (Nakamura et al. 2012). Recently, Hiroshi Hamada's lab showed that the Bicc1-Ccr4 RNA degradation complex binds the 3' UTR of *Cerl2* and is required for its degradation (Minegishi et al. 2021). They also showed that the degradation of *Cerl2* is dependent on the direction of nodal flow and on PKD2 function (Minegishi et al. 2021).

Downregulation of *Cerl2* on the left prevents the inhibition of NODAL activity in the left side of the node. Asymmetric left-sided expression of NODAL in the node leads to expression of NODAL in the left lateral plate mesoderm (LPM), where it activates the nodal signalling cascade (Little and Norris 2021; Norris 2012). In the lateral plate, NODAL upregulates expression of itself, *Pitx2* and *Lefty2* (Little and Norris 2021). LEFTY2 is an antagonist of NODAL, which diffuses further than NODAL and restricts its activity to the left LPM (Nakamura et al. 2006). PITX2 is a transcription factor and key effector of the nodal signalling cascade; it regulates the expression of genes driving cell proliferation and migration, essential to the correct patterning and positioning of organs such as the lungs (Grimes and Burdine 2017; Shiratori et al. 2006).

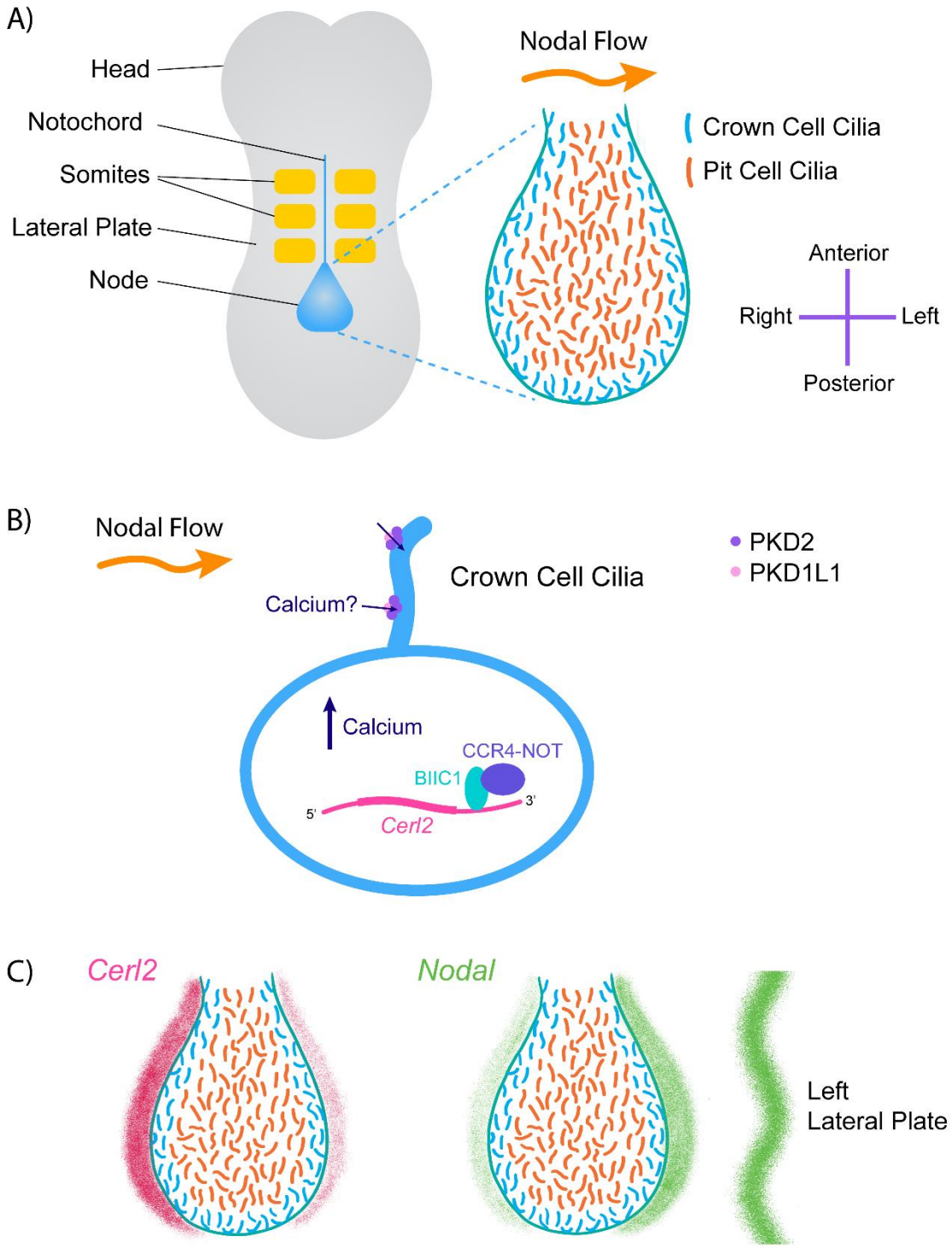


Figure 1.1 The nodal signalling cascade

A) An 8 d.p.c. embryo at the three somite stage, highlighting the position of the embryonic node. The teardrop shaped pit contains both motile pit cell cilia (orange) which rotate to generate leftward fluid flow, and immotile crown cell cilia (blue) which respond to nodal flow, B) Nodal flow is detected by PKD2 and likely PKD1L1 in the crown cell cilia on the left side of the node, this may lead to an influx of calcium into the cilia. In response to flow, intracellular calcium increases leading to upregulation of BIIC1 and the CCR4-NOT complex, together these bind the 3' UTR of *Cerl2* to stimulate its degradation. C) *Cerl2* is degraded on the left side of the node allowing NODAL to upregulate itself, leading to expression of NODAL in the left lateral plate.

1.3. Polycystins

The polycystins form one subfamily of the Transient Receptor Potential (TRP) superfamily of cation channels (Samanta et al. 2018). The TRP superfamily all contain at least 6 transmembrane domains and are cation permeable; they play key roles in responding to a variety of external stimuli including: light, sound, chemicals, temperature and touch (Venkatachalam and Montell 2007). They mediate transmembrane flux of cations, raising intracellular Ca2+ and Na+ which depolarises the cell (Hofherr and Köttgen 2011; Ramsey et al. 2006). The first member of the TRP family, was identified in 1969 when Cosens and Manning discovered drosophila that exhibited blindness in the presence of bright light; the mutant stain was named *transient receptor potential* (*trp*) (Cosens and Manning 1969; Samanta et al. 2018). The TRP superfamily is divided into seven subfamilies, based on sequence homology, across two groups (Ramsey et al. 2006; Samanta et al. 2018; Venkatachalam and Montell 2007). Group one includes: TRPC (Canonical), TRPV (Vanilloid), TRPM (Melastatin), TRPA (Ankyrin) and TRPN. Group two consists of: TRPP (Polycystic) and TRPML (Mucolipin). The group two TRP channels, which includes the polycystins, are also distinguished from the group one TRP channels by a large extracellular loop between transmembrane domains one and two (Venkatachalam and Montell 2007).

1.3.1. The family of polycystin proteins

The polycystins form the TRPP subfamily, also known as the polycystic kidney disease (PKD) proteins. The TRPP subfamily is said to be the most ancient of the TRP superfamily as members extend from yeast to mammals (Samanta et al. 2018; Venkatachalam and Montell 2007). The founding members of this group, PKD1 and PKD2, were first identified as disease causing genes in autosomal dominant polycystic kidney disease (Hofherr and Köttgen 2011; Hughes et al. 1995; Mochizuki et al. 1996; The European Polycystic Kidney Disease 1994). PKD1 is also referred to as TRPP1, or Polycystin1 (PC1), similarly PKD2 can be referred to as TRPP2 or Polycystin2 (PC2). For this thesis I will be using the PKD terminology throughout. Since their discovery, 6 other PKD proteins have been identified (Samanta et al. 2018). Four in the PKD1L family: PKD1L1, PKD1L2, PKD1L3, PKDREJ. Two in the PKD2L family: PKD2L1 and PKD2L2. The family of PKD2 and PKD2L proteins contain the 6 transmembrane domains, classically seen in TRP channels (Samanta et al. 2018). In comparison, PKD1 and PKD1L proteins all contain a large extracellular N-terminus and 11 transmembrane domains (Ramsey et al. 2006). The six C-terminal transmembrane domains in PKD1 proteins share homology with the transmembrane domains in PKD2 proteins (Venkatachalam and Montell 2007). PKD1 and PKD2 interact through coiled-coil domains in their C-terminal domains to form a cation permeable channel (Hanaoka et al. 2000). Structural analysis of the PKD1-PKD2 complex showed that the complex is assembled in a 1:3 ratio or PKD1:PKD2 (Su et al. 2018). PKD2 has also been shown to form a homodimeric complex (Shen et al. 2016).

1.3.2. The polycystins and disease

ADPKD is one of the most common causes of end stage kidney disease, mutations in PKD1 account for ~85% of cases and are associated with more severe renal disease (Gainullin et al. 2015). The severity of PKD1-mediated disease has been associated to the maturation of PKD1; loss of PKD2 has been shown to prevent PKD1 maturation and acts as a determinant of disease severity (Gainullin et al. 2015). Expression of PKD1 and PKD2 has been shown in kidney cilia, which may play a key role in the ADPKD pathogenesis (Douguet et al. 2019; Nauli et al. 2003). It is suggested that PKD1, with its large extracellular N-terminus, functions as a mechanosensor (Dalagiorgou et al. 2010; Nauli et al. 2003). This may lead to a conformational change in the complex, activating the associated PKD2 cation channels (Nauli et al. 2003). Recent work has suggested that PKD1 may act as a mechanosensor for extracellular stiffness (Nigro and Boletta 2021).

As well as its role in ADPKD, PKD2 is required for correct left-right pattern determination; this was discovered in the generation of a knockout allele of Pkd2 (Pennekamp et al. 2002). *Pkd2*$^{-/-}$ mice showed right isomerism of the lungs and randomised embryonic turning, heart looping and stomach situs (Pennekamp et al. 2002). Whilst PKD2 interacts with PKD1 in the kidney, *Pkd1*$^{-/-}$ embryos show no laterality defects and PKD1 is not detected in the embryonic node (Karcher et al. 2005). This left the question of whether PKD2 acted alone in the embryonic node for correct left right patterning. In 2010, Vogel and colleagues published data showing situs inversus in one third of *Pkd1l1*$^{-/-}$ mice (Vogel et al. 2010). Around the same time, Sarah Field (from the Norris lab) had been investigating the ENU induced mutant *rikishi* (*rks*), which exhibited left-right patterning defects; she discovered *rks* resulted from a mutation in *Pkd1l1* (Field et al. 2011).

1.3.3. Role of polycystins in L-R pattern determination

The first insight into the role of PKD2 in left-right patterning came from McGrath and colleagues. As described in section 1.2.3, they observed PKD2 localisation in both motile and immotile cilia in the node and proposed the PKD2-containing immotile cilia sense nodal flow initiating asymmetric calcium signaling (McGrath et al. 2003).

The role of PKD2 in nodal cilia was further examined by Yoshiba and colleagues. They used three transgenic mouse models to investigate regions of the node PKD2 is required: the first transgene was driven by the node and notochord specific enhancer of *Foxa2*, the second driven by the node specific enhancer of *Nodal* (NDE) active specifically in the crown cells around the edge of the node, and the third driven by the pit cell specific enhancer of *Foxa2* from dwarf gourami fish (*dgFoxa2*) (Yoshiba et al. 2012). When the transgenes were introduced to *Pkd2*$^{-/-}$ embryos, which show a loss of nodal signalling in the lateral plate mesoderm, left sided *Nodal* expression was restored using the *Foxa2* (whole node and notochord) and NDE (crown cell specific) transgenes (Yoshiba et al. 2012). However, when the pit cell specific transgene was tested in *Pkd2*$^{-/-}$ embryos, left sided expression of *Nodal* was not restored (Yoshiba et al. 2012). This provided key evidence that PKD2 is required specifically in the crown cells for correct left-right patterning. They examined the subcellular localisation of PKD2, using a transgenic mouse expressing PKD2-Venus, which revealed preferential expression to the cilia of crown cells (Yoshiba et al. 2012). To test PKD2 function in crown cell cilia, five PKD2 mutants were examined for ciliary localisation. *Pkd2*^{E442G}, also known as *lrm4,* was among these mutants and exhibits similar situs defects to *Pkd2*$^{-/-}$ embryos (Ermakov et al. 2009). PKD2^{E442G}

failed to localise to crown cell cilia and did not rescue left-sided *Nodal* expression in *Pkd2*$^{-/-}$ embryos; however, they showed PKD2^{E442G} retained channel activity (Yoshiba et al. 2012). Their results suggested nodal flow is sensed by crown cell cilia in a PKD2-dependant manner (Yoshiba et al. 2012). For the rest of this thesis, I will be using the term *Pkd2*^{lrm4} rather than *Pkd2*^{E442G}.

Phenotypic analysis of *Pkd1l1*$^{rks/rks}$ embryos showed situs defects that phenocopy *Pkd2*$^{lrm4/lrm4}$ embryos (Field et al. 2011). Both *Pkd1l1*$^{rks/rks}$ and *Pkd2*$^{lrm4/lrm4}$ embryos fail to show expression of the asymmetric genes *Nodal*, *Lefty2* and *Pitx2* in the left lateral plate (Field et al. 2011). Co-immunoprecipitation experiments showed interaction between a C-terminal fragment of PKD1L1 and full length PKD2, and *Pkd1l1* mRNA is strongly enriched in the embryonic node (Field et al. 2011). These findings suggested a joint role for PKD1L1 and PKD2 in the response to nodal flow in crown cell cilia.

Interestingly, when *Pkd1l1*$^{-/-}$ embryos (first described in Vogel et al. were analysed by the Norris lab, they showed an almost opposite situs phenotype (Grimes et al. 2016). Whilst the majority of *Pkd2*$^{lrm4/lrm4}$ and *Pkd1l1*$^{rks/rks}$ embryos exhibit right isomerism of the lungs, *Pkd1l1*$^{-/-}$ embryos exhibited mostly left lung isomerisms (Field et al. 2011; Grimes et al. 2016). *Pkd1l1*$^{-/-}$ embryos also showed bilateral activation of *Nodal* and downstream asymmetric genes *Pitx2* and *Lefty2* (Grimes et al. 2016). Genetic analysis revealed *Pkd1l1* to act as an upstream repressor of *Pkd2* (Grimes et al. 2016).

The *Pkd1l1*^{rks} point mutation lies within and structurally disrupts one of the two PKD domains in the extracellular N-terminus of PKD1L1 (Field et al. 2011; Grimes et al. 2016). PKD1 contains 16 PKD domains in its N-terminal

extracellular tail; human mutations in these PKD domains have been implicated in the onset of ADPKD (Ma et al. 2009). When tested, several PKD domain missense mutations altered the mechanical stability of the domains; they hypothesised this may affect the ability to sense mechanical signals (Ma et al. 2009). The *Pkd1l1*^{rks} mutation similarly affected mechanical properties of its PKD domain (Grimes et al. 2016).

1.4. Aims

The importance of PKD2 ciliary localisation in the embryonic node has been clearly demonstrated by the failure to undergo correct left-right patterning in *Pkd2*$^{lrm4/lrm4}$ embryos. PKD2 ciliary localisation is also essential for preventing cyst formation in the kidneys, ciliary exclusion of PKD2^{lrm4} leads to significant kidney cysts in 15.5 d.p.c. embryos.

In contrast, the role of PKD1L1 in left-right patterning is less well studied. It is clear from the situs phenotypes exhibited in *Pkd1l1*$^{-/-}$ and *Pkd1l1*$^{rks/rks}$ embryos, that PKD1L1 is essential for correct left-right patterning. However, little is known about the localisation and function of PKD1L1 during this process.

This thesis aims to provide insight into the mechanisms driving ciliary localisation of PKD2, through further investigation of PKD2^{lrm4}, and provide clarity into the localisation of PKD1L1 in the embryonic node. Exploring the relationship between PKD2 and PKD1L1 in the embryonic node aims to deepen our understanding of their roles in left-right pattern determination.

2. Materials & Methods

2.1. Mouse Strains

Animals were maintained in accordance with the Medical Research Council's guidance "Responsibility in the Use of Animal for Medical Research" (July 1993), and in accordance with the Animals (Scientific Procedures) Act, 1986.

Ethical approval for all studies involving mouse work was obtained as part of an application for a UK Home Office Project License (30/2980) and all mice were kept in accordance with UK Home Office welfare guidance and project license restrictions. Mice were bred in a specific pathogen-free environment at the Mary Lyon Centre, MRC Harwell Institute. Mice were maintained in controlled light with a 12 hour light/dark cycle, with controlled temperature (21°C±2°C) and humidity (55±10%). Mice had free access to water (10-12 ppm [parts per million] chlorine) and were fed ad libitum on a commercial diet (5.3% fat [corn oil], 21.2% protein, 57.4% carbohydrate, 4.6% fibre; Rat and Mouse Diet No. 3 [RM3], Special Diet Services, Essex, UK). Mice were socially housed in groups of 2-5 mice, males were singly housed after matings for welfare.

2.1.1. Background Strains

All mouse lines were maintained on a C57BL/6J background.

C57BL/6J (B6J) and C3H/HeH (C3H) wild type mice were used for experimental procedures.

2.1.2. *Pkd2^{lrm4}*

Left-right mutant 4 (lrm4) mice carry an A-to-G transversion in exon 7 of Pkd2 (Ermakov et al., 2009). This line was originally on a C3H/HeH background but had been backcrossed to C57BL/6J to produce a congenic line.

2.1.3. *Pkd2^{del}*

Obtained from a *Pkd2$^{tm1.2Tjwt}$* allele (Garcia-Gonzalez et al. 2010), in the presence of an Actin-cre recombinase allele. The LoxP sites flank exons 11-13; this was obtained by a previous lab member and is described in (Walker, 2016).

2.1.4. *Pkd2^{mNG}*

Designed and engineered at Harwell by the Transgenics core facility, targeted CRISPR-Cas9 insertion of the *mNeonGreen* fluorescent tag to the C-terminus of endogenous *Pkd2.* For simplicity, I refer to this allele as *Pkd2^{mNG}* throughout, rather than *Pkd2^{mNeonGreen}*.

2.1.5. *Pkd1l1$^{-/-}$*

This is the *Pkd1l1^{tm1lex}* used by Vogel and colleagues (Vogel et al. 2010), which was imported to the MLC.

2.1.6. *Pkd1l1^{mTFP1}*

Designed and engineered at Harwell by the Transgenics core facility, targeted CRISPR-Cas9 insertion of the *mTFP1* fluorescent tag to the C-terminus of endogenous *Pkd1l1.*

2.2. Dissection

For analysis by whole-mount in situ hybridisation (WISH) or whole-mount immunofluorescence (WIF), embryos were dissected out of the uterine horn and then the decidua in ice cold PBS under a Nikon SMZ800 microscope. Reichart's membrane was removed. If required, the yolk sac or partial embryonic tissue was taken and stored at -20°C for genotyping. Following dissection embryos were fixed in 4% PFA in PBS overnight at 4°C. Following fixation embryos were dehydrated using a methanol series with 5 minutes in each step: 25% methanol/PBS, 50% methanol/PBS, 75% methanol/PBS, 3 x 100% methanol. Dehydrated embryos were stored in methanol at -20°C until use.

2.2.1. Whole Mount Immunofluorescence (7.5-8.5 d.p.c)

Fixed embryos were selected and transferred to a 24 well plate, they were rehydrated through a methanol series with 5 minutes in each step: 75% methanol/PBS, 50% methanol/PBS, 25% methanol/PBS. Embryos were then washed in PBT (PBS, 0.1% Triton-X 100) 2 x 5 minutes before blocking in 3% BSA, 2.5% donkey serum in PBT for 3 hours at room temperature. Primary antibodies were prepared for each well diluted in: 150 µL block, 150 µL PBT (0.1% Triton-X 100), 300 µL PBS. Embryos were incubated with the primary antibody overnight at 4°C. The following day, embryos were washed 3 x in PBT

(0.04% Triton-X 100) for 1 hour each. Secondary antibodies were diluted 1:300 in: 150 µL block, 150 µL PBT (0.1% Triton-X 100), 300 µL PBS, and incubated with the embryos for 1 hour at room temperature in the dark. Embryos were washed 2 x in PBT (0.04% Triton-X 100) for 10 minutes, once in PBS for 10 minutes, and then left in fresh PBS overnight at 4°C before mounting onto SuperFrost plus slides (ThermoFisher J1800AMNZ). When mounting, the embryo was positioned flat, excess PBS was removed before the adding a drop of Hydromount (National Diagnostics NAT1324), vacuum grease was applied in two generous strips on the slide to prevent the embryo from being squished by the coverslip.

Slides were imaged using an upright Zeiss laser scanning confocal with Airyscan (LSM 710 with Airyscan), embryos were imaged using a 1.4x Plan-Apochromat oil objective with a numerical aperture of 1.4. Airyscan processing, sub setting of Z-stacks and maximum intensity projections were performed in ZEN black, images were then exported and edited further in Adobe Photoshop.

2.2.2. Whole Mount In Situ Hybridisation

Fixed embryos were rehydrated through a methanol series with 5 minutes in each step: 75% methanol/PBS, 50% methanol/PBS, 25% methanol/PBS. Samples were then washed in PBT (PBS, 0.1% Tween-20) for 3 x 5 minutes. Samples were bleached with 6% H_2O_2 in PBT for 1 hr, then washed in PBT (3 x 5 min).

Permeabilisation of embryos was carried out with 10 µg/mL Proteinase K in PBT for 5 minutes. Proteinase K was inactivated by a 20 mg/mL glycine in PBT for 5 minutes. Embryos were washed 2 x 5 minutes in PBT and post-fixed in 0.2% glutaraldehyde, 4% PFA in PBS for 20 minutes.

Embryos were washed 2 x 5 minutes in PBT and blocked for 1 hr at 70°C in pre-warmed pre-hybridisation solution (for 20 mL: 10 mL formamide, 5 mL 20x SSC pH 4.5, 5 mL water, 200 µL 10% Tween-20, 10 µL 100 mg/mL Heparin). Probes to be used were denatured in a 70°C heat block for 10 minutes, 12.5 µL probe was added to each well of pre-warmed hybridisation solution (2.5 mL pre-hybridisation solution, 25 µL 10 mg/mL yeast RNA, 25 µL 10 mg/mL salmon sperm DNA) and incubated with embryos overnight at 70°C.

Embryos were washed 2 x 30 minutes in Solution I (for 20 mL: 10 mL formamide, 4 mL 20X SSC pH 4.5, 1 mL 20% SDS, 5 mL water) at 70°C followed by one wash at 65°C. They were then washed 3 x 30 minutes in Solution III at 65°C (for 20 mL: 10 mL formamide, 2 mL 20x SSC pH 4.5, 8 mL water).

At room temperature, embryos were washed in TBST 3 x 5 minutes, then pre-blocked in 10% HISS (heat inactivated sheep serum) in TBST for 2.5 hours. Antibody (Anti-DIG-AP Fab Fragments (Roche 11093274910)) was blocked in 1% HISS in TBST with heat-inactivated embryo powder rotating for 1 hour at 4°C. Antibody and probe hybridisation occurred overnight in 1% HISS in TBST at 4°C. Sequential washing with TBST then occurred (3 x 5 minutes, 5 x 1 hour, overnight).

Embryos were then washed with filtered NTMT (for 50 mL: 1 mL 5 M NaCl, 5 mL 1 M Tris pH 9.5, 1.5 mL 1 M $MgCl_2$, 0.5 mL 10% Tween, 41 mL water) 1 x 5 minutes then 2 x 15 minutes. After washes, the stain solution (5 µL NBT/BCIP (Roche 11681451001) per mL NTMT) was added and allowed to develop in dark. Following stain development, embryos were washed in NTMT 2 x 5 minutes and post-fixed in 4% PFA in PBS for 30 min. Embryos were stored in PBT at 4°C prior to imaging.

2.2.3. Situs and Kidney Phenotyping

For situs analysis, 15.5 d.p.c. embryos were dissected from the uterine horn, the umbilical artery was severed for exsanguination and they were placed immediately into cold PBS on ice. Embryos were further dissected and imaged under a light microscope. Situs was assessed by the positioning of the heart, heart outflow tracts, lung lobation, and stomach. Kidneys were extracted and fixed in 10% neutral buffered formalin, before processing by the histology core facility. Tail tips were taken for genotyping.

2.3. Molecular Biology

2.3.1. Polymerase Chain Reaction

Polymerase Chain Reaction (PCR) was performed in order to amplify fragments of DNA for further use or analysis. Reactions were prepared using Platinum

SuperFi II DNA Polymerase (Invitrogen 12361010) following manufacturer's instructions.

2.3.2. Agarose Gel Electrophoresis

1% agarose, TBE gels containing 1x GelRed Nucleic Acid Stain were submerged in TBE buffer. Samples mixed with 6x Purple Gel Loading Dye (NEB B7024S) and 1 kb plus DNA ladder (NEB N0550S) were loaded into wells. A constant voltage of 120V was applied across the gel for 30-60 minutes to separate the linear DNA fragments by size. Fluorescence under UV light was visualised using a Gel Doc system (BioRad).

2.3.3. Purification of PCR products

PCR products were purified using the QIAquick PCR Purification Kit (QIAGEN 28106) following manufactures instructions. Bands excised from agarose gels were purified using Monarch DNA Gel Extraction Kit (NEB T1020S) following manufacturer's instructions.

2.3.4. Restriction Digest

Restriction endonucleases from NEB were used with the recommended buffer and incubation temperature. Reactions were routinely set up using 500 ng – 1 µg DNA, 2 µL restriction enzyme buffer (usually cutsmart (NEB B7204)), and 1 µ restriction endonuclease. Digests were usually performed at 37°C (unless otherwise stated in the product information) for 1 hour.

2.3.5. Ligation

Ligation of insert and vector was performed using the Quick Ligation Kit (NEB M2200S) following the manufacturer's protocol. A 3:1 ratio of insert:vector was used with 50-100 ng vector per ligation, the amount of insert was calculated using the NEB Ligation Calculator.

2.3.6. Bacterial Transformation

Bacterial transformation was performed using chemically competent *E. coli* DH5α cells. Either 1 µL plasmid DNA or 5 µL of ligation reaction was added to 50 µL bacterial cells in a pre-chilled 15 mL culture tube with cap. This was incubated on ice for 30 minutes, cells were then heat shocked at 42°C for 45 seconds and

placed back on ice for 2 minutes. 900 µL LB broth was added to the cells before incubation at 37°C in a shaker (225 RPM) for 1 hour. Cells were plated onto LB agar plates, with the appropriate selection antibiotic, and grown overnight. Steps were undertaken in a biological safety cabinet using good aseptic technique.

2.3.7. Inoculating bacterial cultures

Following transformation, individual bacterial colonies were picked from the plates using a P200 pipette tip and added to 5 mL LB broth containing the appropriate antibiotic in a 15 mL culture tube with cap. Cultures were grown overnight in a 37°C shaker (225 RPM).

2.3.8. Isolation of plasmid DNA

Plasmid DNA was isolated from bacterial cultures following the QIAprep Spin Miniprep Kit protocol (QIAGEN 27106).

2.3.9. DNA Sequencing

Purified DNA was sequenced by Source BioScience, using either their stock primers (T7, T3, M13 etc.) or primers targeted to the specific sequence of interest (designed following Source Bioscience recommendations). Samples were prepared according to their guidelines.

2.3.10. In-Situ probe synthesis

Sequence of interest was cloned into the pBluescript II KS (-) Plasmid from cDNA. Blue/white selection was used to confirm for insertion into the pBluescript plasmid. Plates were prepared for this with appropriate antibiotic-containing LB agar. Once set, 100 µl 100 mM IPTG and 35 µl 25 mg/mL X-Gal was spread onto the surface of the agar plates.

Probes were synthesised using a DIG RNA labelling mix (Roche 11277073910). Reactions were set up with 4 µl DIG labelling mix, 4 µl 10X transcription buffer, 1 µg linearized plasmid, 2 µl appropriate T3 or T7 RNA Polymerase (Thermofisher EP0101/EP0111), 0.25 µl RNase OUT™ (ThermoFisher 10777019) and RNase-free water to make up the reaction to 40 µl. Reaction was incubated at 37°C in a water bath for at least 3 hours. After incubation 100 µl water, 15 µl 3M sodium acetate (pH 5.2), and 300 µl ice-cold 100% ethanol was added. The mixture was

incubated overnight at -20°C in order to precipitate RNA. This was then centrifuged at 14,000 RPM for 20 minutes at 4°C. The resulting pellet was washed twice with 70% ethanol, with 5 minute spins at 14,000 RPM at 4°C between washes. The pellet was air-dried and re-suspended in 200 µl TE buffer. Synthesised probes were aliquoted and stored at -80°C.

2.3.11. RNA Extraction

Embryos were snap frozen on dry ice and stored at -80°C until use. RNA was extracted using the RNeasy Plus Micro Kit (QIAGEN 74034).

2.3.12. cDNA Synthesis

cDNA was synthesised from extracted RNA using SuperScript IV VILO Master Mix (Invitrogen 11766050) following manufacturer's instructions, 2 µg template RNA was used in a total reaction volume of 20 µL for a final concentration of ~100 ng/µL.

2.3.13. RT-PCR

RT-PCR was carried out the same as regular PCR, using cDNA synthesised from total RNA, in order to amplify fragments of DNA for further use or analysis. Reactions were prepared using Platinum SuperFi II DNA Polymerase (Invitrogen 12361010) following manufacturer's instructions.

2.3.14. 5' RACE

The SMARTer RACE 5'/3' kit (Takara Bio 634858) was used to generate RACE ready cDNA (from total RNA), 5' RACE PCR, and cloning of RACE fragments. Gene specific primers were designed following the recommended guidelines. All steps were performed following the manufacturer's instructions.

2.3.15. RT-qPCR

Brilliant III Ultra-Fast SYBR Green Low ROX qPCR Master Mix (Agilent 600892) was used to determine relative gene expression. Primers were designed to be uniquely complementary to the cDNA of interest. Standard curves and melting temperature analysis were carried out on each primer pair before use in quantification to ensure efficient amplification of a single product. cDNA was diluted to 10 ng/µL and an 18 µM primer mix was made (18 µL 100 µM forward

primer, 18 µL 100 µM reverse primer, 64 µL water) prior to preparing the qPCR reaction mixes. Reaction mixes consisted of 10 µL Brilliant III master mix, 0.4 µL 18 µM primer mix, 5 µL cDNA, 4.6 µL water. qPCR was carried out in a QuantStudio 5 Real-Time PCR System and analysed using QuantStudio Design & Analysis software.

2.3.16. Genotyping

Genotyping was carried out using assays designed by the MRC Harwell genotyping core facility. DNA was extracted from embryonic tissue using the following lysis buffer: 45 mL distilled water, 2.5 mL 1 M Tris-HCl pH 8, 2.5 mL 10% Tween-20, 100 µL 0.5 M EDTA pH 8. Samples were prepared into a 96 well plate, to each sample 25 µL of lysis buffer and 2 µL 20 mg/mL Proteinase K was added. The sample plate was sealed, briefly centrifuged and placed in the PCR programme with the following programme: 55°C for 90 minutes, 95°C for 5 minutes, 4°C hold. Quantity of DNA was measured using a NanoDrop Microvolume Spectrophotometer. DNA was diluted to 20 ng/µL for genotyping qPCR assays.

Pkd2^{lrm4} used an allelic discrimination qPCR assay, reaction mixes were prepared with 5 µL TaqMan GTXpress Master Mix, 2 µL assay, 3 µL DNA.

All other lines used TaqMan FAM-labelled qPCR assays, *Dot1* primers and VIC-labelled probe used as an internal control. Reaction mixes prepared with 5 µL TaqMan GTXpress Master Mix, 0.225 µL Dot1 Fw primer, 0.225 µL Dot1 Rv primer, 0.2 µL Dot1 probe, 0.3 µL assay, 4 µL DNA.

qPCR was performed on either a 7500 Real-Time PCR System or a QuantStudio 5 Real-Time PCR System using the genotyping programme for allelic discrimination and quantitation relative standard curve for TaqMan assays. CopyCaller software was used to analyse TaqMan assay results.

2.3.17. Primers

Table 2.1. List of *Pkd1l1* primers

RT-PCR Primers (Figure 3.4)	
Fw 1	GCAGGAAGCTGGTGTGCTTAC
Fw 2	ATGGTTGAGGCAAAGGCCAAGG
Fw F (Field)	ATGGATGTGGATGAGGACCA
Fw 3	GATGTGGATGAGGACCAGCAC
Fw 4	CCAGCTGGTTTGCTCTGTTTC
Fw 5	ATCCAGGCTAACCCAGAGC
Fw 6	GAACACAGGTAGTGAAGAAAGGC
Fw 7	TCTCCGATGGCTGTGTGAGC
Fw 8	CAAATGCTCAGGCAGAGTTGC
Fw 9	CTGAAGAAGGAAGTTCTCTGC
Fw 10	GCATTTCTCACACCTGCAACC
Rv F-R (Field)	GCCAATGTACACAGTCTCATC
Rv 1 (1-R)	GTCAGCAAAGGAAAGAGCTTCG
Gene Specific Primers for 5’ RACE (Figure 3.6)	
GSP1	GATTACGCCAAGCTTCAAGGTGGCCCTGGGAGGATGCTGAG
GSP2	GATTACGCCAAGCTTTTCCCAGAGCTGGAAGTGCCTGAGCA
Sequencing Primers for 5’ RACE (provided by Source BioScience)	
M13 Fw	TGTAAAACGACGGCCAGT
M13 Rv	CAGGAAACAGCTATGACC
RT-qPCR Primers	
5’ Short Fw	GTCACACAAAGGTCCCCACC
5’ Short Rv	AGGGTGACAGAGGCACTTGA
5’ Long Fw	GGACCCTTCTGTGGCCATTC
5’ Long Rv	CCATTCTCAGGCAACCTGCT
GAPDH Fw	CGGCCGCATCTTCTTGTG
GAPDH Rv	CCGACCTTCACCATTTTGTCTA
In-situ Probe Primers	
Fw (T3)	ATATATATTAACCCTCACTAAAGGGAAGCTGGTGTGCTTACTGTTGTA
Rv (T7)	ATATATTAATACGACTCACTATAGGGGCACAGCAGTCCTTGTCTATCA

2.4. Protein Biochemistry

2.4.1. Protein Extraction

Tissue samples were snap frozen on dry ice and stored at -80°c until use. Protein was extracted using an appropriate volume of RIPA buffer for the tissue size (100 µL - 1 mL). RIPA buffer: 50 mM Tris pH 7.5, 150 mM NaCl, 1% NP-40, 0.5% Deoxycholate. Tissues were lysed in FastPrep-24 2 mL tubes containing 1 mm silica spheres (MP Biomedicals 6912-050) using the FastPrep-24 5G homogenizer. Homogenised tissues were transferred to 1.5 mL microcentrifuge tubes and centrifuging at 13,000 RPM for 10 minutes at 4°C. The supernatant was collected and stored at -80°C until use.

Cells grown in 10 cm dishes were placed on ice and washed with PBS twice before adding 200 µL RIPA buffer. Plates were scraped and cells transferred to a 1.5 mL microcentrifuge tubes, this was left rotating at 4°C for 30 minutes before centrifuging at 13,000 RPM for 10 minutes at 4°C. The supernatant was collected and stored at -80°C until use.

2.4.2. Protein Quantification

Extracted protein was dilute 1:10 and 1:20 for quantification using the Pierce BCA Protein Assay Kit (Thermo Scientific 23227) following the microplate procedure in the user guide. After the 30 minute incubation at 37 °C, sample absorbance measured in an Agilent BioTek Epoch microplate spectrophotometer at 562 nm.

2.4.3. Immunoprecipitation

Immunoprecipitation was performed using the Dynabeads Protein G Immunoprecipitation Kit and following the manufacturer's protocol. One change was made to the protocol, samples were incubated with the magnetic bead-Ab complex for 1 hour at 4°C rather than 10 minutes at room temperature for optimum binding.

2.4.4. Western Blotting

Samples were prepared for western blot using NuPAGE 4x LDS sample buffer (Invitrogen NP0007) and 10 mM DTT. Samples were reduced and denatured by boiling at 95°C for 5 minutes. Samples and Precision Plus dual colour protein

standard (Bio-Rad 1610374) were loaded into NuPAGE 12%, Bis-Tris Mini Protein Gels (Invitrogen NP0341BOX). Gels were run in an XCell SureLock Mini-Cell electrophoresis system, filled with 1x NuPAGE MOPS SDS Running Buffer (Invitrogen NP0001). Gels were run at 150V for approximately 1 hour 30 minutes.

Gels were blotted using nitrocellulose membrane iBlot Transfer Stacks in an iBlot transfer device following manufacturer's instructions. The nitrocellulose membrane was then blocked for 1hr in 5% skimmed milk in TBST (Tris Buffered Saline (Bio-Rad 1706435), 10% Tween-20) with gently rocking. Primary antibodies were diluted in 5% skimmed milk and incubated with the membrane overnight at 4°C with gently rocking. Membranes were washed with TBST 3 x 5 minutes at room temperature with gently rocking. Secondary antibodies were diluted in 5% skimmed milk and incubated with membranes for 1 hour at room temperature in the dark with gentle rocking. The membranes were washed again with TBST (3 x 5 minutes) before drying and imaging on the Licor Odyssey CLx.

2.4.5. Pilot Protein Induction

The Human PKD2 C terminal fragment (aa 687-961) was cloned into the pRSETa and pET-32a expression plasmids, following steps described in methods section 2.3. This was transformed into BL21 DE3 pLysS *E. coli* bacterial cells following method 2.3.6.. Individual colonies were picked and grown in 5 mL cultures of LB, containing the appropriate selection antibiotics, overnight at 37°c in a shaking incubator (225 RPM). The following day, 1 mL of the overnight culture was used to inoculate a fresh 10 mL LB culture. Cells were incubated at either 30°C or 37°C, until they reached an OD_{600} reading of >0.6. A 1 mL sample (uninduced) was removed before adding IPTG to a final concentration of 1 mM, induced cells were left to grow for either 3 hours, 6 hours or overnight. Another 1 mL sample (induced) was taken before harvesting the rest of the cells by centrifugation at 4,000 RPM for 15 minutes at 4°C. The supernatant was discarded and the cells were resuspended in 1 mL of sonication buffer (20 mM Tris pH 8, 100 mM NaCl) before sonicating for 3 x 15 seconds on ice. The sample was centrifuged at 13,000 x g for 3 minutes at 4°C. The supernatant was collected (soluble), the pellet was resuspended in sonication buffer containing 8 M urea, incubated for 5 minutes at room temperature before sonicating for 3 x 15 seconds on ice (insoluble). The 1 mL uninduced and induced samples were centrifuged at 13,000

x g for 3 minutes at 4°C before resuspending in 200 µL PBS and 200 µL 2x LDS sample buffer. The samples were sonicated 3 x 15 seconds on ice.

For loading on SDS-PAGE, 20 µL of the uninduced and induced samples were placed into 1.5 mL microcentrifuge tubes, for soluble and insoluble samples 10 µL sample and 10 µL 2x LDS sample buffer were added to 1.5 mL microcentrifuge tubes, 10 mM DTT was added to each tube before boiling at 95°C for 5 minutes. All 20 µL samples were loaded into NuPAGE 12%, Bis-Tris Mini Protein Gels (Invitrogen NP0341BOX) for gel electrophoresis. SDS-PAGE gels were stained with InstantBlue Coomassie Protein Stain (ab119211) and imaged on a Gel Doc system (BioRad).

2.4.6 Large Scale Expression

Individual colonies were picked and grown in 15 mL cultures of LB, containing the appropriate selection antibiotics, overnight at 37°c in a shaking incubator (225 RPM). The following day, 12.5 mL of the culture was used to inoculate 250 mL fresh LB, and incubated at either 30°C or 37°C until they reached an OD_{600} reading of >0.6. Once reached, 1 mL sample was collected (uninduced), 1 mM IPTG was added and the cultures were grown for a further 3 hours. A 1 mL sample was taken (induced) before the cells were harvested by centrifugation at 8,000 RPM for 15 minutes, the supernatant was discarded and the pellet was stored at -20°C overnight. The pellet was resuspended in 10 mL sonication buffer (20 mM Tris pH 8, 100 mM NaCl), before sonicating for 3 x 15 seconds on ice and centrifuging at 21,000 x g for 30 minutes at 4°C. The supernatant was saved for purification.

For purification, a resin column was prepared with 2 mL HisPur NiNi-NTA resin (50% slurry = 1 mL bed volume). The column was equilibrated with 5 mL sonication buffer, and emptied by gravity, before plugging the bottom of the column and applying the harvested supernatant. This was mixed gently on a rotator for 30 minutes at room temperature, then emptied by gravity, the flowthrough was collected (flowthrough). The column was washed 3 x 3 mL sonication buffer containing 25 mM imidazole. The protein was eluted using sonication buffer containing 100 mM imidazole into 3 vials, 1 mL for elution 1 and 3, 2 mL for elution 2. The uninduced and induced samples were prepared as

described in section 2.4.5., the flowthrough and elution samples were prepared in the same way as the soluble and insoluble samples in section 2.4.5. All 20 µL samples were loaded into NuPAGE 12%, Bis-Tris Mini Protein Gels (Invitrogen NP0341BOX) for gel electrophoresis. SDS-PAGE gels were stained with InstantBlue Coomassie Protein Stain (ab119211) and imaged on a Gel Doc system (BioRad).

2.4.7 Antibody Affinity Purification

A desalting column was prepared and equilibrated with reduction buffer (0.1 M $NaPO_4$, 5 mM EDTA). The fusion protein, from the final large scale purification elutions, ~ 3 mL was applied to the column and allowed to drip under gravity. The protein was eluted with 4 mL reduction buffer, to this 25 mM DTT was added and the sample was incubated at 37°C for 90 minutes. A new desalting column was prepared and equilibrated with coupling buffer (50 mM Tris pH 8.5, 5 mM EDTA). 2 mL coupling buffer was added to the 4 mL reduced protein, 3 mL was applied to the column and eluted in 4 mL coupling buffer, this was repeated with the other 3 ml. 50 µL was saved for SDS-PAGE (uncoupled). Next, a resin column was prepared with a 2 mL bed volume of SulfoLink coupling resin (Thermo Scientific 20401). This was washed with 12 mL of coupling buffer, before plugging the bottom of the column and applying the 8 mL reduced protein. This was mixed gently on a rotator for 15 minutes at room temperature, before standing upright for 30 minutes. The column was drained and 50 µL was saved for SDS-PAGE (coupled), then washed with 6 mL coupling buffer. The column was capped again and 2 mL of coupling buffer containing 50 mM L-cysteine was applied to the column. This was mixed gently on a rotator for 15 minutes at room temperature, before standing upright for 30 minutes. The column was drained and washed with 12 mL 1 M NaCl, then 10 mL PBS. The column was capped and 15 mL antiserum and 5 mL PBS was added, this was mixed gently on a rotator for 45 minutes at room temperature. The column was washed with 12 mL PBS prior to elution using IgG elution buffer (Thermo Scientific 21004), 2 mL for elution 1 and 3, 4 mL for elution 2. Elutions were neutralized immediately by adding 100 µL 1 M Tris pH 9 per mL of elution. The column was washed with 6 mL IgG elution buffer, then washed with 12 mL PBS and stored in ~5 mL PBS at 4°C for future use.

The uncoupled, coupled and elution samples were prepared as previously described, run on SDS-PAGE. Gels were stained with InstantBlue Coomassie Protein Stain (ab119211) and imaged on a Gel Doc system (BioRad).

2.5. Cell Culture

All cell culture was performed in a class II laminar flow hood with strict aseptic technique. Cells were grown in 37°C incubators with 5% CO_2.

2.5.1. Cell Media

Appropriate media was used for each cell line, 10% FBS was added to media for general maintenance (Gibco 10500).

For HEK-293T, NIH-3T3 and MEF cells: DMEM (Dulbecco's Modified Eagle Medium), high glucose, GlutaMAX™ Supplement (Gibco 61965026).

1% PenStrep was added to MEF media.

For RPE-1 cells: Dulbecco′s Modified Eagle′s Medium/Nutrient Mixture F-12 Ham, With L-glutamine and sodium bicarbonate, without HEPES, liquid, sterile-filtered (Sigma D8062).

For IMCD-3 and IMCD-K2 cells: DMEM/F-12 (Dulbecco's Modified Eagle Medium/Nutrient Mixture F-12), GlutaMAX™ Supplement (Gibco 31331-028).

2.5.2. Thawing Cells

Vials of cells were removed from liquid nitrogen and placed on dry ice. When ready to thaw, cells were placed in a 37°C water bath until only a small piece of ice remained. Cells were mixed by gently pipetting and transferred to a prepared 10 cm dish containing 14 mL of media. Cells were left overnight to adhere before removing the media and replacing with 15 mL of fresh media.

2.5.3. Passaging Cells

Cells were grown in 10 cm dishes and split 2-3 times per week depending on cell growth, when they had reached 80-100% confluency. Cells were washed with PBS before adding 1.5 mL of pre-warmed trypsin - 0.05% trypsin (Gibco 25300054) was used for all cell lines except IMCD-3 and IMCD-K2 cells where 0.25% trypsin was used (Gibco 25200056). Cells were placed in the 37°C until

completely detached from the dish, then 8.5 mL media was added to neutralise the trypsin. Cells were resuspended gently using a stripette and seeded into fresh 10 cm dishes containing 12-15 mL media, cells were usually split at a dilution of 1:10-1:15.

2.5.4. Freezing Cells

Cells were expanded into 5 x 10 cm dishes and grown to ~90% confluency. Cells were washed with PBS and trypsinised as described above. Once resuspended in media, cells were collected into a 50 mL falcon and centrifuged at 1,000 RPM for 5 minutes to pellet the cells. Trypsin containing media was removed and the cell pellet was gently resuspended in 10 mL of freezing media (50% media, 40% FBS, 10% DMSO). Cells were divided into 10 cryovials and transferred to a Mr Frosty before placing in -80°C. After 48 hours, cells were transferred to liquid nitrogen for long term storage.

2.5.5. Making Mouse Embryonic Fibroblasts (MEFs)

14.5 d.p.c embryos were harvested in sterile PBS, each embryo was placed into one well of a 6 well plate containing 3 mL sterile PBS. The head and internal organs were removed, and a portion of the tail was retained for genotyping. Carcases were transferred to a wells of a sterile 6 well plate with 3 mL sterile PBS, and moved to the tissue culture hood. They were moved into another sterile 6 well plate containing 3 mL PBS to ensure they were thoroughly washed. Carcasses were moved to a sterile 6 well plate containing 500 µL of 0.25% Trypsin, a sterile scalpel was used to finely mince the carcass. 5 mL media was added and cells were homogenised further by pipetting before adding to a 10 cm dish containing 10 mL media and placing in the incubator. Media was changed the following day and then every 2-3 days until the cells were ready to split.

2.5.6. Immortalising MEFs

The SV40 large-T antigen plasmid was electroporated into primary MEFs to produce stable cell lines. Cells were trypsinised and resuspended as described above in 2.5.3 before counting with a Haemocytometer. A total of 5 x 10^6 cells were pelleted by centrifugation (1,000 RPM for 5 minutes) and resuspended in 200 µL Opti-MEM (11058021). This was transferred to the 0.4 cm BioRad cuvette,

1 µg of the SV40 plasmid was added before electroporation using the BioRad Gene Pulser Xcell pre-set programme for mammalian cells (0.2kV, 960uF; tau 20-25). After electroporation cells were transferred to a 6 well plate containing 2 mL media. Media was changed every 2-3 days until confluent. Once confluent, cells were split into a 10 cm dish and then passaged 10 times at a dilution of 1:10 before freezing.

2.5.7. Transfecting Cells

Cells were seeded into a 6 well plate the day before transfection. Transfection was carried out using Lipofectamine™ 3000 Transfection Reagent following manufacturer's instructions. DNA to be transfected was purified using the PureYield Plasmid Midiprep kit (Promega A2492). Transfected cells were left for 24 hours before replacing the media with serum free media to induce ciliation.

2.5.8. Immunocytochemistry

Sterile 13 mm coverslips were placed into wells of a 12 well plate, 1.8 mL media was added to each well. Cells were seeded into wells with coverslips (200 µL of confluent cells trypsinised and resuspended in 10 mL media) and allowed to grow until 80-90% confluent. Media was changed to serum free media and cells were serum starved for 48 hours to induce ciliation. Coverslips were washed with PBS twice, and fixed with ice cold methanol placed at -20°C for 5 minutes. After fixation, cells were washed three times with PBS and kept in PBS at 4°C until use. For immunofluorescent staining, cells were blocked with 4% BSA for 45 minutes at room temperature. Primary antibodies were diluted in 4% BSA in PBS and 100 µl per coverslip was dotted onto parafilm, coverslips were placed face down onto the primary antibody solution for 1 hr at room temperature. Coverslips were placed back into a 12 well plate and washed 3 x 5 minutes with PBS on a rocker. Secondary antibodies were diluted 1:400 in 4% BSA, 100 µl per coverslip was dotted onto parafilm and coverslips were placed face down onto the secondary antibody solution for 45 minutes at room temperature in the dark. Coverslips were placed back into a 12 well plate and washed 3 x 5 minutes with PBS on a rocker. DAPI stain was applied for 2 minutes before washing cells with distilled water and mounting onto slides, using Hydromount (National Diagnostics NAT1324) as mounting media.

2.6. Antibodies

Table 2.2. Primary and Secondary Antibodies

Anti-	Company	Product Code	Raised in	Dilution	Use
PKD2	Santa Cruz	sc-25749	Rabbit	1:200	Immunofluorescence
PKD2	In house	N/A	Rabbit	1:250	Immunofluorescence, Western Blot, Immunoprecipitation
PKD1L1	In house	N/A	Rabbit	1:250	Immunofluorescence
PKD1L1	In house	N/A	Mouse	1:250	Immunofluorescence
PKD1L1	Invitrogen	OSP00015W	Rabbit	1:250	Immunofluorescence
ARL13B	In house	N/A	Guinea Pig	1:500	Immunofluorescence
Guinea Pig IgG (H+L) 488	Jackson ImmunoResearch	711-545-148	Donkey	1:300	Immunofluorescence
Guinea Pig IgG (H+L) 594	Jackson ImmunoResearch	711-585-148	Donkey	1:300	Immunofluorescence
Mouse IgG (H+L) 488	Jackson ImmunoResearch	711-545-151	Donkey	1:300	Immunofluorescence
Mouse IgG (H+L) 594	Jackson ImmunoResearch	711-585-151	Donkey	1:300	Immunofluorescence
Rabbit IgG (H+L) 488	Jackson ImmunoResearch	711-545-152	Donkey	1:300	Immunofluorescence
Rabbit IgG (H+L) 594	Jackson ImmunoResearch	711-585-152	Donkey	1:300	Immunofluorescence
Rabbit IgG IRDye 680RD	LI-COR	926-68071	Goat	1:10,000	Western Blot
Rabbit IgG peroxidase conjugate	Sigma	A6154	Goat	1:10,000	Western Blot

3. Identifying Novel *Pkd1l1* Transcripts

3.1 Introduction

PKD1L1 was identified in 2002 by Takeshi Yuasa and colleagues, who published its sequence and chromosomal localisation (Yuasa et al. 2002). Through database searches, they identified genomic sequence on human chromosome 7 with a deduced amino acid sequence showing 43% similarity and 23% identity with PKD2 - suggestive of a novel polycystin. They used 5' and 3' RACE, with a human testis cDNA library, to identify a 9.3 kb cDNA encoding a 2849 amino acid protein. Phylogenetic analysis with the other 5 known polycystins at the time (PKD1, PKDREJ, PKD2, PKD2L1 and PKD2L2), showed it belonged to the PKD1 subfamily – hence it was named polycystic kidney disease 1 like 1 (Yuasa et al. 2002). As well as determining a full length cDNA sequence for Human *PKD1L1*, they characterised a partial cDNA sequence for mouse *Pkd1l1* that was 1594 bp in length (Yuasa et al. 2002).

Current transcripts of mouse *Pkd1l1*, are predictions from computational analysis. The Ensembl-predicted full length transcript (ID ENSMUST00000154153.8; Figure 3.1 B i) marks the 5' sequence as incomplete; it starts with a TTC, encoding a phenylalanine, which is not one of the three recognised start codons. In contrast, there are two predicted transcripts present in the NCBI Reference Sequence database (XM_017314870.1 and XM_036157131.1; Figure 3.1 B ii-iii), generated from different Genome Reference Consortium Mouse Builds, both containing methionine start sites. In previous work from the lab, Sarah Field identified an additional three exons at the 5' end of mouse *Pkd1l1* - with the first exon encoding a methionine start site (Figure 3.1 B iv; Field, 2009). Field's

identified exons are upstream of both the Ensembl and NCBI RefSeq transcripts (Field 2009).

The conflicting and seemingly incomplete predictions, led me to question what the true 5' sequence of *Pkd1l1* is. I initially set out to perform computational analyses to assess current predictions, and to use RT-PCR to test whether the predicted exons are present in mouse cDNA.

3.2 Results

3.2.1 Predicting previously un-annotated *Pkd1l1* 5' exons

Firstly, I used the Clustal Omega Multiple Sequence Alignment tool (COMSA) to investigate the alignment of predicted mouse *Pkd1l1* 5' exons to the human *PKD1L1* cDNA sequence. When aligned to human *PKD1L1*, the first Ensembl-predicted mouse exon correlates to human exon 7 (Figure 3.1 B i). NCBI Reference Sequence transcript XM_017314870.1 has two additional exons upstream of the Ensembl transcript; exon 1 aligns with sequence in the intron between human exons 5 and 6, whilst exon 2 aligns to a portion of human exon 6 (Figure 3.1 B ii). The updated NCBI Reference Sequence transcript XM_036157131.1 predicts a small 14 bp exon, upstream of the Ensembl transcript, which again aligns to human exon 6 (Figure 3.1 B iii). Field's exons 2 and 3 align with human exons 3 and 4; however, exon 1 aligns to the intron between human exons 1 and 2 (Figure 3.1 B iv).

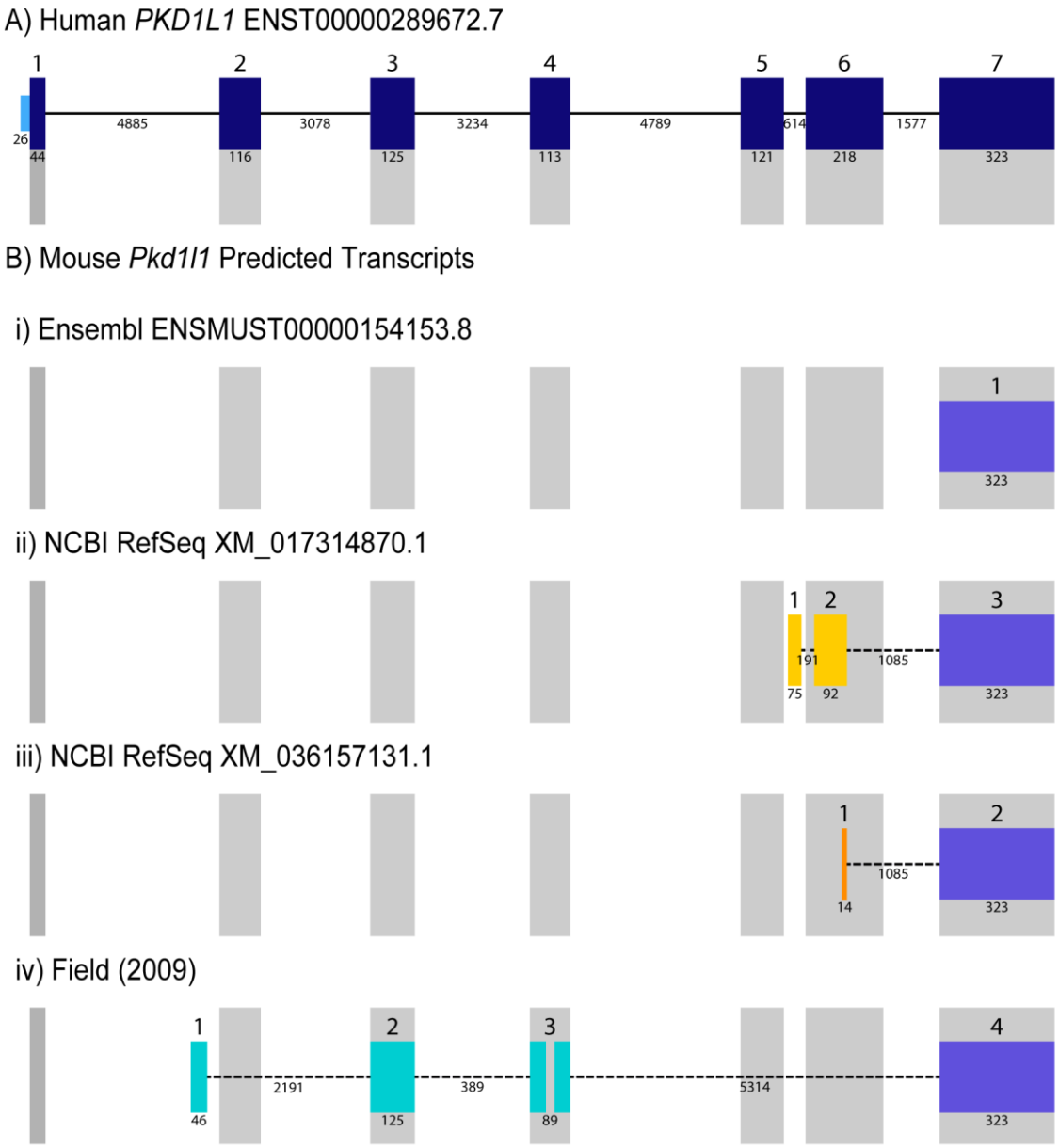


Figure 3.1 Schematic representation of Human *PKD1L1* and predicted Mouse *Pkd1l1* 5' exons

A) First 7 exons of Human *PKD1L1,* from Ensembl transcript ENST00000289672.7. Exons in dark blue, 5' UTR in light blue, solid black lines represent intronic regions. B) 5' exons of four predicted transcripts for mouse *Pkd1l1* aligned to the human transcript using Clustal Omega Multiple Sequence Alignment, dashed black lines represent intronic regions. (i) The first annotated exon from Ensembl transcript ENSMUST00000154153.8, purple, is a common exon for all predicted transcripts and aligns to Human exon 7. NCBI RefSeq has two predicted transcripts with additional 5' exons, (ii) XM_017314870.1 exons in yellow, and (iii) XM_036157131.1 exon in orange. (iv) Field's three identified exons in turquoise. Numbers above boxes indicate the exon number for each transcript, numbers below boxes and lines indicate the exon and intron lengths in base pairs.

Using the UCSC Genome Browser, I examined the 5' region of Human PKD1L1, looking for evidence of predicted mouse *Pkd1l1* 5' exons. Initial observations of multi-species alignments, showed *PKD1L1* to be well conserved across multiple species (Figure 3.2). As expected, primates such as the chimp, baboon and marmoset share the most sequence with human; however more distant species such as dogs and elephants still show strong conservation of exonic sequence (Figure 3.2). Most importantly, there is strong evidence for conservation of 5' *PKD1L1* exon 1 and exons 3-6 in mouse (Figure 3.2), although exon 2 doesn't show a distinct match between human and mouse. This finding encouraged me to look deeper into the mouse genome for these missing exons.

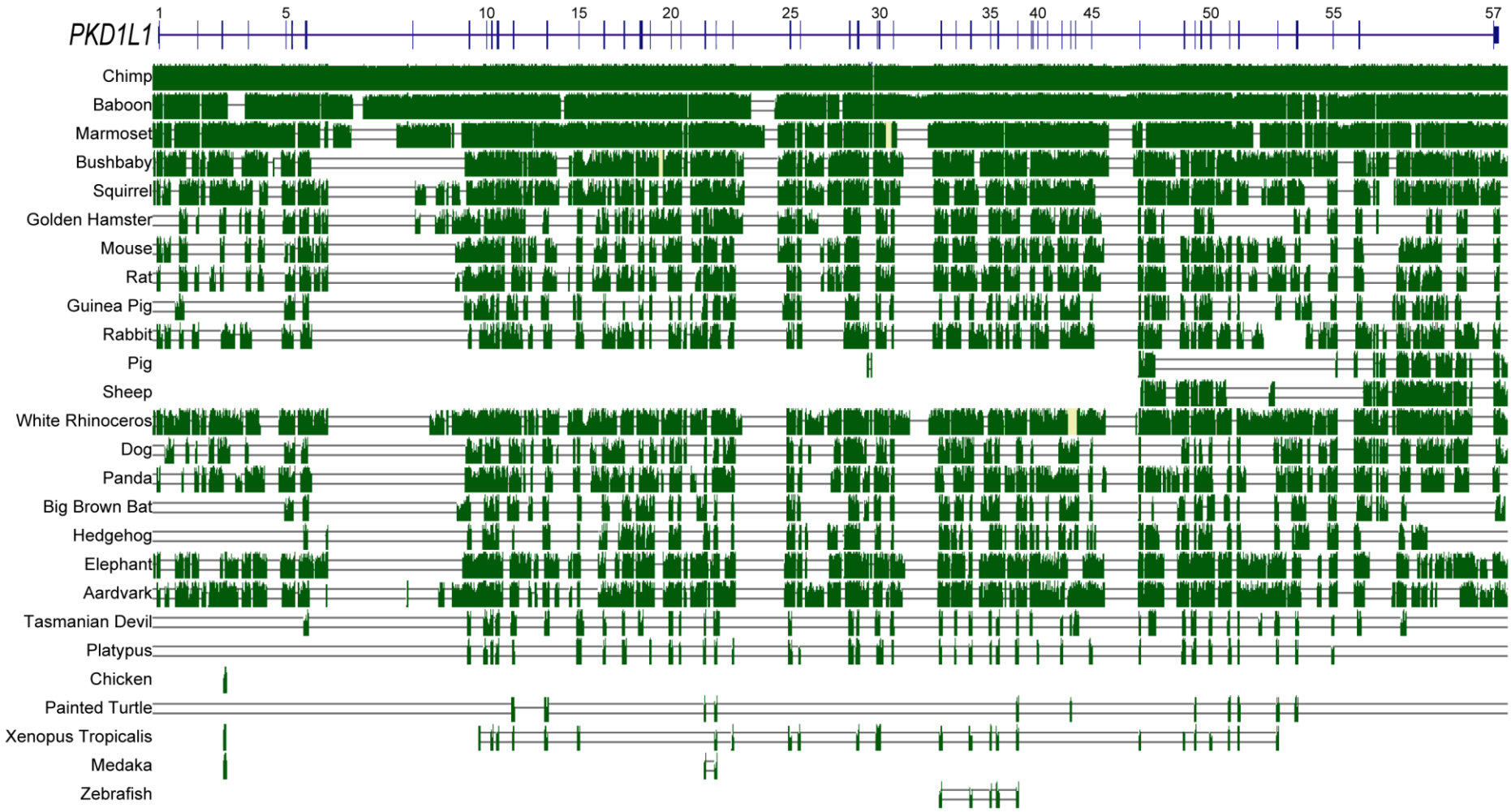


Figure 3.2 Multiple species alignment of *PKD1L1*

Overview of USCS Genome browser showing multiple species alignment in relation to Human *PKD1L1.*

To identify the missing exons in mouse, human *PKD1L1* exon sequences were individually blasted against the B6J mouse reference genome using the Ensembl BLAST/BLAT tool; the BLASTN search was used, with the sensitivity set to 'distant homologies'. Mouse *Pkd1l1* is located on Chromosome 11, between 8,776,708-8,923,266, therefore only BLASTN search results close to that location were considered. Aligning sequences were identified for exons 1, 3, 5 and 6 on chromosome 11, just upstream of *Pkd1l1*, indicating the presence of these exons in mouse. However, no results were returned for exons 2 or 4. BLASTN results for exons 1 and 3 identified full length alignments: 44 bp and 125 bp long respectively (Figure 3.3 B, C i, iii). Whereas the BLASTN result for exon 5 identified a 71 bp alignment, in contrast to the 121 bp human exon 5 input sequence. The alignment for exon 6 was 215 bp, 3 bp less than the 218 bp input sequence.

Having discovered the aligning sequences, I annotated them onto the B6J reference sequence to allow further examination of surrounding sequences. Using the COMSA tool, human exons 5 and 6 were aligned against the corresponding regions of mouse B6J reference sequence. This identified a 118 bp alignment for exon 5, and a 220 bp alignment for exon 6 (Figure 3.3 B, C v, vi). It seems likely that this method gives more accurate results due to the specificity of the input sequences, in comparison to the Ensembl BLAST/BLAT tool, which is identifying regions of alignment by searching against the whole mouse B6J reference genome.

To assess sequence alignment of exons 2 and 4, I again used the COMSA tool. The human exon 2 and 4 sequences were input individually, and aligned against the B6J mouse reference genome sequence between predicted exons 1 and 3

or 3 and 5. Both human exons 2 and 4 aligned to the B6J reference sequence, with a full-length alignment identified for exon 2 (Figure 3.3, B, C ii, iv).

When the human exon 4 sequence was aligned to the mouse sequence, 24 bp of the human sequence was missing in the mouse alignment sequence. It was absent from the B6J reference sequence, consistent with it being deleted in the mouse genome. The missing 24 bp are in the middle of mouse exon 4, and would lead to the loss of 8 amino acids in the translated protein (Figure 3.3 B, C iv). To determine whether this deletion was specific to the mouse genome, I used the Ensembl BLAST/BLAT and COMSA tools to check for the presence of the 24 bp in other mammals. Interestingly, the 24 bp missing in mouse was also absent from the rat, shrew, hamster, squirrel, bushbaby and chimp genomes. However, the 24 bp was present in the baboon genome and only 3bp was missing in marmoset.

The 26 bp 5' UTR from human *PKD1L1* aligned to the B6J reference genome upstream of exon 1 (Figure 3.3 B, C vii). This suggests that I have identified the start site of *Pkd1l1* in mouse; however, 26 bp is very short for a 5' UTR, so it seems likely there is further unidentified 5' UTR upstream.

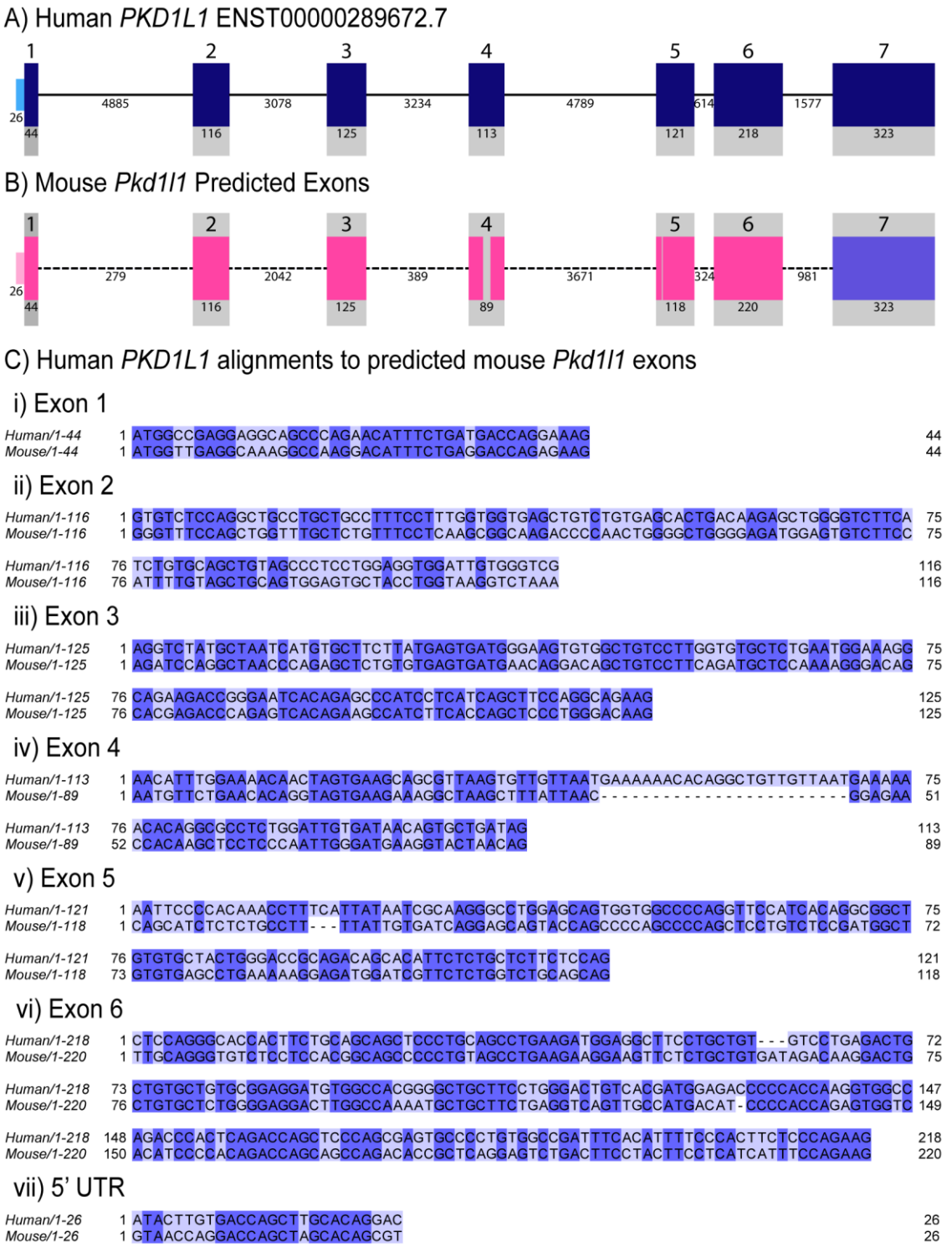


Figure 3.3 Sequence alignments of predicted *Pkd1l1* 5' exons.

A) Schematic representation of the first 7 exons of Human *PKD1L1,* from Ensembl transcript ENST00000289672.7. Exons in dark blue, 5' UTR in light blue, solid black lines represent intronic regions. B) Schematic representation of predicted mouse *Pkd1l1* exons, aligned to the human sequence. Predicted exons in pink, first exon from Ensembl transcript ENSMUST00000154153.8 in purple, predicted 5' UTR in light pink, dashed black lines represent intronic regions. C) Alignments of Human *PKD1L1* and predicted mouse *Pkd1l1* exon sequences and 5'UTR sequence. Alignments created in Jalview using Clustal Omega alignment with default settings. Purple indicates an exact match, light purple indicates a mismatch, and dashes represent gaps in the sequence alignment.

3.2.2 Validating predicted *Pkd1l1* exons

In order to assess the presence of predicted *Pkd1l1* exons in mouse RNA, RT-PCR was carried out using cDNA synthesised from 8 d.p.c mouse embryo total RNA: both C3H and B6J RNA was used, to assess any differences between mouse strains. A forward primer was designed within each of the predicted exons, including both my predictions as well as NCBI and Field predicted exons - Field's previously used forward and reverse primers were also included in the experiment (Figure 3.4 A). As 5' UTRs are generally longer than 26 bp, often exceeding 100 bp, forward primer 1 was designed 5-25bp upstream of the 26 bp 5' UTR alignment to test whether additional 5' sequence could be identified.

The most intense band visualised for each forward primer, except 8, matched the predicted sizes. The band detected using forward primer 8, designed for NCBI exon 1, is larger than predicted; however, the size seems to correlate with the highest band detected for forward primers 1, 2, 4, 5, 6 and 7. No band was detected for Field exon 1 using B6J cDNA for RT-PCR, yet a faint band can be seen for C3H cDNA (Figure 3.4 B, C). The PCRs for Field exon 1 were repeated and re-run on an agarose gel, with more PCR product loaded, to extract sufficient DNA for sequencing (Figure 3.5 B). Multiple bands were detected for most primer pairs, with only a single band detected for forward primers 9 and 10 at the expected size. In order to assess the nature of these PCR products the strongest band for each lane was excised and sent for sequencing, along with a selection of fainter bands from both above and below (Figure 3.5 A).

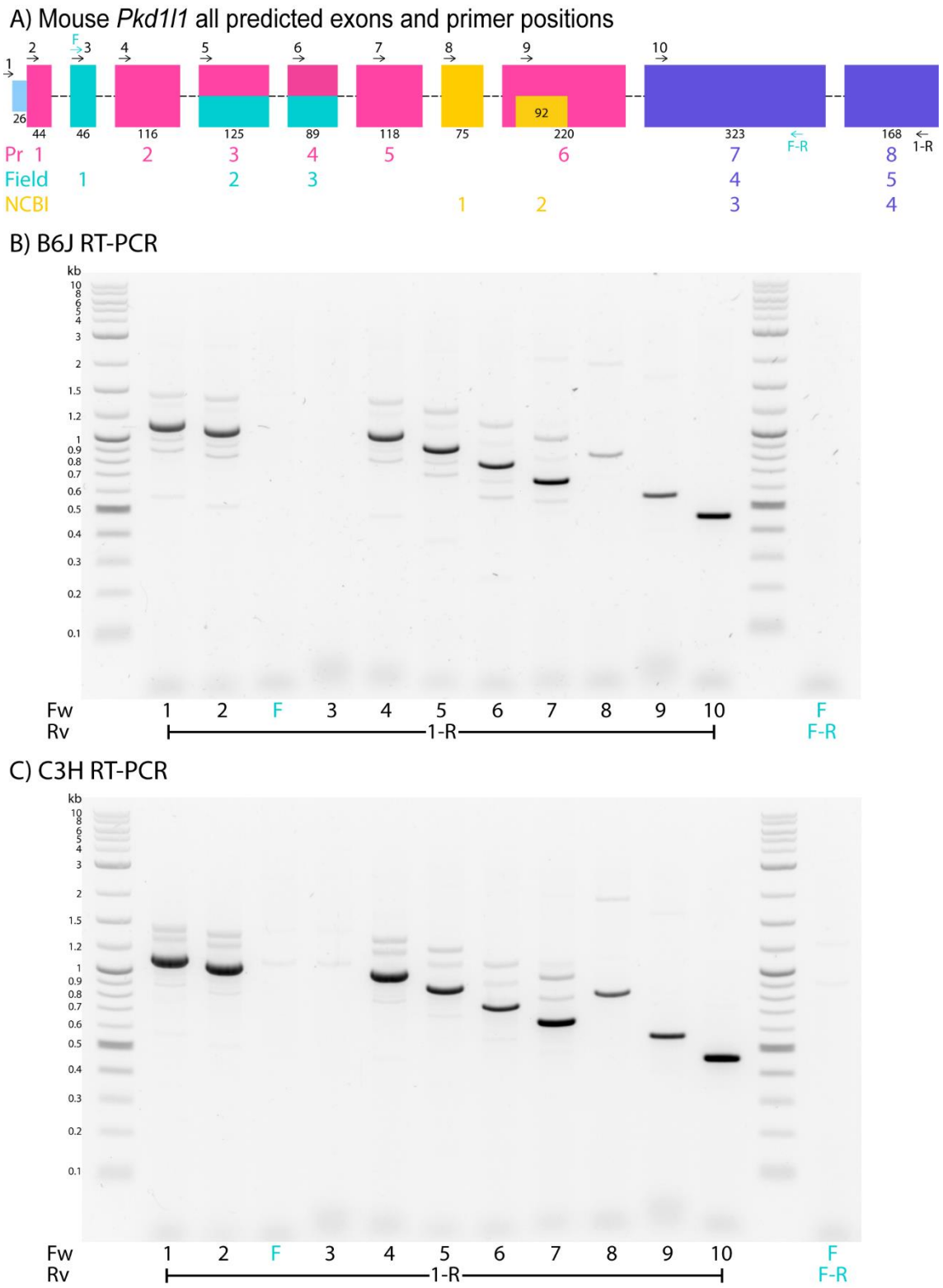


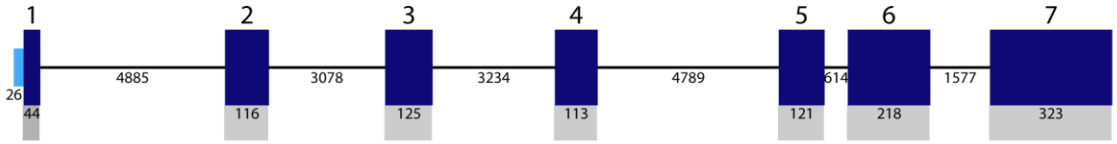
Figure 3.4 RT-PCR of predicted mouse *Pkd1l1* exons

A) Schematic representation of all predicted mouse *Pkd1l1* 5' exons, predicted exons from BLASTN and multiple sequence alignments in pink, 5' UTR alignment in light pink, Field exons in turquoise, NCBI XM_017314870.1 exons in yellow. B) RT-PCR of *Pkd1l1* using mouse B6J 8 d.p.c. cDNA. C) RT-PCR of *Pkd1l1* using mouse C3H 8 d.p.c. cDNA.

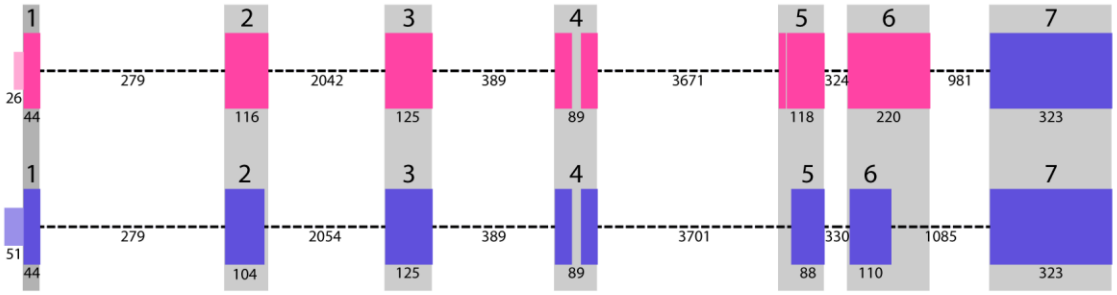
Sequencing results, from the most intense bands, was consistent with one main *Pkd1l1* transcript containing the exons predicted from the sequence alignment (Figure 3.3 B). This included Field exons 2 and 3 (Figure 3.1 B iv), and a larger exon that includes and extends NCBI exon 2 (Figure 3.1 B ii). However, not all exons corresponded to the sizes predicted from the alignments (Figure 3.5 B, C). Sequencing showed exons 1, 3 and 4 matched the exact size and sequence from the predicted alignment, whilst exons 2, 5 and 6 were smaller than predicted. Exon 2 had a predicted size of 116 bp from the alignment, whilst sequencing showed a 104 bp exon. Exon 5 was predicted as 118 bp but sequenced as 88 bp, 30 bp less than predicted. Exon 6 was predicted to be 220 bp, yet sequencing showed this exon to be half the expected size at 110 bp in length. Whilst all three of these exons are smaller than predicted, the size difference between these exons and the aligning human *PKD1L1* exon is always a multiple of three, indicating that the sequence remains in frame.

Sequencing of the CH3 derived bands detected using primers in Field exon 1, gave reads that continue through intronic sequence into predicted exon 2. This is suggestive of a retained intron between predicted exons 1 and 2, which was only detected at low levels using primers for Field exon 1. Sequencing results of the band detected using forward primer 8, starting in NCBI exon 1, included the 330bp intron between predicted exons 5 and 6. The same intron was also present in sequence from the highest band for forward primers 1, 2, 4, 5, 6 and 7. Bands below the most intense bands, showed splicing variants skipping predicted exon 6, exons 5 and 6, or exons 5, 6 and 7.

A) Human *PKD1L1* ENST00000289672.7



B) Mouse *Pkd1l1* Predicted vs Sequenced Exons



C) Mouse *Pkd1l1* new exon sequences

i) 5' UTR

0	GCAGGAAGCTGGTGTGCTTACTGTTGTAACCAGGACCAGCTAGCACAGCGT	51

ii) Exon 1

0	ATGGTTGAGGCAAAGGCCAAGGACATTTCTGAGGACCAGAGAAG	44

iii) Exon 2

0	GGGTTTCCAGCTGGTTTGCTCTGTTTCCTCAAGCGGCAAGACCCCAACTGGG	52
53	GCTGGGGAGATGGAGTGTCTTCCATTTTGTAGCTGCAGTGGAGTGCTACCTG	104

iv) Exon 3

0	AGATCCAGGCTAACCCAGAGCTCTGTGTGAGTGATGAACAGGACAGCTGT	50
51	CCTTCAGATGCTCCAAAAGGGACAGCACGAGACCCAGAGTCACAGAAGCC	100
101	ATCTTCACCAGCTCCCTGGGACAAG	125

v) Exon 4

0	AATGTTCTGAACACAGGTAGTGAAGAAAGGCTAAGCTTTATTAACGGAGA	50
51	ACCACAAGCTCCTCCCAATTGGGATGAAGGTACTAACAG	89

vi) Exon 5

0	GAGCAGTACCAGCCCCAGCCCCAGCTCCTGTCTCCGATGGCTGTGTGAGC	50
51	CTGAAAAAGGAGATGGATCGTTCTCTGGTCTGCAGCAG	88

vii) Exon 6

0	GGTGTCTCCTCCACGGCAGCCCCCTGTAGCCTGAAGAAGGAAGTTCTCTG	50
51	CTGTGATAGACAAGGACTGCTGTGCTCTGGGGAGGACTTGGCCAAAATGC	100
101	TGCTTCTGAG	110

Figure 3.5 Mouse *Pkd1l1* 5' exons confirmed by Sanger sequencing

A) Schematic representation of the first 7 exons of Human *PKD1L1,* from Ensembl transcript ENST00000289672.7. Exons in dark blue, 5' UTR in light blue, solid black lines represent intronic regions. B) Schematic representation of all predicted mouse *Pkd1l1* 5' exons (top) vs exons confirmed by Sanger sequencing (bottom). Predicted exons from BLASTN and multiple sequence alignments in pink, 5'UTR alignment in light pink. Sequenced exons in purple, sequenced 5' UTR in light purple. C) Sequence of each exon and the 5' UTR, confirmed by Sanger sequencing of excised bands from RT-PCR.

3.2.3 5’ RACE identifies an additional *Pkd1l1* exon and transcript

As I had amplified and sequenced additional unpredicted *Pkd1l1* 5’ UTR from mouse RNA, I wanted to ascertain the full 5’ UTR sequence. To do this, I performed 5’ RACE (rapid amplification of cDNA ends) using the Takara SMARTer RACE 5’/3’ Kit. Total RNA was used, from B6J and C3H 8 d.p.c mouse embryos, and 5’ RACE-ready cDNA was prepared (Methods 2.3.14). Two gene specific reverse primers (GSPs) were designed against exon 7, GSP1 and GSP2 (Figure 3.6), using the kit’s primer design recommendations. 5’ RACE PCR was performed using the GSPs, and products were visualised on agarose gels (Figure 3.6 B). Based on previous sequencing data (Figure 3.5), the product was predicted to be at least 800 bp. One strong band was visualised at approximately 1050 bp, just above the 1 kb marker in the ladder (Figure 3.6 B). GSP2 only showed the strong 1050 bp band when amplifying C3H RACE-ready cDNA; no strong bands were visualised using this primer in B6J RACE-ready cDNA. The most intense band in the other three lanes was excised and cloned into the provided pRACE vector, following the kit protocol. Individual cDNA clones, from the three bands excised, were isolated and sequenced.

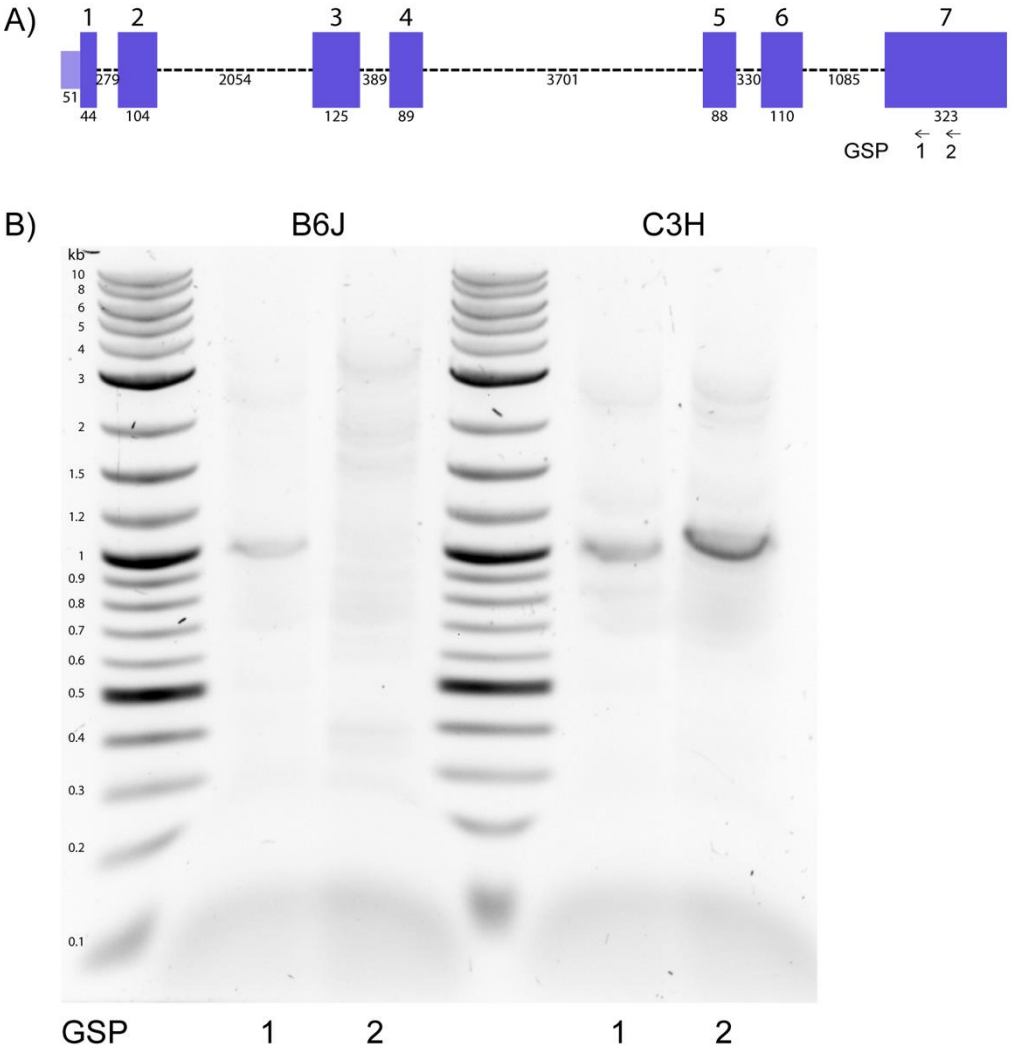


Figure 3.6 5' RACE of mouse *Pkd1l1*

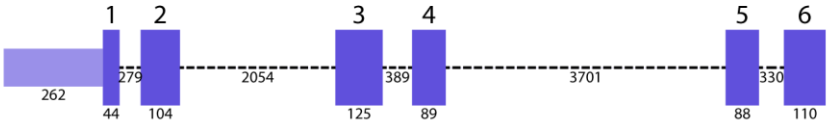
A) Schematic representation of the first 7 sequenced exons of mouse *Pkd1l1*, showing the positions of the two gene specific primers (GSP) designed against exon 7. Exons in purple, 5' UTR in light purple. B) 5' RACE PCR of mouse *Pkd1l1* using RACE ready cDNA, generated from B6J and C3H 8 d.p.c RNA.

Strikingly, analysis of the 5' RACE cDNA clone sequencing revealed the presence of two distinct 5' sequences. From this point, I will refer to the two sequences as 5' short and 5' long for simplicity: these are depicted in Figure 3.7 (Figure 3.7 A, B). Initially, 3 clones from each of the excised bands were sequenced; 5' long was only identified in clones derived from the C3H bands, and wasn't detected in clones from the excised B6J band. An additional 9 B6J and 9 C3H cDNA clones were sequenced for further analysis. All 12 C3H clones showed the 5' long sequence. In contrast, half of the B6J clones showed the 5' short sequence and the other half showed the 5' long sequence.

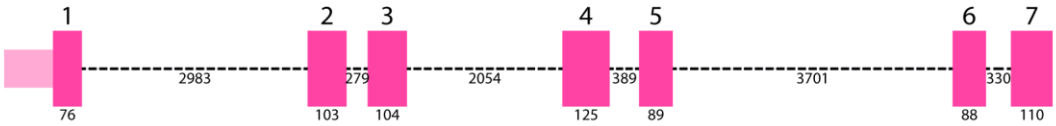
Analysis of the 5' short sequencing data revealed an extra 211 bp of 5' UTR sequence in both B6J and C3H samples (Figure 3.5 C i, Figure 3.7 A), explaining the 1 kb RACE result (Figure 3.6 B). The additional sequence does not contain any Kozak consensus sequences, and all three frames contain multiple stop codons, suggesting this region is not transcribed. In light of the Kozak sequence starting at bp 263, the previously predicted transcriptional start site appears to be correct.

Analysis of the 5' long sequencing data revealed the presence of an additional 5' exon, which splices into the 5' UTR of the previously sequenced exon 1 (Figure 3.5 B). This additional exon contains a Kozak consensus sequence, which is in frame with the rest of *Pkd1l1*. If translated, the additional 5' sequence would encode an additional 45 amino acids in comparison to my originally described sequence.

A) Short 5’



B) Long 5’



C) Short 5’ - UTR and Exon 1 sequence

```
0    AGACCTTAATCTGTCAATGCAGTCACACAAAGGTCCCCACCTACATAAGC   50
51   GTGTCTCCTAAGGAGAGAGTGGAGACCTAAAAGTGTTCTGATTAGCGAAG  100
101  TATTGCTGCAGTATCTCTCTTTCTCTTGTATGATGTGTACCCCACATGAG  150
151  CTCTCAGCACAGAGATTAGAAGCCTCAAGTGCCTCTGTCACCCTGTCTTC  200
201  CAGTGAATGTGGCAGGAAGCTGGTGTGCTTACTGTTGTAACCAGGACCAG  250
251  CTAGCACAGCGTATGGTTGAGGCAAAGGCCAAGGACATTTCTGAGGACCA  300
301  GAGAAG                                              306
```

D) Long 5’ - UTR, Exon 1 and Exon 2 sequence

```
0    ACAGAGGGCCTGCCCTGCCTCTTTCAGGACCCTTCTGTGGCCATTCCCCC   50
51   ACCAGCACTCACTCAGCAGAGCCAGTTGAGATCTTTATGCTGAAGAGAAG  100
101  ACACCCTGGGAGCAGGTTGCCTGAGAATGGGCTGGAGGGTACTCATCACA  150
151  GCCTGGGCTCTGTTCTTAGAGCACTCCTCTCCAGGAATCAGCTCGAGCAA  200
201  CTTGAATGTGGCAGGAAGCTGGTGTGCTTACTGTTGTAACCAGGACCAGC  250
251  TAGCACAGCGTATGGTTGAGGCAAAGGCCAAGGACATTTCTGAGGACCAG  300
301  AGAAG                                               305
```

Figure 3.7 Two 5’ sequences identified by 5’ RACE
Schematic representation of the first 6/7 exons of the two identified mouse *Pkd1l1* 5’ sequences defined as 5’ short (A) and 5’ long (B). Exons in purple and pink, 5’ UTRs in light purple and light pink. C) Sequence of the 5’ UTR and exon 1 of the short 5’ variant, 5’ UTR highlighted in light purple, exon 1 highlighted in purple, overlap with exon 2 of the long 5’ variant underlined in pink. D) Sequence of the 5’ UTR, exon 1 and exon 2 of the long 5’ variant, 5’ UTR highlighted in light pink, exons highlighted in pink, splicing site indicated by a vertical dashed line, overlap with the short 5’ UTR underlined in light purple, overlap with the short 5’ exon 1 underlined in purple.

To assess whether the additional 5' UTR and exon identified in the long 5' variant is specific to mouse, I performed a BLASTN search of the 5' UTR and exon 1 sequence against multiple species. I did not find any matches in human, chimpanzee, gorilla or marmoset. However, alignments were found for most other primates including: colobus monkeys, snub-nosed monkeys, lemurs, baboons, gibbons and macaques. Alignments were found for all mouse strains, as well as other rodents including: rat, rabbit, hamster, gerbil, chinchilla and beaver. There were also alignments identified in other mammals including: leopard, lynx, cat, ferret, polar bear, tiger, sea lion, lion and elephant. No alignments were found for even-toed ungulates or marsupials.

Due to the alignments found for many primates and other mammals, I decided to further investigate the human sequence. Using the COMSA tool, I aligned the 5' UTR and exon 1 from the long 5' mouse variant against 25 kb of sequence upstream of the annotated human 5' UTR. One match was found, with a 60% identity, just under 4 kb away from the annotated human 5' UTR (Figure 3.8).

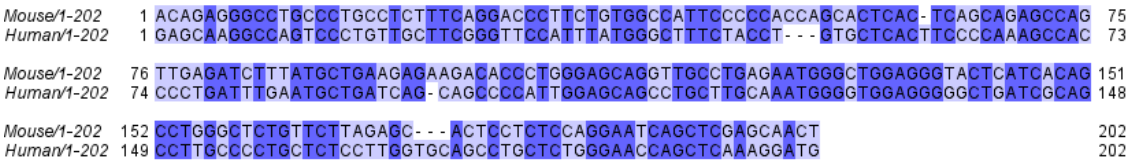


Figure 3.8 Sequence alignment of mouse 5' long variant and sequence upstream of annotated *PKD1L1*

Alignment of mouse Pkd1l1 5' long variant 5' UTR and exon 1 sequence with sequence from the human reference genome. The aligning sequence was identified just under 4 kb upstream of the annotated human PKD1L1 5' UTR sequence. Alignments created in Jalview using Clustal Omega alignment with default settings. Purple indicates an exact match, light purple indicates a mismatch, and dashes represent gaps in the sequence alignment.

Using the BLASTN tool, inputting the aligning human sequence, matches were found for all primates; including those not identified in searches using the mouse sequence. Interestingly, the human sequence BLASTN search didn't reveal any alignments in rats, mice or lagomorphs. However, there were some overlapping results for other rodents when compared with the mouse search results; gerbil, prairie vole and hamster. This suggests that there is enough variation between human and mouse for BLASTN searches to fail to recognise homology, yet there is some overlap between humans and rodents.

3.2.4 Confirmation of additional 5' exons in RNA-Seq data

Around the time I was investigating the newly identified exons, another member of the lab received RNA-Seq data from staged 7.5-8.5 d.p.c. B6J embryos. Briefly, RNA extracted from multiple B6J embryos at six different stages (LS, LHF, 1ss, 3ss, 4ss and 6ss), had been sent to the Wellcome Centre for Human Genetics in Oxford for RNA-Seq; each dataset is from one embryo. I mined this RNA-Seq data looking at *Pkd1l1* coverage. All of the RNA-Seq datasets showed the same findings; for simplicity all of the data shown is from one embryo at the 1ss stage (Figures 3.9 - 3.12).

Integrated genome viewer (IGV) software was used to view the RNA-Seq data. Looking at an overview of the sequence between *Hus1* and the previously described start of *Pkd1l1* on mouse genome build GRCm38/mm10, 5 RNA-Seq read peaks are visible (Figure 3.9 A). These are of a similar height to the peaks that align with annotated *Pkd1l1* exons, suggesting that they are linked to *Pkd1l1*. The RefSeq for this mouse genome build (GRCm38/mm10) in IGV is the same sequence as NCBI XM_017314870.1.

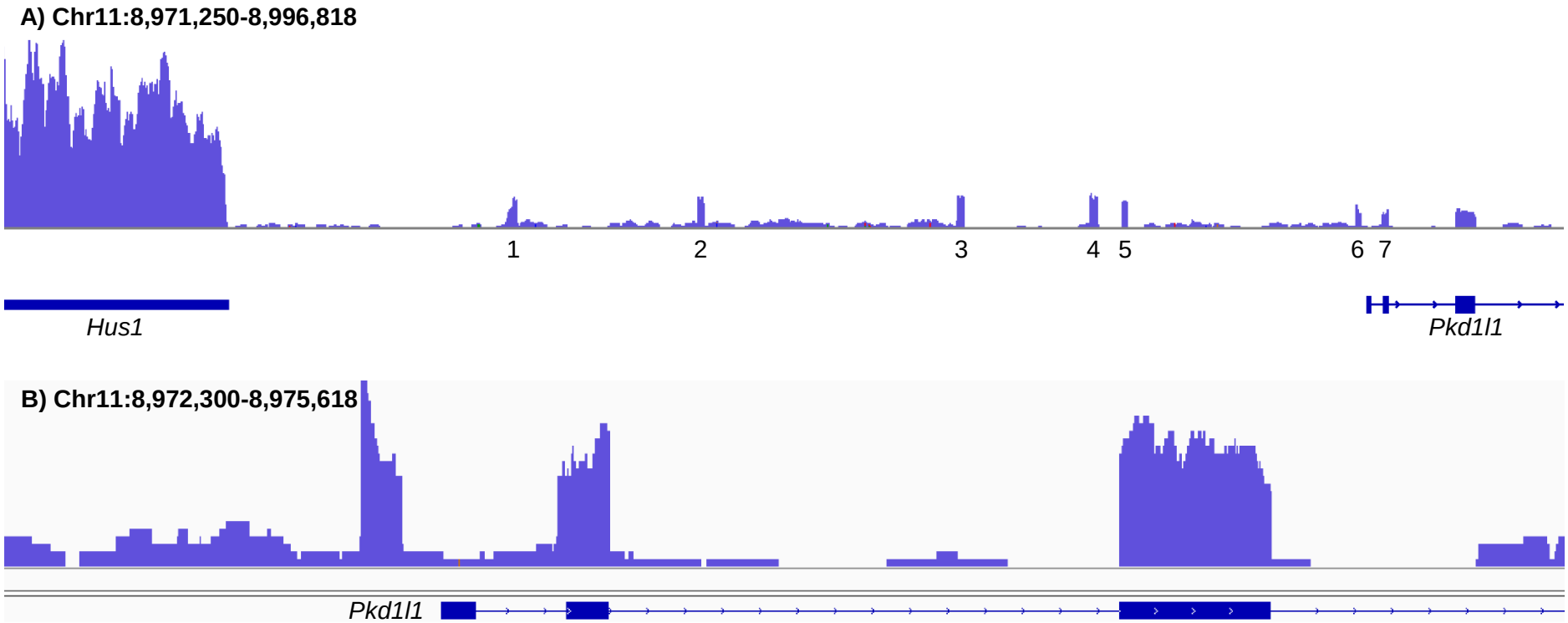
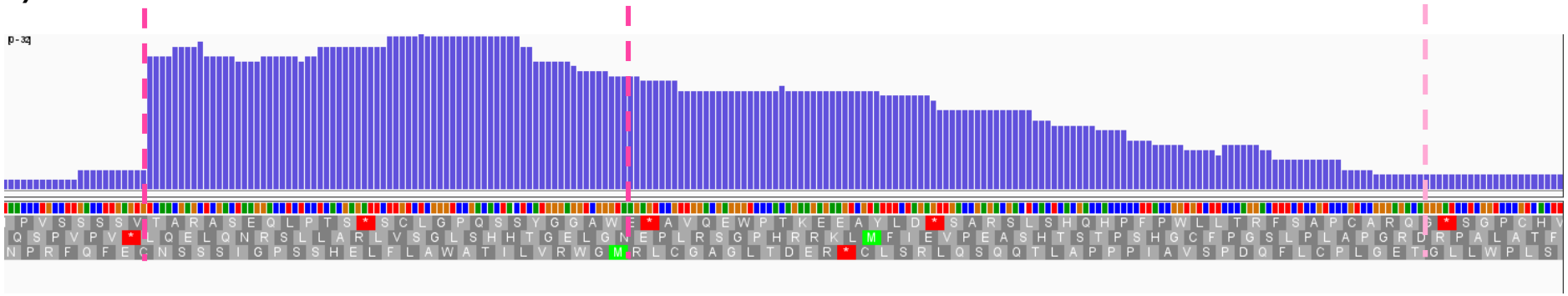


Figure 3.9 B6J 1ss RNA-Seq read coverage track with RefSeq track positioned to the 5' end of *Pkd1l1*

A) Exported tracks from IGV, read coverage and reference genome track Mouse (GRCm38/mm10), showing the 5' end of *Pkd1l1*. Five peaks are visible at a similar height to *Pkd1l1* peaks, located between *Pkd1l1* and *Hus1* on the reference genome; peaks numbered 1 to 7 below the read coverage track. The tracks cover 25 kb of sequence at position Chr11:8,971,250-8,996,818, image flipped to view left to right.

B) A zoomed in view of the first three annotated exons; position Chr11:8,972,300-8,975,618, image flipped to view left to right. This IGV RefSeq annotation (Mouse (GRCm38/mm10)) uses the *Pkd1l1* sequence from NCBI (XM_017314870.1). My previous analysis showed that NCBI exon 1 aligned to an intronic region and NCBI exon 2 was shorter than my predictions and 5' RACE sequence; the RNA-Seq coverage supports this. The third annotated exon here, is the first annotated exon on Ensembl, and this aligns with the RNA-Seq read coverage.

A) Exon 1



B) Exon 2

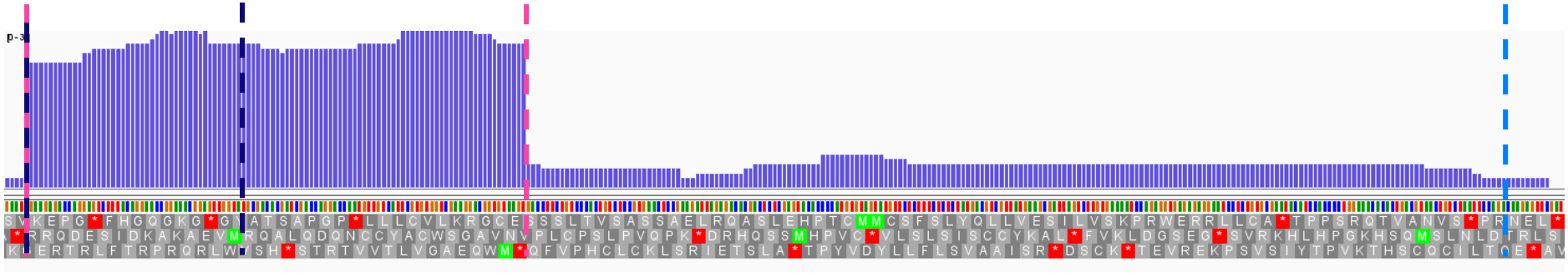
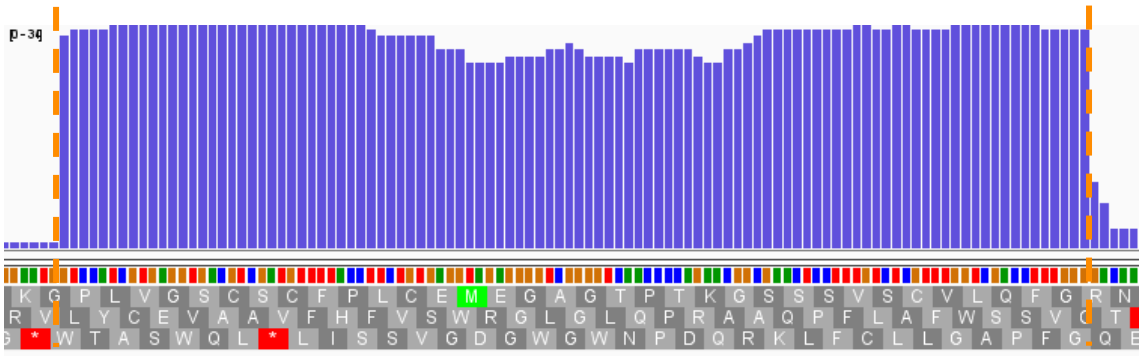


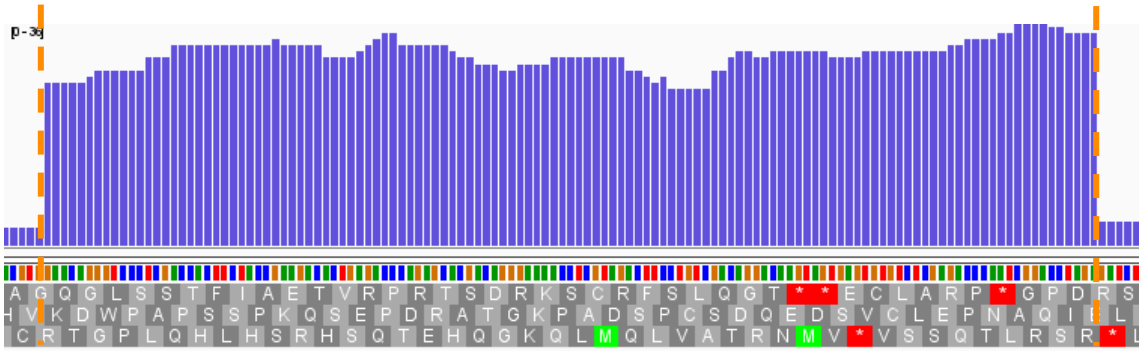
Figure 3.10 B6J 1ss RNA-Seq read coverage track for peaks/exons 1 and 2

Exported tracks from IGV, read coverage for peaks 1 (A) and 2 (B) zoomed from Figure 3.9. Sequence is in the reverse orientation, and reads from right to left. 5' UTRs and exon sequences align with the 5' RACE for the long and short 5' sequences (Figure 3.7). The 5' UTR for the long sequence (A) is more apparent than the 5' UTR for the short sequence (B). The read coverage for the long 5' UTR (A) decreases gradually, in comparison to the sharp drop seen for the short variant 5' UTR (B). Long 5' sequence exons marked with pink dashed lines (A and B), 5' UTR with light pink dashed lines (A). Short 5' sequence exon marked with dark blue dashed line, 5' UTR with blue dashed line (B).

A) Exon 3



B) Exon 4



C) Exon 5

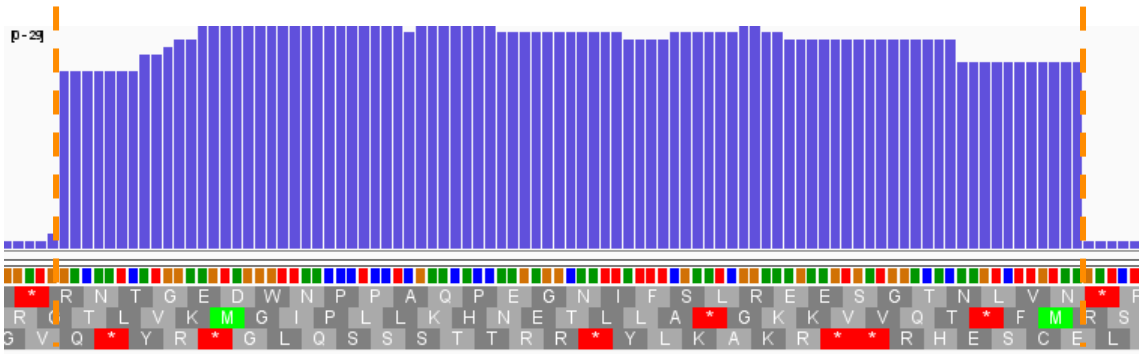
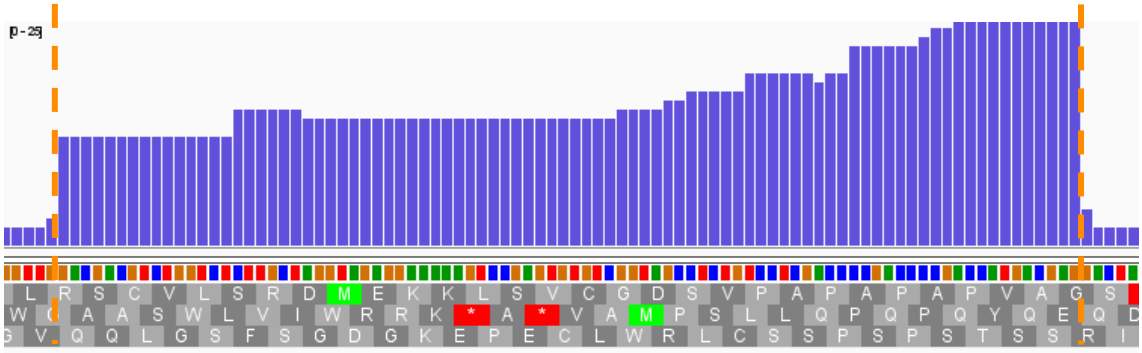


Figure 3.11 B6J 1ss RNA-Seq read coverage for peaks/exons 3, 4 and 5
Exported tracks from IGV, read coverage for peaks 3 (A), 4 (B) and 5 (C) - zoomed from Figure 3.9. Sequence is in the reverse orientation, and reads from right to left. The peaks align with the 5' RACE sequences – marked with orange horizontal dashed lines.

A) Exon 6



B) Exon 7

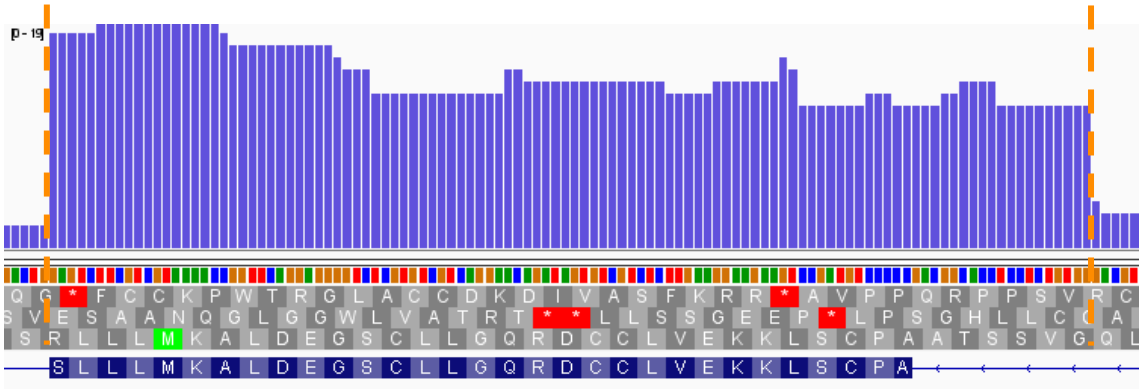


Figure 3.12 B6J 1ss RNA-Seq read coverage for peaks/exons 6 and 7
Exported tracks from IGV, read coverage for peaks 6 (A) and 7 (B) and reference genome track Mouse (GRCm38/mm10) – zoomed from figure 3.9. Sequence is in the reverse orientation, and reads from right to left. The peaks align with 5' RACE sequences – marked with orange horizontal dashed lines.

The first annotated exon (NCBI 1) does not align with the RNA-Seq read coverage (Figure 3.9 B). This was to be expected in light of my alignment predictions and Sanger sequencing results (Figure 3.1 B ii, 3.5, 3.9 B). This provides further evidence to suggest the NCBI prediction is incorrect and NCBI exon 1 is not a true exon. The second annotated exon (NCBI 2) does align with the RNA-Seq reads; however, as previously shown, the sequence is slightly longer than the NCBI prediction (Figure 3.9 B, 3.12 B). Exons 3, 4, 5 and 6 align perfectly with the peaks of the RNA-Seq read coverage.

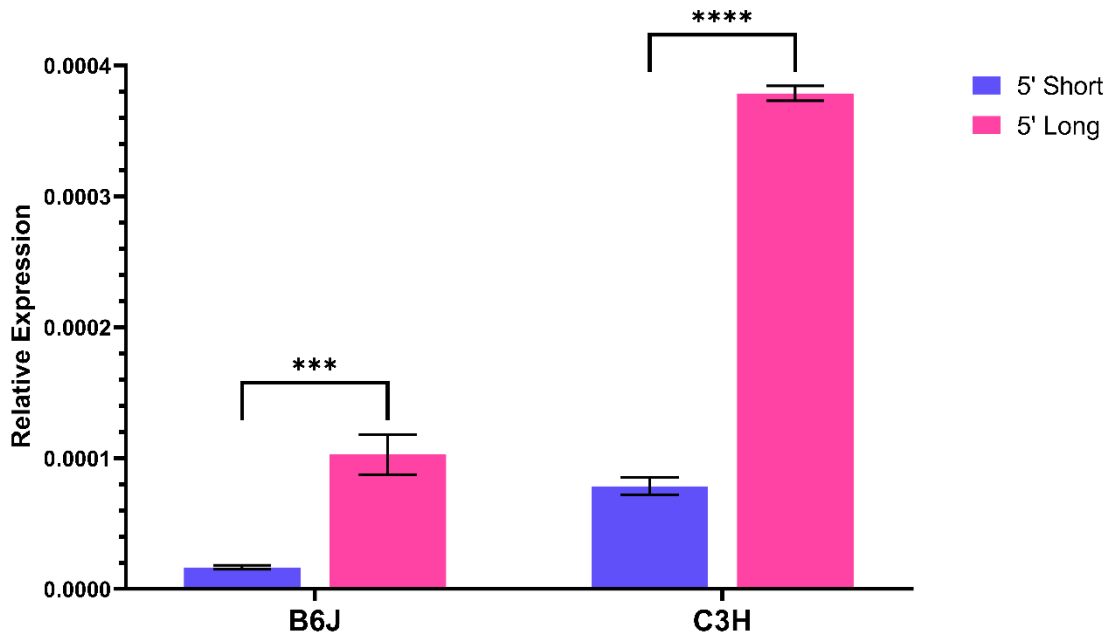
Analysis of the sequence shows RNA-Seq peaks 1 and 2 correspond to the 5' UTRs and first exons of the long and short 5' variants (Figure 3.7, 3.9 A, 3.10). The RNA-Seq read coverage for the long 5' variant shows high levels of coverage for the coding exon, which gradually decreases over the length of the 5' UTR as you head towards the 5' end (Figure 3.10 A). This is what you might expect to see for a 5' UTR in RNA-Seq due to the preparation of the cDNA library; the reverse transcriptase will often drop off before it reaches the 5' cap. In contrast, the region of 5' UTR for the short 5' variant has very low read coverage, and there is a sharp reduction in coverage between where the long variant splices into the 5' UTR and the upstream 5' UTR (Figure 3. 10 B). There is also no significant increase in read coverage between where the extended exon 2 from the long 5' variant meets the ATG start site for the short 5' variant. This suggests that the 5' long variant is the predominant sequence, and the 5' short variant may be expressed at lower levels.

3.2.5 Assessing the expression of the two identified *Pkd1l1* 5' variants

As previously described, when I first identified the 5' long variant from the 5' RACE, all of the C3H samples sequenced contained the long variant; whereas there was a 50:50 ratio of long:short in B6J samples. With the RNA-Seq read coverage suggesting the long variant may be the predominant variant, I wanted to investigate the abundance of each variant further. I performed RT-qPCR using RNA from B6J and C3H embryos to quantify the expression of the 5' long and 5' short variants. Three pools of, approximately 30, B6J and C3H 8 d.p.c embryos were used for RNA extraction and reverse transcription, to generate the cDNA for qPCR.

When analysing the qPCR data, the C_t (threshold cycle) values were normalised to the housekeeping gene *Gapdh*, using the $2^{-\Delta C_t}$ method for relative expression and $2^{-\Delta\Delta C_t}$ method for fold change; the 5' short variant used to set the baseline for fold change. Statistical analysis was performed, using multiple unpaired t-tests, on the relative expression data to determine significance. The difference between relative expression of the 5' short and 5' long variants is statistically significant for both B6J ($P=0.000636$) and C3H ($P=<0.000001$), showing the 5' long variant is more highly expressed than the 5' short variant (Figure 3.13 A). The relative fold change shows the 5' long variant is expressed around 5-7 times more than the 5' short variant (Figure 3.13 B). This suggests that, in 8 d.p.c. mouse embryos, the main *Pkd1l1* transcript contains the 5' long variant.

A)



B)

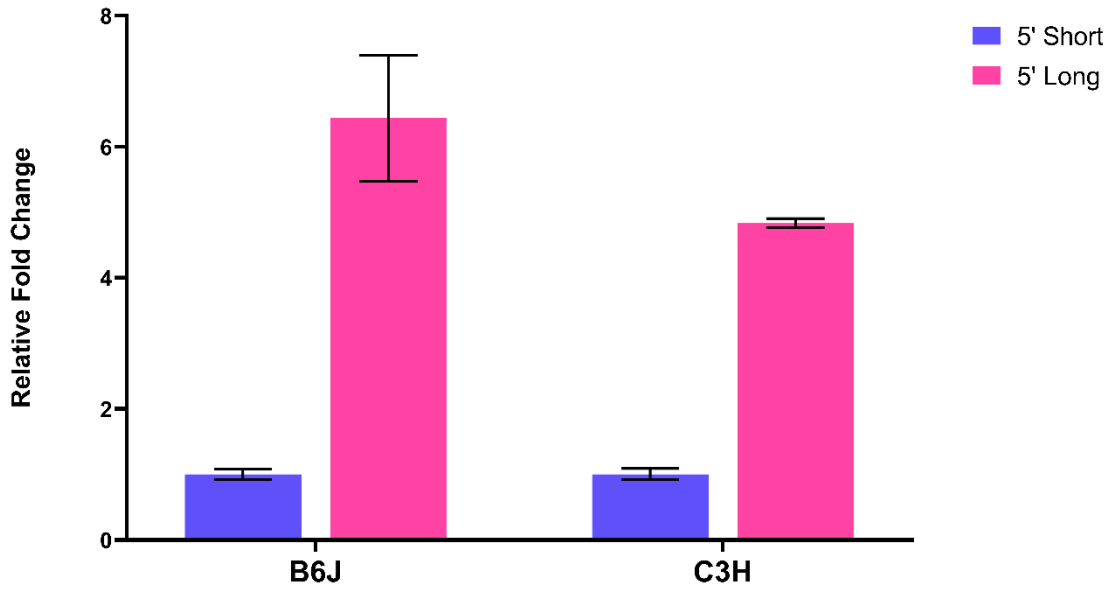


Figure 3.13 Relative expression and fold change of 5' Short and 5' Long variants
RT-qPCR results showing relative expression (A) and relative fold change (B) of *Pkd1l1* 5' short and 5' long variants in B6J and C3H 8 d.p.c. embryo RNA. A) $2^{-\Delta C_t}$ values plotted, calculated using GAPDH as the internal control. B) $2^{-\Delta\Delta C_t}$ values plotted, using the 5' short to normalise. Error bars represent standard deviation. *** = P<0.001, **** = P<0.0001, multiple unpaired t-test performed on relative expression.

Although my data confirmed these 7 additional exons are present in mouse embryos, I wanted to assess whether they are expressed in the embryonic node during development. I designed an in-situ probe covering common sequence for both variants, starting the in the 5' UTR (short) / Exon 2 (long) and ending in exon 6 (short) / 7 (long). Both sense and anti-sense probes were generated, and used for in-situ hybridisation. Unfortunately, during the experiment I experienced an issue with contamination in a buffer solution and due to time constraints I was not able to repeat this. This meant visible strands of contamination attached to the embryos, and were stained, which can be seen in the images (Figure 3.14). I do not, however believe this has impacted the data. The in-situ showed strong expression in the embryonic node and along the notochord in different staged embryos; interestingly, the stain seemed strongest at the posterior edge of the node (Figure 3.14). The stain was strong in the node at all stages assessed, 1ss-5ss, but was slightly weaker in the later 5ss embryo (Figure 3.14 F). The notochord staining was also weaker in later 5ss stage as well as the earlier 1ss and 2ss embryos (Figure 3.13 A, B, F).

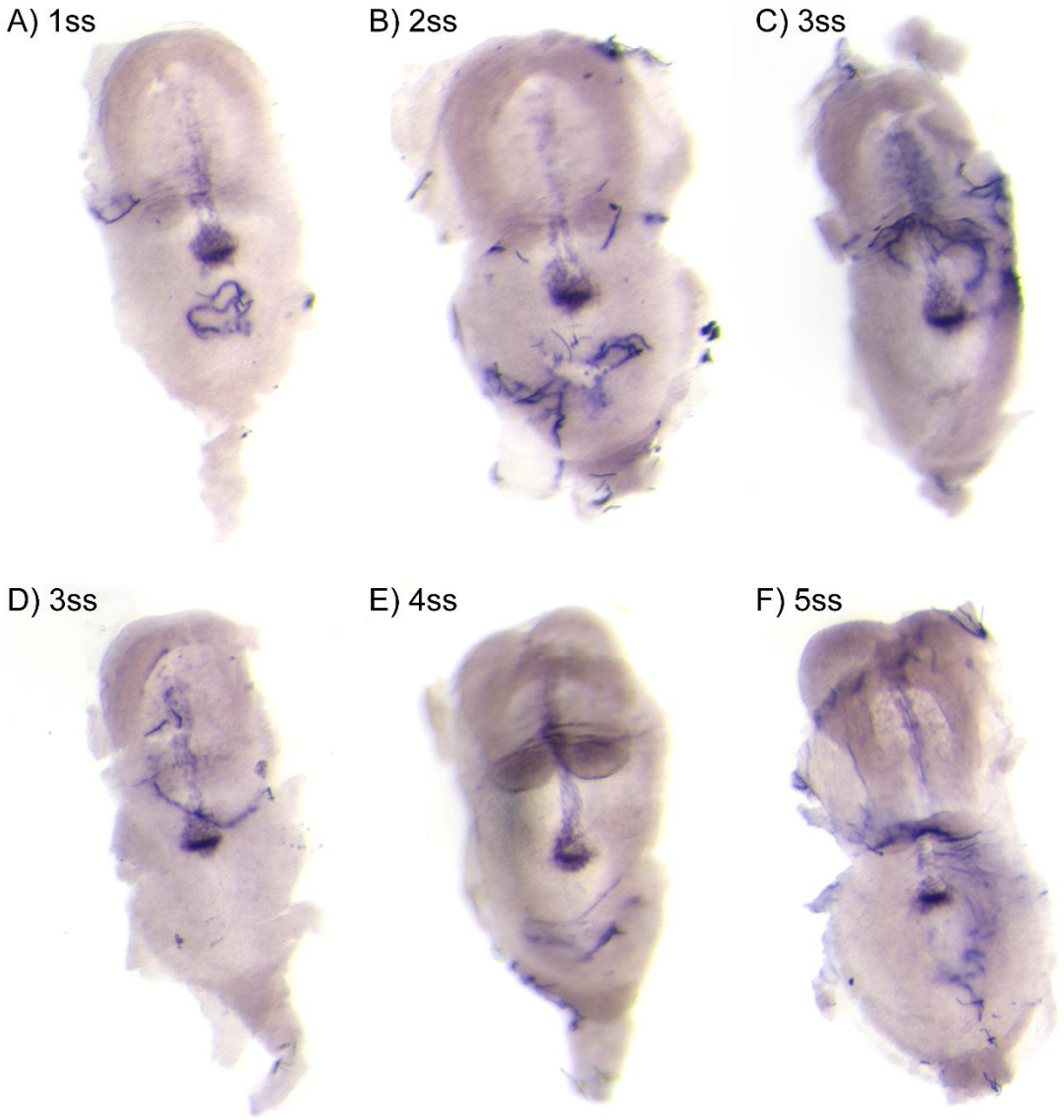


Figure 3.14 *Pkd1l1* 5' exons are expressed in the node and notochord.
In-situ hybridisation staining for the newly identified 5' exons of *Pkd1l1* in B6J embryos, between 7.5 and 8.5 d.p.c., ranging from 1ss to 5ss. Stain is strongest in the embryonic node and clearly present along the notochord. Steaks of stain randomly distributed on the embryos is a remnants of a contaminant from one of the buffers.

3.3 Discussion

Through the experiments in this chapter I have identified two novel 5' transcripts of *Pkd1l1*. The 5' short sequence, containing 6 additional exons over those annotated for mouse *Pkd1l1*, and the 5' long sequence containing an addition 7 exons. Both the RNA-Seq read data and my qPCR data suggest the 5' long variant is the predominant sequence transcribed in 7.5-8.5 d.p.c embryos. This brings about questions of how the two transcripts may vary in other tissues and at different developmental time points. This could be readily tested by qPCR, in a similar way to how I compared relative expression of the two variants in 7.5-8.5 d.p.c. embryos.

The 5' short sequence encodes an additional 187 amino acids, compared to the current Ensembl annotation; the 5' long sequence encodes an additional 45 amino acids over the 5' short sequence. The additional amino acids are at the N-terminal extracellular tail of PKD1L1. Interestingly, PKD1L1 is depicted with an N-terminal signal peptide in a review by Albert Ong and Peter Harris; however I could not find any further information about the specific signal peptide for *Pkd1l1* (Ong and Harris 2015). Usually, N-terminal signal peptides are present in membrane proteins to targeting to specific organelles or translocation to the plasma membrane.

This leads me to question whether the sequence variation between the 5' long and 5' short may have an impact of the localisation of *Pkd1l1*. It would be informative to investigate this further, initially using computational analysis to assess N-terminal signalling peptides in the two variants. One way to test this is in cells would be to express tagged versions of the two variants and investigate

localisation. We can assume that all other exons are present in the two variants, however the remaining sequence of the two *Pkd1l1* variants is unknown. Ideally it would be best to confirm the full length sequence of each of the transcripts first. Indeed, it would be intriguing to assess this, perhaps one variant shows better localisation to cilia. This could have significant impacts in the functions of the two variants.

Previously, *Pkd1l1* plasmids have been difficult to transfect and visualise in ciliated cells, and other members of the lab have opted for C-terminal fragments of *Pkd1l1* instead. It seems plausible that these issues could be due to missing information contained in the additional exons identified.

If both variants can localise to cilia, it would be interesting to test whether the difference in the N-terminal tail has any implications on the response to flow. This could be tested in a flow chamber, using a calcium dye to assess the response, as done in previous studies of PKD1 and PKD1L1 (Grimes et al. 2016; Kotsis et al. 2007; Praetorius and Spring 2001).

The identification of novel exons in *Pkd1l1*, highlights a broader need for the validation of full length cDNA sequences and begs the question of how many other annotated genes are missing exons. The NCBI annotation for *Pkd1l1* was purely computational, and was proven incorrect in my experiments. With ~25,000 genes predicted in the mouse genome, there is likely a large number of incorrectly annotated genes on databases such as Ensembl and NCBI (Guénet 2005).

4. Investigating PKD2 ciliary localisation

4.1 Introduction

The importance of PKD2 ciliary localisation has been defined in both the kidneys, in the development of kidney cysts in ADPKD, and in the embryonic node for correct left-right pattern determination (Walker et al. 2019; Yoshiba et al. 2012). The *Pkd2*^{lrm4} allele has been a key part of this, and has provided great insight into the requirement of PKD2 in nodal cilia. As described in the main introduction (section 1.3.3), PKD2^{lrm4} fails to localise to nodal cilia, leading to absent expression of *Nodal* in the lateral plate mesoderm; defects observed in most *Pkd2*$^{lrm4/lrm4}$ embryos include oedema, right pulmonary isomerism and random positioning of the heart apex and stomach situs (Ermakov et al. 2009; Field 2009). These embryos also develop kidney cysts at 15.5 d.p.c., which is due to the loss of ciliary localisation in kidney cilia rather than any reduction in protein levels (Walker 2016; Walker et al. 2019). PKD2^{lrm4} is not the only mutation shown to lose ciliary localisation, another mutation PKD2^{W414G} fails to localise to cilia and has been shown to retain channel activity similar to PKD2^{lrm4} (Cai et al. 2014; Yoshiba et al. 2012). Both lrm4 and W414G point mutations are located in the TOP domain of PKD2, which sits on the extracellular surface of membrane localised PKD2 (Grieben et al. 2017). Approximately 60% of ADPKD-associated missense variants in PKD2 are located in the TOP domain (Grieben et al. 2017). PKD2^{lrm4} has been shown to localise at the base of kidney cilia, in a ring like formation consistent with distal appendage localisation (Walker et al. 2019). This suggests that ciliary entry of PKD2 is regulated in a TOP domain dependent manner.

There are three main models for how membrane proteins are trafficked to into the cilium (Hoffmeister et al. 2011; Witzgall 2005). The first is that proteins traffic to the basal body and are transported into the cilium via intraflagellar transport before subsequent fusion with the ciliary membrane; however it is thought that the cilium does not contain vesicles, and it is unclear whether machinery for membrane fusion is present in cilia (Hoffmeister et al. 2011; Witzgall 2005). The second proposed mechanism is that proteins are first integrated into the apical plasma membrane and diffuse across a barrier into the cilia membrane (Witzgall 2005). The third model suggests that proteins are trafficked to a docking station at the base of the cilia, where they are integrated into the ciliary membrane (Hoffmeister et al. 2011; Witzgall 2005). Evidence supporting the third mechanism has been presented in data by Hoffmeister and colleagues, where they uncovered distinct trafficking mechanisms to the plasma membrane and the ciliary membrane (Hoffmeister et al. 2011). Their data suggests that PKD2 is released from the ER in a COPII-dependent manner for transport to the golgi apparatus, PKD2 trafficking vesicles to the cilia leave the Golgi apparatus in the cis-compartment, and that RAB8A regulates trafficking of PKD2 into primary cilia (Hoffmeister et al. 2011). RAB8A localises to the basal body and is involved in primary cilia formation, it also interacts with ODF2 - basal body and ciliary microtubule binding protein (Yoshimura et al. 2007). The data revealing $PKD2^{lrm4}$ accumulation to distal appendages at the base of cilia, also supports the third mechanism involving protein docking at the base of cilia prior to ciliary entry (Hoffmeister et al. 2011; Walker et al. 2019; Witzgall 2005).

To continue investigating the mislocalisation of PKD2^{lrm4}, and mechanisms of ciliary entry of PKD2, I wanted to examine interacting partners of PKD2 in *Pkd2*$^{+/+}$ and *Pkd2*$^{lrm4/lrm4}$ samples. For this, I needed specific antibodies that could be used to immunoprecipitate PKD2 and its interacting partners.

4.2 Results

4.2.1 Developing PKD2 antibodies

Previously, the lab used a PKD2 rabbit polyclonal antibody from Santa Cruz (Polycystin-2 (H-280), sc-25749) for western blot, immunoprecipitation and immunocytochemistry. This antibody was discontinued in 2016 and replaced with a mouse monoclonal antibody (Anti-Polycystin-2 Antibody (YCE2), sc-47734). When tested, by previous lab members, the replacement antibody was unable to provide a good PKD2 signal for immunofluorescence or western blot. When I joined the lab, the last stocks of H-280 antibody were running low so we decided to generate our own PKD2 antibody. Another commonly used PKD2 antibody, was developed by Stefan Somlo's lab in the late 1990's, however this was also no longer available (Cai et al. 1999; Wu et al. 1998). Both the Santa Cruz and Stefan Somlo's antibodies were designed against the C-terminal region of human PKD2, amino acids 687-961 (SC) and 689-968 (YCE2). As both of these antibodies worked well, we decided to use the same region as YCE2 to generate our antibody.

Initially, I cloned the region of interest (PKD2 amino acids 689-968) into the bacterial expression vector pRSETa. This was transformed into BL21 DE3 pLysS bacterial cells (*E. coli)* for protein expression. When performing the first pilot protein expression at 37°C (Methods 2.4.5), the cells failed to exceed an optical density (OD_{600}) reading of 0.22. For protein expression in bacterial cells, an OD_{600} reading above 0.6 is recommended before IPTG induction. The pilot protein expression was repeated using four new cultures, which were diluted and allowed to grow overnight at 37°C and 30°C. The following day, two of the cultures grown

at 37°C had reached OD readings of >0.8 and were induced for 6 hours at 37°C; the other two had OD readings below 0.45 and were discarded. The 30°C cultures were all induced at an OD >0.65; two cultures were induced for 6 hours, and two induced overnight.

Protein expression was assessed by running the uninduced, induced, soluble and insoluble samples on SDS-PAGE followed by Coomassie staining; the insoluble sample was isolated using 8 M urea in sonication buffer. Under all conditions protein expression was very low, with little difference observed between the uninduced and induced samples (Figure 4.1 A, B); a strong increase of the expected sized band in the induced sample is expected with good protein expression. Less protein was observed in the insoluble sample compared to the soluble sample, suggesting the fusion protein was mostly soluble.

Due to the low levels of protein expression and variability in cell growth, it seemed likely that the fusion protein was having a toxic effect in the cells. In an attempt to overcome this, the pilot protein expression was repeated using a different bacterial expression vector - pET-32a. This vector contains a large TRX tag, a thermostable *E. coli* protein, which can be useful for stabilising proteins, improving solubility and reducing toxicity (Costa et al. 2014; LaVallie et al. 1993). The same region of PKD2 was cloned into the pET-32a vector, and pilot protein expressions conducted at 37°C and 30°C.

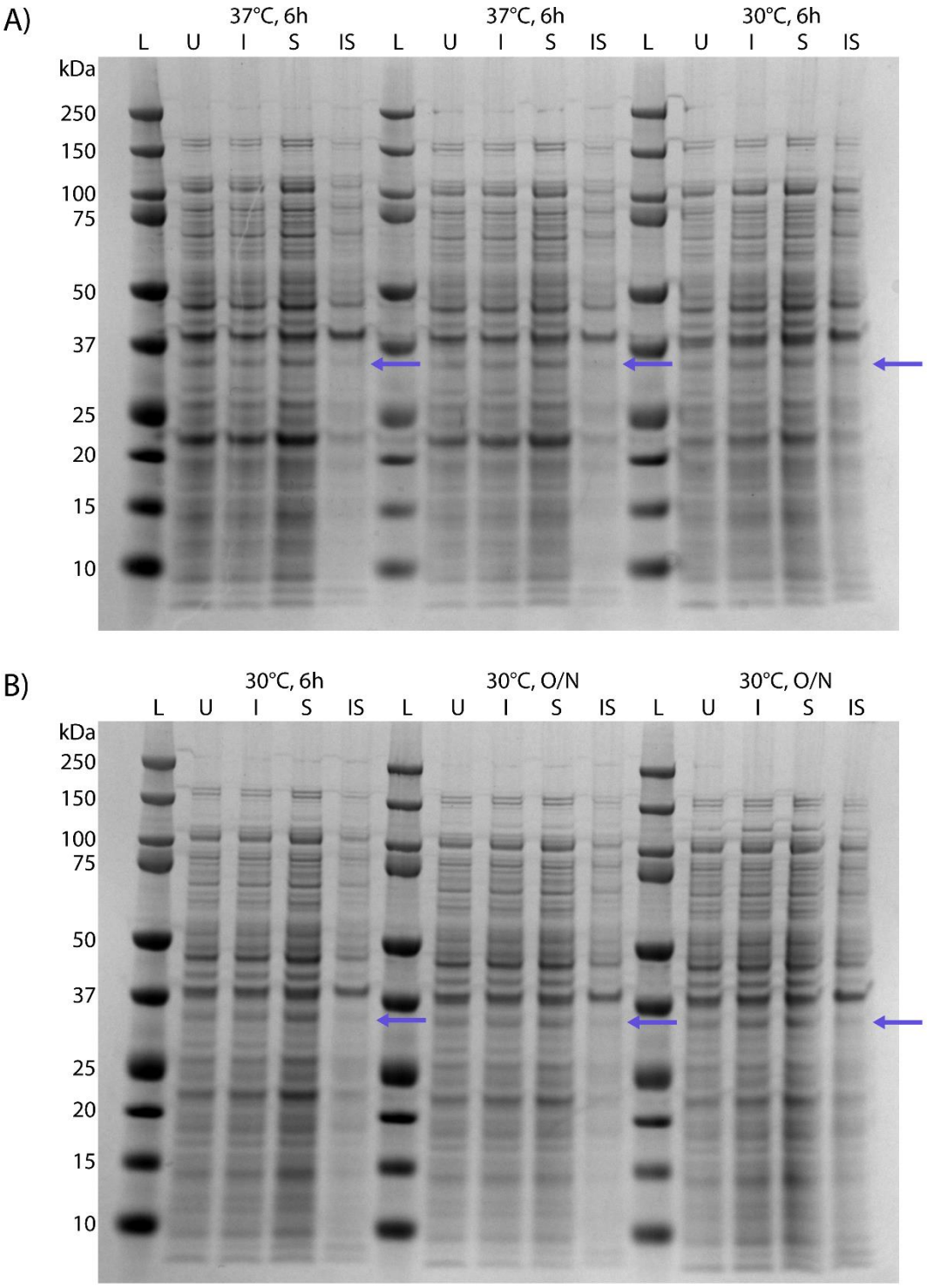


Figure 4.1 Pilot protein expression of PKD2 (aa689-968) in the pRSETa vector
Coomassie stained SDS-PAGE gels, showing the protein expression of PKD2 (aa689-968) in the pRSETa vector. A) Cultures grown at 37°C or 30°C and induced for 6 hours. B) Cultures grown at 30°C and induced for 6 hours or overnight. Purple arrows indicate the bands at the expected molecular weight (35.3 kDa). L = Precision Plus Ladder, U = Uninduced, I = Induced, S = Soluble, IS = Insoluble

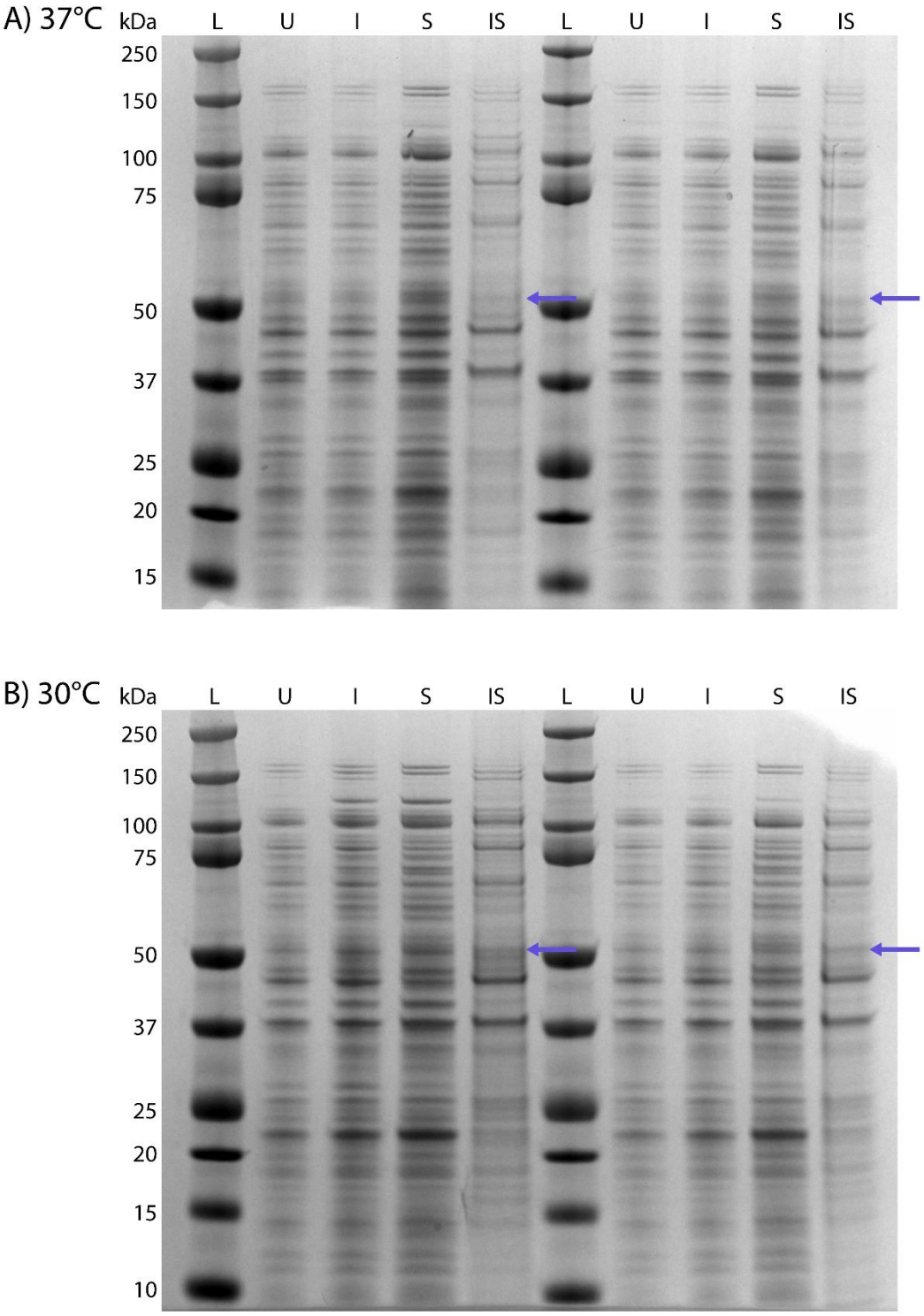


Figure 4.2 Pilot protein expression of PKD2 (aa689-968) in the pET-32a vector
Coomassie stained SDS-PAGE gels, showing the protein expression of PKD2 (aa689-968) in the pET-32a vector. A) Cultures grown at 37°C and induced for 3 hours. B) Cultures grown at 30°C and induced for 3 hours. Purple arrows indicate the bands at the expected molecular weight (48.8 kDa). L = Precision Plus Ladder, U = Uninduced, I = Induced, S = Soluble, IS = Insoluble

When the pilot protein expression was performed using the pET-32a vector, all four cultures grew to OD_{600} >0.6 within 3 hours; this suggested that changing the expression vector improved the putative toxicity seen using the pRSETa vector. Expression was again assessed using SDS-PAGE and Coomassie staining (Figure 4.2 A, B). Protein expression was still low, with little difference between the uninduced and induced samples. However, there were signs of protein induction, particularly in one of the samples induced at 30°C (Figure 4.2 B left). Similar to the pRSETa vector, the protein expressed from the pET-32a vector was mostly in the soluble sample, with little insoluble protein observed.

As there was expression and improved cell growth in the pilot protein expression, using the pET-32a vector, I proceeded with large scale protein expression and purification (methods 2.4.6). It was unclear from the pilot protein expression whether 30°C or 37°C incubation was optimal; for that reason, the large scale was performed at both temperatures. Briefly, 250 mL cultures were grown to an OD_{600} >0.6 and induced, with IPTG, for 3 hours before harvesting the pellet by centrifugation. The cell pellet was resuspended in sonication buffer, sonicated and centrifuged again, the supernatant was then purified on a Ni-NTA resin column. Uninduced, induced, lysate, flow through and four elution samples were run on SDS-PAGE and Coomassie stained for analysis (Figure 4.3 A, B).

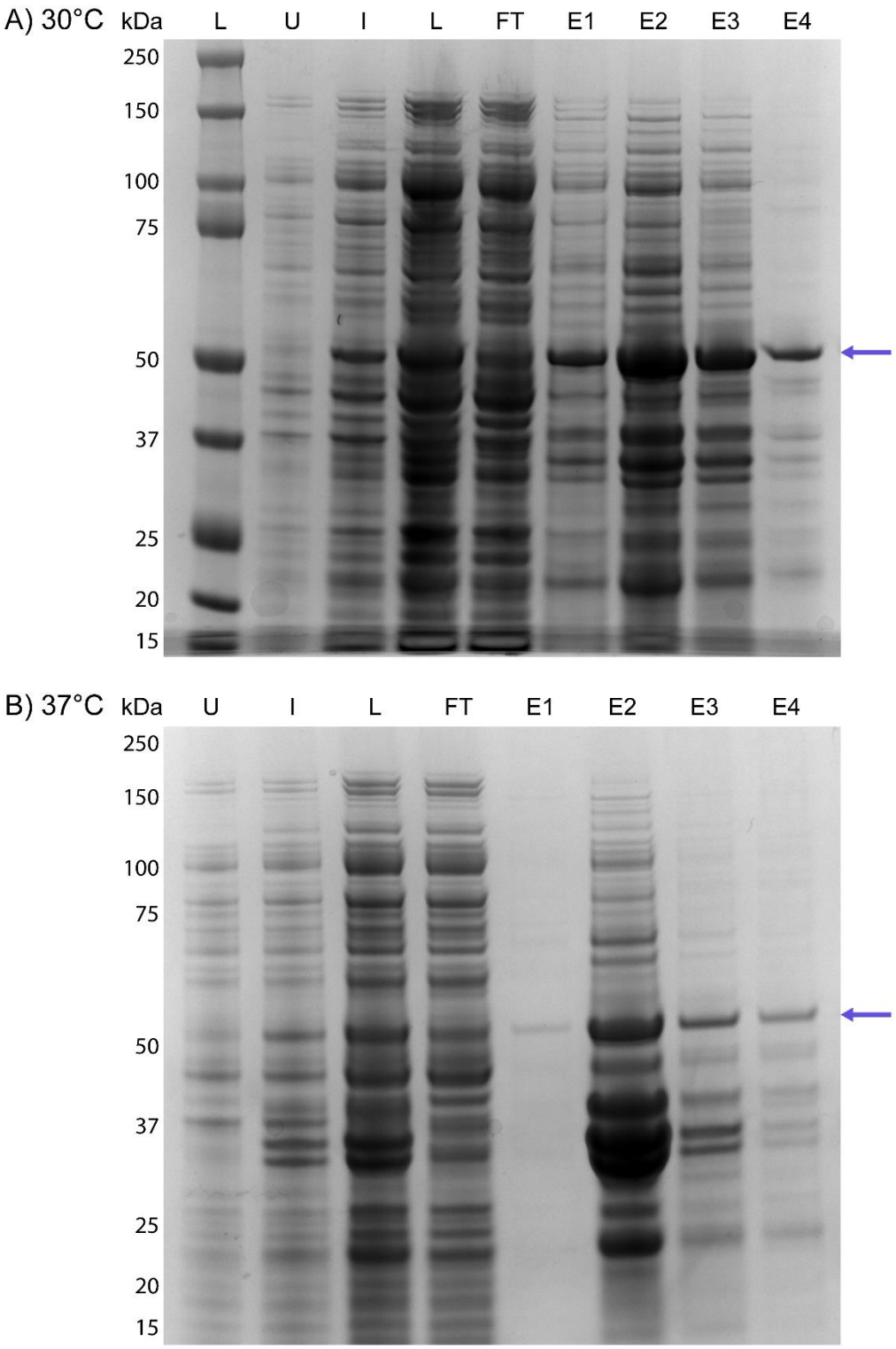


Figure 4.3 Large scale expression of PKD2 (aa689-968) in the pET-32a vector
Coomassie stained SDS-PAGE gels, showing the protein expression of PKD2 (aa689-968) in the pET-32a vector. A) Cultures grown at 30°C, B) Cultures grown at 37°C. Purple arrows indicate the bands at the expected molecular weight (48.8 kDa). L = Precision Plus Ladder, U = Uninduced, I = Induced, L = Lysate, FT = Flow Through, E1-E4 = Elution 1-4

Comparison of the uninduced and induced samples revealed the large scale expression exhibited stronger protein induction than the pilot protein expression experiments (Figure 4.2 A, B and 4.3 A, B). More protein was observed in the lysate sample than the flow through sample, indicative of good binding of the PKD2 fusion protein to the Ni-NTA resin (Figure 4.3 A, B). A strong band at the expected size was evident in the elution samples, with most of the protein present in elution 2. Although cell growth was not affected by the incubation temperature; the bands observed by SDS-PAGE Coomassie staining in the elution samples were different at 30°C and 37°C (Figure 4.3 A, B). At 30°C the strongest band seen in the elution samples is at the expected size ~48.8 kDa (Figure 4.3 A). However, at 37°C there are two stronger bands visible between 25-37 kDa (Figure 4.3 B). The same bands can be seen in the 30°C samples, however they are weaker than the expected band. It seemed likely the bands were cleavage products of the fusion protein, caused by toxicity in the cell, which is more prevalent at higher incubation temperatures.

The large scale protein expression gave promising results at 30°C, however there were high levels of non-specific bands in the elution samples. To improve the purity of the elution different concentrations of imidazole were added to the wash buffer, to find an optimal concentration for removing non-specific bands. Adding 50 mM imidazole to the wash buffer, reduced non-specific band intensity (data not shown). For the final purification, adjustments were made to the large scale purification protocol (Methods 2.4.6). This included an additional wash with 50 mM imidazole, and the imidazole concentration for the elution buffer was increased from 100 mM to 250 mM to improve recovery from the column.

The final large scale expression showed a strong band at the size expected for our fusion protein and fewer non-specific bands than the initial large scale induction (Figure 4.4 A). Elution 2 had a concentration of 0.5219 mg/mL, and was sent to Covalab for immunisations. As well as the simple elution, I loaded 40 µL of elution 2 to nine wells of an SDS-PAGE gel; this was run and stained with Coomassie and bands at the expected size were excised. The bands were also sent to Covalab, who used them for the final injection (of four injections) (Figure 4.4 B).

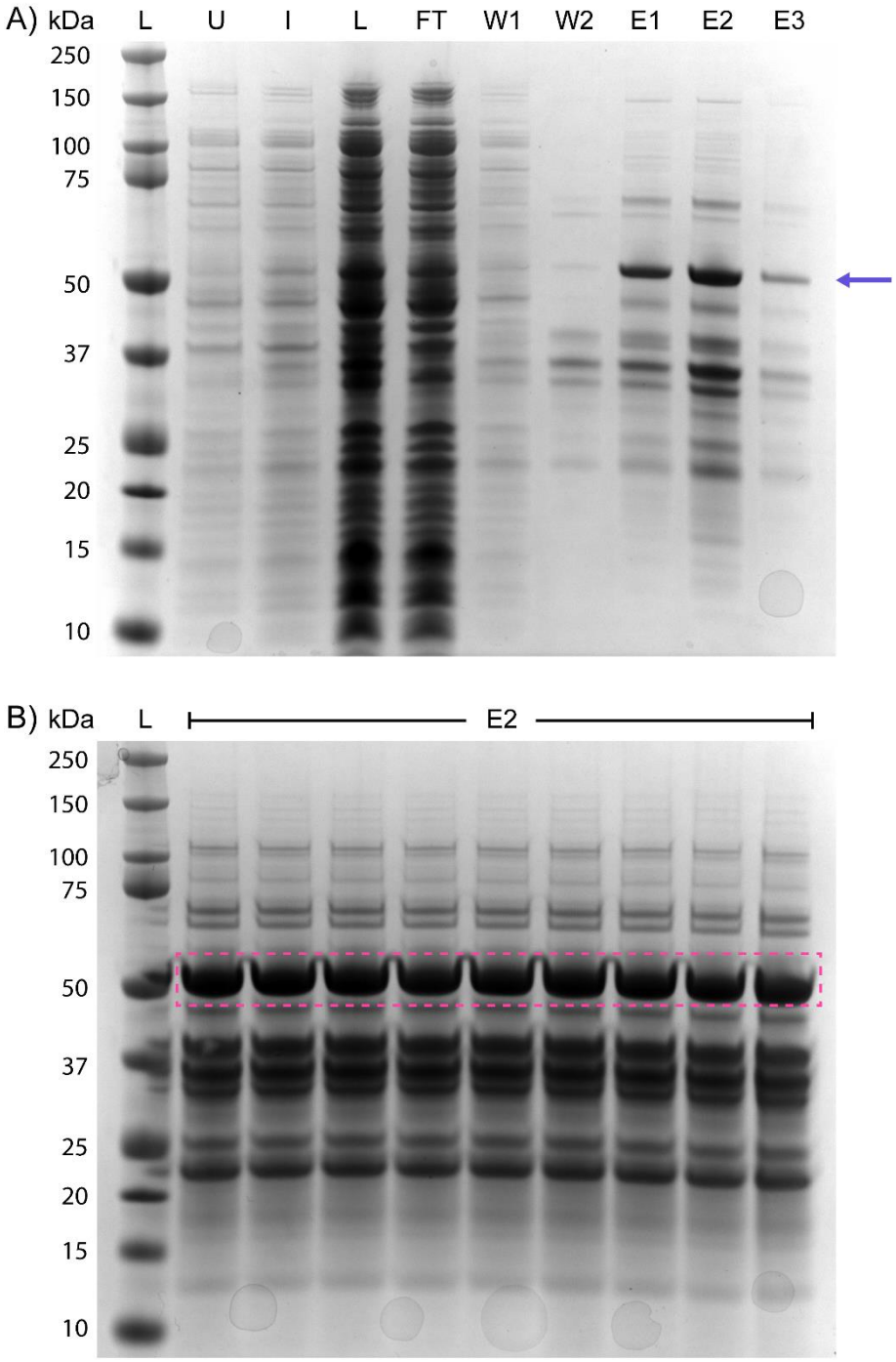


Figure 4.4 Final purification of PKD2 in the pET-32a vector for immunisation
Coomassie stained SDS-PAGE gels. A) Purification with additional 50 mM wash, purple arrow indicates the bands at the expected molecular weight (48.8 kDa). B) Maximum loading of elution 2, pink dashed box indicates the excised area. L = Precision Plus Ladder, U = Uninduced, I = Induced, L = Lysate, FT = Flow Through, W1 = 25 mM imidazole washes, W2 = 50mM imidazole wash, E1-E3 = Elution 1-3.

4.2.2 Testing new PKD2 antibodies

Two rabbits were immunised by Covalab to generate PKD2 polyclonal anti-sera, distinguished as Rb8 and Rb12. The rabbits were injected with the antigen on days 0, 21, 42 and 63. Test bleeds were collected pre-injection on day 0, and post-injection on days 53 and 74. The pre-bleed and test bleeds were shipped for analysis before the terminal bleeds were collected on day 88.

To ascertain how well the anti-sera could detect PKD2, tissues were collected from a WT B6J mouse and HEK-293T cells were transfected with a *Pkd2-V5-HIS* plasmid (Methods 2.5.7). Protein was extracted from brain, kidney and the transfected HEK-293T cells, which was used for western blot analysis (Methods 2.4.1). The anti-sera from the pre-bleeds and day 53 test bleeds were used at a 1:100 dilution. No bands were detected using the pre-bleed anti-sera from Rb8 or Rb12, whilst a band was visible in the transfected HEK-293T sample and faint bands were seen in the brain and kidney samples using the day 53 anti-sera from Rb8 or Rb12 (data not shown).

After receiving the day 88 terminal bleeds, 20 mL from each rabbit was affinity purified. For affinity purification, the original antigen (elution 1 and elution 3) was immobilized onto a SulfoLink resin column (Methods 2.4.7); the 20 mL anti-sera was bound to the column for 1 hour, the column was washed with PBS and the affinity purified antibodies eluted using IgG elution buffer (Methods 2.4.7).

In order to assess the effectiveness and specificity of the affinity purified PKD2 antibodies, *Pkd2*$^{+/+}$*, Pkd2*$^{+/-}$ *and Pkd2*$^{-/-}$ mouse embryonic fibroblast cells (MEFs) were generated using 14.5 d.p.c. embryos from a *Pkd2*$^{+/-}$ intercross (Methods 2.5.5). Protein was extracted from the MEFs as well as IMCD-3 cells, and HEK-293T cells transfected with the *Pkd2-V5-HIS* plasmid. IMCD-3 cells (mouse) are kidney cells lines, and were selected for antibody testing as PKD2 is known to be highly expressed in the kidney. Extracted protein was separated by SDS-PAGE and transferred for western blot, PKD2 antibodies were used to probe this at a 1:250 dilution.

Both Rb8 and Rb12 antibodies detected a band at the expected size for PKD2 (110 kDa) in *Pkd2*$^{+/+}$ and *Pkd2*$^{+/-}$ MEFs, while this band was not detected in *Pkd2*$^{-/-}$ MEF samples, supporting its identity as PKD2 (Figure 4.5 A, B). This same band was also detected in the untransfected IMCD-3 cells using either Rb8 or Rb12 antibodies (Figure 4.5 A, B). A strong band was detected in *Pkd2-V5-HIS* transfected HEK-293T cells, albeit at a slightly higher MW due to the addition of the V5-HIS tag (Figure 3.5 A, B). Non-specific bands were present in the western blots with both the Rb8 and Rb12 antibodies. The strongest non-specific bands were detected using the Rb8 antibody and appear in all four MEF cell lines, at approximately 150 kDa and 140 kDa, however these strong bands do not appear in the IMCD-3 or HEK-293T cells (Figure 4.5 A).

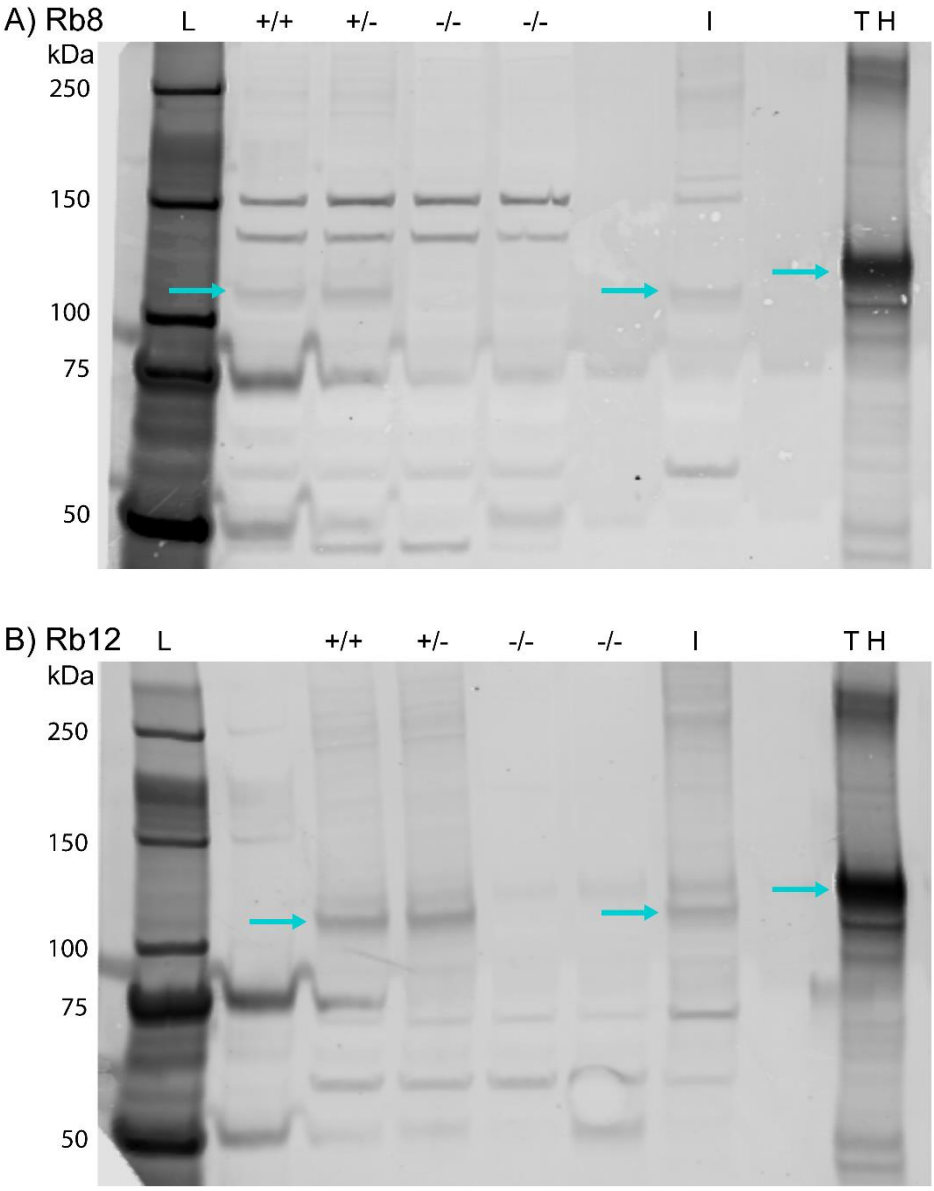


Figure 4.5 Western blots using Rb8 and Rb12 antibodies
Western blot of PKD2$^{+/+}$, $^{+/-}$ and $^{-/-}$ MEFs, IMCD-3 cells and HEK-293T cells transfected with PKD2-V5-HIS. PKD2 Rb8 (A) and Rb12 (B) antibody used at 1:250, turquoise arrows indicate expected band for PKD2 (~110 kDa) and transfected PKD2-V5-HIS (~113 kDa). L = Precision Plus Ladder, +/+ = *Pkd2*$^{+/+}$, +/- = *Pkd2*$^{+/-}$, and -/- = *Pkd2*$^{-/-}$ MEF cells, I = IMCD-3 cells, T H = transfected HEK-293T cells.

Next, the Rb8 and Rb12 antibodies were tested for their ability to immunoprecipitate PKD2 protein. Protein from *Pkd2*$^{+/+}$, *Pkd2*$^{+/-}$ *and Pkd2*$^{-/-}$ MEFs was extracted and quantified using the Pierce BCA assay (Methods 2.4.2), 1 mg of protein was used for immunoprecipitation. Immunoprecipitation was performed using Dynabeads protein G magnetic beads and approximately 5 µg of Rb8 or Rb12 antibody (Methods 2.4.3). The lysate, flowthrough and elution were separated using SDS-PAGE, and transferred for western blot; Rb8 and Rb12 antibodies were used at a 1:250 dilution to detect PKD2, the same antibody was used for both the immunoprecipitation and western blot. Clear bands were visualised in the elution samples of *Pkd2*$^{+/+}$ and *Pkd2*$^{+/-}$ at the expected size for PKD2 (110 kDa), with both Rb8 and Rb12 antibodies (Figure 4.6 A, B). The band seen for *Pkd2*$^{+/-}$ appears approximately half the strength of the *Pkd2*$^{+/+}$ band, consistent with previous data (Walker et al. 2019), due to the cells only carrying one copy of *Pkd2*. No band was detected at the expected size in the *Pkd2*$^{-/-}$ elution samples using Rb8 or Rb12 antibodies, again consistent with our antibodies specifically immunoprecipitating and identifying PKD2 (Figure 4.6 A, B). No bands were detected in the lysate samples, however less protein was loaded to the gel than the previous western blot (Figure 4.6 A, B).

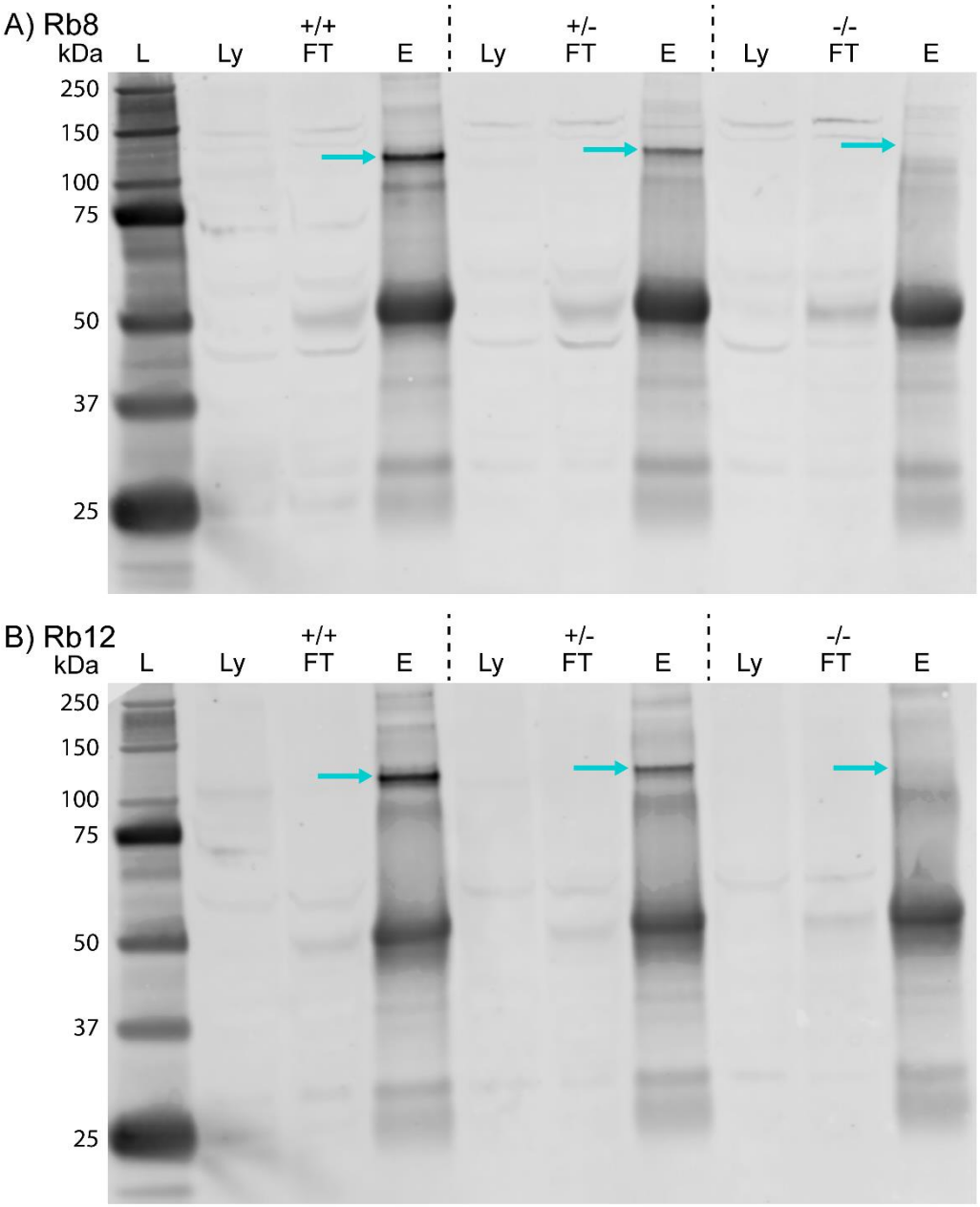


Figure 4.6 Immunoprecipitation using Rb8 and Rb12 antibodies
Western blot of *Pkd2*$^{+/+}$, *Pkd2*$^{+/-}$ and *Pkd2*$^{-/-}$ MEF immunoprecipitations. PKD2 Rb8 (A) and Rb12 (B) antibody used at 1:250, turquoise arrows indicate expected band for PKD2 (110 kDa). L = Precision Plus Ladder, +/+ = *Pkd2*$^{+/+}$, +/- = *Pkd2*$^{+/-}$, and -/- = *Pkd2*$^{-/-}$, Ly = Lysate, FT = Flowthrough, E = Elution.

Following on from the positive results for western blot and immunoprecipitation, I wanted to test whether the antibodies could detect PKD2 in the MEF cell lines using immunofluorescent staining. *Pkd2*$^{+/+}$ and *Pkd2*$^{-/-}$ MEFs were grown on coverslips and serum starved to promote ciliogenesis, the cells were fixed with methanol and stained using a 1:250 dilution of the PKD2 Rb8 or Rb12 primary antibody. The cells were also stained using an ARL13B antibody and with DAPI; ARL13B is a membrane protein highly enriched in primary cilia and is commonly used to mark cilia.

Staining in *Pkd2*$^{+/+}$ MEFs, using Rb8 or Rb12 antibodies, showed punctate expression along the cilia, overlapping the ARL13B cilia marker staining (Figure 4.7). As well as ciliary staining, Rb8 and Rb12 antibodies showed perinuclear staining suggestive of endoplasmic reticulum expression (Figure 4.7). The ciliary and ER staining is consistent with previously published data for PKD2 expression, both from our lab using the Santa Cruz H280 antibody (Walker et al. 2019) and Stefan Somlo's original characterisation of their PKD2 antibodies (Cai et al. 1999). Staining in *Pkd2*$^{-/-}$ MEFs was much weaker than staining in *Pkd2*$^{+/+}$ MEFS, and required a higher laser power to detect a signal for imaging. The staining did not show clear perinuclear or ciliary expression with either Rb8 or Rb12 antibodies (Figure 4.7). This further confirms the specificity of our antibodies against PKD2.

Next, I assessed whether our antibodies could detect PKD2 in the embryonic node, using whole mount immunofluorescent staining of wild type B6J 8 d.p.c. embryos (Methods 2.2.2). Previous work has demonstrated the requirement for PKD2 in nodal cilia for correct left-right patterning, and shown its expression in nodal cilia (Grimes et al. 2016; Walker et al. 2019; Yoshiba et al. 2012). For

comparison, I also performed the staining using the Santa Cruz H280 antibody - from stocks purchased before it was discontinued. Both antibodies showed specific staining in nodal cilia, particularly around the edge of the node where the crown cell cilia are located (Figure 4.8). This finding was interesting based on the work from Hiroshi Hamada's group, which showed PKD2 expression in the crown cells is essential for correct left-right patterning (Yoshiba et al. 2012); however endogenous expression of PKD2 being enriched in the crown cells has not been shown. Ciliary staining was detected using the Santa Cruz H280 antibody, however staining was much weaker compared to Rb8 and Rb12 staining (Figure 4.8). The H280 staining was also significantly weaker when compared with previous data from the lab (Grimes et al. 2016; Walker et al. 2019), consistent with age-related degradation of the H280 antibody.

The Rb8 antibody exhibited the strongest staining when used for whole mount immunofluorescent staining of 8 d.p.c. embryos (Figure 4.8 A and B), it also showed better ciliary staining than the Rb12 antibody when used for immunofluorescence in MEFs (Figure 4.7 A and B). Additional staining was performed using the Rb8 antibody to examine the expression of PKD2 at different stages of 8 d.p.c. embryos. PKD2 was widely expressed among nodal cilia across the node at all stages examined, with slightly increased levels of expression around the peripheries of the node (Figure 4.9).

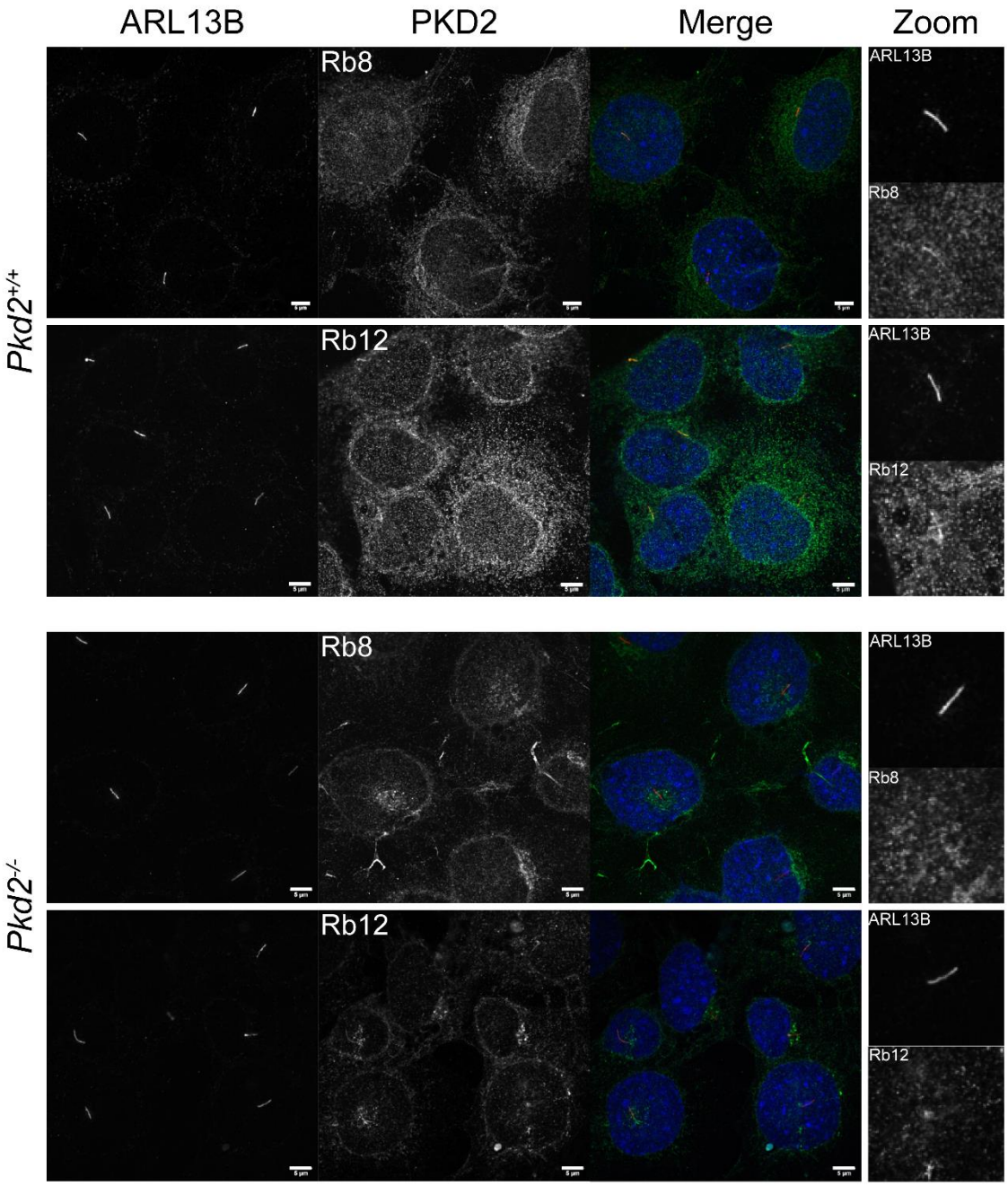


Figure 4.7 Immunofluorescence in Pkd2 MEFs using Rb8 and Rb12 antibodies
Immunofluorescent staining of *Pkd2*$^{+/+}$ (top) and *Pkd2*$^{-/-}$ (bottom) MEFs, showing expression of PKD2 using Rb8 and Rb12 antibodies (middle panel & green in merge). ARL13B antibody used to label the cilia (left panel & red in merge) and DAPI used to label the nucleus (blue in merge). In *Pkd2*$^{+/+}$ MEFs (top), both Rb8 and Rb12 antibodies show staining in the cilia and the endoplasmic reticulum. *Pkd2*$^{-/-}$ MEFs (bottom) showed much fainter staining, with no specific ciliary or ER localisation.
Scale bars represent 5 µm.

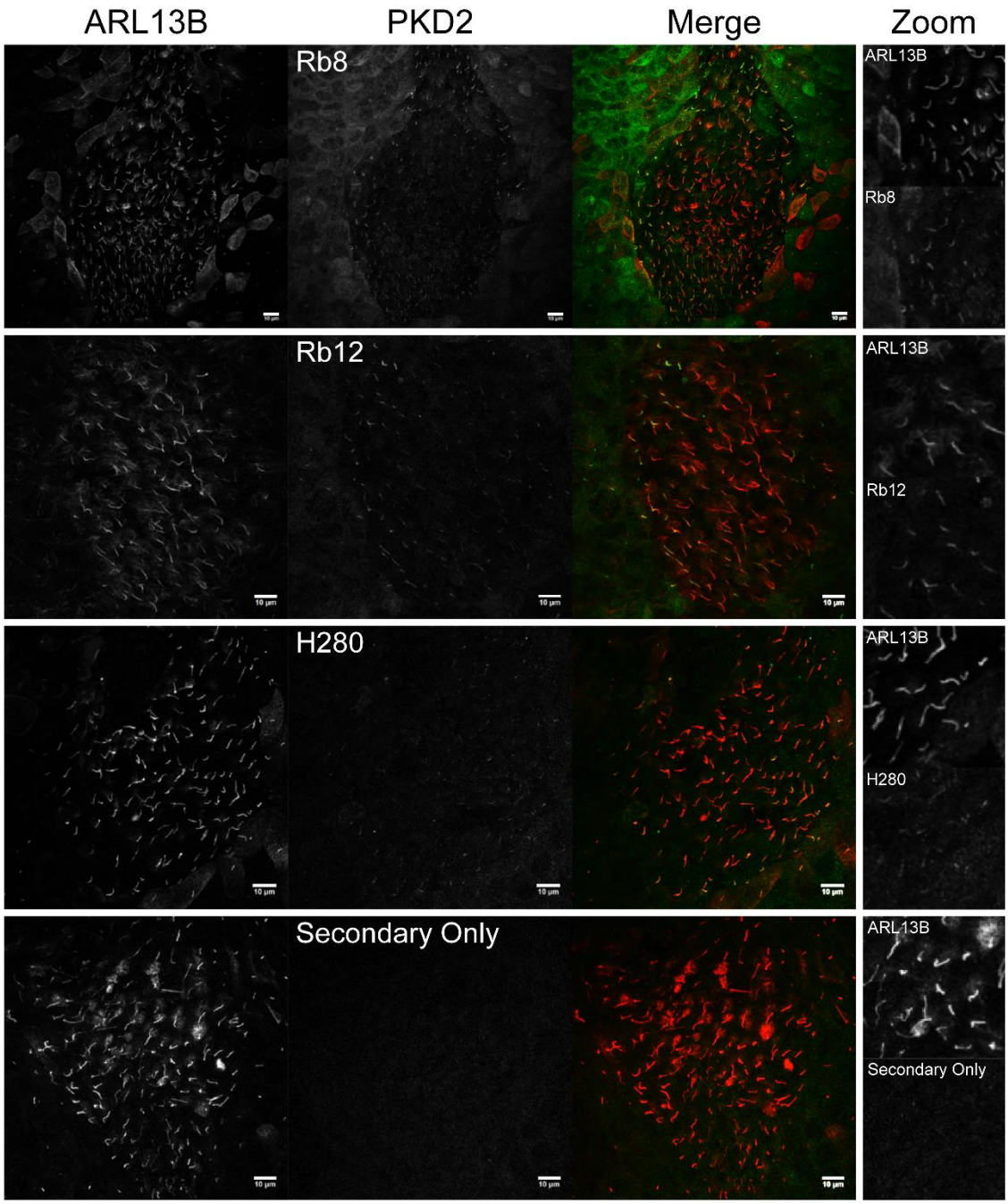


Figure 4.8 Immunofluorescence in 8 d.p.c. mouse embryos using Rb8, R12 and H280 antibodies

Immunofluorescent staining of wild type B6J 8 d.p.c. mouse embryos, using Rb8, Rb12 and H280 PKD2 antibodies, showing PKD2 expression in the embryonic node. From left to right, ARL13B staining (Red), PKD2 staining (Green), and merge. Zooms of cilia from the peripheries of the node on the right hand side, ARL13B (top) and PKD2 (bottom) shown in greyscale. Scale bars represent 10 µm.

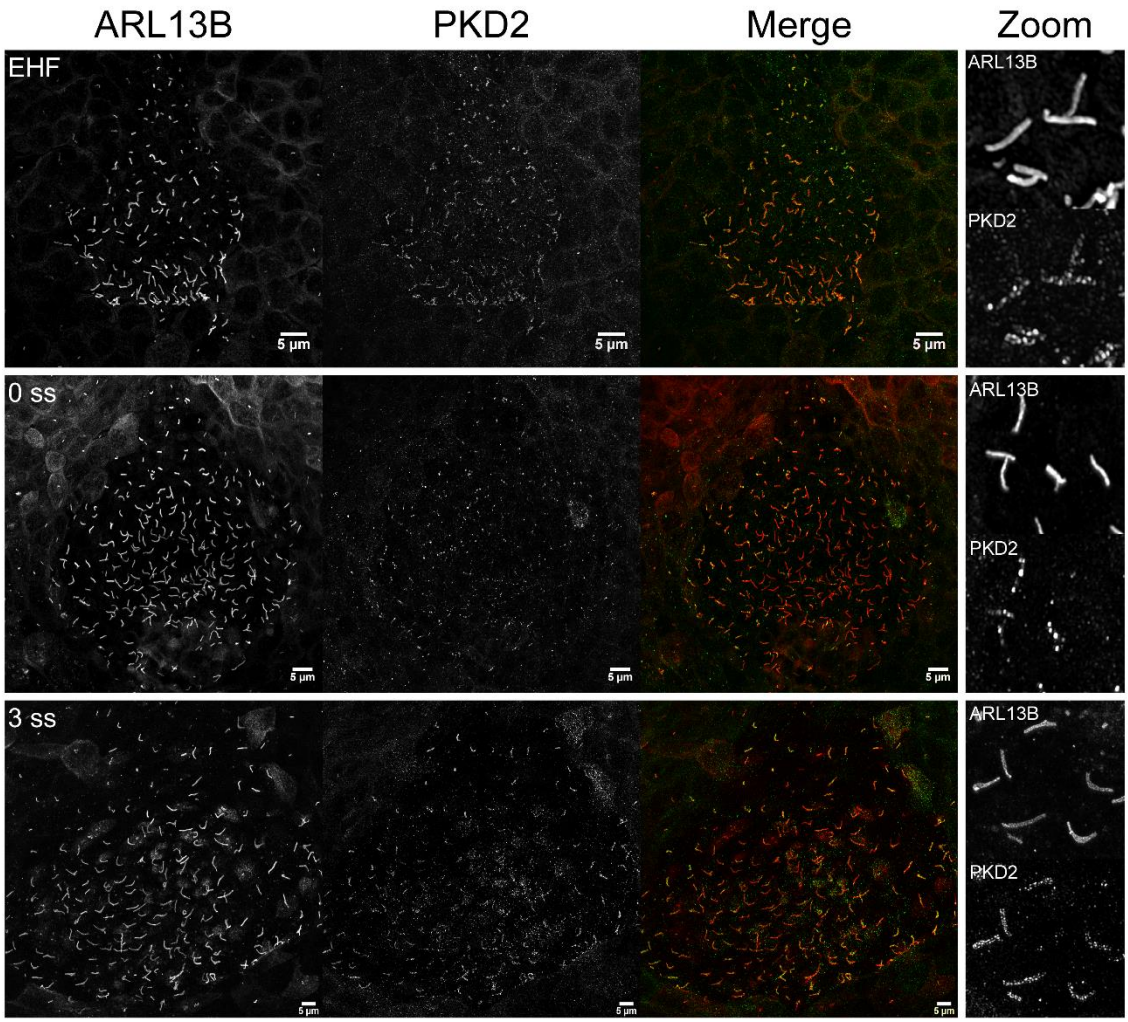


Figure 4.9 Additional examples of immunofluorescence in 8 d.p.c. mouse embryos using the Rb8 PKD2 antibody

Immunofluorescent staining of wild type B6J 8 d.p.c. mouse embryos, using the Rb8 PKD2 antibody, showing PKD2 expression in the embryonic node. From left to right, ARL13B staining (Red), PKD2 staining (Green), and merge. Zooms of cilia from the peripheries of the node on the right hand side, ARL13B (top) and PKD2 (bottom) shown in greyscale. Scale bars represent 5 µm.

4.2.3 Novel PKD2 isoform identified

The left-right patterning defects caused by the mislocalisation of PKD2^{lrm4}, led me to question the underlying mechanisms driving PKD2 ciliary localisation. Work from previous lab member Rebecca Walker, showed that PKD2^{lrm4} accumulated at the base of cilia, in a ring like formation in *Pkd2$^{lrm4/lrm4}$* MEFs and primary kidney cells (Walker et al. 2019). This work highlighted the high probability for distinct mechanisms controlling PKD2 trafficking to the base of cilia and its entry into the cilium. In order to better understand the mechanisms of PKD2 trafficking and ciliary entry, I wanted to investigate the *Pkd2$^{lrm4/lrm4}$* mouse allele further.

I considered many possibilities for investigation: genetics, looking for similar phenotypes; visual trafficking using tags and reagents to follow PKD2 trafficking; the use of pharmacological compounds to screen for similar effects in vitro; and proteomics, to capture and identify interacting partners. Having weighed up the options, I decided to follow the route of proteomics, making use of the newly developed antibodies. I aimed to use the antibodies for immunoprecipitation of PKD2 and its interacting partners, which could then be identified using mass spectrometry.

For my immunoprecipitation experiments, I wanted to use samples that express PKD2 at high levels, and samples that are phenotypically relevant for PKD2 function. In order to find suitable candidate interacting partners, I wanted to be able to compare *Pkd2$^{+/+}$* samples with both *Pkd2$^{-/-}$* and *Pkd2$^{lrm4/lrm4}$* samples. This would enable me to assess whether interacting partners identified in the mass spectrometry results are true interacting partners of PKD2 by comparing the *Pkd2$^{+/+}$ and Pkd2$^{-/-}$* results. And also to assess whether there are any changes in

the interacting partners identified between *Pkd2*$^{+/+}$ *and* *Pkd2*$^{lrm4/lrm4}$*.* This narrowed down the sample type down to either tissues I could gather from *Pkd2*$^{+/+}$, *Pkd2*$^{-/-}$ *and* *Pkd2*$^{lrm4/lrm4}$ mice, or cell lines derived from those mice. I considered using the MEF cell lines I had generated from all three mouse lines, however I was concerned that PKD2 in-vitro may behave differently than in-vivo and interacting partners could vary. From previous work, we know that *Pkd2*$^{lrm4/lrm4}$ mice fail to undergo correct left right patterning and develop cystic kidneys by 15.5 d.p.c. (Ermakov et al. 2009; Field et al. 2011; Walker et al. 2019). Both patterning defects and kidney cysts are a result of PKD2 mislocalisation; ether in the embryonic node at 7.5-8.5 d.p.c. or within the embryonic kidneys. From previous work in the lab, I knew it would be possible to gather sufficient amounts of protein for immunoprecipitation and mass spectrometry from embryonic kidneys; however, I could not find any publications for western blot or immunoprecipitation using 8 d.p.c embryos. This led me to question whether it could be possible to perform immunoprecipitations using protein extracted from 8 d.p.c. B6J embryos.

Due to the size of 8 d.p.c. embryos (~200-500 microns in diameter), I knew a large number of embryos would be needed to isolate enough protein for immunoprecipitation. I began by collecting 17 8 d.p.c. embryos (from 3 litters), and lysed in 500 µL buffer. I quantified the amount of protein from the 17 embryos using the Pierce BCA protein assay, which determined I had 0.52 mg/mL; based on this, I had ~0.25 mg of protein for the immunoprecipitation. Using the same Dynabeads protein G magnetic beads and our PKD2 Rb8 antibody, I immunoprecipitated proteins as previously described in section 5.2.2, (Methods

2.4.3). The elution sample from the immunoprecipitation was separated by SDS-PAGE and transferred for western blot. The membrane was probed using the same Rb8 PKD2 antibody to detect bands on western blot. This preliminary experiment at immunoprecipitation using protein from 8 d.p.c. B6J embryos did not identify at the expected size for PKD2 (110 kDa) (Figure 4.10 A); however, there was a smeary band identified at a lower molecular weight of approximately 85 kDa (Figure 4.10 A).

When performing a repeat I collected 5 litters of 8 d.p.c. embryos (~30 embryos) and included lysate from IMCD-K2 cells; another mouse inner medullary collecting duct cell line, similar to IMCD-3 cells which I have previously shown to express PKD2 (Figure 4.5). For the repeat experiment, I decided the Licor may not be sensitive enough to detect the low intensity bands; instead I opted for x-ray film exposure and development in an automatics processor, a highly sensitive method, which is more likely to detect low levels of protein expression. Instead of using Licor secondary antibodies and imaging on the Licor Odyssey, the western blot membrane was probed with HRP secondary antibodies and ECL western blot detection reagents were used to detect the signal, the blot was then exposed to X-ray film for 30 second, 45 seconds and 2 minutes and developed in an automatic processor. With a 30 second exposure, the band between 75 and 100 kDa was detected, in both IMCDK2 and the 8 d.p.c elution samples, however no band was visible at the expected 110 kDa size (Figure 4.10 B). By extending the exposure time to 45 seconds, a faint band was detected around 110 kDa for the IMCDK2 sample but not in the embryo sample (Figure 4.10 C). A 2 minute exposure confirmed the presence of the 110 kDa band in the IMCDK2 sample, however for the embryo oversaturation of the 85 kDa band made it impossible to

ascertain whether there was a 110 kDa band (Figure 4.10 D). This made me question whether the lower 85 kDa band is a true isoform of PKD2 that is strongly expressed in 8 d.p.c. embryos. Ideally, the 85 kDa band in the embryo sample would have been excised and sent for mass spectrometry analysis; however the band was not visible on SDS-PAGE with Coomassie staining (data not shown) suggesting there would not be enough protein for mass spec. To scale up the experiment any further, to visibly detect a band on SDS-PAGE with Coomassie staining, would have required a huge number of 8 d.p.c. embryos – more than could be justified. Looking back at the previous immunoprecipitation data (Figure 4.6 A and B), it was noticeable that the 85 kDa band was also visible in MEFs. Interestingly, using the Rb8 antibody the 85 kDa band seemed to decrease in the *Pkd2*$^{+/-}$ and *Pkd2*$^{-/-}$ MEF samples (Figure 4.6 A), while the difference was less apparent using the Rb12 antibody (Figure 4.6 B).

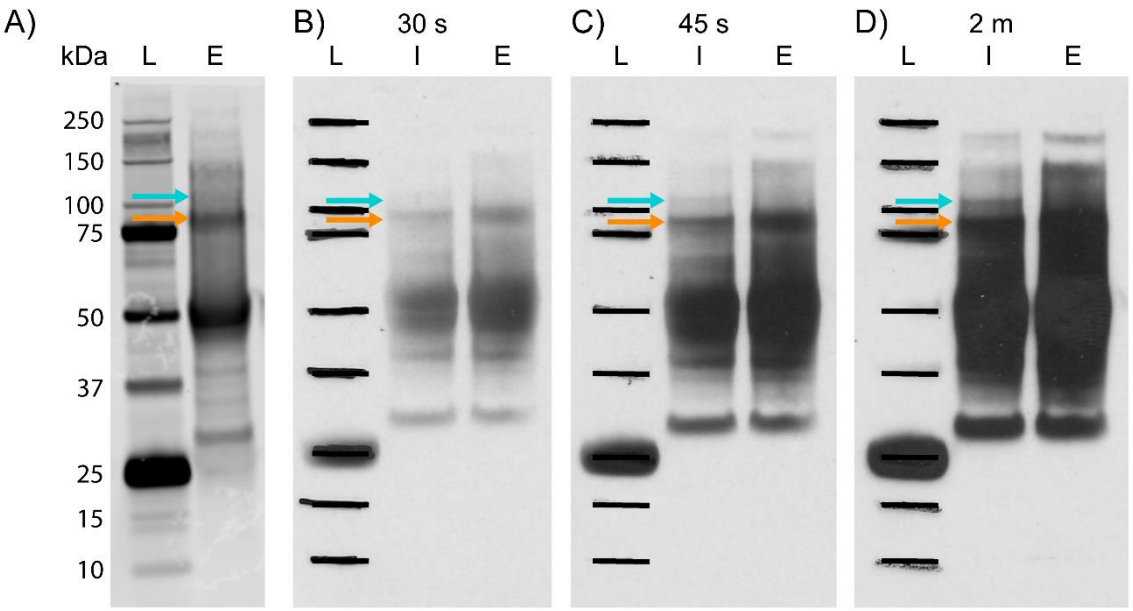


Figure 4.10 Immunoprecipitation using 8 d.p.c. B6J embryos
Western blot of PKD2 immunoprecipitations using 8 d.p.c. B6J embryos. A) First experiment imaged using the Licor Odyssey, B-D) Second experiment using ECL detection reagents exposed to X-Ray film for 30 seconds (B), 45 seconds (C), and 2 minutes (D). PKD2 antibody used at 1:250 in both experiments, Turquoise arrows indicate expected band for PKD2 (110 kDa), orange arrows indicate lower band detected at ~85 kDa. L = Precision Plus Ladder, E = 8 d.p.c. embryo, I = IMCD-K2.

As the 85 kDa band was detected at a stronger level than the expected 110 kDa band in the IMCD-K2 sample (4.10 B-D), opposite to the levels visualised in MEF cells (Figure 4.6 A, B), I decided to assess whether this was specific to IMCD cell lines or if is present across multiple cell lines and mouse tissues. I collected cell lysates from all of the main cell lines used in the lab: HEK-293T, IMCD-3, IMCD-K2, NIH-3T3, RPE-1, as well as the *Pkd2*$^{+/+}$ and *Pkd2*$^{-/-}$ MEFs. And extracted protein from adult mouse brain, heart, kidney, liver, lung, spleen and testes; I also collected brain and kidney from a *Pkd2*$^{+/-}$ adult mouse. The protein was quantified using the BCA assay and 1 mg of protein used for immunoprecipitations with the Rb8 antibody. Western blot was performed on the elution sample from each sample, using the Rb8 antibody to probe the membrane for PKD2 protein.

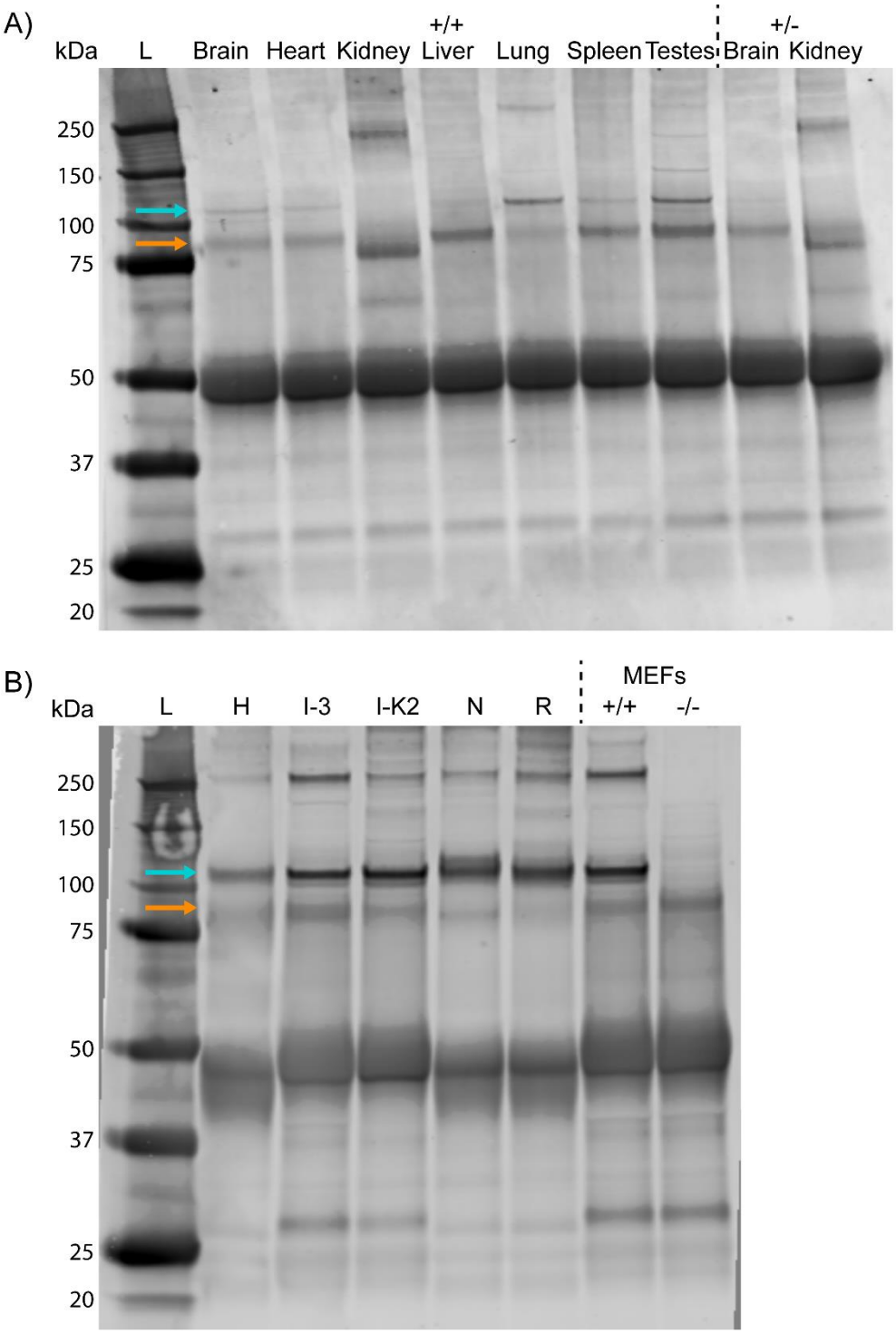


Figure 4.11 Immunoprecipitation using multiple adult mouse tissues and cell lines
Western blot of PKD2 immunoprecipitations in mouse tissues (A) and cell lines (B). Turquoise arrows indicate expected band for PKD2 (110 kDa), orange arrows indicate lower band detected at ~85 kDa. L = Precision Plus Ladder, +/+ = *Pkd2*$^{+/+}$, +/- = *Pkd2*$^{+/-}$, -/- = *Pkd2*$^{-/-}$, H = HEK-293T, I-3 = IMCD-3, I-K2 = IMCD-K2, N = NIH-3T3, R = RPE-1, MEFs = mouse embryonic fibroblasts.

The western blot, of elution samples, from mouse tissue immunoprecipitations showed a variation in the banding pattern of the 110 kDa expected PKD2 size band and the lower 85 kDa band (Figure 4.11 A). Brain, heart and spleen appeared very similar, showing a faint band at 110 kDa and a slightly stronger band at 85 kDa (Figure 4.11 A). In contrast, kidney did not show a band at the expected or the lower size, however showed a strong band at approximately 75 kDa (Figure 4.11 A). Liver and testes exhibited a similar high level of expression of the 85 kDa band; although, liver appeared to have an almost invisible band at 110 kDa, whereas this was much stronger in testes. Interestingly, lung was the only tissue showing a stronger band at 110 kDa than 85 kDa. The brain and kidney samples from the *Pkd2*$^{+/-}$ adult mouse exhibited the same pattern of the two bands as the brain and kidney samples from the *Pkd2*$^{+/+}$ adult mouse, however the bands for the kidney sample were approximately half the strength in the *Pkd2*$^{+/-}$ sample, consistent with previous data (Walker et al. 2019). In both the *Pkd2*$^{+/+}$ and *Pkd2*$^{+/-}$ kidney samples, two other bands were clearly visible one at approximately 230 kDa and one at approximately 65 kDa. A faint higher band at approximately 250 kDa was detected in the lung sample. PKD2 is known to form dimers and trimers as well as interacting with PKD1 in a heterotetramer (Su et al. 2018; Yu et al. 2009), the higher bands at ~230 kDa for kidney and ~250 kDa in lung are indicative of dimers at distinct molecular weights due; speculation could suggest this is due to the observed isomer variation.

In the experiment testing the observed ratios of the two bands in multiple cells lines, similar to the different tissues, there was variation between the different cell lines (Figure 4.11 B). In all of the cell lines tested the expected 110 kDa band for PKD2 was the strongest, except the *Pkd2*$^{-/-}$ MEFs where this band was not

observed (Figure 4.11 B). A higher band at ~250 kDa was detected in all of the cell lines except the *Pkd2*$^{-/-}$ MEFs, consistent with this band being a PKD2 dimer (Figure 4.11 C).

The 85 kDa band was detected in all of the cell lines, including the *Pkd2*$^{-/-}$ MEFs which was unexpected (Figure 4.11 B). This was not detected in previous immunoprecipitations using the Rb8 antibody (Figure 4.6 A). It is difficult to suggest why this band may be visible in this experiment when not seen previously. One possibility is that the band is non-specific binding of the antibody to another protein affected by the loss of PKD2, potentially another member of the TRPP subfamily.

The 85 kDa band was strongest in the IMCD-3, IMCD-K2 and MEF cells, and much weaker in the HEK-293T and NIH3T3 cells, the band is almost invisible in the RPE1 cells, appearing as a faint smear (Figure 4.11 B). This variation is likely linked to the origin of the cell lines: HEK-293T cells are derived from embryonic kidney; both IMCD3 and IMCDK2 cells are derived from the inner medullary collecting duct of mouse kidneys; NIH-3T3 cells from mouse fibroblasts; and RPE-1 cells from human retinal pigment epithelial cells. Interestingly, although adult kidney tissue showed a lower band at ~75 kDa, the kidney cell lines exhibited the ~85 kDa band seen in other cell lines and tissues. The smearing of the 75 kDa band in kidney tissue suggests this may be a result of post translational modification, which may be tissue specific and not required in cultured kidney cells.

Another noticeable finding in the cell line IPs was the presence of a band at ~ 27 kDa in the IMCD-3, IMCD-K2 and MEFs (Figure 4.11 B). This band was much

weaker in the HEK-293T, NIH-3T3 and RPE-1 cells and seemed consistent across all of the tissue samples (Figure 4.11 A and B).

4.2.4 Mass spectrometry analysis confirms presence of PKD2 in 75/85 kDa band

To confirm the identity of the lower 75/85 kDa band identified in kidney and other tissues, the immunoprecipitations were scaled up to recover sufficient protein for mass spectrometry analysis. Kidney, liver, lung and testes were selected for the experiment as they showed strong expression of the higher and lower bands in the western blot (Figure 4.11 A). Kidney was of particular interest due to the 75 kDa band, as opposed to the 85 kDa band detected in other tissues. Immunoprecipitation was performed using Dynabeads protein G on two 5 mg samples from each tissue: one was incubated with the Rb8 PKD2 antibody and the other with Rb8 pre-bleed serum, providing an IgG only control. After immunoprecipitation, the elution sample from each sample was separated by SDS-PAGE and the gel stained using Coomassie (Figure 4.12 A). On the gel, the amount of protein was evidently stronger in the kidney and lung samples; therefor, these became the focus for mass spectrometry.

In contrast to the previous western blot (Figure 4.11 A), the SDS-PAGE Coomassie staining did not show a strong band at 75 kDa in kidney; however, two bands were visible between 75 kDa and 100 kDa and faint bands detected at approximately 110 kDa (Figure 4.12). Whereas the lung sample showed a strong band at ~75 kDa and ~110 kDa (Figure 4.12). Regions covering these bands (~75-90 kDa and ~100-130 kDa) were excised for mass spec analysis along with the equivalent regions in the IgG control samples (Figure 4.12, turquoise and orange boxes). An intense band was visible between 150 and 250 kDa, similar to the band detected by western blot, indicative of a PKD2 dimer; this region and the corresponding IgG region were excised from the kidney sample for confirmation (Figure 4.12 red boxes).

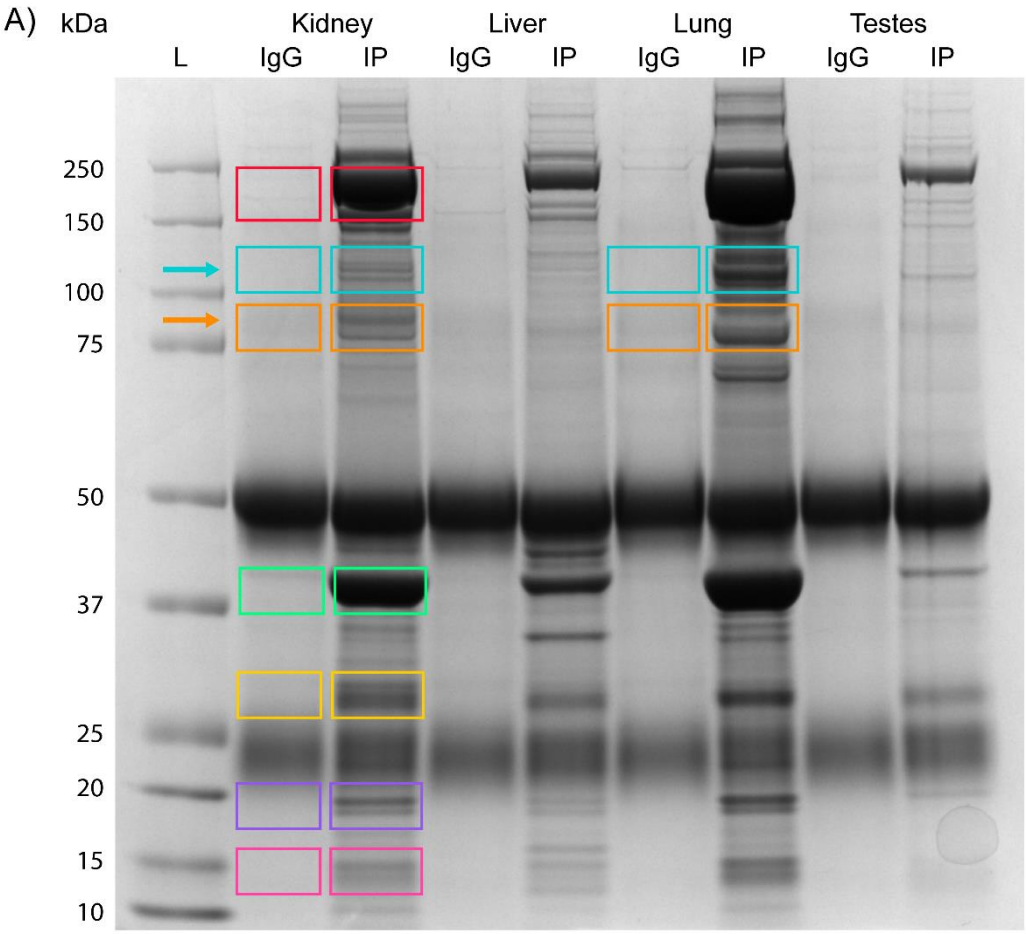


Figure 4.12 Immunoprecipitation for mass spectrometry analysis
SDS-PAGE with Coomassie staining of kidney, liver, lung and testes immunoprecipitations using either Rb8 pre-bleed serum (IgG) or Rb8 PKD2 antibody (IP). Arrows indicate either the expected sized PKD2 (turquoise ~110kDa) or the lower band detected by western blot (orange ~85 kDa). Coloured boxes represent the regions excised for mass spectrometry analysis – red ~150-250 kDa, turquoise ~100-130 kDa, orange ~75-90 kDa, green ~37-42 kDa, yellow ~26-30 kDa, purple ~17-20 kDa, pink ~13-16 kDa.

When examining the Coomassie staining, four sets of bands were noticeable in all of the tissues that weren't present in the IgG controls (Figure 4.12). All of these were below 50 kDa, and were excised and sent for mass spec analysis. The strongest of these was at ~37-42 kDa where the band was almost as intense as the~150-250 kDa band (Figure 4.12 green boxes). Next was a cluster of 2-3 bands detected between ~26 and 30 kDa, the lowest of these bands was highly expressed in all four tissue samples (Figure 4.12 yellow boxes). Below this were two bands, at ~ 17-20 kDa, expressing most in kidney and lung samples (Figure 4.12 purple boxes). And finally, another pair of bands showed good expression in kidney and lung at ~13-16 kDa (Figure 4.12 pink boxes). Although all four of these regions showed stronger bands in the lung samples, the kidney samples were selected for mass spec due to the known functions of PKD2 in the kidney.

Excised gel fragments were sent to the Advanced Mass Spectrometry Facility at the University of Birmingham for Protein/Peptide Identification. Results were sent as excel spreadsheets for each individual sample, full datasets can be seen in the appendix (Appendix 7.1).

Once the results were received, the first thing I wanted to check was whether the lower 75-90 kDa region contained PKD2 (Figure 4.12 orange boxes). The simple answer is yes, PKD2 was identified in the 75-90 kDa region in both the kidney and lung sample. In kidney this region identified 35 peptides, all unique to PKD2, covering 38% of the protein (Table 4.1). In contrast, the 75-90 kDa region in lung contained only 4 peptides covering 5% of PKD2 (Table 4.1). These results suggest that the lower 85 kDa band is a distinct lower molecular weight isoform of PKD2, and I will refer to this band as the lower isoform from now on.

Next, I wanted to check the coverage and peptides identified for expected size (110 kDa) PKD2 in the 100-130 kDa region (Figure 4.12 turquoise boxes). In kidney 19 peptides were identified covering 24% of the protein, whereas in lung 29 peptides were identified covering 36% (Table 4.1). This finding coincided with the western blot analysis (Figure 4.11 A), where the lower band was more prominent in kidney and the expected sized band was expressed more in lung.

Following on from this I checked to see whether the higher band between 150-250 kDa contains PKD2, indicative of PKD2 dimers, 12 peptides were identified covering 17% (Table 4.1). Considering the strength of the band excised and sent for mass spec analysis, I expected to see more coverage of PKD2; however, PKD2 was 14th on the list when ranked by the number of PSMs (peptide spectrum matches), which is the total number of identified peptide spectra matched for the protein.

Above PKD2 in the list were Myosins (9, 11, 10 and 14), Clathrin heavy chain 1, Spectrin alpha and beta chains, Unconventional myosins (VI, Vb, XVIIIa and VIIb), and the Ras GTPase-activating-like protein IQGAP1 (Appendix).

As well as finding PKD2 in the regions expected, PKD2 peptides were also identified in two of the lower regions - 17-20 kDa and 12-15 kDa (Figure 4.12 purple and pink boxes). In the 17-20 kDa region, 4 peptides were identified covering 6% of the protein; whilst in the 12-15 kDa region, 5 peptides were identified covering 5% of the protein (Table 4.1).

Table 4.1. Summary of PKD2 detected in samples sent for mass spec analysis

Tissue	Excised region (kDa)	PKD2 detected	Coverage (%)	No. of peptides	Modifications
Kidney	150-250	Yes	17	12	Phospho [S810]
	100-125	Yes	24	19	Phospho [S810]
	75-100	Yes	38	35	Phospho [S810; S827; S829]
	37-45	No			
	25-30	No			
	17-20	Yes	6	4	None
	12-15	Yes	5	5	Phospho [S810]
Lung	100-125	Yes	36	29	Phospho [S810; S827]
	75-100	Yes	5	4	None

Using the peptide sequences identified in the mass spec analysis, I mapped the reads onto PKD2 (Figure 4.13). As well as annotating the peptides, the main PKD2 domains were also mapped (Figure 4.13 A); this enabled me to view which regions of PKD2 were being identified in the mass spec analysis. Visually, it was intriguing that none of the peptides identified cover all domains except for the voltage sensor like domain (Figure 4.13). The main purpose of mapping the peptides, was to investigate which regions may be missing from the lower isoform (Figure 4.13 D and H). It was clear that the 5% coverage in the lung sample would not give much information, however the mapped peptides can confirm the presence of the 1st extracellular loop and the end of the c-terminal tail (Figure 4.13 H). This left just the kidney sample to assess further, although this sample had the most peptides and best PKD2 coverage of all the samples.

As seen in the peptide mapping, most regions and domains of PKD2 were covered by the peptide reads; however two large regions with no coverage can be observed (Figure 4.13 D). The first gap in coverage is at the N-terminus, the

first peptide mapped begins at amino acid 153, leaving a 152 amino acid gap with a predicted size of 15.7 kDa. The second gap covers the voltage sensor like domain from amino acid 461-578 (118 aa), with a predicted size of 14.2 kDa.

The difference in size between the two isoforms appears to be approximately 25-35 kDa, however the peptide mapping leaves only these two large gaps predicted to be 15.7 and 14.2 kDa. Neither of these appear to be large enough, however the true molecular weight may be different to what is observed on western blot.

Considering the voltage sensor like domain was not covered in any of the samples, and spans three transmembrane domains, it seems unlikely that the 14.2 kDa portion of protein would be truly missing in the lower isoform. On the other hand, N-terminal cleavage is more likely, and is observed in other polycystins (Streets and Ong 2020).

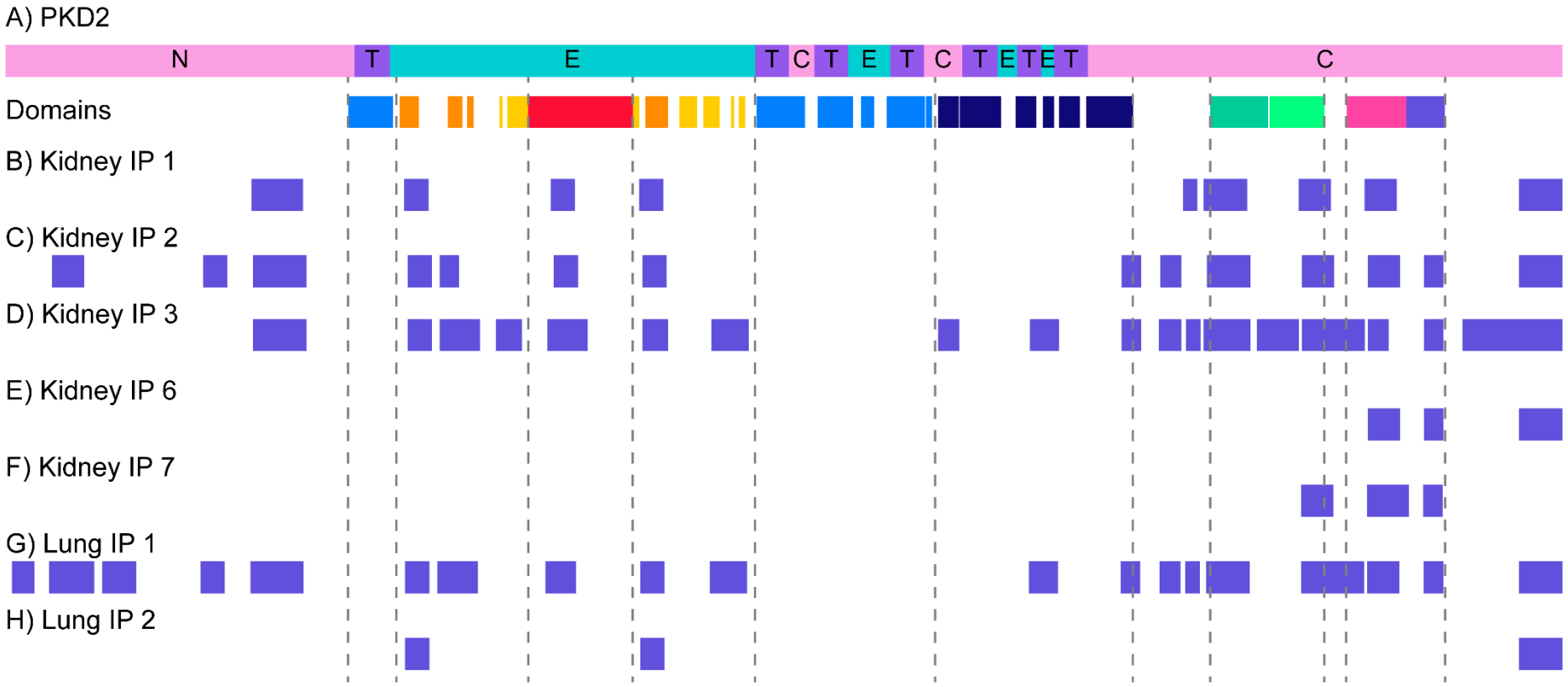


Figure 4.13 Mapping of PKD2 peptides identified by mass spectrometry

PKD2 – Pink (N/C) = intracellular, purple (T) = transmembrane, turquoise (E) = extracellular

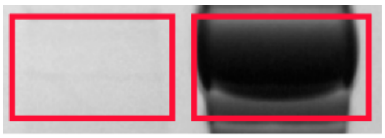
Domains – Blue = VSLD (voltage sensor like domain), orange = TOP domain α-helices, yellow = TOP domain β-sheets red = TLC, dark blue = pore helix, dark green = EF hand, light green = ER retention sequence, pink = coiled-coil domain (homodimerization), purple = coiled-coil domain (heterodimerization).

4.2.5 Interacting partners in adult kidney and lung identified by mass spectrometry

As well as detecting PKD2 in the mass spectrometry data, many potential interacting partners were identified. Due to the large number of proteins detected, a cut off needed to be applied to reduce the amount I assessed further. Proteins were ranked by the number of PMSs, anything with a PSM >4 was included in the analysis. Proteins with a PSM of 3 were assessed, and included if they appeared in multiple samples, were related to another protein with a PSM >4, or seemed functionally relevant. Using protein descriptions and GO-annotations from UniProt, or other protein/gene databases and literature searches when little information was available on UniProt, protein were grouped into 9 categories: Actin and actin binding proteins, Trafficking, Ion transport, Cell adhesion, Extracellular, Mitochondrial, DNA/RNA binding or transcriptional/translational regulation, Keratin, and Other.

Kidney IP 1 ~150-250 kDa

PKD2 identified - Yes
17% coverage, 12 unique peptides



Actin and Actin binding proteins

Myosins (9, 10, 11, 14)
Spectrin alpha and beta chains
(non erythrocytic 1 and erythrocytic 1)
Unconventional myosins
(VI, Vb, XVIIIa, VIIb, Va, Ic, VIIa)
Ras GTPase-activating-like protein
(IQGAP1 and IQGAP2)
Filamins (A and B)
Protein Flightless-1
Villin-1
Rootletin
Plectin
Actin (cytoplasmic 1)

Trafficking

Clathrin heavy chain 1

Ion Transport

None

Cell Adhesion

None

Extracellular

Basement membrane-specific heparan sulfate proteoglycan core protein
A disintegrin and metalloproteinase with thrombospondin motifs 8

Mitochondrial

None

DNA/RNA binding, Transcription/Translation Regulation

Origin recognition complex subunit 1

Keratin

None

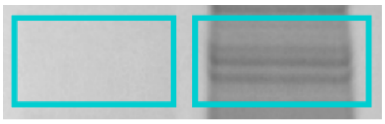
Other

Guanidinoacetate N-methyltransferase

Figure 4.14 Interacting partners identified by mass spectrometry in kidney IP 1
Red text = identified in IgG control

Kidney IP 2 ~100-130 kDa

PKD2 identified - Yes
24% coverage, 19 unique peptides



Actin and Actin binding proteins

Unconventional myosins
(Ic, Id, VI, Ib, Ie, Vb, VIIa, XIX)
Villin-1
Myosin-9
Nck-associated protein 1
Alpha-actinin-4
Actin cytoplasmic 1
Myosin phosphatase Rho-interacting protein

Trafficking

AP-3 complex subunit beta-1
AP-2 complex subunit beta
Alpha-actinin-4
Clathrin heavy chain 1
Exportin-4
Huntingtin-interacting protein 1-related
Protein transport protein Sec16A
Stonin-2
Huntingtin-interacting protein 1

Ion Transport

Sodium/potassium-transporting ATPase subunit alpha-1
Electrogenic sodium bicarbonate cotransporter 1
Solute carrier family 12 member 1

Cell Adhesion

Plakophilin-4
Cadherin-1

Extracellular

Collagen alpha-1(VI) chain

Mitochondrial

Pyruvate carboxylase
Hexokinase-1
2-oxoglutarate dehydrogenase

DNA/RNA binding, Transcription/Translation Regulation

DNA damage-binding protein 1

Keratin

Keratin type I cytoskeletal (10, 19)
Keratin type II cytoskeletal 1

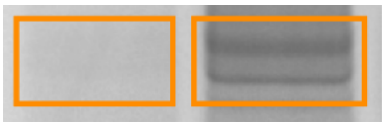
Other

C-1-tetrahydrofolate synthase cytoplasmic
Cullin-associated NEDD8-dissociated protein 1
Serine/threonine-protein phosphatase 4 regulatory subunit 1
Pleckstrin homology domain-containing family A member 6
Ubiquitin-protein ligase E3C

Figure 4.15 Interacting partners identified by mass spectrometry in kidney IP 2
Red text = identified in IgG control, Blue text = fits into multiple categories, Orange text = PSM below cut off (3)

Kidney IP 3 ~75-90 kDa

PKD2 identified - Yes
38% coverage, 35 unique peptides



Actin and Actin binding proteins

Villin-1
Gelsolin
Alpha-actinin (4 and 1)
Scinderin
Unconventional myosins
(Id, Ic, VIIb, VI, Ie, Vb)
Catenin alpha-1
Myosin-9
Villin-like protein
Actins
(cytoplasmic 1, alpha cardiac muscle 1)
Drebrin
Nexilin
LIM domain and actin-binding protein 1
Alpha-adducing

Trafficking

AP-2 complex subunits
(alpha-2, alpha-1, beta)
Alpha-actinin-4
Clathrin heavy chain 1
Coatomer subunits
(beta', gamma-1, beta, gamma-2)
Disabled homolog 2
F-BAR domain only protein 2
Exportin-2
Dynamin-2
Transportin-3
AP-3 complex subunit beta-1
Endoplasmin

Ion Transport

Sodium/potassium-transporting ATPase
subunits (alpha-1, alpha-2)
V-type proton ATPase 116 kDa
subunit a 4
Sarcoplasmic/endoplasmic reticulum
calcium ATPase 2
Electrogenic sodium bicarbonate
cotransporter 1
Band 3 anion transport protein

Cell Adhesion

Catenins (beta-1 and delta-1)
Plakophilin-4
Cadherin-16

Extracellular

None

Mitochondrial

MICOS complex subunit Mic60
Dynamin-like 120 kDa protein
Aconitate hydratase
Acyl-CoA dehydrogenase family
member 11
Trifunctional enzyme subunit alpha
Mitofusin-1

DNA/RNA binding, Transcription/Translation Regulation

Elongation factor 2
Nucleolin

Keratin

Keratin type I cytoskeletal (18 and 10)
Keratin type II cytoskeletal 1

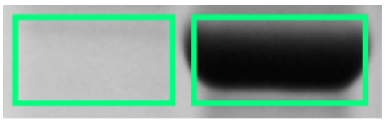
Other

Heat shock protein HSP 90
(alpha and beta)
Complement subcomponents
(C1r-A and C1s-A)
Hexokinase-1
Meprin A subunit alpha
Cytosolic 10-formyltetrahydrofolate
dehydrogenase
ATP-dependent 6-phosphofructokinase
muscle type
von Willebrand factor A
domain-containing protein 5A
26S proteasome non-ATPase
regulatory subunit 2
Major vault protein

Figure 4.16 Interacting partners identified by mass spectrometry in kidney IP 3
Red text = identified in IgG control, Blue text = fits into multiple categories

Kidney IP 4 ~37-42 kDa

PKD2 identified - No



Actin and Actin binding proteins

Actin (cytoplasmic 1 and 2,
aortic smooth muscle)
Beta-actin-like protein 2
Tropomodulin-3
Actin-related protein 2
Drebrin

Mitochondrial

Succinate--CoA ligase [ADP-forming]
subunit beta
Creatine kinase U-type
Medium-chain specific acyl-CoA
dehydrogenase

Trafficking

None

DNA/RNA binding, Transcription/Translation Regulation

None

Ion Transport

None

Keratin

Keratin type I cytoskeletal (19 and 18)

Cell Adhesion

None

Extracellular

None

Other

Erlin-2

Figure 4.17 Interacting partners identified by mass spectrometry in kidney IP 4
Red text = identified in IgG control, Orange text = PSM below cut off (3)

Kidney IP 5 ~26-30 kDa

PKD2 identified - No



Actin and Actin binding proteins

Tropomyosin chains (alpha-3, alpha-4, alpha-1)
Actin cytoplasmic 1
Myosin light polypeptide 6

Trafficking

Clathrin light chain A
Clathrin light chain B

Ion Transport

V-type proton ATPase subunit E 1

Cell Adhesion

None

Extracellular

None

Keratin

None

Mitochondrial

ADP/ATP translocases (1 and 2)
Mitochondrial dicarboxylate carrier
Phosphate carrier protein
Mitochondrial 2-oxoglutarate/malate carrier protein
Voltage-dependent anion-selective channel proteins (3 and 2)
ATP synthase subunit gamma
Enoyl-CoA delta isomerase 1
Mitochondrial ornithine transporter 1
Tricarboxylate transport protein
Electron transfer flavoprotein subunit beta
Mitochondrial brown fat uncoupling protein 1

DNA/RNA binding, Transcription/Translation Regulation

40S ribosomal protein S3
60S ribosomal protein L7a
Elongation factor 1-alpha 1

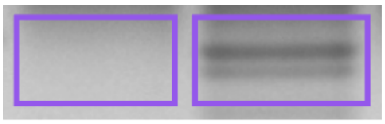
Other

Prohibitin 1
Complement C1q subcomponent subunits (C, B and A)
Carbonyl reductase [NADPH] 1
Very-long-chain enoyl-CoA reductase

Figure 4.18 Interacting partners identified by mass spectrometry in kidney IP 5
Red text = identified in IgG control, Orange text = PSM below cut off (3)

Kidney IP 6 ~17-20 kDa

PKD2 identified - Yes
6% coverage, 4 unique peptides



Actin and Actin binding proteins

Myosin regulatory light chain 12B
Myosin regulatory light polypeptides (9 and 6)
Actin-related protein 2/3 complex subunits (4, 5-like)
Cofilin-1
Destrin
Actin-related protein 2/3 complex subunit 3

Trafficking

Clathrin light chain B
ADP-ribosylation factors (3, 5)
Clathrin light chain A
ADP-ribosylation factor 4

Ion Transport

None

Cell Adhesion

None

Extracellular

None

Mitochondrial

None

DNA/RNA binding, Transcription/Translation Regulation

40S ribosomal protein S11
60S ribosomal proteins (L28, L27a, L12)

Keratin

Keratin type I cytoskeletal 10
Keratin type II cytoskeletal (1 and 5)

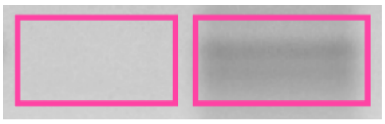
Other

Calmodulin-2
Peptidyl-prolyl cis-trans isomerase B
Peroxiredoxin-1
Probable N-acetyltransferase CML1

Figure 4.19 Interacting partners identified by mass spectrometry in kidney IP 6
Red text = identified in IgG control, Orange text = PSM below cut off (3)

Kidney IP 7 ~13-16 kDa

PKD2 identified - Yes
5% coverage, 5 unique peptides



Actin and Actin binding proteins

Myosin light polypeptide 6
Myosin light chain 3
Actin cytoplasmic 1
Allograft inflammatory factor 1-like
Actin-related protein 2/3 complex subunit 5
Myosin regulatory light chain 12B
Myosin regulatory light polypeptide 9

Trafficking

Clathrin light chains (B and A)
AP-2 complex subunit sigma

Ion Transport

None

Cell Adhesion

None

Extracellular

None

Keratin

Keratin type I cytoskeletal 10
Keratin type II cytoskeletal 5

Mitochondrial

Cytochrome c oxidase subunits (4 isoform 1, 5a, NDUFA4, 5B, 6B1, 6A1, 6C)
Mitochondrial pyruvate carrier 2
NADH dehydrogenase [ubiquinone] 1 alpha subcomplex subunits (6, 13, 5)
Peroxiredoxin-5
CDGSH iron-sulfur domain-containing protein 1
NADH dehydrogenase [ubiquinone] 1 subunit C2
ADP/ATP translocase 1
NADH dehydrogenase [ubiquinone] 1 beta subcomplex subunit 4
Cytochrome b-c1 complex subunit 7

DNA/RNA binding, Transcription/Translation Regulation

60S ribosomal proteins (L30, L27, L23, L35a)
40S ribosomal proteins (S16, S19, S18, S20, S14, S25)
60S acidic ribosomal protein P2
Histones (H2A.Z, H4, H2A type 1-E)

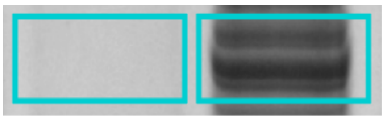
Other

Glyceraldehyde-3-phosphate dehydrogenase
Hemoglobin subunits (alpha and beta-1)
Thioredoxin
SH3 domain-binding glutamic acid-rich-like protein 2
Cytochrome b5
Uroplakin-2

Figure 4.20 Interacting partners identified by mass spectrometry in kidney IP 7
Red text = identified in IgG control

Lung IP 1 ~100-130 kDa

PKD2 identified - Yes
36% coverage, 29 unique peptides



Actin and Actin binding proteins

Unconventional myosins (Ic, Id, Ib, Ig, Ie)
Alpha-actinins (4, 1, 2)
Ankycorbin
LIM and calponin homology domains-containing protein 1
LIM domain and actin-binding protein 1
Myosin-9
Neurabin-2
Drebrin
Band 4.1-like protein 2
Actin cytoplasmic 1
Smoothelin

Trafficking

Alpha-actinin-4
Kinesin-1 heavy chain
Exportin-7
AP-2 complex subunit beta

Ion Transport

Sarcoplasmic/endoplasmic reticulum calcium ATPases (2 and 3)

Cell Adhesion

Catenin delta-1

Extracellular

None

Mitochondrial

None

DNA/RNA binding, Transcription/Translation Regulation

ATP-binding cassette sub-family F member 1
Heterogeneous nuclear ribonucleoprotein U
KN motif and ankyrin repeat domain-containing protein 2
116 kDa U5 small nuclear ribonucleoprotein component
Nucleolar RNA helicase 2
Serrate RNA effector molecule homolog

Keratin

None

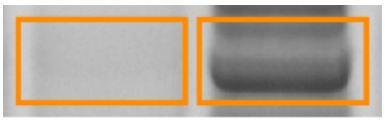
Other

A-kinase anchor protein 2
Ras-interacting protein 1
Rho guanine nucleotide exchange factors (15 and 2)
Serine/threonine-protein phosphatase 4 regulatory subunit 1
Serine/threonine-protein kinase TAO3
C-1-tetrahydrofolate synthase cytoplasmic
Dipeptidyl peptidase 4
MAP7 domain-containing protein 1

Figure 4.21 Interacting partners identified by mass spectrometry in lung IP 1
Red text = identified in IgG control, Blue text = fits into multiple categories

Lung IP 2 ~75-90 kDa

PKD2 identified - Yes
5% coverage, 4 unique peptides



Actin and Actin binding proteins

Gelsolin
Nexilin
LIM domain and actin-binding protein 1
Myosin phosphatase Rho-interacting protein
Unconventional myosins (Id and Ic)
LIM and calponin homology domains-containing protein 1
Actins (cytoplasmic 1 and alpha cardiac muscle 1)
Fermitin family homolog 2
Myosin-9
Moesin
Radixin
Drebrin
Leiomodin-1
Vinexin
Adseverin
SUN domain-containing protein 2
Gamma-adducing
Ezrin

Trafficking

Translocation protein SEC63 homolog
Coatomer subunit gamma-2
Exocyst complex component 3-like 4
Conserved oligomeric Golgi complex subunit 4
Exocyst complex component 3

Ion Transport

Band 3 anion transport protein
Sodium-dependent phosphate transport protein 2B

Cell Adhesion

Junction plakoglobin
Fermitin family homolog 2
Catenin delta-1
Platelet glycoprotein 4
Periostin

Extracellular

None

Mitochondrial

MICOS complex subunit Mic60
Mitofusin-1
Trifunctional enzyme subunit alpha

DNA/RNA binding, Transcription/Translation Regulation

ATP-dependent RNA helicase DDX1
Signal transducer and activator of transcription 3

Keratin

None

Other

Heat shock protein HSP 90 (beta and alpha)
von Willebrand factor A domain-containing protein 5A
Complement subcomponents (C1r-A and C1s-A)
Leucine-rich repeat and calponin homology domain-containing protein 1
A-kinase anchor protein 2
Platelet glycoprotein 4
Ribosomal protein S6 kinases (alpha-3, alpha-1, alpha-4)
Immunoglobulin heavy constant mu
Steryl-sulfatase
Threonine--tRNA ligase 1 cytoplasmic
Retinoic acid-induced protein 3
Rho guanine nucleotide exchange factor 7
Serine/threonine-protein kinase MARK2
ATP-dependent 6-phosphofructokinase liver type

Figure 4.22 Interacting partners identified by mass spectrometry in lung IP 2
Red text = identified in IgG control, Blue text = fits into multiple categories, Orange text = PSM below cut off (3)

The first category, Actin and actin binding partners, was created due to the frequency of the actin-binding GO-annotation appearing in searches; in fact all but kidney IP5 had an actin binding protein at the top of the list when ranked by the number of PSMs. The list of actin-binding proteins identified was extensive and includes:

Actin-related proteins, Actins, Adseverin, Allograft inflammatory factor 1-like, Alpha-actinins, Ankycorbin, Band 4.1-like protein 2, Catenins, Cofilin-1, Drebrin, Ezrin, Fermitin family homolog 2, Filamins, Gamma-adducing, Gelsolin, Leiomodin-1, LIM domain and actin-binding proteins, Moesin, Myosin phosphatase Rho-interacting protein, Myosins, Nck-associated protein 1, Neurabin-2, Nexilin, Plectin, Protein flightless-1, Radixin, Ras GTPase-activating-like proteins, Rootletin, Scinderin, Smoothelin, Spectrins, SUN domain-containing protein 2, Tropomodulin, Tropomyosins, Unconventional myosins, Villin, Vinexin. (Figures 4.14-4.22)

Although PKD2 is not commonly associated with actin and actin binding proteins, the actin cytoskeleton is known to play a key role in ciliogenesis and cilia maintenance (Brücker et al. 2020; Copeland 2020; Ge et al. 2022; Hoffman and Prekeris 2022; Smith et al. 2020). The actin based cytoskeleton is known to associate with the ciliary pocket, which is involved in the transport of membrane associated proteins to cilia (Hoffman and Prekeris 2022; Molla-Herman et al. 2010; Smith et al. 2020). Actin is also found at the ciliary tip, where it mediates cilia shedding by ectocytosis for actin-dependent cilia disassembly or removal of cilia components and signalling molecules (Brücker et al. 2020; Ge et al. 2022; Hoffman and Prekeris 2022; Nager et al. 2017).

Some of the actin binding partners identified in my mass spec data appear to play significant roles in these processes. The onset of ciliogenesis is said to begin with myosin-Va, listed as unconventional myosin-Va in the mass spec dataset (Figure 4.14) (Brücker et al. 2020; Ge et al. 2022; Hoffman and Prekeris 2022; Wu et al. 2018). Myosin-Va associated preciliary vesicles are transported to the pericentrosomal region along microtubules by dynein; from here, it is trafficked along the Arp2/3-associated branched actin network to the distal appendages of the mother centriole (Hoffman and Prekeris 2022; Wu et al. 2018). Four subunits of the actin-related protein 2/3 complex were identified in my kidney samples (Figures 4.17, 4.19 and 4.20). The ARP2/3 complex is involved in actin polymerisation and branching of F-actin to establish a supportive meshwork (Brücker et al. 2020; Ge et al. 2022; Smith et al. 2020). It is also thought to be required for ectosome release along with myosin VI, drebrin and α-actinin 4 (Nager et al. 2017), all of which were identified in the mass spec datasets (Figures 4.14, 4.15, 4.16, 4.17, 4.21 and 4.22). In contrast, Gelsolin and Cofilin-1 are known to be F-actin depolymerising and actin severing proteins; cofilin preferentially disassembles branched actin networks (Brücker et al. 2020; Kim et al. 2015; Kim et al. 2010; Smith et al. 2020). Both of these were identified in my mass spec datasets (Figures 4.16, 4.19 and 4.22).

One study used targeted proximity labelling (cmAPEX) to identify the ciliary membrane-associated proteome (Kohli et al. 2017; Smith et al. 2020). This showed enrichment of actin-binding proteins in cilia including: α-actinins (1 & 4), actin-related protein 2/3 complex subunits (Arpc3, Arpc4, Arpc5, and Arpc5l), Actin-related protein 3 (Arp3), coronins (Coro1b and Coro1c), cortactin, drebrin-like protein, ezrin, gelsolin, myosins (Myo6, Myl12a, Myl6b, and Myl9),

tropomyosins (1, 2, 3 and 4) and utrophin. There is clear overlap of some proteins identified in their experiments and in mine from PKD2 immunoprecipitations.

There are studies directly linking PKD2 to actin binding partners such as Hax-1, cortactin, α-actinin, filamin, gelsolin, profilin and tropomyosin-1; interactions between these and PKD2 have been shown to be important for anchoring it to the plasma membrane and in influencing its channel activity. (Brücker et al. 2020; Cantero and Cantiello 2015; Gallagher et al. 2000; Hardy and Tsiokas 2020; Li et al. 2003; Li et al. 2005; Wang et al. 2012; Wang et al. 2015). The first paper to suggest a link between PKD2 and the actin cytoskeleton was in 2000, when a yeast two-hybrid screen identified Hax-1 as an interacting partner (Gallagher et al. 2000). This interaction was confirmed in mammalian cells, and expression of PKD2 and HAX-1 co-localised to the endoplasmic reticulum; they suggested Hax-1 also binds to cortactin, which mediates the association with the actin cytoskeleton (Gallagher et al. 2000). Yeast two-hybrid screens were later used to identify interactions between PKD2 and Tropomyosin, α-actinins and filamins; all of which were shown to co-localise in the endoplasmic reticulum and perinuclear regions in transfected cells (Li et al. 2003; Li et al. 2005; Wang et al. 2012). Interestingly, when Li et al. assessed endogenous PKD2 and α-actinin co-localisation, in subconfluent MDCK and IMCD cells, they found substantial overlap on the plasma membrane and cell-cell junctions (Li et al. 2005).

One study by María Cantero and Horacio Cantiello looked at the effects of actin binding partners on calcium regulation of PKD2. They found that α-actinin, gelsolin and profilin all increased channel activity in the presence of Ca^{2+}, whilst filamin inhibited channel activity (Cantero and Cantiello 2015). This work highlighted the regulation of PKD2 channel activity by Ca^{2+} in the presence of

actin binding partners and the functional effects this may have on the channel (Cantero and Cantiello 2015).

The next category “Trafficking” was of interest as I hoped to detect candidate interacting partners involved in PKD2 ciliary trafficking. Most of the trafficking related proteins identified fit into either clathrin related, COPI mediated or COPII mediated, with the exception of the exportins/transportins involved in nuclear export and import respectively.

Clathrin is most commonly known for being involved in clathrin-mediated endocytosis, which is a major endocytic pathway (Royle 2006; Smith and Smith 2022). The plasma membrane is coated by clathrin and adaptor proteins to form a clathrin-coated pit, membrane scission is driven by Dynamin to internalise the clathrin-coated vesicle into the cytoplasm, inside the cell the coat disassembles to allow the delivery of cargo to early endosomes (Mettlen et al. 2018; Royle 2006; Smith and Smith 2022). Clathrin itself does not directly bind to the cargo located in the plasma membrane, cargo selection is coordinated by adaptor proteins and accessory proteins (McMahon and Boucrot 2011; Royle 2006; Smith and Smith 2022). The main adaptor is the AP-2 complex, which mediates endocytosis from the plasma membrane (Park and Guo 2014; Royle 2006). The mass spec datasets from kidney immunoprecipitations identified all of those key proteins: Clathrin heavy chain 1, Clathrin light chains A and B, Dynamin-2 and AP-2 complex subunits alpha-1, alpha-2, beta and sigma (Figures 4.14, 4.15, 4.16, 4.18 and 4.19). Four other clathrin adaptor proteins were also identified in the mass spec datasets; Huntingtin-interacting proteins 1 and 1-related and

Disabled homolog 2 are both involved in clathrin-mediated endocytosis from the plasma membrane (Legendre-Guillemin et al. 2002; Mishra et al. 2002; Owen et al. 2004), whilst Stonin-2 facilitates Clathrin-mediated synaptic vesicle retrieval. The F-BAR domain only protein 2 (Fcho2) reaches the plasma membrane ahead of Clathrin, recruited by plasma membrane phosphatidylinositol-4,5-bisphosphate ($PI(4,5)P_2$); this promotes $PI(4,5)P_2$ clustering at cargo boundaries, which enhances and speeds up Clathrin assembly (El Alaoui et al. 2022; Uezu et al. 2011).

After Clathrin related interacting partners, the next abundant group of trafficking interacting partners were related to COPI protein complexes – another form of vesicle coat protein for vesicle formation and cargo selection (Arakel and Schwappach 2018). COPI vesicles are involved in Golgi to ER transport as well as intra-Golgi transport (Arakel and Schwappach 2018; Béthune and Wieland 2018). There are seven core subunits of COPI: α, β, β', ε, δ, γ and ζ (Arakel and Schwappach 2018), of which three were identified in the mass spec datasets: β, β' and both gamma subunits γ1 and γ2 (Figure 4.16, and 4.22). The γ and ζ subunits are both encoded by two genes, hence γ1 and γ2. Different combinations of these subunits create four isoforms of the COPI coat, which may have distinct trafficking routes or key functions (Arakel and Schwappach 2018; Sahlmüller et al. 2011). Related to COPI are the Arf (ADP-ribosylation factor) family of proteins, which recruit COPI coats to Golgi membranes (Dejgaard and Presley 2020; Kahn et al. 2005; Popoff et al. 2011). In the kidney samples, three Arf proteins were identified: Arf3, Arf4 and Arf5 (Figure 4.18). Arf3 is a class I Arf required for trafficking from the ER–Golgi intermediate compartment to the *cis*-Golgi, it has also been shown to localise to recycling endosomes for the integrity

of recycling endosomes (Kahn et al. 2005; Kondo et al. 2012; Nakai et al. 2013). Afr4 and Arf5 are class II Arfs, both involved in transport between the ER–Golgi intermediate compartment and Golgi (Chun et al. 2008; Nakai et al. 2013). Arf4 has also been shown to play a role in ciliary cargo transport through binding to the VxPx ciliary targeting motif (Mazelova et al. 2009; Nakai et al. 2013).

In addition to these, two unrelated Sec proteins linked to trafficking were identified – Sec16 in kidney and Sec63 in lung (Figures 4.15 and 4.22). Sec16 functions in COPII-mediated endoplasmic reticulum to Golgi transport of secretory proteins (Tang 2017; Wilhelmi et al. 2016). More recently, Sec16 has shown involvement in endoplasmic reticulum exit of the cystic fibrosis (CF) transmembrane conductance regulator (CFTR) during GRASP-mediated unconventional secretion (Piao et al. 2017; Tang 2017).

Sec63 interacts with the Sec61 complex and is involved in protein targeting and translocation across the endoplasmic reticulum membrane (Fedeles et al. 2015; Jung et al. 2019; Jung and Kim 2021). Mutations in Sec63 are known to cause autosomal dominant polycystic liver disease (Cornec-Le Gall et al. 2018; Davila et al. 2004; Fedeles et al. 2015). Interestingly, loss of Sec63 has been shown to cause kidney cysts using the tissue specific *Ksp-Cre* transgene, which was exacerbated in *Pkd1*$^{+/-}$ and *Pkd2*$^{+/-}$ mice (Fedeles et al. 2011).

The third category “Ion Transport”, revealed a selection of proteins involved in transport of various ions including chloride, bicarbonate, calcium, sodium, potassium and hydrogen. The list of ion transport proteins includes: Band 3 anion transport protein, Electrogenic sodium bicarbonate cotransporter 1,

Sarcoplasmic/endoplasmic reticulum calcium ATPases (2 and 3), Sodium/potassium-transporting ATPase subunits (alpha-1, alpha-2), Sodium-dependent phosphate transport protein 2B, Solute carrier family 12 member 1, V-type proton ATPase 116 kDa subunit a 4, and V-type proton ATPase subunit E 1. Although none of these have been directly linked to PKD2 previously, some of them localise to the plasma membrane and have known roles in the kidney (Reithmeier et al. 2016; Stehberger et al. 2003). Interestingly, the Solute carrier family 12 member 1 (also known as NKCC2) is a kidney specific sodium-potassium-chloride cotransporter, and shows significantly reduced protein levels in *Pkd1*$^{-/-}$ mice (Lakshmipathi et al. 2020).

A few proteins were identified that are associated with cell-cell adhesion including: Cadherins (1 and 16), Catenins (beta-1 and delta-1), Fermitin family homolog 2, Junction plakoglobin, Periostin, Plakophilin-4, and Platelet glycoprotein 4. Cadherin 1 (also known as E-cadherin) and associated catenins play important roles in cell proliferation and polarity; these have been shown to co-localise with PKD1 at the apical and lateral plasma membrane in fetal kidney tubules (Huan and van Adelsberg 1999). Co-immunoprecipitation revealed that PKD1 is in a complex containing E-cadherin and catenins (Huan and van Adelsberg 1999). The PKD1-PKD2 complex has also been shown to localise to the lateral plasma membrane of kidney epithelial cells, and it has been suggested that PKD2 may be involved in cell adhesion alongside PKD1 (Newby et al. 2002; Streets et al. 2003). *PERIOSTIN* mRNA is overexpressed in ADPKD kidney cells, and the protein has been shown accumulate in the fluid of ADPKD cysts and promote cell proliferation (Wallace et al. 2008).

Three extracellular matrix proteins were identified in the mass spec analysis: A disintegrin and metalloproteinase with thrombospondin motifs 8, Basement membrane-specific heparan sulfate proteoglycan core protein, and Collagen alpha-1(VI) chain. However, my literature searches did not find any links between these three proteins and the polycystins.

A large number of mitochondrial proteins were identified in the mass spec data comprising: 2-oxoglutarate dehydrogenase, Aconitate hydratase, Acyl-CoA dehydrogenase family member 11, ADP/ATP translocases (1 and 2), ATP synthase subunit gamma, CDGSH iron-sulfur domain-containing protein 1, Creatine kinase U-type, Cytochrome b-c1 complex subunit 7, Cytochrome c oxidase subunits (4 isoform 1, 5a, NDUFA4, 5B, 6B1, 6A1, 6C), Dynamin-like 120 kDa protein, Electron transfer flavoprotein subunit beta, Enoyl-CoA delta isomerase 1, Hexokinase-1, Medium-chain specific acyl-CoA dehydrogenase, MICOS complex subunit Mic60, Mitochondrial 2-oxoglutarate/malate carrier protein, Mitochondrial brown fat uncoupling protein 1, Mitochondrial dicarboxylate carrier, Mitochondrial ornithine transporter 1, Mitochondrial pyruvate carrier 2, Mitofusin-1, NADH dehydrogenase [ubiquinone] 1 subunits (alpha 5, 6 and 13, beta 4, and C2), Peroxiredoxin-5, Phosphate carrier protein, Pyruvate carboxylase, Succinate--CoA ligase [ADP-forming] subunit beta, Tricarboxylate transport protein, Trifunctional enzyme subunit alpha, Voltage-dependent anion-selective channel proteins (3 and 2).

Not much is known about the polycystins and mitochondria; however, a few papers have been released over the last few years providing evidence for roles of the polycystins associated with mitochondria. One study identified mitochondrial abnormalities within cells lining kidney cysts in Ksp-Cre *Pkd1*$^{flox/flox}$ mice, which they suggested may facilitate cyst formation in ADPKD (Ishimoto et al. 2017). More recently, Kuo and colleagues showed that PKD2 functions to reduce tethering of mitochondria to the ER, preventing inappropriate calcium dependent increases in mitochondrial function and cell proliferation (Kuo et al. 2019).

4.2.6 Investigating PKD2^{lrm4} interacting partners

To address the question of why PKD2^{lrm4} fails to localise to cilia, I wanted to investigate whether there were any differences in the interacting partners of PKD2$^{+/+}$ and PKD2$^{lrm4/lrm4}$. To do this, I collected kidneys and lungs from *Pkd2*$^{+/+}$, *Pkd2*$^{-/-}$ and *Pkd2*$^{lrm4/lrm4}$ 14.5 d.p.c. embryos; this stage was selected as kidney cysts are observed in *Pkd2*$^{-/-}$ and *Pkd2*$^{lrm4/lrm4}$ embryos at 15.5 d.p.c. but not at 14.5 d.p.c., and I didn't want the presence of kidney cysts to impact the data collected (Walker 2016; Walker et al. 2019).

In contrast to the previous samples sent for mass spec (Section 4.2.5), the whole elution sample from immunoprecipitations were sent to the Advanced Mass Spectrometry Facility (at the University of Birmingham), rather than separating proteins by SDS-PAGE and excising bands to send. *Pkd2*$^{+/+}$ samples were sent as controls from both *Pkd2*$^{+/-}$ and *Pkd2*$^{lrm4/lrm4}$ intercrosses, *Pkd2*$^{-/-}$ and *Pkd2*$^{lrm4/lrm4}$ samples were compared to their respective littermate controls. In order to analyse the data, the results from both *Pkd2*$^{+/+}$ samples were pooled to give a larger dataset of interacting partners.

Initially, I decided to compare the data collected in this experiment, from *Pkd2*$^{+/+}$ 14.5 d.p.c. embryonic kidneys, with the previously data collected from *Pkd2*$^{+/+}$ adult kidneys – to assess whether I was detecting the same interacting partners in both experiments. Only 196 proteins were identified in the mass spec analysis of 14.5 d.p.c. kidney immunoprecipitation elution samples, whereas 501 proteins were detected in the seven bands excised from SDS-PAGE separation of the adult kidney immunoprecipitation elution. The most notable difference was the loss of actin and actin binding partners in the 14.5 d.p.c. samples, which were

abundant in the adult kidney datasets (Figure 4.23). The ion transport and cell-adhesion associated proteins were also not identified in the 14.5 d.p.c. samples (Figure 4.23). Only one trafficking (Huntingtin-interacting protein 1) and one extracellular protein (Basement membrane-specific heparan sulfate proteoglycan core protein) were identified in both 14.5 d.p.c. and adult kidney samples (Figure 4.23).

Found in both *Pkd2*$^{+/+}$ adult and 14.5 d.p.c. embryonic kidneys

PKD2 identified - Yes

Actin and Actin binding proteins

None

Trafficking

Huntingtin-interacting protein 1

Ion Transport

None

Cell Adhesion

None

Extracellular

Basement membrane-specific heparan sulfate proteoglycan core protein

Mitochondrial

60 kDa heat shock protein
MICOS complex subunit Mic60
Cytochrome c oxidase subunit NDUFA4
Cytochrome b-c1 complex subunit 8

DNA/RNA binding, Transcription/Translation Regulation

Histones
(H4, H2A.Z, H3.3C)
60s ribosomal proteins
(L27, L23a, L32, L35, L31, L3, L23, L35a, L8, L34, L12, L27a)
Elongation factor 1-alpha 1
40s ribosomal proteins
(S3a, S10, S4 X isoform, S25, S20, S2)
Small nuclear ribonucleoprotein -associated protein
Small nuclear ribonucleoprotein Sm (D2, D3, D1)
Nucleolin
RNA-binding protein 14

Keratin

Keratin, type II cytoskeletal 1
Keratin, type I cytoskeletal 17

Other

Tubulin alpha-1B
Tubulin beta-4B
Enhancer of rudimentary homolog
Peptidyl-prolyl cis-trans isomerase B
Ubiquitin-40S ribosomal protein S27a
Thioredoxin

Figure 4.23 Interacting partners identified by mass spectrometry in both *Pkd2*$^{+/+}$ adult and 14.5 d.p.c. embryonic kidneys

List of interacting partners that were identified by mass spectrometry in bands excised from *Pkd2*$^{+/+}$ adult kidney immunoprecipitations (separated by SDS-PAGE), and whole elution sample from *Pkd2*$^{+/+}$ 14.5 d.p.c. embryonic kidneys.

To assess the changes in interacting partners between *Pkd2*$^{+/+}$ and *Pkd2*$^{lrm4/lrm4}$ 14.5 d.p.c. embryonic kidneys, I first needed to rule out proteins that may not be true interacting partners of PKD2. To do this, I compared the data from *Pkd2*$^{+/+}$ samples with the data from *Pkd2*$^{-/-}$ samples, kidney and lung datasets were assessed separately. Proteins that appeared in both *Pkd2*$^{+/+}$ and *Pkd2*$^{-/-}$ samples were removed from the list of *Pkd2*$^{+/+}$ proteins, as these are likely non-specific interacting partners detected in the mass spec data; to differentiate this list from *Pkd2*$^{+/+}$ I will refer to it as *Pkd2*$^{+/+\Delta}$. The lists of remaining proteins, for kidney and lung samples, were then compared with the proteins detected in *Pkd2*$^{lrm4/lrm4}$.

For the 14.5 d.p.c. kidney samples, this revealed 111 proteins in *Pkd2*$^{+/+\Delta}$ that were not detected in *Pkd2*$^{lrm4/lrm4}$. Based on what I had learned from the initial mass spec data, and GO annotations from Uniprot, I assessed all 111 proteins and identified three intriguing interacting partners: Charged multivesicular body protein 4b (*Chmp4b*), Huntingtin-interacting protein 1 (*Hip1*), and Ras-related protein Rab-26 (*Rab26*).

CHMP4B is a subunit of the endosomal sorting complexes required for transport (ESCRT), Jung and colleagues demonstrated that CHMP4B localises to primary cilia and is required for ciliogenesis (Jung et al. 2020). CHMP4B can stabilise membrane curvature in cytokinetic abscission and retroviral budding; therefore, they suggested it may play a role in stabilising the curvature of the ciliary membrane (Jung et al. 2020).

Huntingtin-interacting protein 1 showed up in the previous mass spec data, from *Pkd2*$^{+/+}$ adult kidney samples (Section 4.2.5, Figure 4.15). As described in that

section, HIP1 is a clathrin adaptor protein which helps regulate clathrin-coat assembly at the plasma membrane (Mishra et al. 2002; Owen et al. 2004). It has been suggested that HIP1 and its interacting partner Hippi may play a role in ciliogenesis (Keryer et al. 2011). Hippi is essential for nodal cilia formation, *Hippi*$^{-/-}$ embryos exhibit a complete loss of nodal cilia and left-right patterning defects (Houde et al. 2006).

Rab26 is one of many Rab GTPases, part of the Ras-related GTPase superfamily, these proteins regulate endomembrane organisation and are involved in vesicle-mediated endocytosis and exocytosis (Blacque et al. 2018; Wang et al. 2018). Rab8 was the first Rab GTPase linked to cilia, in 1995 it was revealed to localise along the ciliary stalk in retinal photoreceptors (Deretic et al. 1995). Since then, numerous Rab GTPases have been shown to play key roles in ciliogenesis with involvement in ciliary vesicle formation, centriole uncapping, ciliary membrane elongation, and IFT regulation (Blacque et al. 2018). Rab GTPases known to be involved in ciliogenesis include: Rab5, Rab8, Rab11, Rab17, Rab23, Rab28, Rab29 (Blacque et al. 2018; Yoshimura et al. 2007). So far, Rab26 has not been linked to ciliogenesis and is not as well characterized as other Rab GTPases; however, it has been shown to play a role in Golgi-to-cell surface transport of GPCRs, similar to Rab8 (Wang et al. 2018). Interestingly, Rab26 is encoded within the PKD1 locus and has been examined in ADPKD cells due to its homology with Rab8, which shows altered expression in ADPKD cells; conversely, Rab26 did not show any changed in expression or localisation in ADPKD cells (Charron et al. 2000).

There were also 32 proteins detected in *Pkd2*$^{lrm4/lrm4}$ 14.5 d.p.c. kidney samples that were not in the list of *Pkd2*$^{+/+\Delta}$ proteins. I compared these 32 proteins to the proteins that were found in both *Pkd2*$^{+/+}$ and *Pkd2*$^{-/-}$ samples, and likely non-specific, which left me with 3 proteins: Heterogeneous nuclear ribonucleoproteins C1/C2 (*Hnrnpc*), 40S ribosomal protein S4 (*Gm15013*), and Adenylyltransferase and sulfurtransferase MOCS3 (*Mocs3*). The first two are both RNA binding proteins, involved in mRNA processing and splicing, and the third is involved in Molybdenum cofactor synthesis. It seems unlikely that any of these three proteins are involved in the retention of PKD2^{lrm4} at the ciliary base.

In the 14.5 d.p.c. lung samples, 75 proteins were identified that were present in *Pkd2*$^{+/+\Delta}$ but not *Pkd2*$^{lrm4/lrm4}$. The same assessment, as kidney proteins, was performed using GO annotations on Uniprot. In the lung samples, this highlighted just one protein of interest based on protein roles/localisation - T-complex protein 1 subunit epsilon (*Cct5*). CCT5 (also known as CCTε) is one of the CCT chaperonin proteins that form the CCT/TRiC complex; six of the CCT proteins (including CCT5) have been shown to form a complex with chaperonin-like BBS proteins (BBS6, BBS10 and BBS12) to mediate BBSome assembly (Seo et al. 2010). Four of the six CCT proteins showed enriched localisation at the centrosome: CCT1, CCT4, CCT5, and CCT8 (Seo et al. 2010; Zhang et al. 2021). In *Tetrahymena*, CCT5 exhibits expression along the full length of cilia (Seixas et al. 2003). Zhang and colleagues demonstrated that CCT5 also forms a complex with CEP55 and Aurora A during cilia disassembly (Zhang et al. 2021).

Comparing proteins detected in *Pkd2*$^{lrm4/lrm4}$ 14.5 d.p.c. lungs with those detected in both *Pkd2*$^{+/+}$ and *Pkd2*$^{-/-}$ lungs, left me with a list of 32 proteins expressed specifically in *Pkd2*$^{lrm4/lrm4}$. Using GO annotations, I narrowed this down to two proteins of interest: Sorting nexin (*Snx9*) and Septin-2 (*Septin2*).

Sorting nexin 9 (SNX9) is an adaptor protein involved in clathrin-mediated endocytosis (Lundmark and Carlsson 2003; Owen et al. 2004). Sorting nexin 9 binds to clathrin, AP-2 and dynamin-2, they are recruited and co-assembled at the plasma membrane for the formation of clathrin-coated vesicles (Lundmark and Carlsson 2003). SNX9 has been shown to stimulate N-WASP/Arp2/3-mediated actin polymerisation, implicating SNX9 in actin dynamics and membrane remodelling during endocytosis (Yarar et al. 2007); it also localises to cilia and accumulates at the cilia excision site prior to decapitation, where it is thought to play a role in actin nucleation in cilia decapitation (Phua et al. 2017).

Septin-2 (SEPT2) is part of the septin family of GTB-binding proteins, they form hetero-oligomers that interact with the cytoskeleton and microtubules. Septins were originally identified in budding yeast where they form a diffusion barrier between the mother and the bud, which limits the diffusion of membrane proteins (Hu et al. 2010; Palander et al. 2017). Septin-2 localises in a ring like formation at the ciliary base, forming a diffusion barrier which restricts the movement of membrane proteins between the ciliary and periciliary membrane (Hu et al. 2010).

Analysis of the mass spec datasets, from *Pkd2*$^{+/+}$, *Pkd2*$^{-/-}$ and *Pkd2*$^{lrm4/lrm4}$ 14.5 d.p.c. kidney and lung samples, has revealed some intriguing candidate interacting partners that may be affected by the *lrm4* mutation. However, the

number of peptides detected in the mass spec were extremely low, with only 1 peptide detected of each protein in the samples.

4.3 Discussion

In this chapter, I have demonstrated the development of two new rabbit polyclonal antibodies that are specific for PKD2. Through the use of these antibodies, immunoprecipitations revealed the presence of a lower band at approximately 85 kDa compared to the expected 110 kDa band for PKD2. Mass spectrometry analysis of the lower band confirmed its identity as PKD2. Based on the peptide mapping of PKD2 for the ~85 kDa band, it seems likely that a portion of the N-terminus is missing in this lower isoform. N-terminal cleavage via a GSP motif is a key post-translational modification of PKD1, but cleavage sites have not been described for PKD2 (Streets and Ong 2020). As suggested for *Pkd1l1*, it is possible that an alternative transcript may be present which lacks this N-terminal region, this could be examined using 5' and 3' RACE and qPCR analysis. Further investigation is needed to ascertain whether the lower isoform is a product of transcriptional changes or post-translational modification.

Mass spec analysis of bands excised from provided some insight into possible trafficking mechanisms involved in PKD2 ciliary localisation. Both clathrin and COPI vesicles are associated with ciliogenesis and the transport of ciliary membrane proteins (Jin et al. 2010; Molla-Herman et al. 2010). The identification of clathrin and COPI related proteins, in the mass spec from PKD2 immunoprecipitations, is consistent with PKD2 trafficking within clathrin and COPI vesicles; however, further investigation is needed to assess whether either of these mechanisms are involved specifically in the ciliary trafficking of PKD2.

The identification of interacting partners associated with cell adhesion, such as cadherins and catenins, in the mass spec datasets from wild type B6J kidney samples provides further evidence for the involvement of PKD2 in cell adhesion.

Comparison of the two sets of mass spec data, one from excised bands from adult kidney and lung immunoprecipitations and the other from 14.5 d.p.c. kidney and lung immunoprecipitations where the whole elution fraction was sent, revealed quite a contrast in interacting partners identified. In total, 501 unique proteins were identified in the seven bands excised from adult kidney samples, whereas only 196 unique proteins were detected in the 14.5 d.p.c. kidney samples – even though the same amount (5 mg) of total protein was used when performing the immunoprecipitations. There was also a distinct difference in the number of unique peptides and PSMs detected between the whole lysate and the excised bands; for kidney, the highest number of PSMs was 31 in the whole lysate samples compared with 635 in the excised bands. With hindsight, it seems likely that more interacting partners may have been identified in *Pkd2*$^{+/+}$, *Pkd2*$^{-/-}$ and *Pkd2*$^{lrm4/lrm4}$ embryonic kidneys and lungs, if the samples were separated by SDS-PAGE and bands excised as performed with the adult samples previously.

The mass spectrometry data from 14.5 d.p.c. kidneys and lungs did highlight a few candidate proteins, for missing interacting partners; these were proteins identified in the *Pkd2*$^{+/+}$ samples, that were not present in *Pkd2*$^{lrm4/lrm4}$ samples. Candidate proteins from the kidney samples includes: Charged multivesicular body protein 4b (*Chmp4b*), Huntingtin-interacting protein 1 (*Hip1*), and Ras-related protein Rab-26 (*Rab26*). Whilst only one candidate protein was observed in the lung sample data - T-complex protein 1 subunit epsilon (*Cct5*).

Analysis of proteins detected in *Pkd2*$^{lrm4/lrm4}$ samples, that were not present in *Pkd2*$^{+/+}$ samples, did not reveal any candidate interacting partners for proteins that may be involved in the retention of PKD2^{lrm4} at the ciliary base in the kidney sample. However, two intriguing interacting partners were detected in *Pkd2*$^{lrm4/lrm4}$ 14.5 d.p.c. lung samples: Sorting nexin (*Snx9*) and Septin-2 (*Septin2*).

PKD2^{lrm4} accumulates in a ring-like pattern at the ciliary base (Walker et al. 2019). Based on the localisation of SEPT2 at the ciliary base and its role in forming a diffusion barrier between the periciliary and ciliary membranes (Hu et al. 2010), it seems plausible that PKD2^{lrm4} may be restricted to the ciliary base via a SEPT2 interaction; making this a highly intriguing interaction to investigate further. As previously explained, only one peptide was identified for SEPT2 in only the lung *Pkd2*$^{lrm4/lrm4}$ sample; therefore, more experimental data is required to confirm the specificity of this interaction with PKD2^{lrm4} and not wild type PKD2.

To ascertain whether these interactions are important in the mislocalisation of PKD2^{lrm4}, the interactions first need to be confirmed using co-immunoprecipitation. This could either be performed using specific antibodies for CHMP4B, HIP1, RAB26, CCT5, SNX9, and SEPT2, or by co-expressing affinity-tagged proteins in a suitable cell line and using antibodies for the tags (e.g. His, Myc, HA, FLAG, etc.). Once the interaction has been confirmed, it would be ideal to assess whether the proteins co-localise either at the ciliary base or within the cilia axoneme. Following on from that, alterations to the interaction and localisation with PKD2^{lrm4} could be investigated.

5. Examining PKD2 and PKD1L1 expression during L-R patterning

5.1 Introduction

Previous research has established a clear requirement for PKD2, in nodal cilia, for correct left-right patterning, as described in the main introduction (section 1.3.2). The main finding being that of Yoshiba and colleagues, who provided clear evidence of the requirement for PKD2 in crown cell cilia using a PKD2-Venus transgenic mouse line driven by the crown cell specific *Nodal* enhancer (NDE) (Yoshiba et al. 2012). The loss of ciliary localisation in *Pkd2*^{lrm4} embryos, leading to abnormal left-right patterning, highlights the importance of localisation in PKD2 function (Ermakov et al. 2009; Grimes et al. 2016; Walker et al. 2019; Yoshiba et al. 2012).

There is strong evidence that PKD1L1 is required for the development of normal situs, with both *Pkd1l1*$^{-/-}$ and *Pkd1l1*$^{rks/rks}$ embryos exhibiting situs defects (Field et al. 2011; Grimes et al. 2016; Vogel et al. 2010). Thus far, the only evidence for PKD1L1 localising to nodal cilia is in medaka fish; Kamura and colleagues showed co-localisation of Pkd1l1 and Pkd2 in Kupffer's vesicle, equivalent to the embryonic node (Kamura et al. 2011). They also showed a loss of Pkd2 ciliary localisation in *pkd1l1*^{abc} mutants, which exhibit randomised expression of the usually asymmetrically expressed genes *nodal* and *lefty*, and a loss of Pkd1l1 ciliary localisation in a *pkd2* morphant (Kamura et al. 2011). This suggested a co-dependent relationship for the ciliary localisation of Pkd1l1 and Pkd2 in the medaka Kupffer's vesicle. One of the biggest differences between the medaka Kupffer's vesicle and the mouse embryonic node, is that all KV cilia are motile and positive for Lrd (Kamura et al. 2011). In mouse, McGrath and colleagues

showed two distinct populations of nodal cilia; central LRD positive, motile cilia and non-motile cilia at the peripheries that do not contain LRD (McGrath et al. 2003).

It is currently unknown whether PKD1L1 co-localises with PKD2 in mouse nodal cilia, answering this question would reveal important information and provide further insight into the possible mechanisms of PKD1L1-PKD2 function in left-right pattern determination.

5.2 Results

5.2.1 Testing PKD1L1 antibodies in B6J WT embryos

To begin investigating whether PKD1L1 localises to nodal cilia in the mouse, I tested three PKD1L1 antibodies in whole mount immunofluorescent staining of 7.5-8.5 d.p.c. B6J embryos. Another member of the lab, David Asante, had been generating mouse monoclonal antibodies raised against a combination of three peptides of PKD1L1. Due to the homology of polycystin proteins, computational analysis was performed by the bioinformatics group at Harwell, which was used to select the most unique regions of PKD1L1 against which to raise the mouse monoclonal antibodies. Multiple mouse monoclonal antibodies were generated, and data from David Asante using Structured Illumination Microscopy (SIM) suggested the 10B4d3 antibody provided the best immunofluorescent staining in cell lines; therefore this was the main one tested in my experiments.

Previously, the lab had generated a rabbit polyclonal antibody, however the specificity of this antibody to PKD1L1 was undetermined. There are a few commercial rabbit polyclonal antibodies available. One of which is raised against human PKD1L1 (Invitrogen PA5-54588), in a similar region of the REJ domain of PKD1L1 to our labs rabbit polyclonal antibody and one of the peptides used to raise the mouse monoclonal antibodies; this region shares 77% homology with mouse. Another commercial rabbit polyclonal antibody was raised against the 1st extracellular loop of mouse PKD1L1 (Invitrogen OSP00015W); because this one was raised against a different region of mouse sequence to our antibodies, I decided to use this one for testing.

The regions these antibodies were raised against are depicted in Figure 5.1.

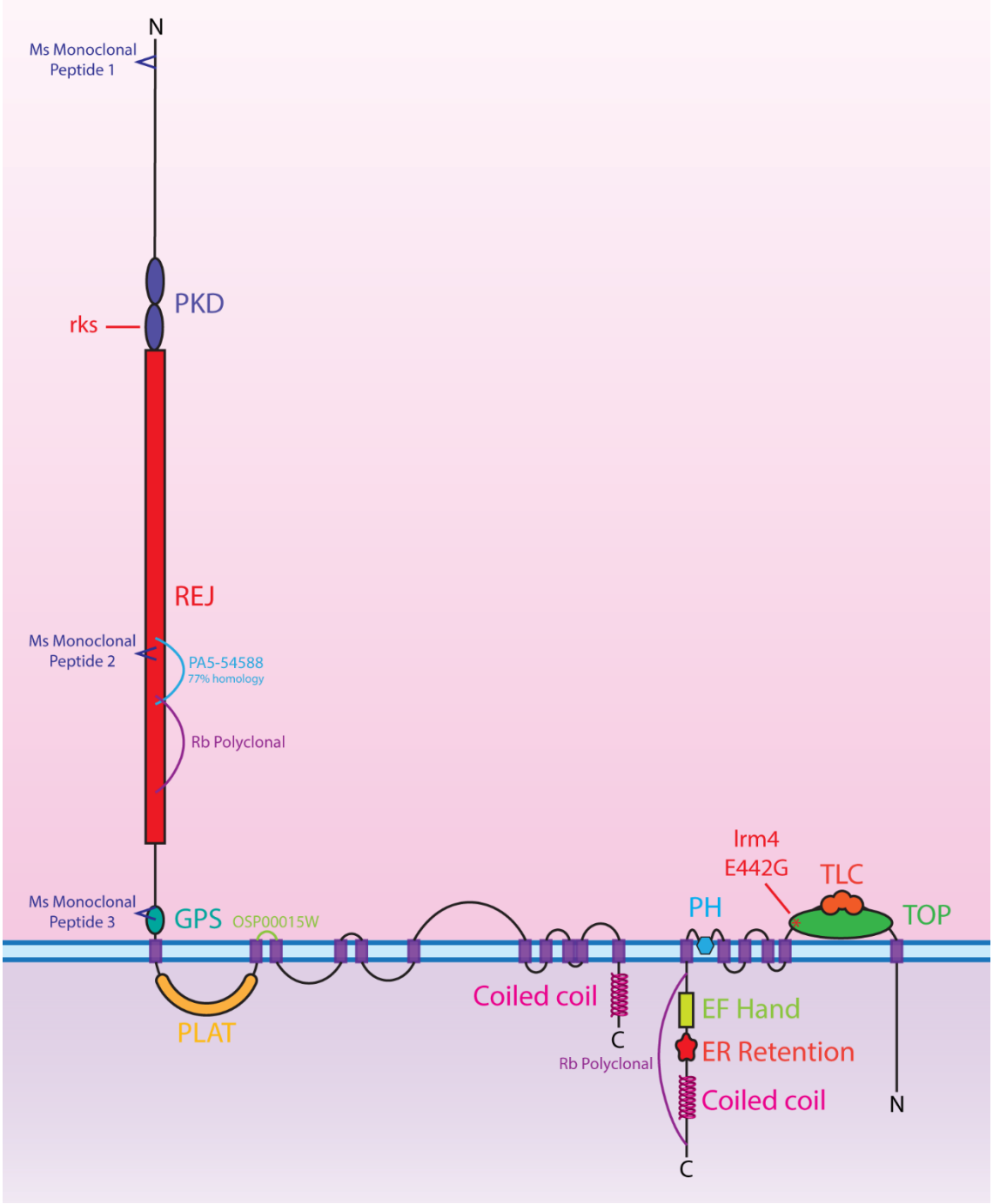


Figure 5.1 Diagrammatic representation of PKD1L1 and PKD2
Schematic diagram showing the main protein domains of PKD1L1 and PKD2, the *rks* and *lrm4* point mutations are marked. Antigen regions used to generate our mouse monoclonal and rabbit polyclonal antibodies, as well as the commercial antibodies PA5-54588 and OSP00015W are labelled.

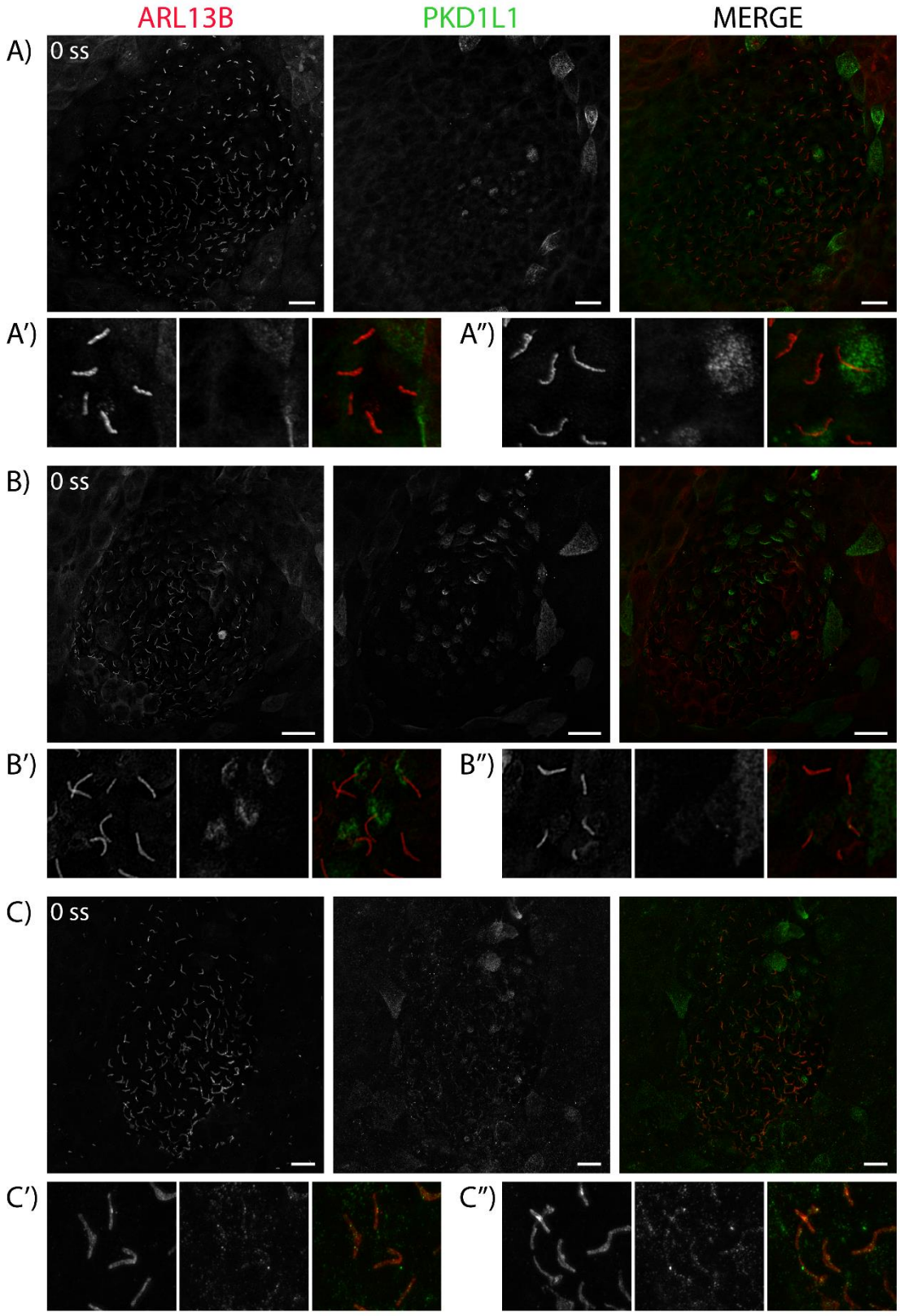


Figure 5.2 PKD1L1 mouse monoclonal antibody staining in WT B6J nodes
Immunofluorescent staining of three 7.5-8.5 d.p.c embryonic nodes (A, B and C), using the mouse monoclonal antibody 10B4d3. A, B, C ‘ and ‘‘ are zooms of nodal cilia from A, B and C. Staining is in the same order for whole node images and zooms, from left to right: ARL13B (Red), PKD1L1 (Green), Merge. Scale bars represent 10 µm.

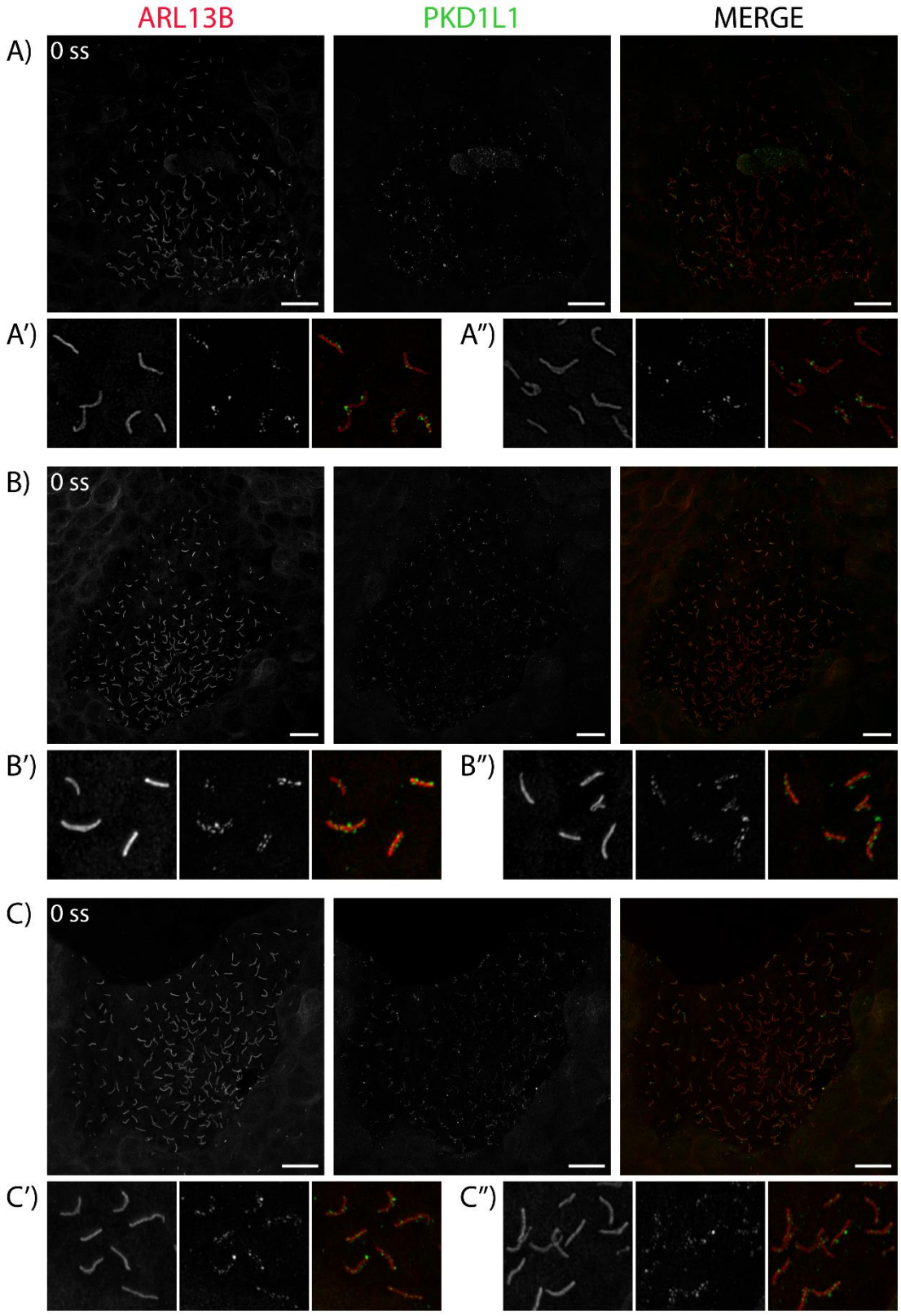


Figure 5.3 PKD1L1 rabbit polyclonal antibody staining in WT nodes
Immunofluorescent staining of three 7.5-8.5 d.p.c embryonic nodes (A, B and C), using our rabbit polyclonal antibody. A, B, C ‘ and ‘‘ are zooms of nodal cilia from A, B and C. Staining is in the same order for whole node images and zooms, from left to right: ARL13B (Red), PKD1L1 (Green), Merge. Scale bars represent 10 µm.

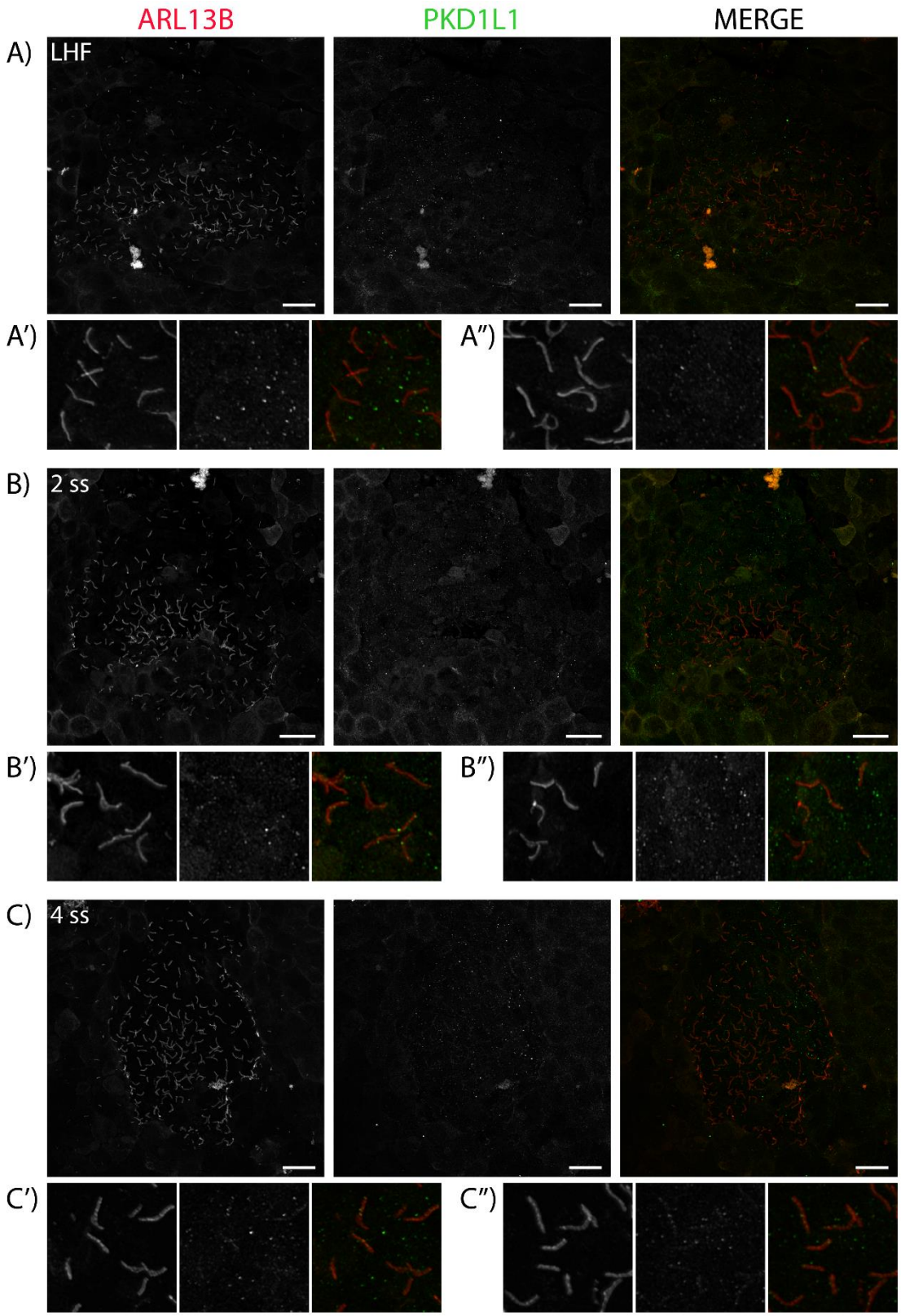


Figure 5.4 PKD1L1 OSP00015W antibody staining in WT nodes
Immunofluorescent staining of three 7.5-8.5 d.p.c embryonic nodes (A, B and C), using the commercial rabbit polyclonal antibody OSP00015W A, B, C ‘ and ‘‘ are zooms of nodal cilia from A, B and C. Staining is in the same order for whole node images and zooms, from left to right: ARL13B (Red), PKD1L1 (Green), Merge. Scale bars represent 10 µm.

Immunofluorescent staining using the mouse monoclonal antibody (10B4d3), showed variation of staining between samples (Figure 5.2). Most embryos showed staining in the cell body, particularly in cells around the edge of the node and in the centre of the pit, with no specific staining of nodal cilia (Figure 5.2 A, A', B, B'). One embryo showed clear staining in nodal cilia (Figure 5.2 C, C'); however this was one embryo of ~15 that were assessed.

In comparison, staining using the rabbit polyclonal antibody showed clear punctate expression of PKD1L1 in nodal cilia in all embryos assessed (Figure 5.3 A, A', B, B', C, C'). Staining appeared stronger towards the peripheries of the node, but could also be detected in nodal cilia in the pit of the node.

Staining using the commercial OSP00015 antibody showed some ciliary localisation, however there appeared to be a lot of background staining (Figure 5.4). This varied between embryos, one embryo seemed to show very little cilia specific staining (Figure 5.4. A, A'), whilst others showed slightly clearer ciliary localisation (Figure 5.4 C, C').

All three antibodies showed some level of staining in nodal cilia, however this was highly variable between antibodies and between different embryos.

5.2.2 Testing PKD1L1 antibodies in *Pkd1l1*$^{+/+}$, *Pkd1l1*$^{+/-}$ *and Pkd1l1*$^{-/-}$ embryos

In order to test the specificity of PKD1L1 antibodies, the *Pkd1l1*$^{-/-}$ mouse line was re-derived. This allele was first described in Vogel et al. and was imported to MRC Harwell where the mice were further characterised by previous members of the lab (Field 2009; Field et al. 2011; Grimes et al. 2016; Vogel et al. 2010); the line was archived as frozen sperm a few years prior to my arrival to the lab, so mice were not readily available when I joined. This required the rederivation of the stock through *in vitro* fertilisation.

Numbers of embryos were limited for these experiments due to the availability of mice after Covid lockdowns; in total I had 45 embryos which were split into three groups of 15 to test the three antibodies. While this ensured that the results came from a fully blinded experiment, it did leave me with unequal genotype numbers in each group. However, each group had at least 3 *Pkd1l1*$^{-/-}$ embryos, but not every group had 3 *Pkd1l1*$^{+/+}$ embryos; for this reason *Pkd1l1*$^{+/-}$ embryos were also included in the analysis. Embryos were imaged, processed and scored blind to the genotypes to prevent any bias.

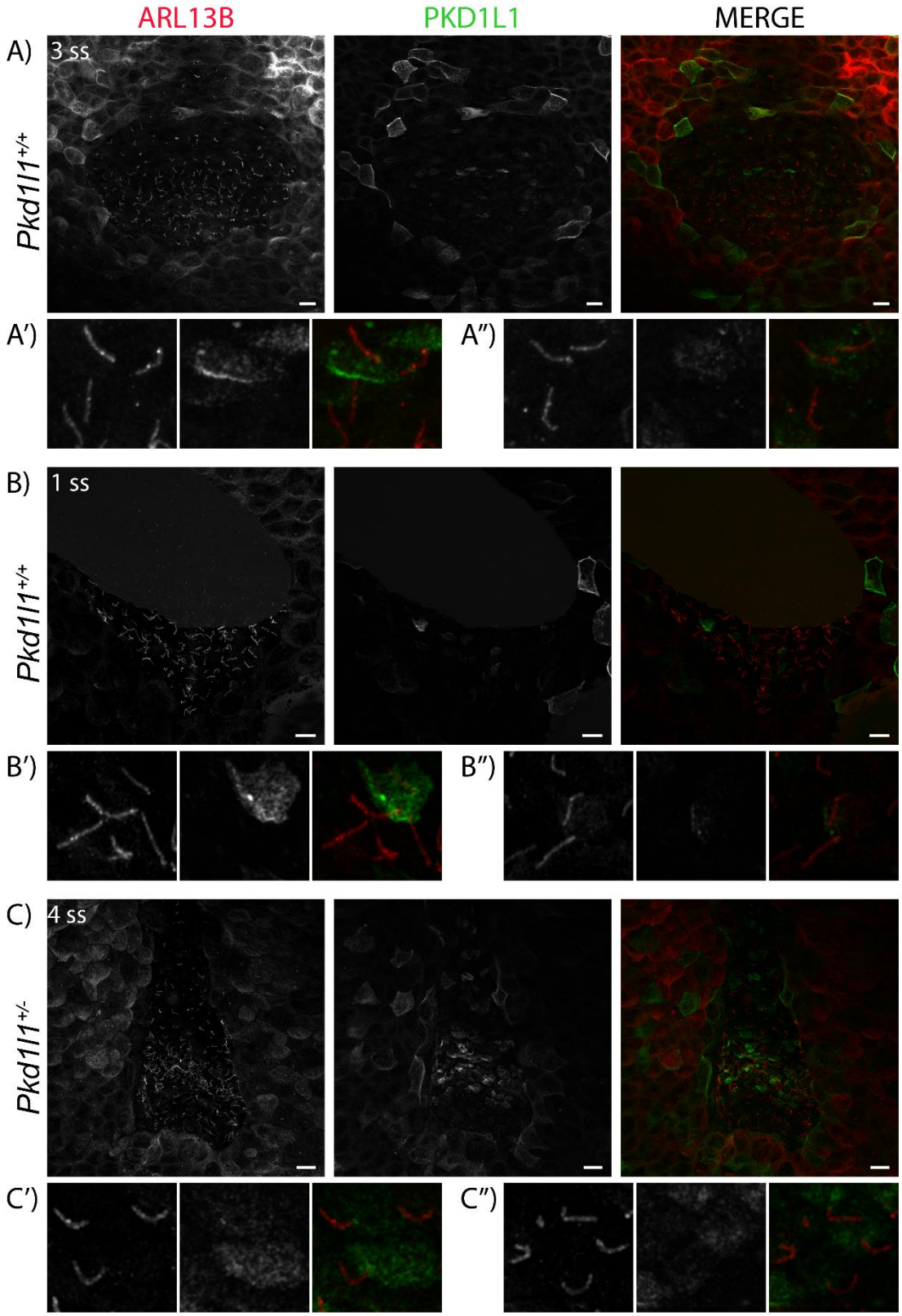


Figure 5.5 PKD1L1 mouse monoclonal antibody staining in *Pkd1l1*$^{+/+}$ and *Pkd1l1*$^{+/-}$ nodes

Immunofluorescent staining of three embryonic nodes (A, B and C), using the mouse monoclonal antibody (10B3d4). A, B, C ‘ and ‘‘ are zooms of nodal cilia from A, B and C. Staining is in the same order for whole node images and zooms, from left to right: ARL13B (Red), PKD1L1 (Green), Merge. Scale bars represent 10 µm.

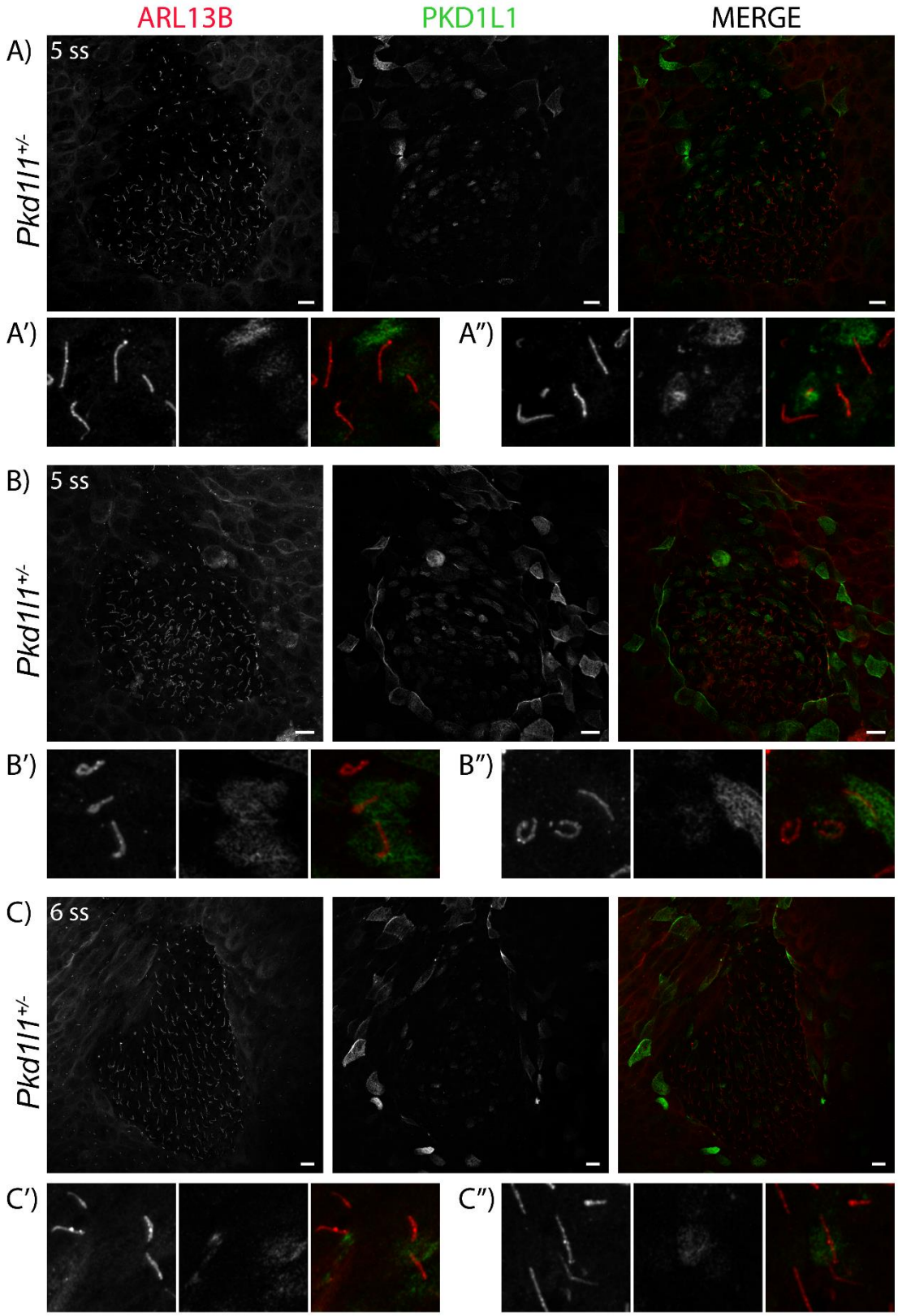


Figure 5.6 PKD1L1 mouse monoclonal antibody staining in *Pkd1l1*$^{+/-}$ nodes
Immunofluorescent staining of three embryonic nodes (A, B and C), using the mouse monoclonal antibody (10B3d4). A, B, C ‘ and ‘‘ are zooms of nodal cilia from A, B and C. Staining is in the same order for whole node images and zooms, from left to right: ARL13B (Red), PKD1L1 (Green), Merge. Scale bars represent 10 µm.

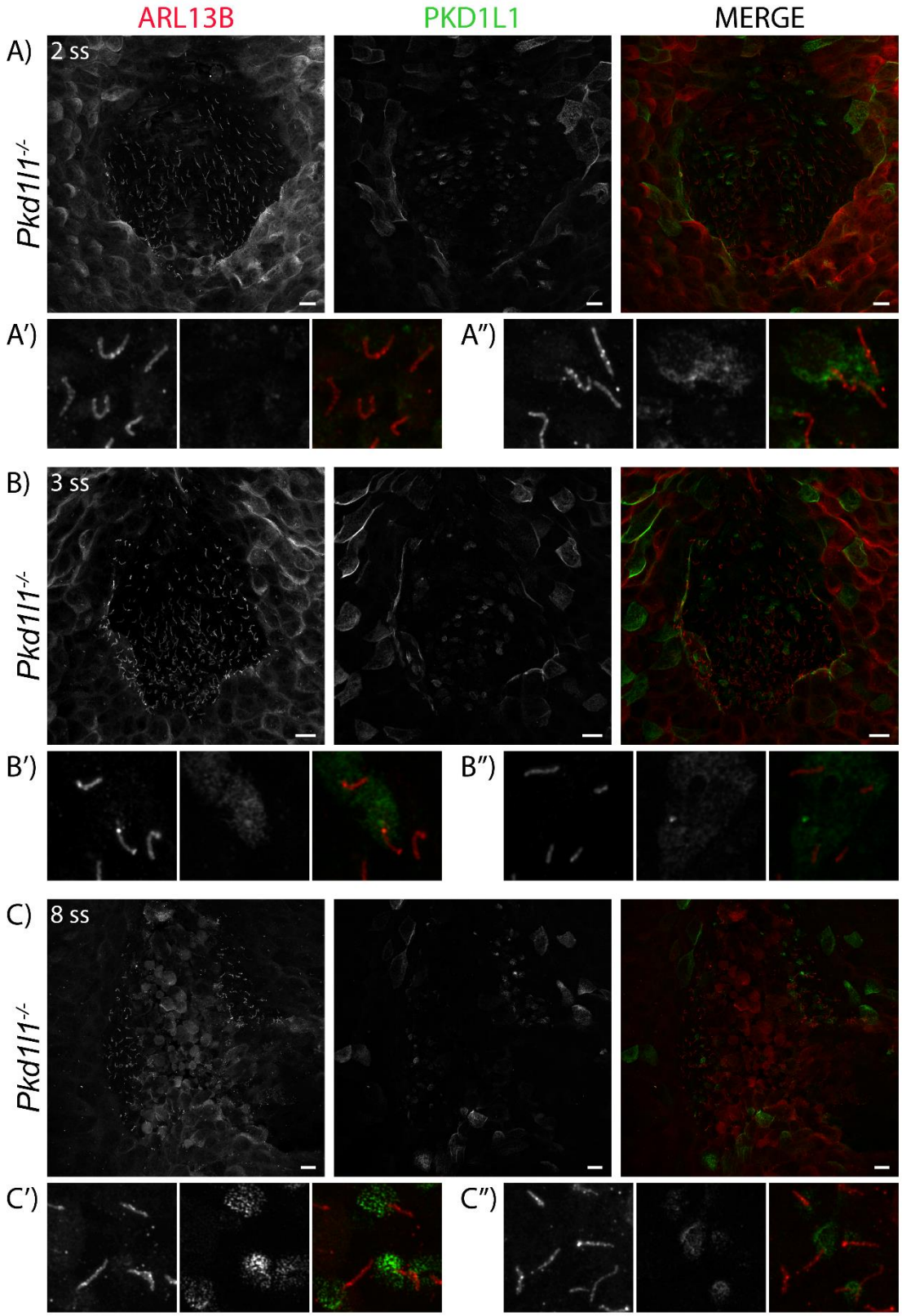


Figure 5.7 PKD1L1 mouse monoclonal antibody staining in *Pkd1l1*$^{-/-}$ nodes
Immunofluorescent staining of three embryonic nodes (A, B and C), using the mouse monoclonal antibody (10B3d4). A, B, C ‘ and ‘‘ are zooms of nodal cilia from A, B and C. Staining is in the same order for whole node images and zooms, from left to right: ARL13B (Red), PKD1L1 (Green), Merge. Scale bars represent 10 µm.

Staining using the mouse monoclonal antibody (10B4d3) in *Pkd1l1*$^{+/+}$ and *Pkd1l1*$^{+/-}$ embryos was consistent with previous staining in wild type B6J embryos (Figures 5.5 and 5.6). PKD1L1 ciliary staining was not detected in any of the embryos, and staining mostly localised to the cytoplasm of cells. In some samples, the staining appeared stronger towards the plasma membrane of cells surrounding the node (Figure 5.5 A, 5.6 B).

When analysing the images taken in *Pkd1l1*$^{-/-}$ embryos, it was clear that staining looked very similar to that of *Pkd1l1*$^{+/+}$ and *Pkd1l1*$^{+/-}$ embryos. Staining was visible in cells surrounding the node (Figure 5.7 B), and in the cytoplasm of cells within the node (Figure 5.7 A, A', B, B', C, C'). This is indicative of non-specific binding of the mouse monoclonal primary antibody.

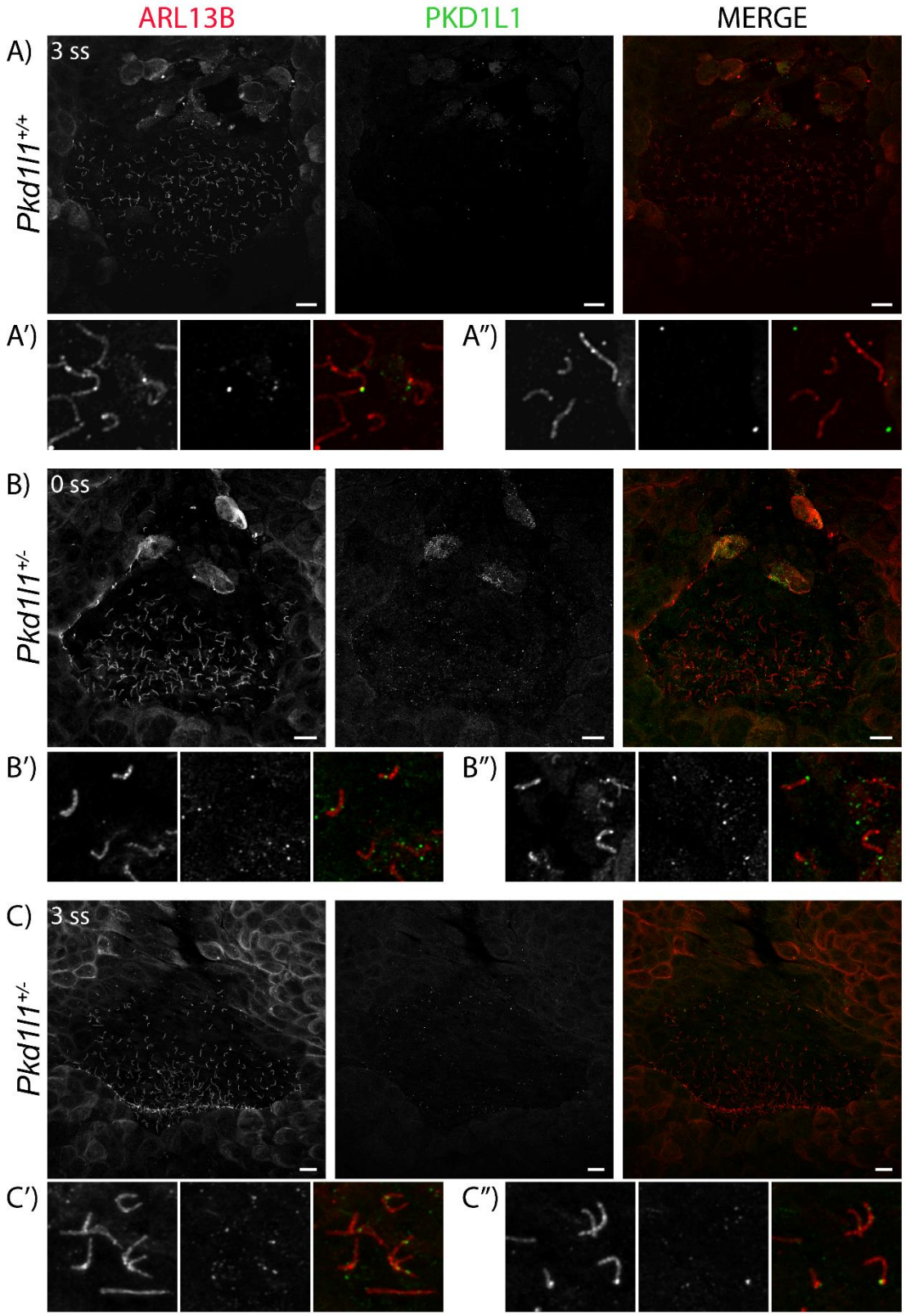


Figure 5.8 PKD1L1 rabbit polyclonal antibody staining in *Pkd1l1*$^{+/+}$ and *Pkd1l1*$^{+/-}$ nodes

Immunofluorescent staining of three embryonic nodes (A, B and C), using the rabbit polyclonal antibody. A, B, C ‘ and ‘‘ are zooms of nodal cilia from A, B and C. Staining is in the same order for whole node images and zooms, from left to right: ARL13B (Red), PKD1L1 (Green), Merge. Scale bars represent 10 µm.

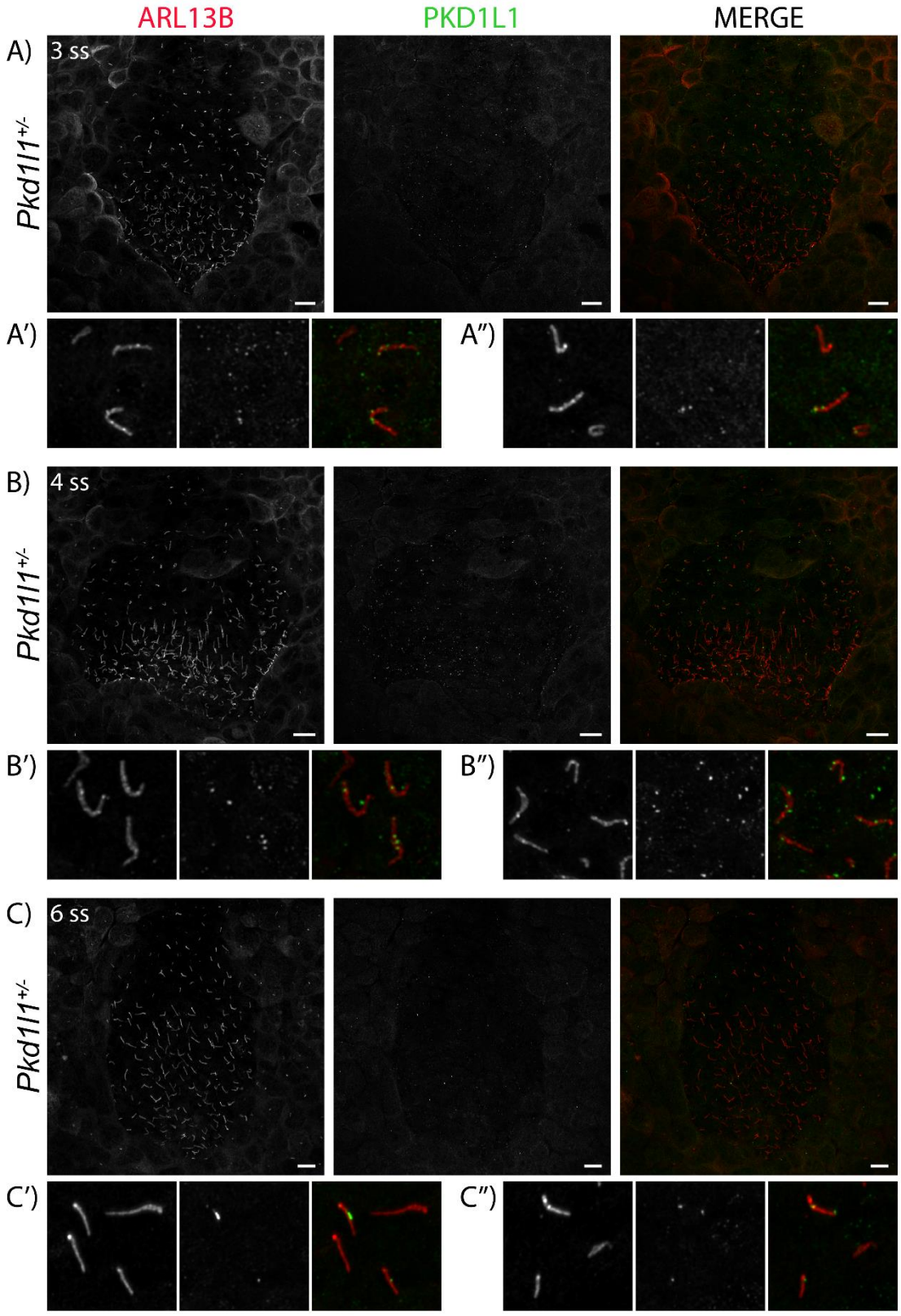


Figure 5.9 PKD1L1 rabbit polyclonal antibody staining in *Pkd1l1*$^{+/-}$ nodes
Immunofluorescent staining of three embryonic nodes (A, B and C), using the rabbit polyclonal antibody. A, B, C ‘ and ‘‘ are zooms of nodal cilia from A, B and C. Staining is in the same order for whole node images and zooms, from left to right: ARL13B (Red), PKD1L1 (Green), Merge. Scale bars represent 10 µm.

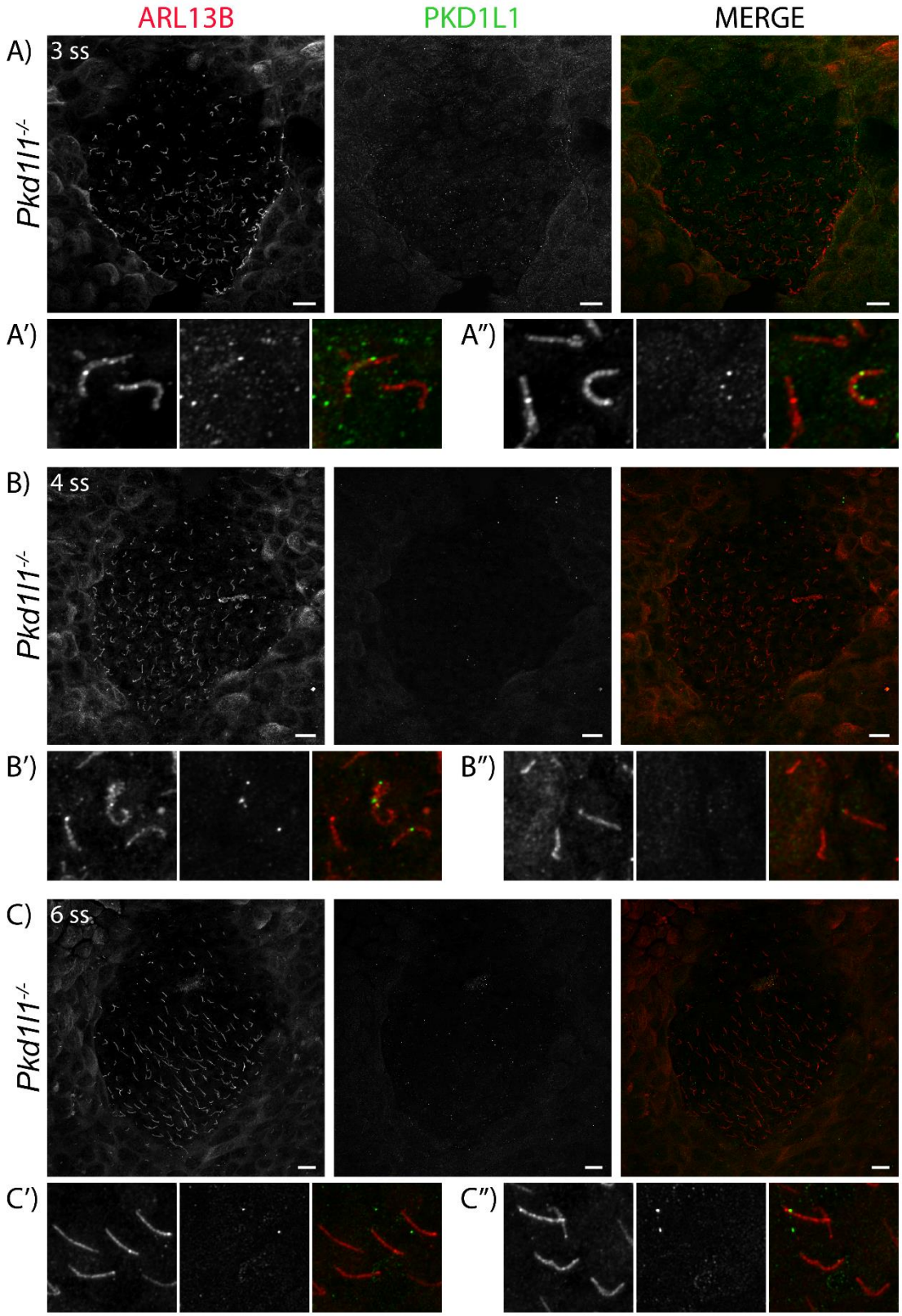


Figure 5.10 PKD1L1 rabbit polyclonal antibody staining in *Pkd1l1*$^{-/-}$ nodes
Immunofluorescent staining of three embryonic nodes (A, B and C), using the rabbit polyclonal antibody. A, B, C ‘ and ‘‘ are zooms of nodal cilia from A, B and C. Staining is in the same order for whole node images and zooms, from left to right: ARL13B (Red), PKD1L1 (Green), Merge. Scale bars represent 10 µm.

Using the rabbit polyclonal antibody, developed by the lab, staining in nodal cilia was observed in *Pkd1l1*$^{+/+}$ and *Pkd1l1*$^{+/-}$ embryos (Figures 5.8 and 5.9). However, the staining was not as strong or clear as the original staining performed (Figure 5.3). The staining varied between embryos, with some showing stronger ciliary expression than others (Figure 5.8 C, C' and Figure 5.9 B, B').

In *Pkd1l1*$^{-/-}$ embryos, staining was again variable (Figure 5.10). One embryo showed clear ciliary localisation across the node (Figure 5.10 A, A'), whilst the other two appeared to show a reduction in staining compared to *Pkd1l1*$^{+/+}$ and *Pkd1l1*$^{+/-}$ embryos (Figure 5.10 B, B', C, C').

Although ciliary localisation was detected using this antibody, the observation of similar staining in *Pkd1l1*$^{-/-}$ embryos suggests it is non-specific.

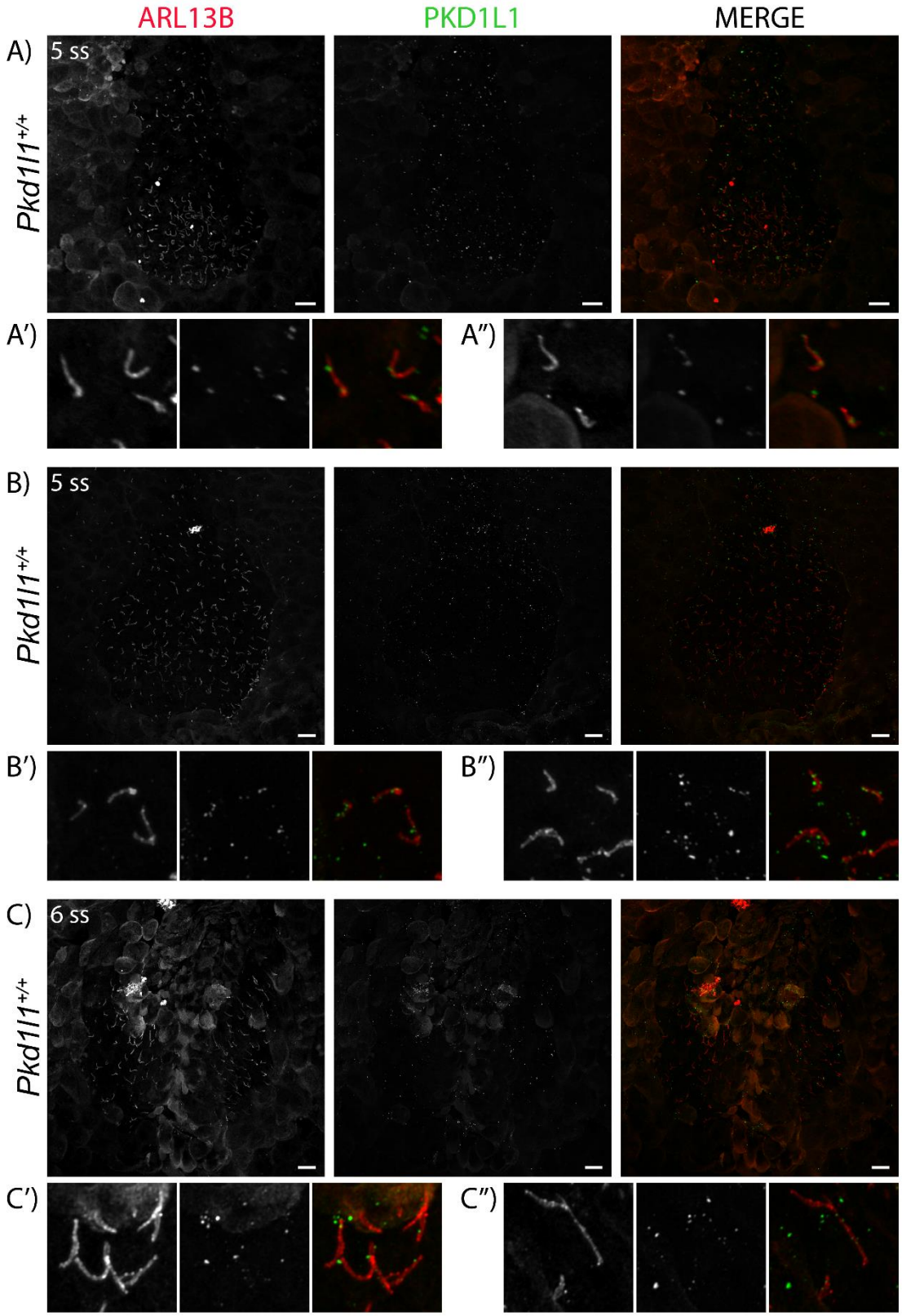


Figure 5.11 PKD1L1 OSP00015W antibody staining in *Pkd1l1*$^{+/+}$ nodes
Immunofluorescent staining of three embryonic nodes (A, B and C), using the commercial rabbit polyclonal antibody OSP00015W. A, B, C ‘ and ‘‘ are zooms of nodal cilia from A, B and C. Staining is in the same order for whole node images and zooms, from left to right: ARL13B (Red), PKD1L1 (Green), Merge. Scale bars represent 10 µm.

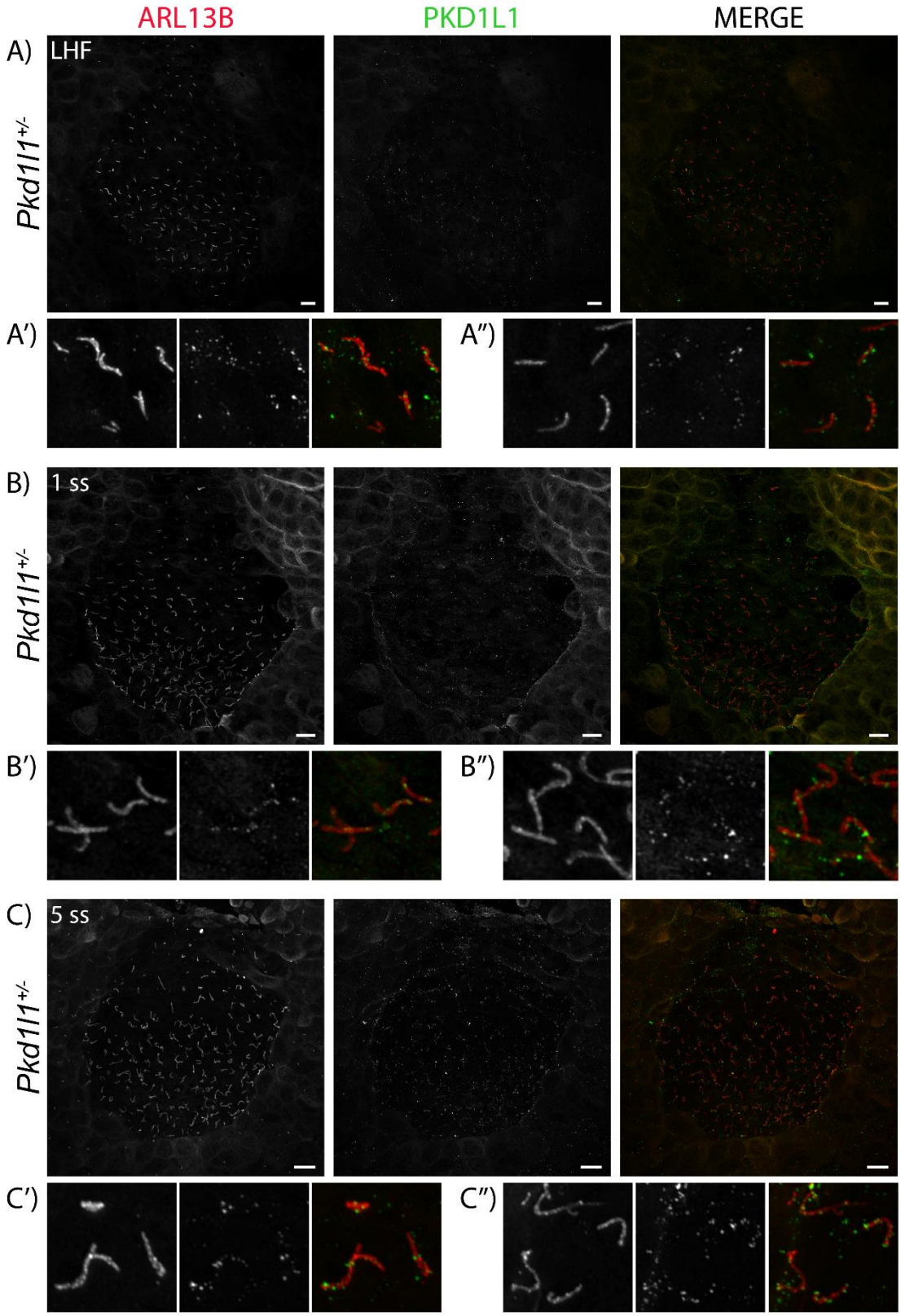


Figure 5.12 PKD1L1 OSP00015W antibody staining in *Pkd1l1*$^{+/-}$ nodes
Immunofluorescent staining of three embryonic nodes (A, B and C), using the commercial rabbit polyclonal antibody OSP00015W A, B, C ‘ and ‘‘ are zooms of nodal cilia from A, B and C. Staining is in the same order for whole node images and zooms, from left to right: ARL13B (Red), PKD1L1 (Green), Merge. Scale bars represent 10 µm.

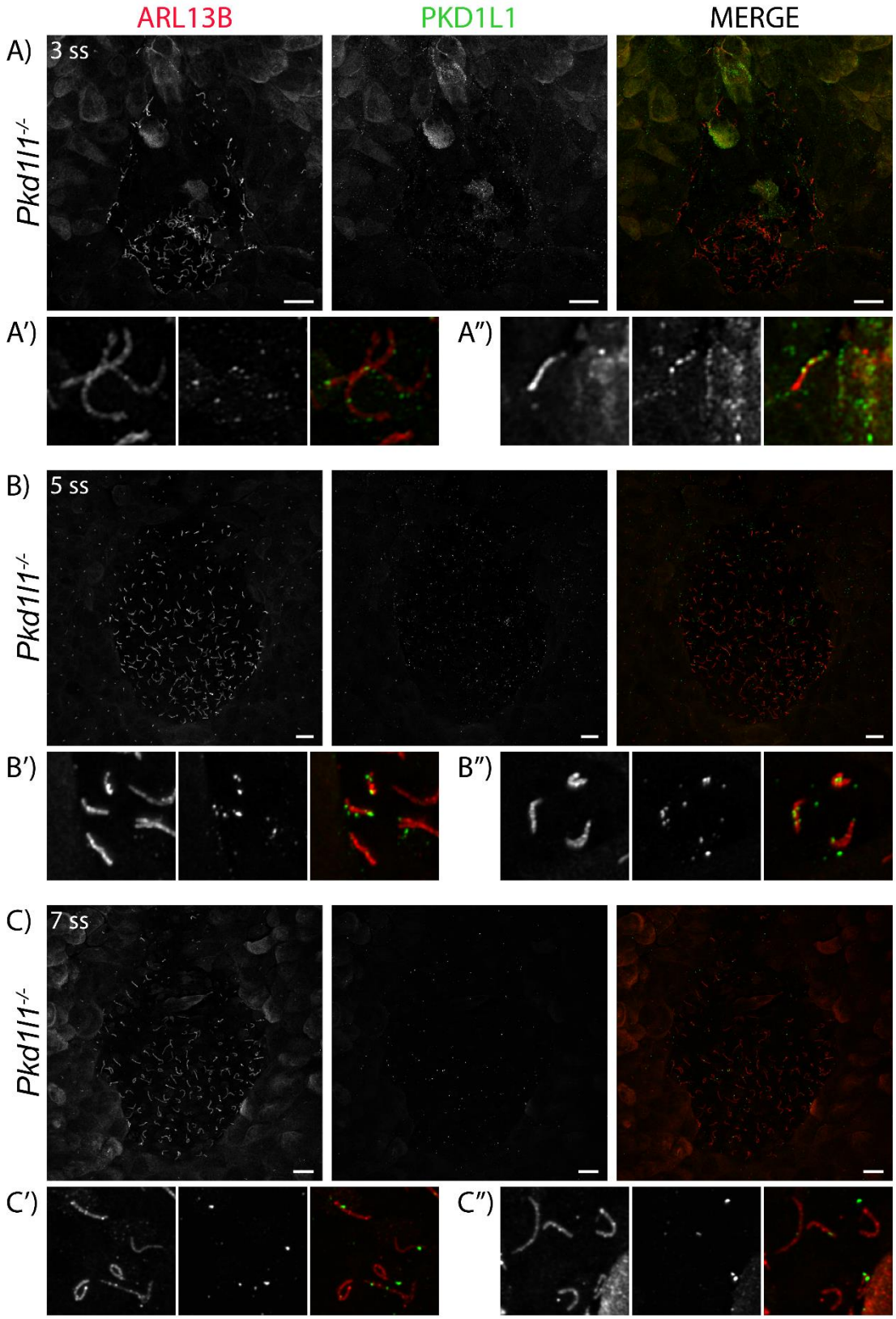


Figure 5.13 PKD1L1 OSP00015W antibody staining in PKD1L1-/- nodes
Immunofluorescent staining of three embryonic nodes (A, B and C), using the commercial rabbit polyclonal antibody OSP00015W A, B, C ‘ and ‘‘ are zooms of nodal cilia from A, B and C. Staining is in the same order for whole node images and zooms, from left to right: ARL13B (Red), PKD1L1 (Green), Merge. Scale bars represent 10 µm.

Staining using the commercial rabbit polyclonal antibody (OSP00015W), showed clear cilia expression in both *Pkd1l1*$^{+/+}$ and *Pkd1l1*$^{+/-}$ embryos (Figures 5.11 and 5.12). Some cilia showed clear punctate expression along the cilium (Figure 5.12 A', B', and C'). And expression appeared in cilia across the node, in both the pit and peripheral crown cells (Figure 5.11 A, Figure 5.12 B, C).

However, the same staining was also observed in *Pkd1l1*$^{-/-}$ embryos (Figure 5.13), with punctate cilia staining clearly evident (Figure 5.13 A' and B'), and expression was seen in cilia across the node (Figure 5.13 B).

In conclusion, all three antibodies showed the same staining in *Pkd1l1*$^{-/-}$ embryos as was observed in *Pkd1l1*$^{+/+}$ and *Pkd1l1*$^{+/-}$ embryos. This data suggests that the *Pkd1l1* antibodies may not be binding specifically to *Pkd1l1*, and the expression analysis cannot be trusted.

To overcome this, we asked the transgenics core facility to generate tagged alleles to further study the localisation of PKD1L1. At the same time, we decided to generate *Pkd2* tagged alleles; this was to enable us to investigate the localisation and co-localisation of *Pk1l1* and *Pkd2* in embryos and cells derived from these embryos without the need of antibodies. Importantly, I wanted to visualise endogenous expression, rather than assess the localisation of overexpressed protein. We requested the tags to be inserted at the C-terminus of the endogenous loci via CRISPR-Cas9 gene editing. The tags chosen to be inserted were mNeonGreen (shortened to mNG for this thesis) for *Pkd2*, and mTFP1 for *Pkd1l1*; these selections were based on the expected brightness and compatibility with the lasers available on the Zeiss LSM 710 with Airyscan microscope used for imaging (Cranfill et al. 2016).

5.2.3 *Pkd2*^{mNG} and *Pkd1l1*^{mTFP1} are homozygous viable

As well as using these new alleles to evaluate localisation, I wanted to assess whether introducing the tags to the endogenous C-terminal loci of *Pkd1l1* and *Pkd2* caused any pathogenic effects. Situs or kidney cyst phenotypes would suggest that the function of the proteins is affected by the tag insertion, which might in theory have an effect on the endogenous localisation of the proteins.

For this analysis, 15.5 d.p.c. embryos from het-het intercrosses were dissected and internal organs were examined for situs; stomach situs, heart apex, great vessel patterning, and lung lobation were all assessed along with any signs of oedema. Tissue samples were taken for genotyping and Chi-squared tests were performed, on the genotyping data, to assess the significance of the distribution of genotypes compared to expected Mendelian ratios. Samples for genotyping were collected from both 15.5 d.p.c. embryos and weaning age mice (~3 weeks old) from het-het intercrosses.

In *Pkd2*$^{+/mNG}$ intercrosses, observations during dissections of 15.5 d.p.c. embryos revealed no indication of oedema, the heart apex was positioned correctly, the great vessels were patterned normally, and all lungs showed expected lobation with a 4:1 ratio of right:left (Figure 5.14 C). The observations were the same in all embryos dissected, which included 21 homozygous *Pkd2*$^{mNG/mNG}$ embryos.

These 15.5 d.p.c embryos showed genotyping frequencies similar to expected Mendelian rations, and the data was not significant using Chi-squared test P = 0.2765 (Figure 5.14 A). When looking at the graph for mice born from *Pkd2*$^{+/mNG}$ intercrosses, both the observed numbers of *Pkd2*$^{mNG/mNG}$ and *Pkd2*$^{+/mNG}$ were lower than expected, while nearly twice as many *Pkd2*$^{+/+}$ mice were born than

estimated (figure 5.14 B); this observed difference was significant, using Chi-squared test P = 0.0079.

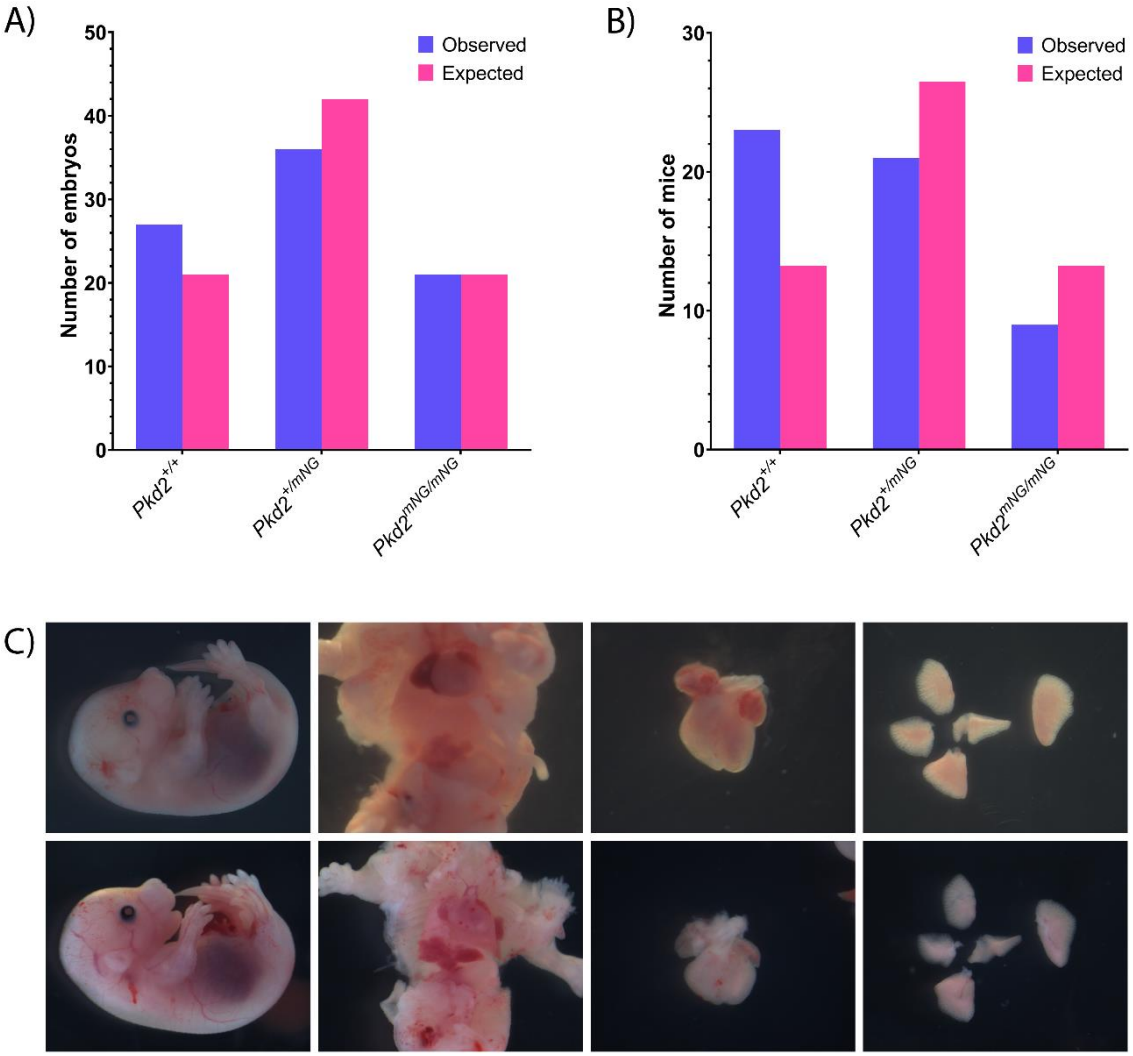


Figure 5.14 *Pkd2*^{mNG} mice are homozygous viable and show no situs defects
Graphs showing the expected and observed ratios of 15.5 d.p.c. embryos (A) and born mice (B) from *Pkd2*$^{+/mNG}$ intercrosses. C) Images of two 15.5 d.p.c. *Pkd2*$^{mNG/mNG}$ embryos showing no indication of oedema, correct positioning of the internal organs, heart apex and great vessel patterning and lung lobation (4:1 R:L).

Similar observations were made for *Pkd1l1*$^{+/mTFP1}$ intercrosses. The genotyping frequencies for both 15.5 d.p.c. embryos and weaning age mice were close to the expected values. Interestingly, there were more homozygous embryos and born mice than estimated numbers, however neither proved significant in a chi-squared test - 15.5 d.p.c. P = 0.2150, born P = 0.1108 (Figure 5.15 A, B). Situs was normal in all embryos assessed, including 27 *Pkd1l1*$^{mTFP1/mTFP1}$ homozygous embryos, with no sign of oedema (Figure 5.15 C).

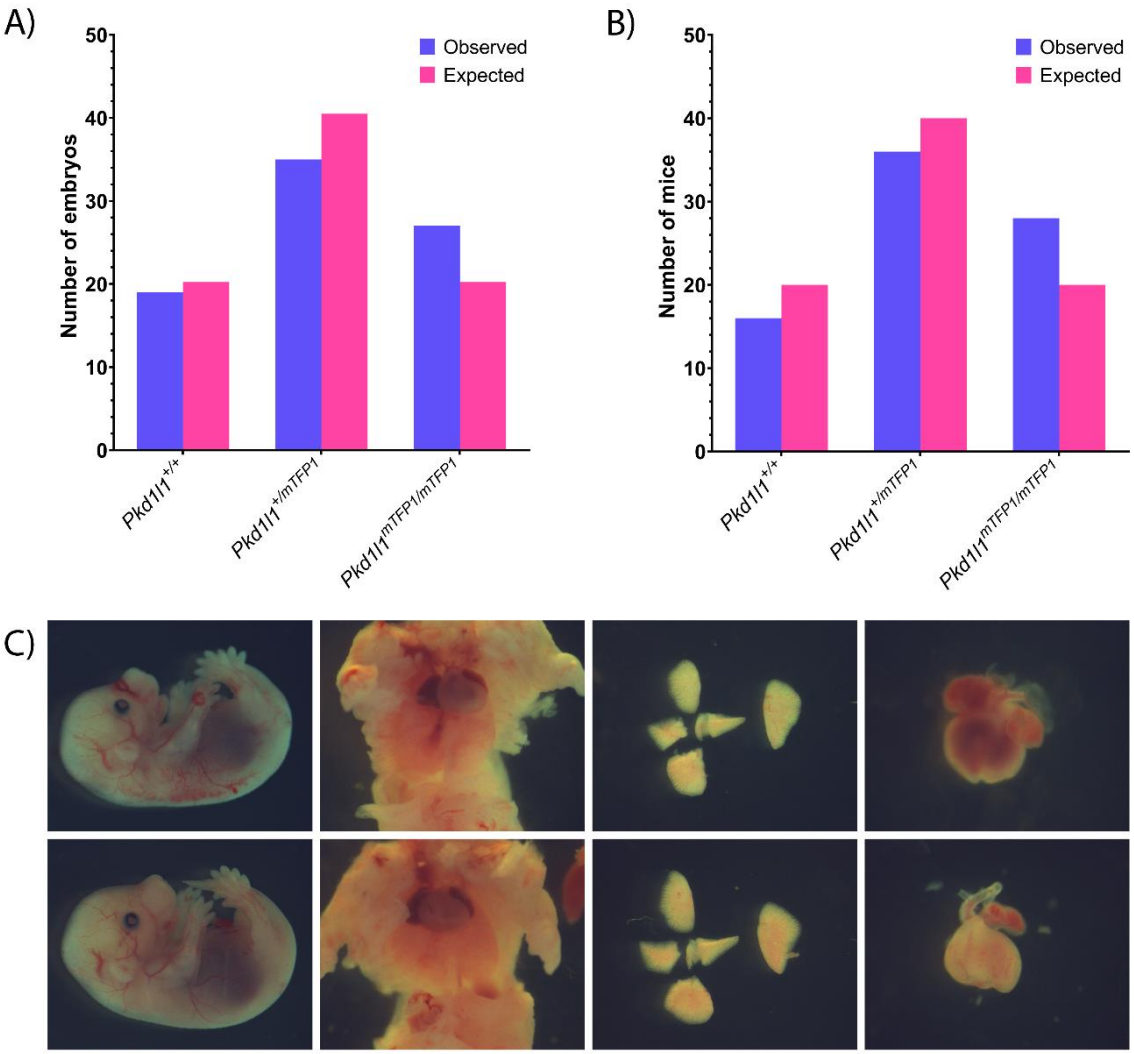


Figure 5.15 *Pkd1l1*^{mTFP1} mice are homozygous viable and show no situs defects
Graphs showing the expected and observed ratios of 15.5 d.p.c. embryos (A) and born mice (B) from *Pkd1l1*$^{+/mTFP1}$ intercrosses. C) Images of two 15.5 d.p.c. *Pkd1l1*$^{mTFP1/mTFP1}$ embryos showing no indication of oedema, correct positioning of the internal organs, heart apex and great vessel patterning and lung lobation (4:1 R:L).

As both lines were homozygous viable, with no obvious defects, the lines were crossed to generate *Pkd2*$^{mNG/mNG}$;*Pkd1l1*$^{mTFP1/mTFP1}$ embryos and mice. Again, situs analysis was performed in 15.5 d.p.c embryos; no abnormalities were observed in any embryo, including the 8 double homozygous embryos examined (Figure 5.16 B). Statistical analysis of the genotyping data revealed no significant difference between observed and expected values, based on Mendelian ratios, P = 0.5538 (Figure 5.16 A). More *Pkd2*$^{mNG/mNG}$;*Pkd1l1*$^{mTFP1/mTFP1}$ double homozygous embryos were observed than expected, consistent with no reduction in the viability of 15.5 d.p.c. embryos (Figure 5.16 A).

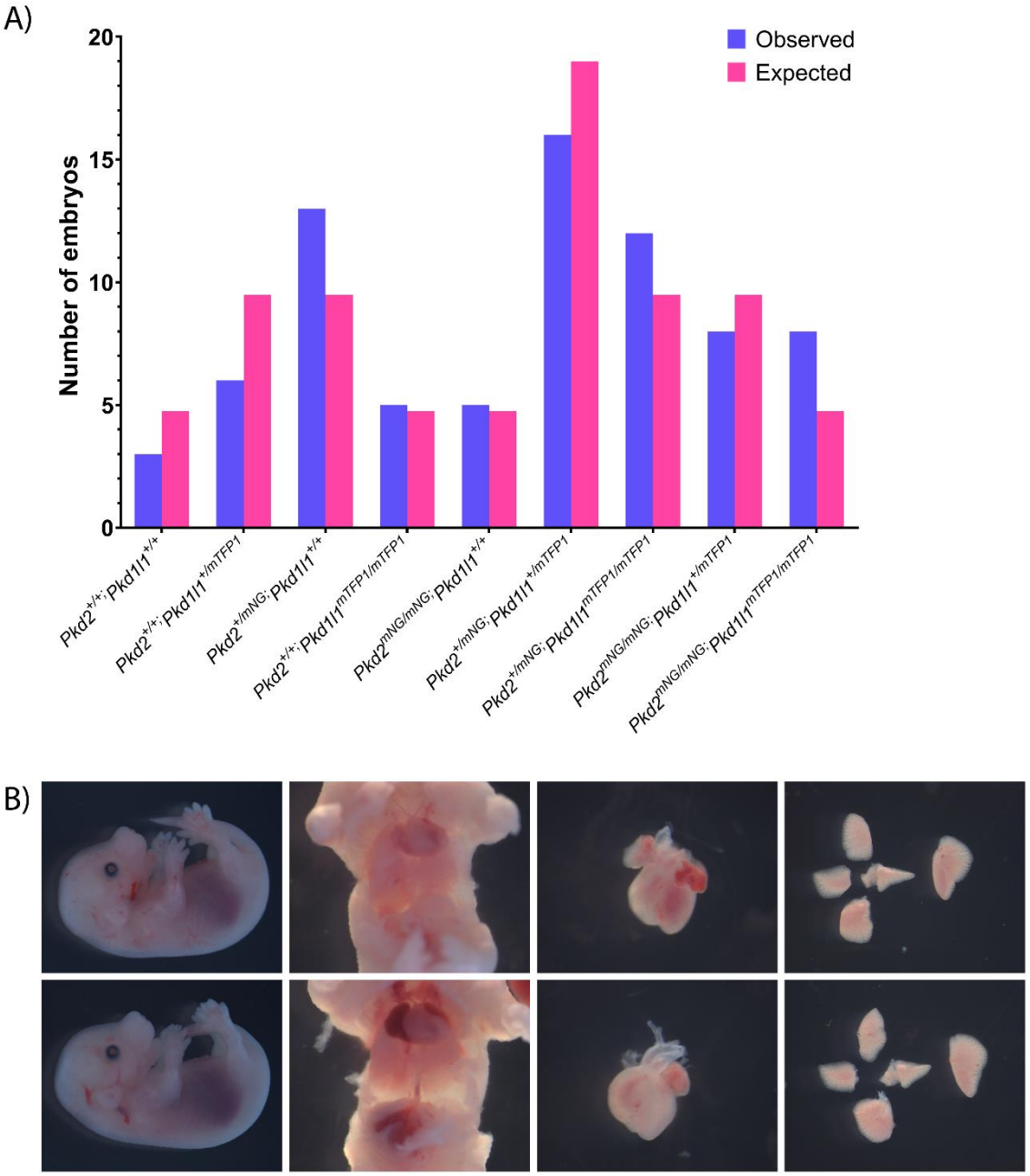


Figure 5.16 *Pkd2*$^{mNG/mNG}$;*Pkd1l1*$^{mTFP1/mTFP1}$ embryos are viable and show no situs defects

Graphs showing the expected and observed ratios of 15.5 d.p.c. embryos (A) and born mice (B) from *Pkd2*$^{+/mNG}$;*Pkd1l1*$^{+/mTFP1}$ intercrosses. C) Images of two 15.5 d.p.c. embryos showing no indication of oedema, correct positioning of the internal organs, heart apex and great vessel patterning and lung lobation (4:1 R:L).

As double homozygous *Pkd2*$^{mNG/mNG}$;*Pkd1l1*$^{mTFP1/mTFP1}$ embryos showed no left-right patterning defects or reduced viability at 15.5 d.p.c., it seemed unlikely they would show abnormalities at birth. The same crosses were then allowed to go to birth, allowing me to examine whether double homozygous mice are viable. Genotyping revealed no loss of *Pkd2*$^{mNG/mNG}$;*Pkd1l1*$^{mTFP1/mTFP1}$ mice, chi-squared analysis of expected and observed genotypes was not significant P = 0.3758 (Figure 5.17 C). These double homozygous mice exhibit no gross phenotype and are capable of breeding successfully.

Pkd2$^{+/-}$ and *Pkd1l1*$^{+/-}$ mice show no abnormalities, highlighting that one copy of wild type *Pkd2* or *Pkd1l1* is sufficient for normal function. To assess whether one copy of *Pkd2*^{mNG} or *Pkd1l1*^{mTFP1} is functional in a similar manner to the wild type allele, *Pkd2*$^{+/mNG}$ mice were crossed with *Pkd2*$^{+/-}$ mice and similarly *Pkd1l1*$^{+/mTFP1}$ mice were crossed with *Pkd1l1*$^{+/-}$ mice. Embryos were dissected at 15.5 d.p.c. for situs analysis and genotyping. All embryos showed correct left-right patterning of internal organs (data not shown). Genotyping data indicated no loss in the viability of *Pkd2*$^{-/mNG}$ or *Pkd1l1*$^{-/mTFP1}$ 15.5 d.p.c. embryos. Chi-squared tests performed on the observed and expected genotyping numbers showed no significant difference, P = 0.2839 for *Pkd2*$^{+/mNG}$ x *Pkd2*$^{+/-}$ crosses, and P = 0.1515 for *Pkd1l1*$^{+/mTFP1}$ x *Pkd1l1*$^{+/-}$ crosses.

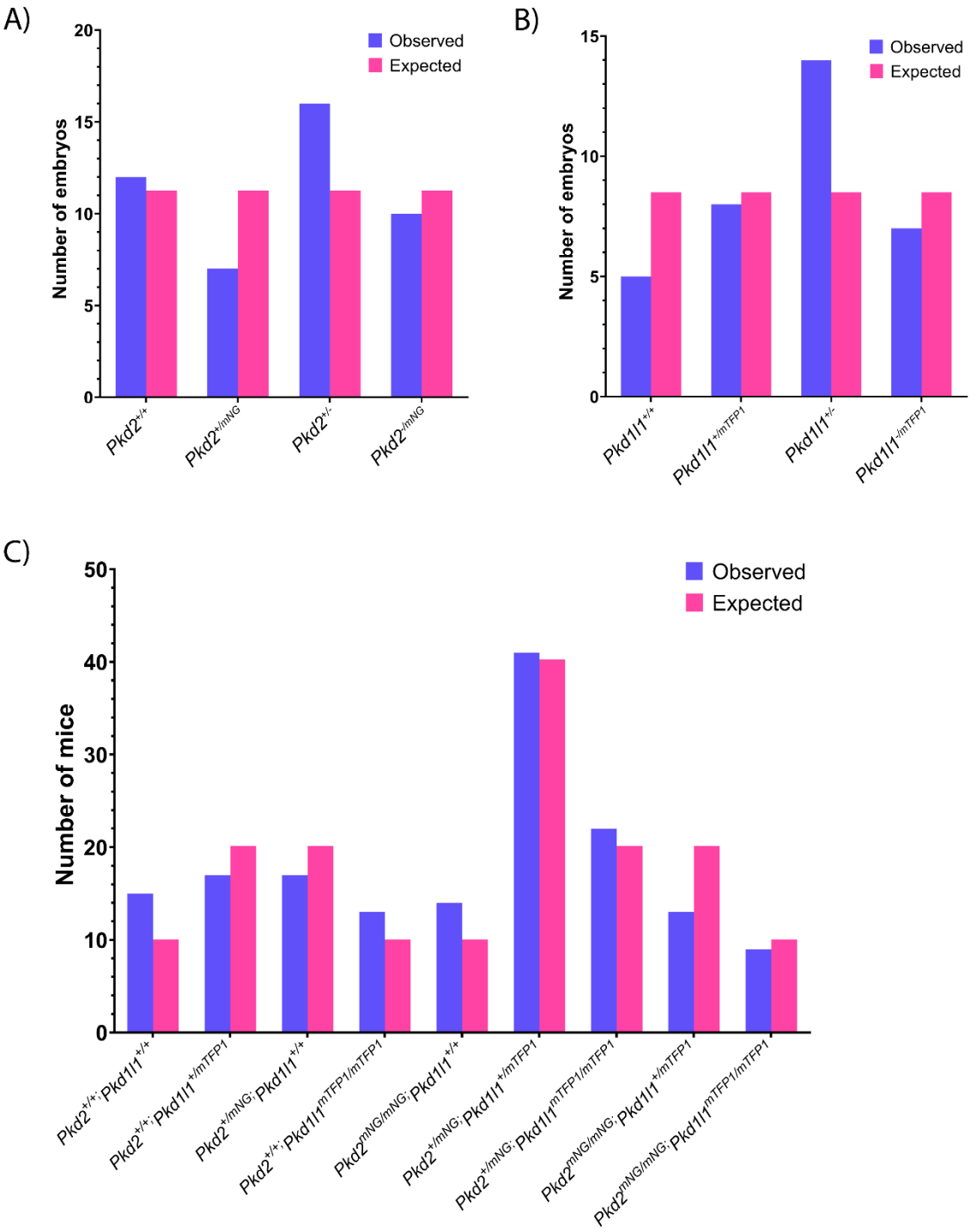


Figure 5.17 *Pkd2*$^{-/mNG}$ and *Pkd1l1*$^{-/mTFP1}$ embryos and *Pkd2*$^{mNG/mNG}$;*Pkd1l1*$^{mTFP1/mTFP1}$ mice are viable

Graphs showing the expected and observed ratios of genotyping from A) 15.5 d.p.c. embryos from *Pkd2*$^{+/mNG}$ x *Pkd2*$^{+/-}$ crosses, B) 15.5 d.p.c. embryos from *Pkd1l1*$^{+/mTFP1}$ x *Pkd1l1*$^{+/-}$ crosses, C) mice born from *Pkd2*$^{+/mNG}$;*Pkd1l1*$^{+/mTFP1}$ intercrosses.

As kidney cysts are observed at 15.5 d.p.c. in *Pkd2*$^{lrm4/lrm4}$ and *Pkd2*$^{-/-}$ embryos, I examined the kidneys of *Pkd2*$^{mNG/mNG}$ and *Pkd2*$^{-/mNG}$ embryos. Kidneys were dissected from 15.5 d.p.c. embryos, fixed in 10% formalin and sent to the histology core facility for processing, sectioning and staining. Kidney section slides were imaged on the Hamamatsu NanoZoomer slide scanner using a 20X lens. Glomerular dilations were measured using the Hamamatsu NDP.view2 software, as performed previously (Walker 2016; Walker et al. 2019); see supplementary figure for examples of glomerular measurements (Supplementary Figure 7.1). Only glomerular dilations >50 µm were included in the analysis, as this is the average size of a 15.5 d.p.c. glomerulus (Walker 2016).

Analysis of kidney sections showed no evidence of glomerular cysts, as reported in *Pkd2*$^{lrm4/lrm4}$ and *Pkd2*$^{-/-}$ embryos (Walker et al. 2019). Kidneys were dissected from both *Pkd2*$^{+/mNG}$ intercrosses and *Pkd2*$^{+/mNG}$ x *Pkd2*$^{+/-}$ crosses. Indeed, kidney sections from *Pkd2*$^{mNG/mNG}$ and *Pkd2*$^{-/mNG}$ were indistinguishable from *Pkd2*$^{+/+}$ sections (Figure 5.18 A-D). Glomerular measurements were taken from two sections per kidney, and a minimum of 6 kidneys per genotype for each cross. When all measurements were plotted, there was no apparent difference between glomerular dilation measurements and genotype (Figure 5.18 E, F). One way ANOVA was performed to test statistical significance between genotypes, where n = the number of genotypes (3 or 4). There was no significant difference for *Pkd2*$^{+/mNG}$ intercross kidney sections with a P-value of 0.1302.

Although the glomerular measurements in kidney sections from *Pkd2*$^{+/-}$ x *Pkd2*$^{mNG/mNG}$ crosses did not appear overtly different, the one way ANOVA test revealed a significant difference with a P-value of 0.0012 (Figure 5.18 E). *Pkd2*$^{+/+}$ kidney sections showed a higher average diameter of glomerular dilations than

Pkd2$^{+/mNG}$, *Pkd2*$^{+/-}$ and *Pkd2*$^{-/mNG}$ kidney sections (Figure 5.18 F). Multiple comparisons tests, performed alongside the one way ANOVA, revealed the wild type measurements were significantly higher than measurements from all three other genotypes.

In summary, *Pkd2*$^{mNG/mNG}$ and *Pkd1l1*$^{mTFP1/mTFP1}$ mice are completely viable, fertile, and show no obvious abnormalities. No abnormal situs, oedema or loss of viability was observed in *Pkd2*$^{mNG/mNG}$, *Pkd2*$^{-/mNG}$, *Pkd1l1*$^{mTFP1/mTFP1}$, *Pkd1l1*$^{-/mTFP1}$ and *Pkd2*$^{mNG/mNG}$;*Pkd1l1*$^{mTFP1/mTFP1}$ 15.5 d.p.c. embryos. Glomerular cysts were not identified in 15.5 d.p.c. kidneys from *Pkd2*$^{mNG/mNG}$ or *Pkd2*$^{-/mNG}$ embryos. This data is all consistent with *Pkd2*^{mNG} and *Pkd1l1*^{mTFP1} being fully function alleles.

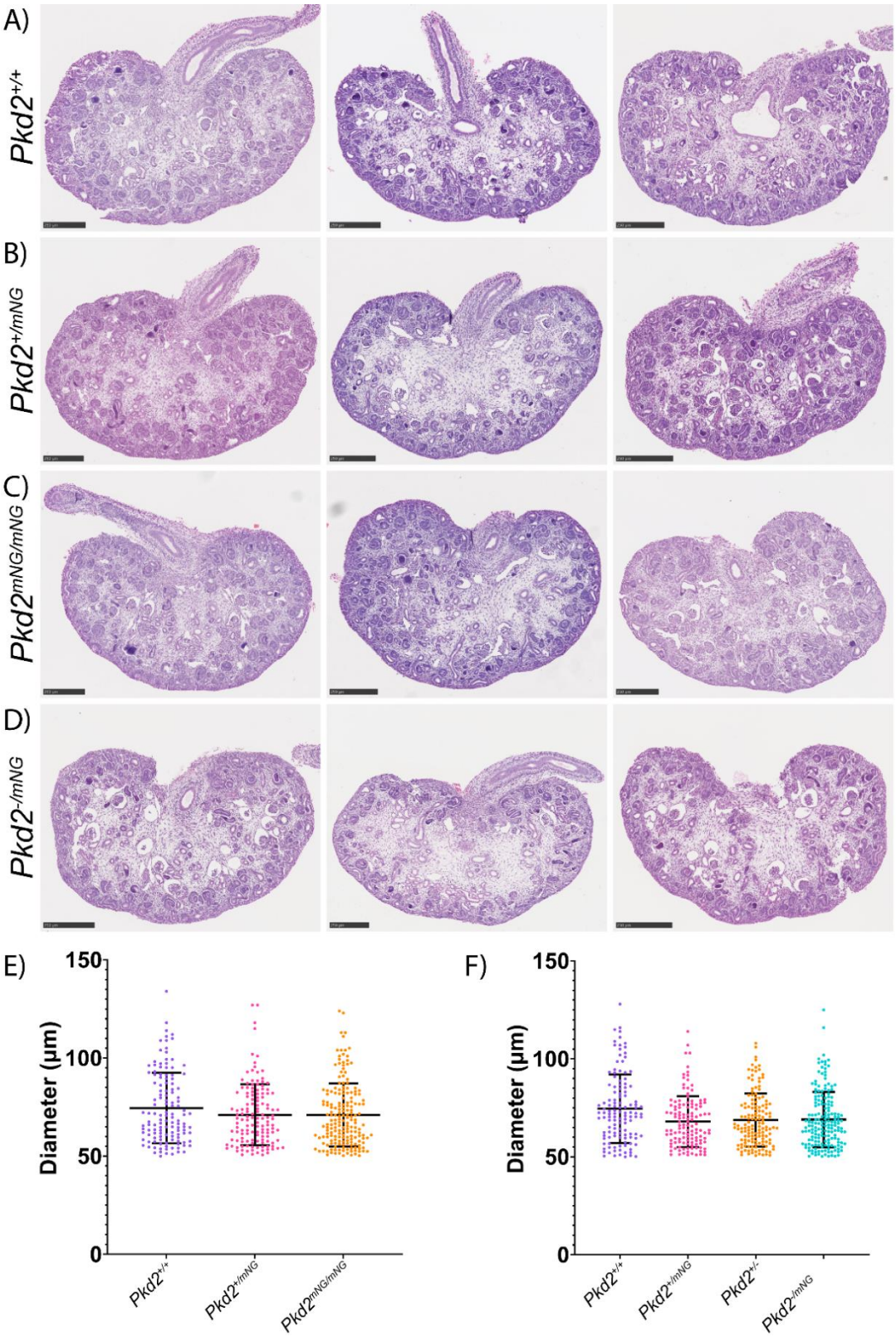


Figure 5.18 *Pkd2*^{mNG} kidneys are indistinguishable from *Pkd2*$^{+/+}$ Kidneys

Kidney sections from *Pkd2*$^{+/+}$ (A), *Pkd2*$^{+/mNG}$ (B), *Pkd2*$^{mNG/mNG}$ (C) and *Pkd2*$^{-/mNG}$ (D) 14.5 d.p.c. embryos show no indication of glomerular cyst formation. Graphs showing glomerular dilation measurements >50 µm from *Pkd2*$^{+/mNG}$ intercrosses (E) and *Pkd2*$^{+/mNG}$ x *Pkd2*$^{+/-}$ crosses (F). Measurements were taken from two sections per kidney, and a minimum of 6 kidneys per genotype.

5.2.4 PKD1L1^{mTFP1} localises to nodal cilia

To assess the localisation of PKD1L1^{mTFP1}, *Pkd1l1*$^{+/mTFP1}$ x *Pkd1l1*$^{+/+}$ crosses were set up and embryos dissected at ~8 d.p.c.. Initially, I examined the embryos live on the Zeiss LSM 710 microscope using the Airyscan super-resolution imaging mode; however, the signal was too faint to visualise. Instead, embryos were fixed and stained with the cilia marker ARL13B, for identification of nodal cilia, before mounting and imaging. Similar to PKD1L1 antibody testing (section 5.2.2), embryos were imaged and processed blind and only genotyped afterwards.

Control *Pkd1l1*$^{+/+}$ embryos showed small amounts of background staining, as is to be expected, due to autofluorescence (Figure 5.19 A, B, C). No specific staining of nodal cilia was observed (Figure 5.19 A', B', C').

In contrast, *Pkd1l1*$^{+/mTFP1}$ embryos exhibited low levels of fluorescence across the node and revealed mTFP1 localised in nodal cilia (Figures 5.20 and Figure 5.21). Although staining was faint, it was consistent across all embryos examined. PKD1L1^{mTFP1} displayed the strongest expression in nodal cilia at the periphery of the node, and heading into the notochord at the anterior surface of the node (Figures 5.20 B, 5.21 A, B). In most instances, the staining was persistent across the entire length of the cilium (Figures 5.20 A', 5.21 A', C').

This provides the first direct evidence of PKD1L1 localising in mammalian nodal cilia.

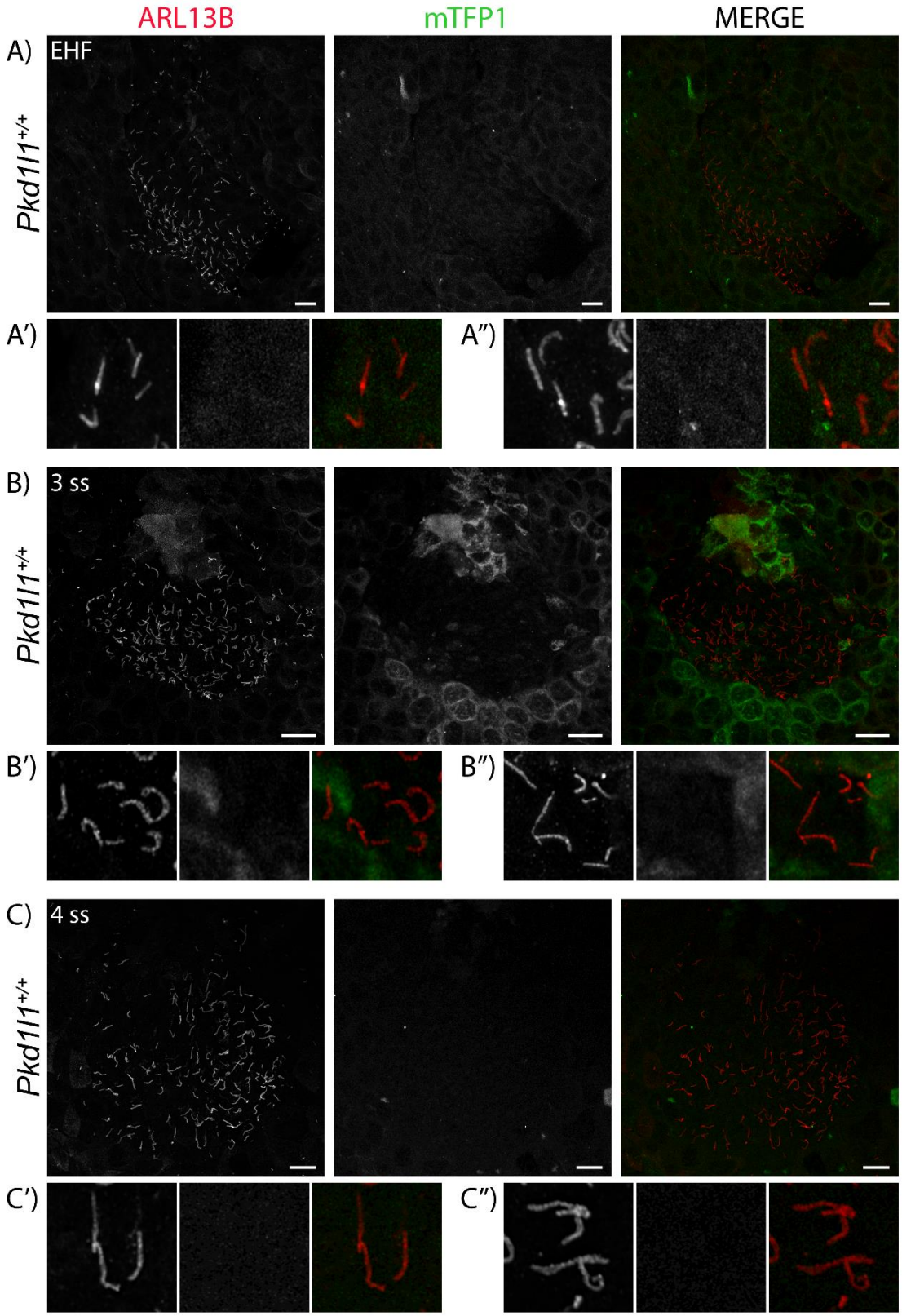


Figure 5.19 Immunofluorescence in *Pkd1l1*$^{+/+}$ embryos
Immunofluorescence of three embryonic nodes (A, B and C), stained with ARL13B to label cilia. A, B, C ‘ and ‘‘ are zooms of nodal cilia from A, B and C. Staining is in the same order for whole node images and zooms, from left to right: ARL13B (Red), PKD1L1 ^{mTFP1} (Green), Merge. Scale bars represent 10 µm.

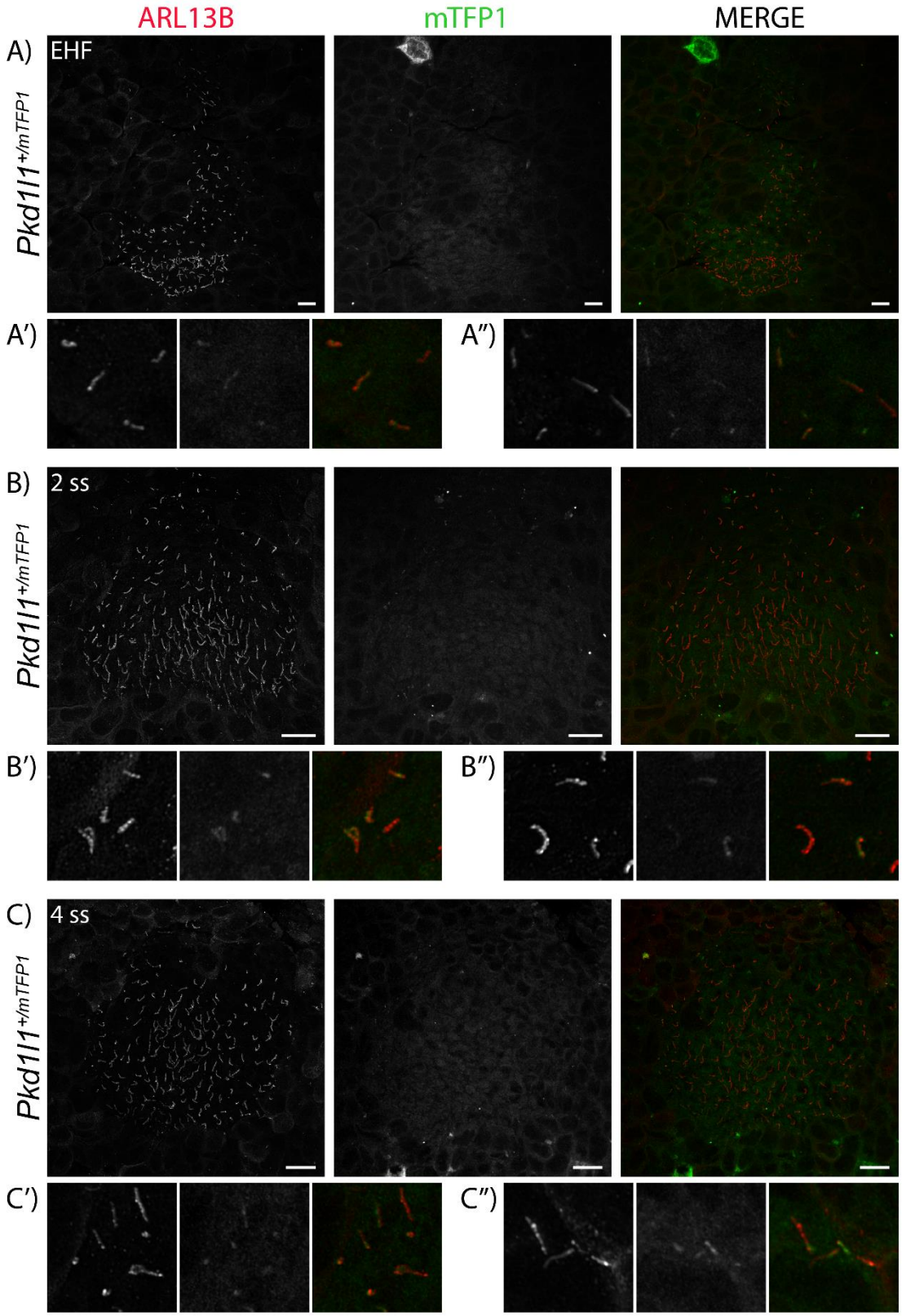


Figure 5.20 PKD1L1^{mTFP1} fluorescence in *Pkd1l1*$^{+/mTFP1}$ embryos
Immunofluorescence of three embryonic nodes (A, B and C), endogenously expressing PKD1L1^{mTFP1} and stained with ARL13B to label cilia. A, B, C ‘ and ‘‘ are zooms of nodal cilia from A, B and C. Staining is in the same order for whole node images and zooms, from left to right: ARL13B (Red), PKD1L1^{mTFP1} (Green), Merge. Scale bars represent 10 µm.

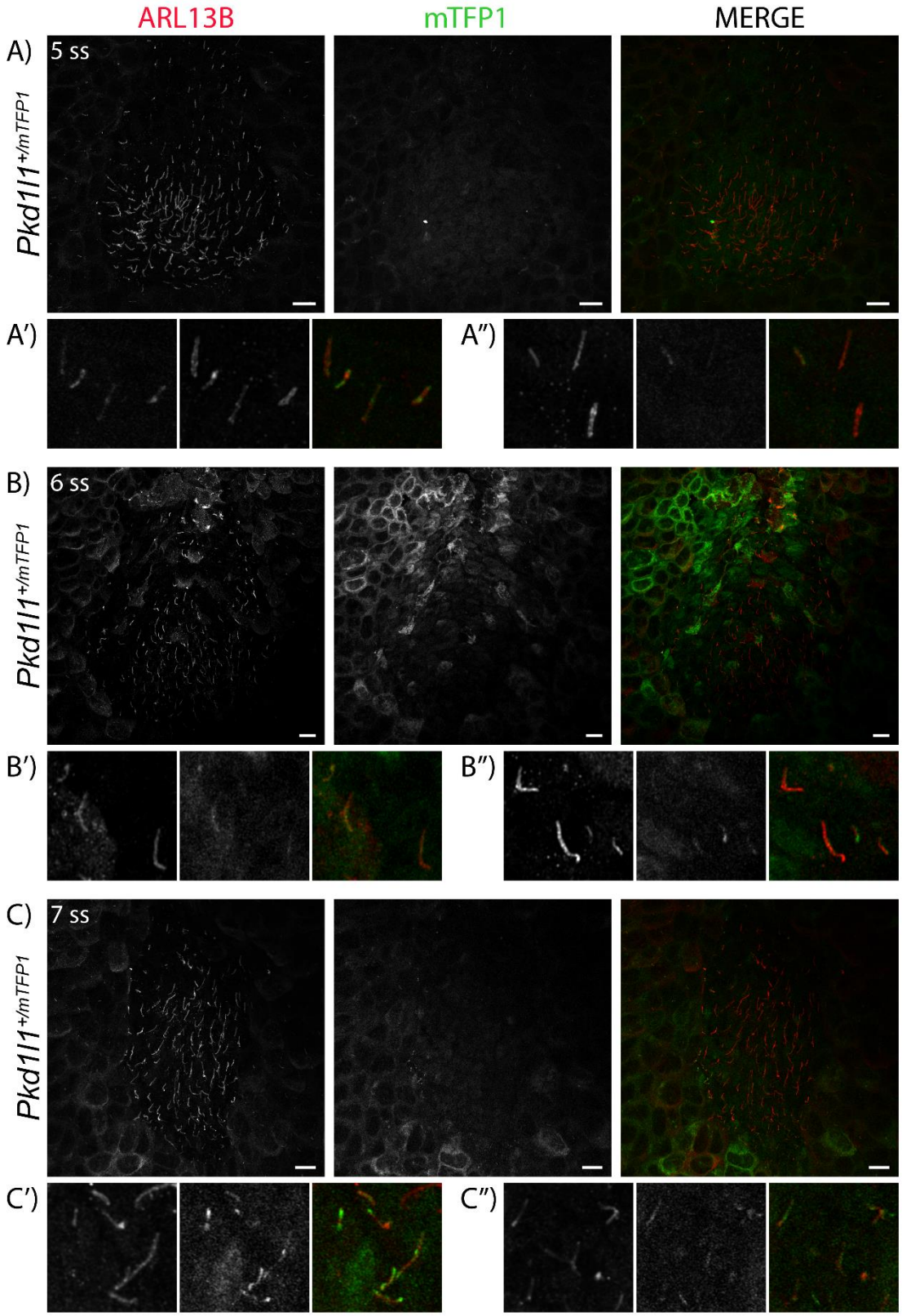


Figure 5.21 PKD1L1^{mTFP1} fluorescence in *Pkd1l1*$^{+/mTFP1}$ embryos cont.
Immunofluorescence of three embryonic nodes (A, B and C), endogenously expressing PKD1L1^{mTFP1} and stained with ARL13B to label cilia. A, B, C ‘ and ‘‘ are zooms of nodal cilia from A, B and C. Staining is in the same order for whole node images and zooms, from left to right: ARL13B (Red), PKD1L1^{mTFP1} (Green), Merge. Scale bars represent 10 µm.

5.2.5 PKD2^{mNG} localises to nodal cilia

Although the localisation of PKD2 in nodal cilia has been previously described using antibody staining and Venus-tagged transgenic lines (Grimes et al. 2016; McGrath et al. 2003; Yoshiba et al. 2012). I wanted to characterise the expression of our endogenously tagged PKD2^{mNG} in the embryonic node.

As attempted with PKD1L1^{mTFP1}, I first examined whether I could detect mNG signal in live embryos. *Pkd2*$^{+/+}$ x *Pkd2*$^{+/mNG}$ crosses were set up and embryos dissected at ~8 d.p.c. These were mounted straight away for imaging. Signal could be detected in approximately half of the embryos, consistent with the expected genotype frequency. In contrast to live imaging of PKD1L1^{mTFP1}, PKD2^{mNG} showed strong and clearly visible staining (Figure 5.22). Although no cilia marker was present, staining was consistent with that of nodal cilia. In most embryos, expression was enriched around the edge of the node and at the anterior end heading in to the notochord (Figure 5.22 A, B, C); however, some embryos showed expression in cilia across the node (Figure 5.22 D).

Embryos were also fixed then co-stained with ARL13B to confirm ciliary localisation of PKD2^{mNG} (Figure 5.23). As expected, PKD2^{mNG} fluorescence co-expressed with ARL13B staining of nodal cilia (Figure 2.3 A', B', C'). Expression was mostly along the whole length of nodal cilia, consistent with expression of PKD1L1^{mTFP1}. Similar to live embryos, most embryos showed stronger expression of PKD2^{mNG} in nodal cilia at the sides and anterior edge of the node heading into the notochord (Figure 2.3 A, B, C).

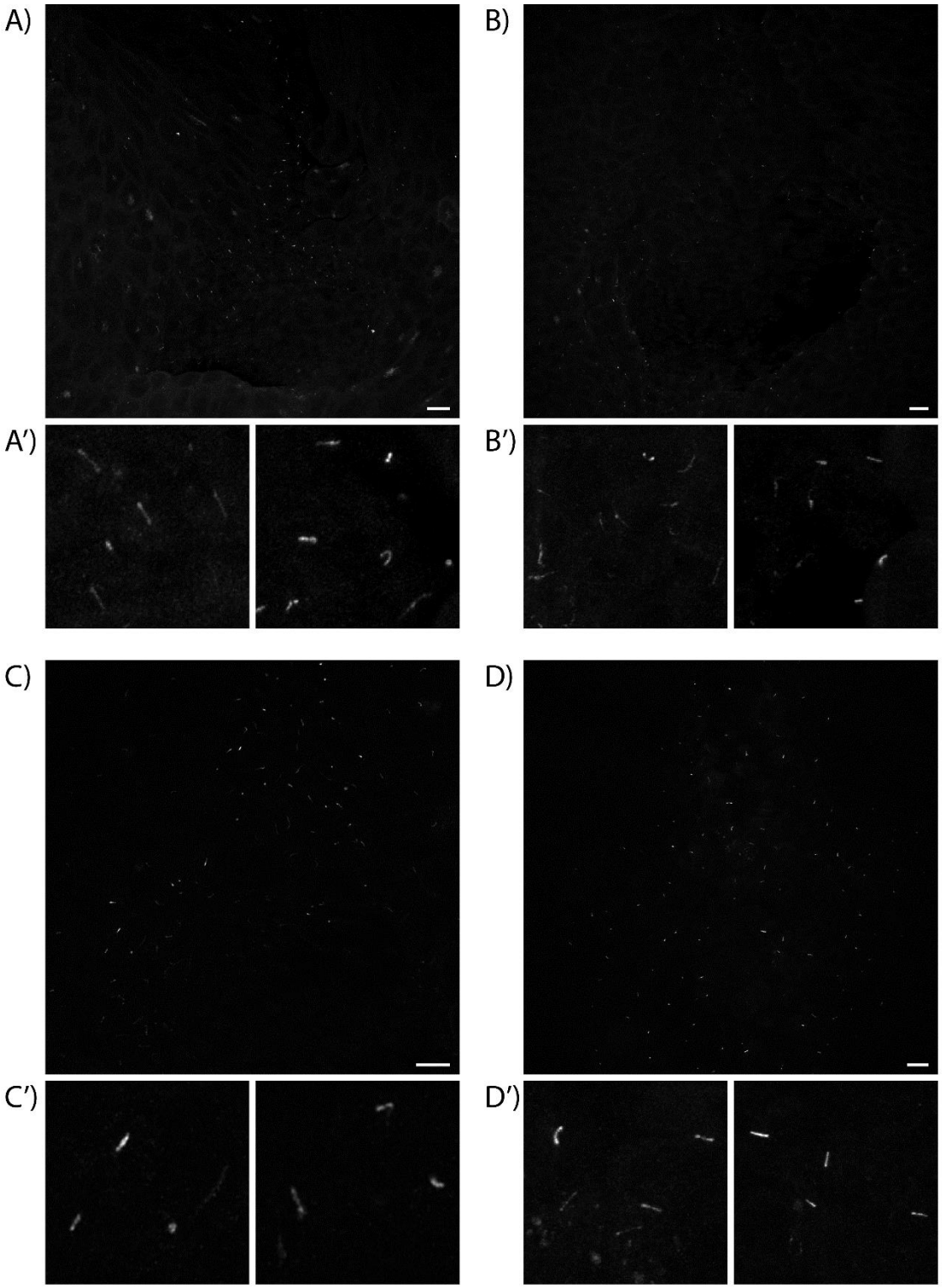


Figure 5.22 Live imaging of PKD2^{mNG} in 8 d.p.c. embryos
Fluorescence in four embryonic nodes (A, B, C and D), endogenously expressing PKD2^{mNG}. A', B', C' and D' are two zooms of nodal cilia from A, B, C and D respectively. All staining is in greyscale with one channel imaged (488 nm laser). Scale bars represent 10 µm.

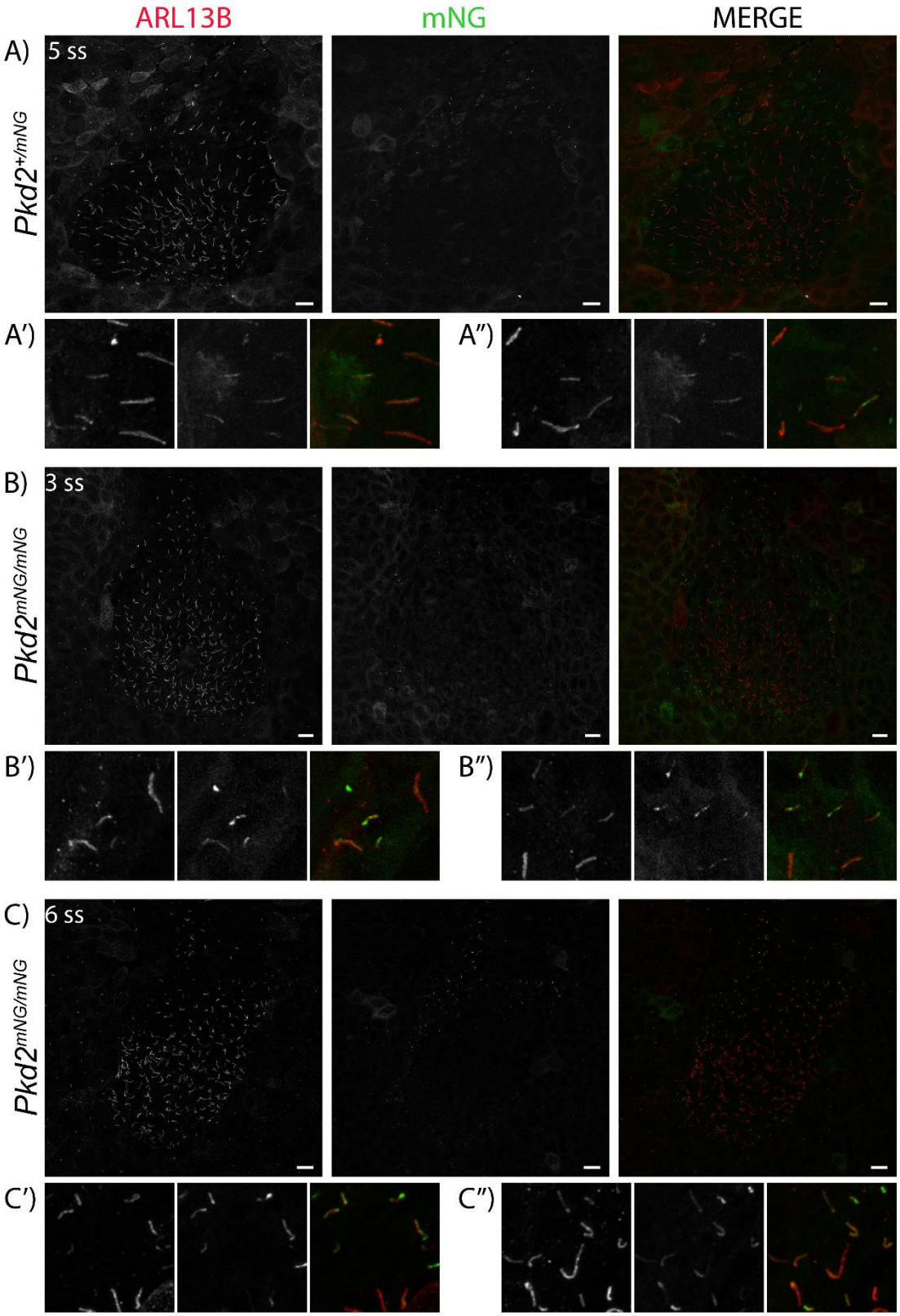


Figure 5.23 PKD2^{mNG} fluorescence in *Pkd2$^{+/mNG}$* and *Pkd2$^{mNG/mNG}$* embryos
Immunofluorescence of three embryonic nodes (A, B and C), endogenously expressing PKD2^{mNG} and stained with ARL13B to label cilia. A, B, C ‘ and ‘‘ are zooms of nodal cilia from A, B and C. Staining is in the same order for whole node images and zooms, from left to right: ARL13B (Red), PKD2^{mNG} (Green), Merge. Scale bars represent 10 µm.

One experiment I envisioned when requesting the endogenously tagged *Pkd2* and *Pkd1l1* alleles, was to perform live imaging using lightsheet microscopy. The advantage of lightsheet microscopy is the ability to perform live imaging of whole embryos with minimal photobleaching, enabling imaging over long time periods (Dyer et al. 2022). Jeremy Sanderson and Andrew Parker, from the bioimaging core facility at Harwell, self-built a lightsheet system in house; however when tested with 8 d.p.c. embryos, the resolving power proved insufficient to visualise nodal cilia. I was fortunate to have the opportunity to image some fixed samples on a Zeiss lattice Lightsheet 7 microscope, at the Kennedy Institute of Rheumatology in Oxford. Imaging showed strong expression of PKD2^{mNG} in nodal cilia at the edges of the node and in the notochord (Figure 5.24). Due to the travelling time to get to the Kennedy Institute, and the unpredictability of mouse matings, it was not feasible to use this option for live imaging.

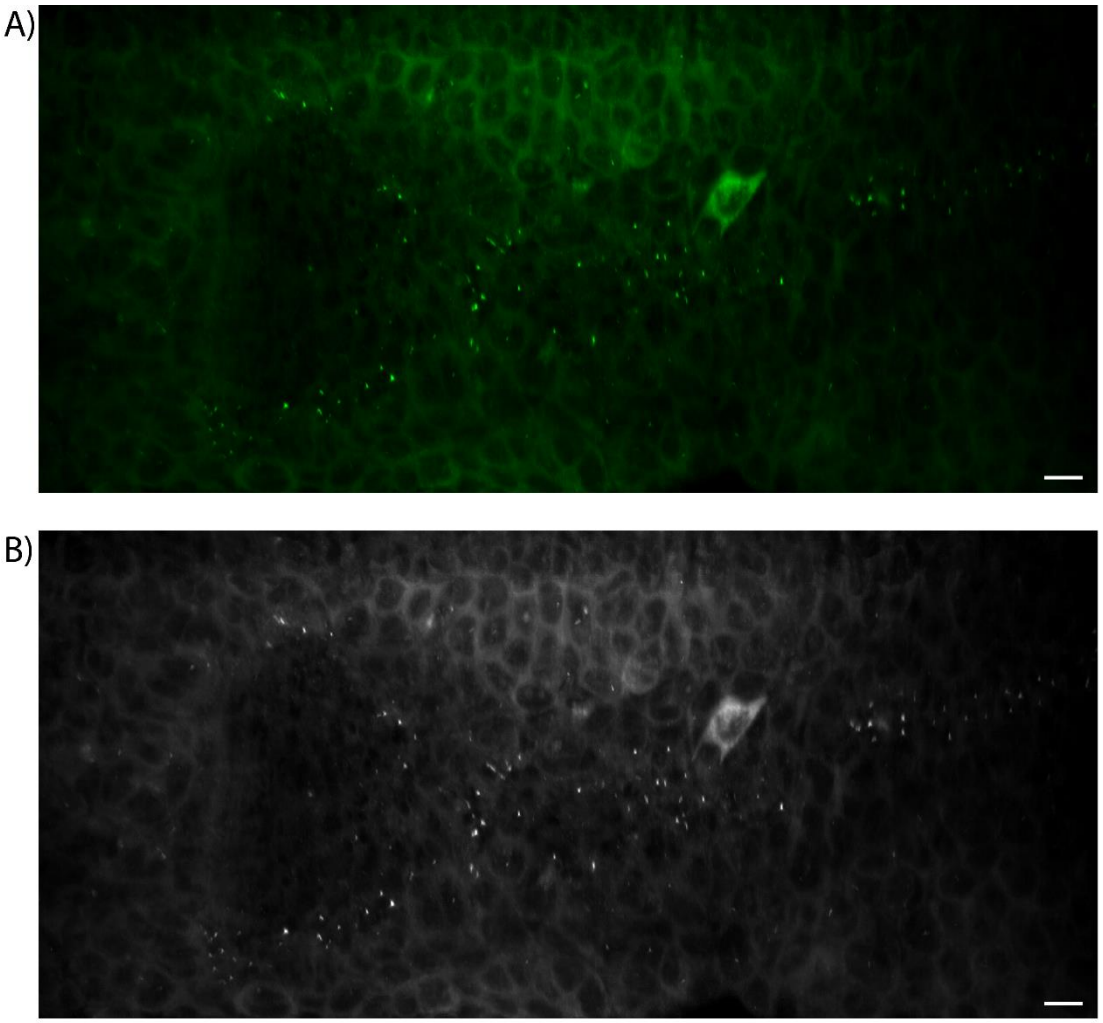


Figure 5.24 Lightsheet imaging of PKD2^{mNG} in an 8 d.p.c. embryo
Fluorescence of an 8 d.p.c. embryo, endogenously expressing PKD2^{mNG}. A & B both depict the same sample and image A) green, B) greyscale. Scale bars represent 10 µm.

5.2.6 PKD1L1^{mTFP1} and PKD2^{mNG} co-localise in nodal cilia

Having shown that both PKD1L1^{mTFP1} and PKD2^{mNG} localise to nodal cilia, particularly in crown cells and at the anterior edge into the notochord, I wanted to assess whether they co-localised in nodal cilia. To determine this, crosses were set up using *Pkd2$^{mNG/mNG}$*;*Pkd1l1$^{mTFP1/mTFP1}$* and *Pkd2$^{+/mNG}$*;*Pkd1l1$^{mTFP1/mTFP1}$* mice. Ideally, only double homozygous mice would have been used for intercrosses; however, few double homozygous mice were available whilst plenty of het-homs were available. *Pkd2$^{+/mNG}$*;*Pkd1l1$^{mTFP1/mTFP1}$* mice were selected over *Pkd2$^{mNG/mNG}$*;*Pkd1l1$^{+/mTFP1}$* mice due to the weaker fluorescence of PKD1L1^{mTFP1}.

Immunofluorescence imaging of PKD2^{mNG} and PKD1L1^{mTFP1} in *Pkd1l1$^{mTFP1/mTFP1}$*; *Pkd2$^{mNG/mNG}$* 8 d.p.c. embryos revealed similar expression to that seen in embryos containing only one tagged allele. Three figures have been assembled showing the expression of PKD2^{mNG} and PKD1L1^{mTFP1} in six different embryos (Figures 5.25 – 5.27). In all samples, PKD2^{mNG} shows strong fluorescence in nodal cilia compared to background autofluorescence, whereas PKD1L1^{mTFP1} exhibits much weaker fluorescence that is more difficult to visualise against the background (Figures 5.25 – 5.27). PKD2^{mNG} expression demonstrated the same pattern of peripheral and anterior localisation in most embryos, as seen previously. One exception is Figure 5.26 B, which shows a wider distribution of nodal cilia expressing PKD2^{mNG}.

It was difficult to ascertain whether PKD2^{mNG} and PKD1L1^{mTFP1} co-localised from whole overviews of the embryonic node. However, when areas of the image showing cilia expressing PKD2^{mNG} were cropped and enlarged, co-localisation of PKD1L1^{mTFP1} was clear (Figures 5.25 – 5.27 A', A'', B', B''). Notably,

PKD1L1^{mTFP1} was not observed in every PKD2^{mNG} positive cilium, and was mostly seen in cilia expressing PKD2^{mNG} at higher levels (Figure 5.25 B'', 5.26 A'').

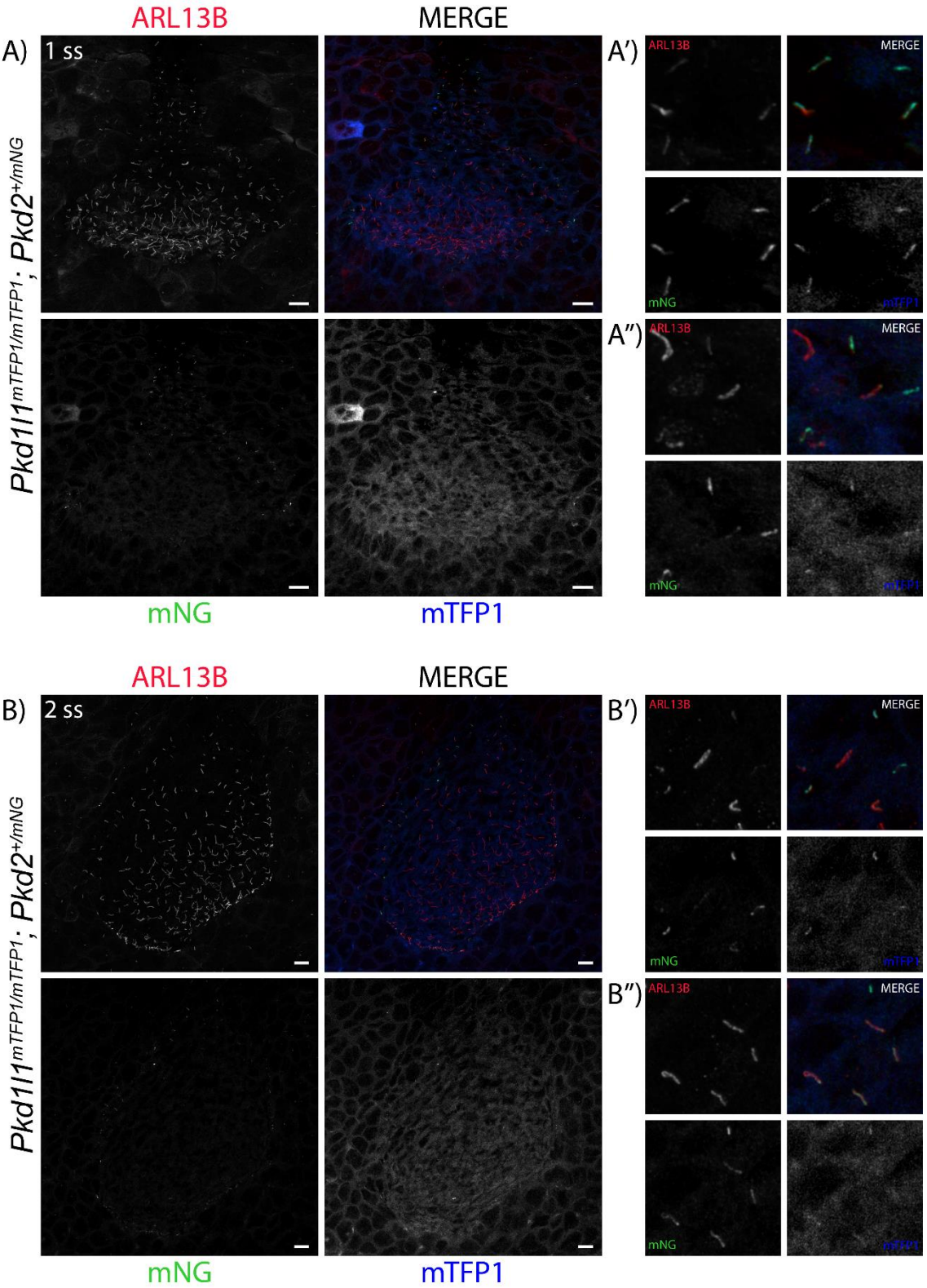


Figure 5.25 PKD2^{mNG} and PKD1L1^{mTFP1} fluorescence in 8 d.p.c. embryos
Immunofluorescence of two embryonic nodes (A and B), endogenously expressing PKD2^{mNG} and PKD1L1^{mTFP1}, stained with ARL13B to label cilia. A', A'', B', B'' are zooms of nodal cilia from A and B respectively. Staining is in the same order for whole node images and zooms: top left = ARL13B (Red), top right = Merge, bottom left = PKD2^{mNG} (Green), bottom right = PKD1L1^{mTFP1} (Blue). Scale bars represent 10 µm.

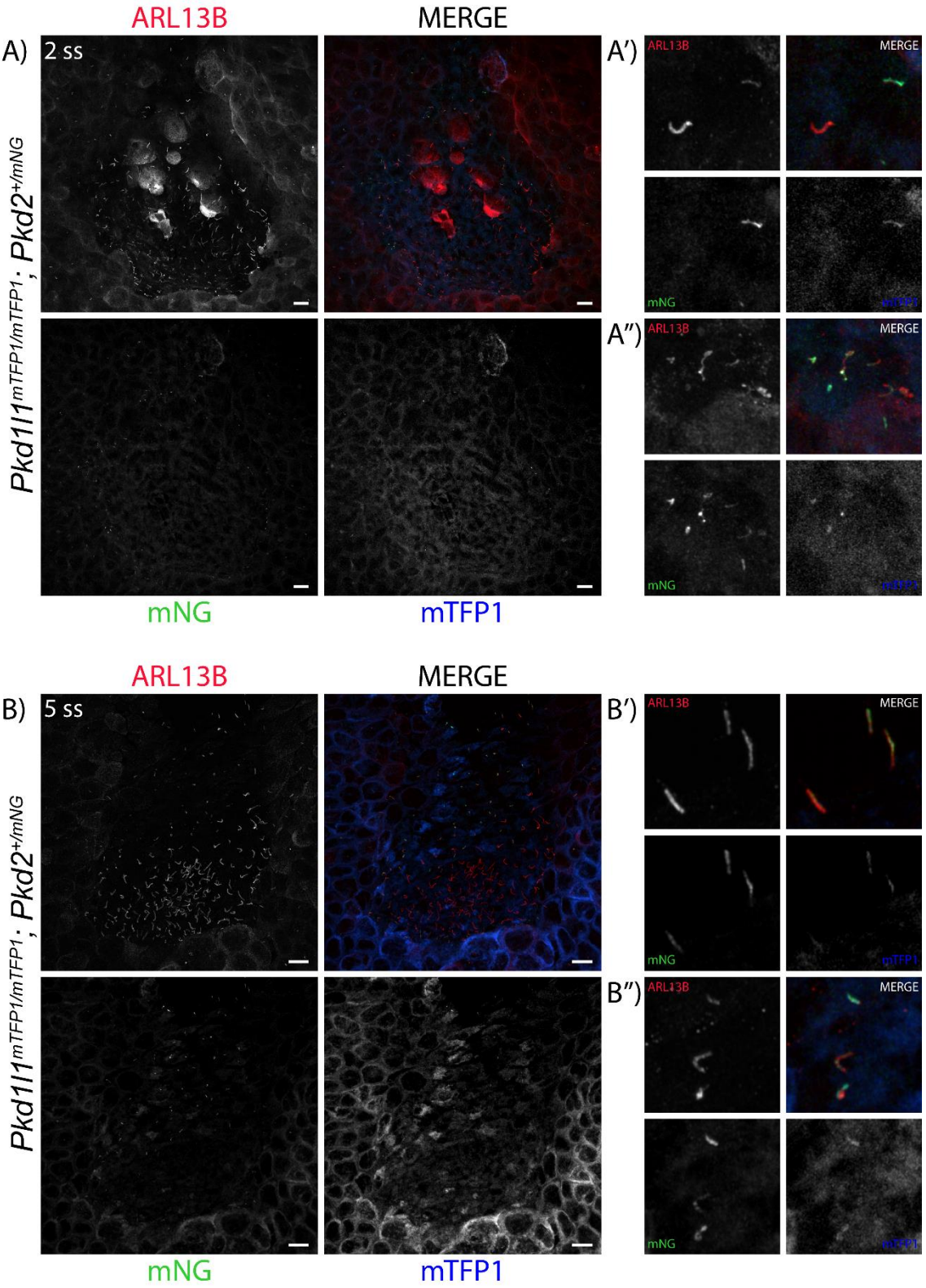


Figure 5.26 PKD2^{mNG} and PKD1L1^{mTFP1} fluorescence in 8 d.p.c. embryos
Immunofluorescence of two embryonic nodes (A and B), endogenously expressing PKD2^{mNG} and PKD1L1^{mTFP1}, stained with ARL13B to label cilia. A', A'', B', B'' are zooms of nodal cilia from A and B respectively. Staining is in the same order for whole node images and zooms: top left = ARL13B (Red), top right = Merge, bottom left = PKD2^{mNG} (Green), bottom right = PKD1L1^{mTFP1} (Blue). Scale bars represent 10 µm.

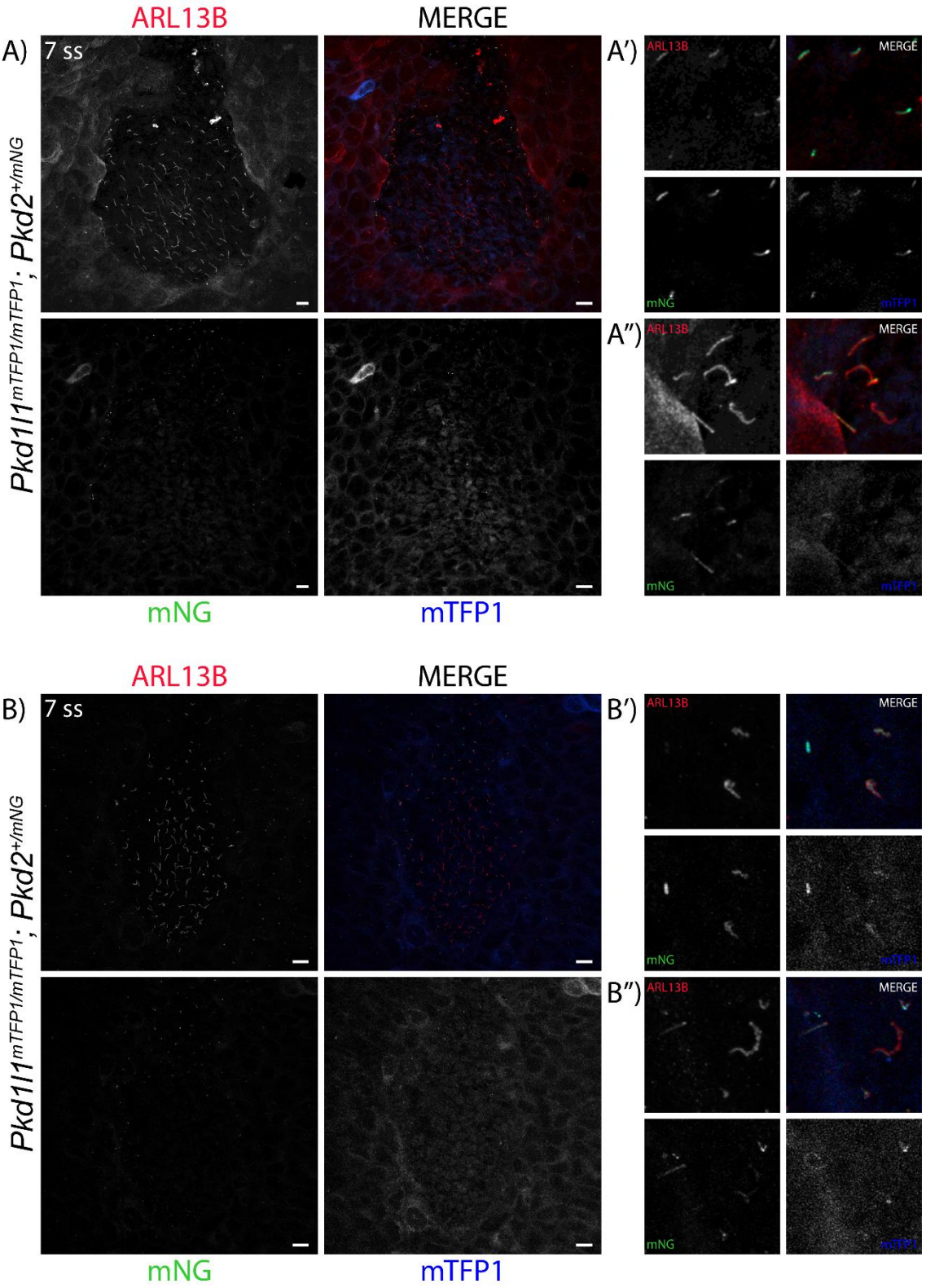


Figure 5.27 PKD2^{mNG} and PKD1L1^{mTFP1} fluorescence in 8 d.p.c. embryos
Immunofluorescence of two embryonic nodes (A and B), endogenously expressing PKD2^{mNG} and PKD1L1^{mTFP1}, stained with ARL13B to label cilia. A, B, C ‘ and ‘‘ are zooms of nodal cilia from A, B and C. Staining is in the same order for whole node images and zooms: top left = ARL13B (Red), top right = Merge, bottom left = PKD2^{mNG} (Green), bottom right = PKD1L1^{mTFP1} (Blue). Scale bars represent 10 µm.

5.2.7 PKD1L1 and PKD2 are co-dependent for nodal cilia localisation

Observations in medakafish suggested a co-dependent relationship between Pkd1l1 and Pkd2 for localisation to cilia in Kupffer's vesicle (Kamura et al. 2011). To assess whether the same is true in the mammalian node, *Pkd2*$^{mNG/mNG}$ mice were bred with *Pkd1l1*$^{+/-}$ mice to generate *Pkd2*$^{+/mNG}$;*Pkd1l1*$^{+/-}$ mice. These were crossed to generate embryos homozygous null for *Pkd1l1* and either homozygous or heterozygous for *Pkd2*^{mNG}. Similarly, *Pkd1l1*$^{mTFP1/mTFP1}$ mice were crossed with *Pkd2*$^{+/-}$ mice to generate *Pkd1l1*$^{+/mTFP1}$;*Pkd2*$^{+/-}$ mice; these were intercrossed to generate embryos homozygous null for *Pkd2* and either homozygous or heterozygous for *Pkd1l1*^{mTFP1}. Embryos were dissected at 8 d.p.c., stained with ARL13B to label cilia, mounted and imaged. Embryos were imaged and processed blind to genotyping, to prevent any unconscious bias in scoring.

In *Pkd1l1*$^{-/-}$ embryos, one embryo showed clear localisation of PKD2^{mNG} in nodal cilia (Figure 2.9 A, A'); the other 5 embryos examined did not exhibit any obvious expression of PKD2^{mNG} in nodal cilia (Figures 5.28 A, B, C and 5.29 B, C). As there was no clear expression, regions were cropped and enlarged covering nodal cilia from the peripheries and anterior of the node leading into the notochord where I had previously characterised PKD2^{mNG} expression (section 5.2.4). Enlargements confirmed there was no specific expression of PKD2^{mNG} in nodal cilia in *Pkd1l1*$^{-/-}$ embryonic nodes (Figures 5.28 A', B', C', 5.29 B', C'). With one embryo being an exception to this (Figure 5.29 A, A'). As this one data point appeared anomalous with the other data, I re-investigated its genotype. A close examination of the genotyping data revealed a very slight peak of WT DNA in the qPCR data, casting some doubts on its identity as a *Pkd1l1*$^{-/-}$ embryo

(Supplementary Figure 7.2). I cannot be certain as to the underlying cause of this, but expression and genotyping data of more samples could provide further insight. It may suggest that it is possible for very small amounts of *Pkd1l1* to be expressed in some *Pkd1l1*$^{-/-}$ mice, which is sufficient for ciliary PKD2^{mNG} expression.

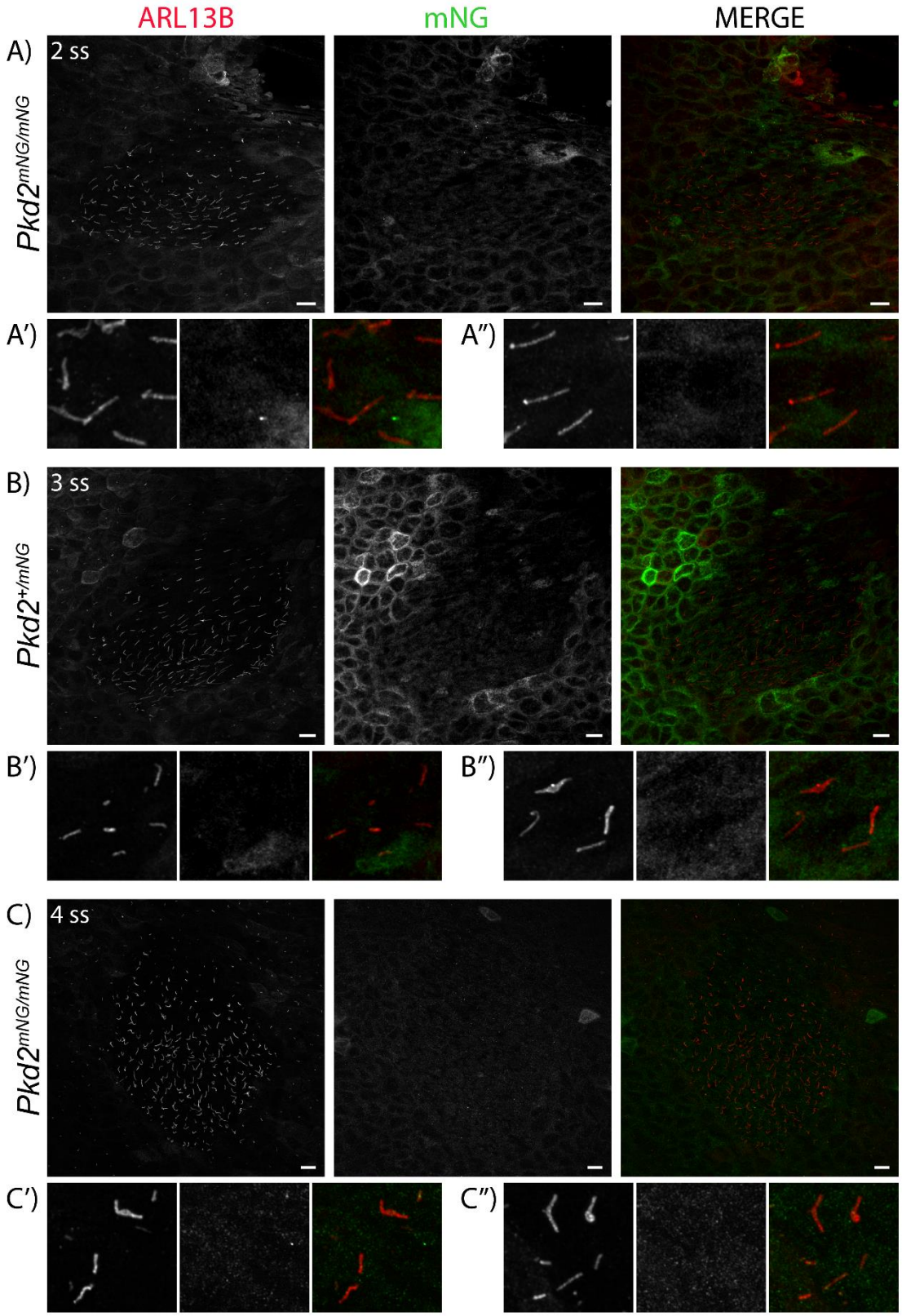


Figure 5.28 PKD2^{mNG} fluorescence in *Pkd1l1*$^{-/-}$ 8 d.p.c. embryos
Immunofluorescence of three *Pkd1l1*$^{-/-}$ embryonic nodes (A, B and C), endogenously expressing PKD2^{mNG} and stained with ARL13B to label cilia. A, B, C ‘ and ‘‘ are zooms of nodal cilia from A, B and C. Staining is in the same order for whole node images and zooms, from left to right: ARL13B (Red), PKD2^{mNG} (Green), Merge. Scale bars represent 10 µm.

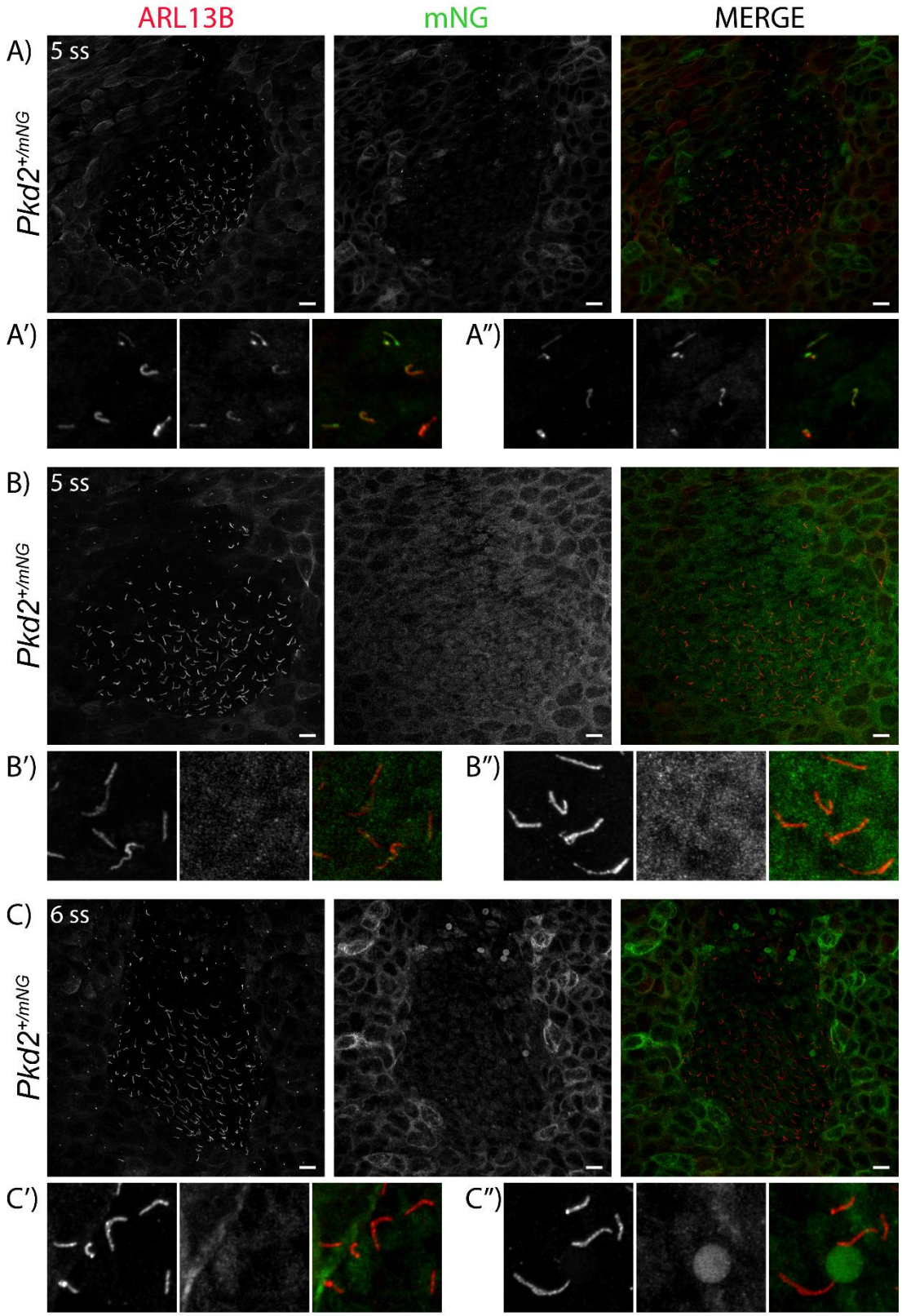


Figure 5.29 PKD2^{mNG} fluorescence in *Pkd1l1*$^{-/-}$ 8 d.p.c. embryos continued
Immunofluorescence of three *Pkd1l1*$^{-/-}$ embryonic nodes (A, B and C), endogenously expressing PKD2^{mNG} and stained with ARL13B to label cilia. A, B, C ‘ and ‘‘ are zooms of nodal cilia from A, B and C. Staining is in the same order for whole node images and zooms, from left to right: ARL13B (Red), PKD2^{mNG} (Green), Merge. Scale bars represent 10 µm.

In *Pkd2*$^{-/-}$ embryos, it was difficult to identify any nodal cilia expressing PKD1L1^{mTFP1} (Figures 5.30 and 5.31). Similar to *Pkd1l1*$^{-/-}$ embryos, enlargements of nodal cilia were taken from the edges of the node and anterior notochord region. None of these showed any indication of PKD1L1^{mTFP1} expression in nodal cilia (Figures 5.30 A', B', C' and 5.31 A', B', C').

This data is consistent with the findings in medakafish, and supports the idea that there is a co-dependent relationship between PKD1L1 and PKD2 for correct localisation to nodal cilia.

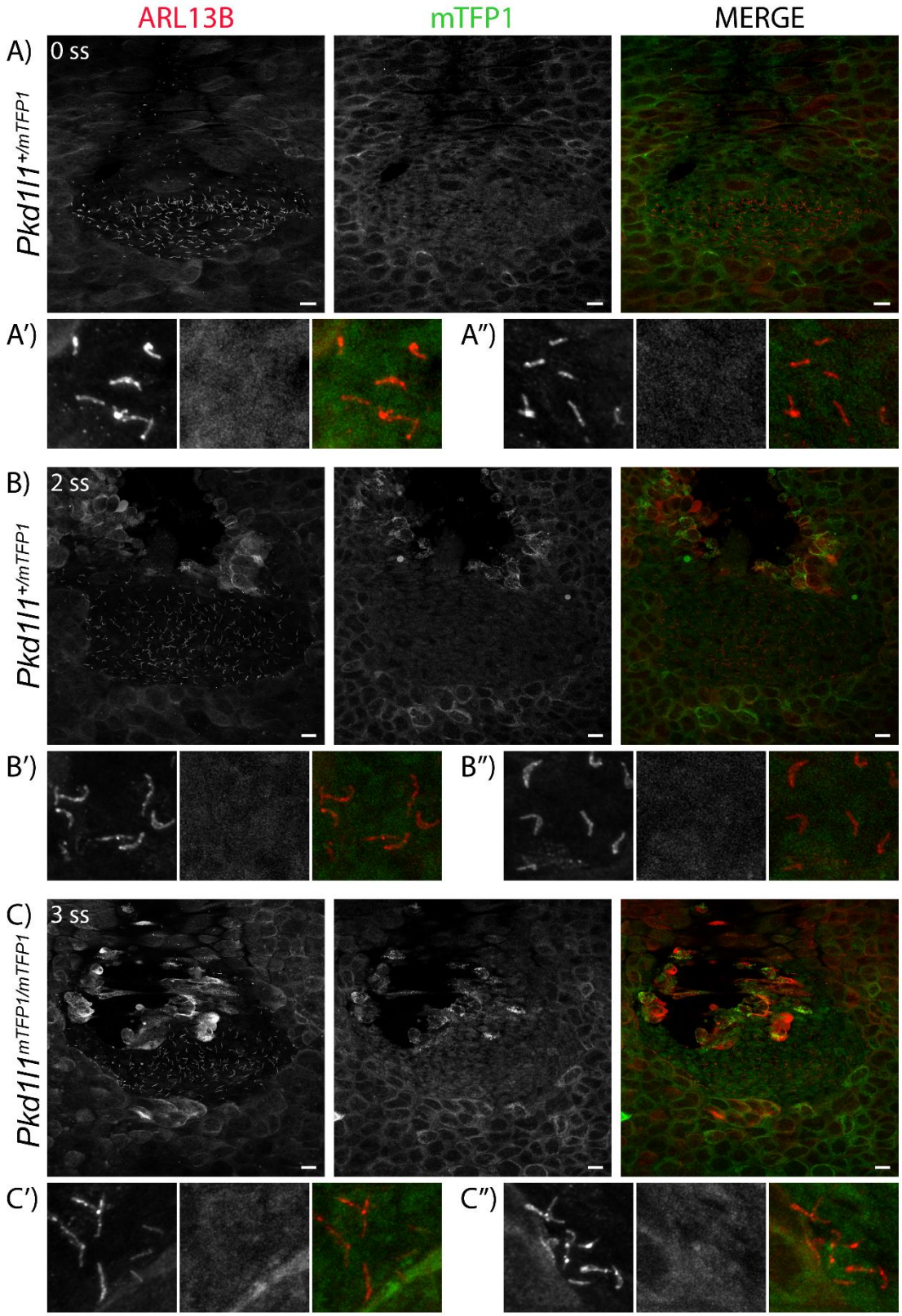


Figure 5.30 PKD1L1^{mTFP1} fluorescence in *Pkd2*$^{-/-}$ 8 d.p.c. embryos
Immunofluorescence of three *Pkd2*$^{-/-}$ embryonic nodes (A, B and C), endogenously expressing PKD1L1^{mTFP1} and stained with ARL13B to label cilia. A, B, C ‘ and ‘‘ are zooms of nodal cilia from A, B and C. Staining is in the same order for whole node images and zooms, from left to right: ARL13B (Red), PKD1L1^{mTFP1} (Green), Merge. Scale bars represent 10 µm.

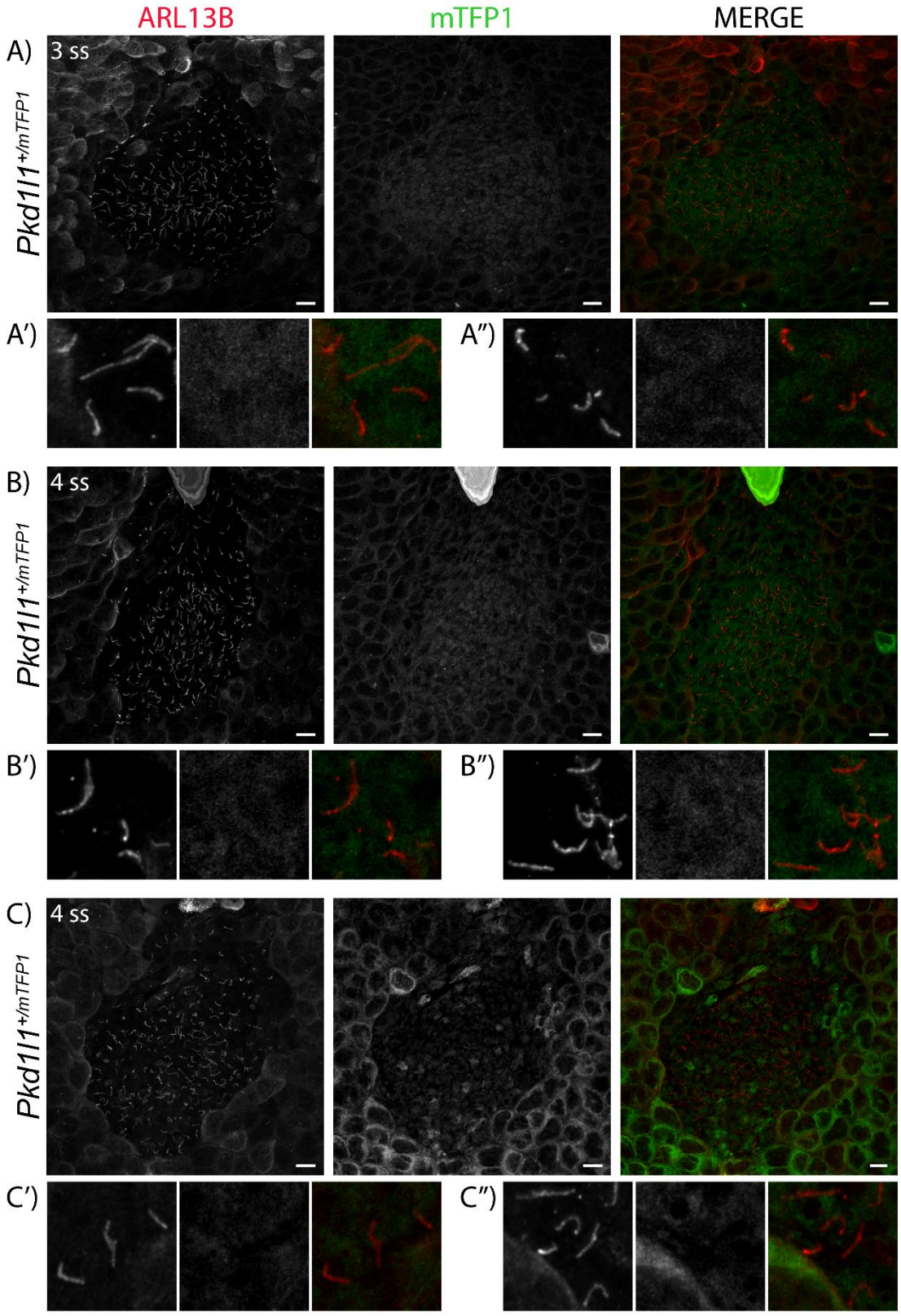


Figure 5.31 PKD1L1^{mTFP1} fluorescence in *Pkd2*$^{-/-}$ 8 d.p.c. embryos
Immunofluorescence of three *Pkd2*$^{-/-}$ embryonic nodes (A, B and C), endogenously expressing PKD1L1^{mTFP1} and stained with ARL13B to label cilia. A, B, C ‘ and ‘‘ are zooms of nodal cilia from A, B and C. Staining is in the same order for whole node images and zooms, from left to right: ARL13B (Red), PKD1L1^{mTFP1} (Green), Merge. Scale bars represent 10 µm.

5.3 Discussion

The data in this chapter has provided the first direct evidence of PKD1L1 localisation in nodal cilia within the mouse embryonic node. I have also shown that PKD1L1 co-localises with PKD2 in nodal cilia, and that they both appear to preferentially localise in nodal cilia at the periphery and the anterior edge of the node. Imaging of *Pkd1l1*^{mTFP1};*Pkd2*$^{-/-}$ and *Pkd2*^{mNG};*Pkd1l1*$^{-/-}$ 8 d.p.c. embryos, suggests a similar co-dependent relationship for ciliary localisation as the observations in medakafish (Kamura et al. 2011). Previous work from the lab demonstrated that PKD2 and PKD1L1 interact via the coiled-coil domain of PKD1L1 (Field et al. 2011), this interaction may be involved in the ciliary localisation of PKD1L1 and PKD2. Similarly, PKD1 and PKD2 interactions have been shown to play a role in ciliary localisation; however, there is conflicting data with studies arguing both for and against their co-dependent relationship for ciliary localisation (Gainullin et al. 2015; Geng et al. 2006; Kim et al. 2014; Liu et al. 2018).

My initial testing of PKD1L1 antibodies in mouse proved inconclusive, with the staining being indistinguishable between *Pkd1l1*$^{+/+}$ and *Pkd1l1*$^{-/-}$ embryos. Initially, it seemed that perhaps the antibodies were binding non-specifically. Strikingly, both our rabbit polyclonal antibody and the commercial OSP00015W rabbit polyclonal antibody stained nodal cilia, which we now know to be true for *Pkd1l1* localisation. The question remains as to what those PKD1L1 antibodies may be binding to in *Pkd1l1*$^{-/-}$ embryos. I suggest that further testing of the rabbit polyclonal antibodies should be performed in the future, it would be intriguing to examine the staining in *Pkd2*$^{-/-}$ embryos to assess whether the ciliary staining is lost, as observed for PKD1L1^{mTFP1}. One possible explanation lies in the potential

alternate transcripts of *Pkd1l1*. I have provided evidence for additional exons in mouse *Pkd1l1* (Section 3.2), and it is possible that more alternative transcripts may exist. There is a Kozak consensus sequence towards the end of exon 6 (Ensembl transcript), located after the gene trap in the *Pkd1l1*$^{-}$ allele which is inserted in place of exons 3, 4 and 5 (Ensembl transcript). However, if this transcript exists, the only portion missing in the resulting protein would be the end of the N-terminal tail containing no known domains; both PKD domains and all subsequent transmembrane domains should still be present in any translated protein. However, both rabbit polyclonal antibodies would be able to bind to this hypothetical truncated protein, providing an explanation for staining in *Pkd1l1*$^{-/-}$ embryos. If this were the case, how can we explain the left-right pattering defects observed in *Pkd1l1*$^{-/-}$ embryos?

With the new evidence for a co-dependent relationship of PKD1L1 and PKD2 for correct localisation to nodal cilia, we can attempt to further understand the mechanisms involved with PKD1L1 and PKD2 in nodal cilia for correct left-right patterning. Previous work from the lab showed a reduction of PKD2 antibody staining in *Pkd1l1*$^{-/-}$ mice (Grimes et al. 2016). This led me to question whether PKD2 may function as constitutively active homotetrameric channel in nodal cilia in the absence of PKD1L1, which could bilaterally activate the nodal signalling cascade as seen in *Pkd1l1*$^{-/-}$ embryos. However, the evidence shown in this chapter revealing a complete loss of PKD2 nodal ciliary localisation in *Pkd1l1*$^{-/-}$ embryos does not support this.

The imaging data in section 5.2.7 shows that in *Pkd2*$^{-/-}$ embryos, PKD1L1 fails to localise to nodal cilia and would be unable to respond to flow in nodal cilia. *Pkd2*$^{-/-}$ embryos show an absence of nodal in the lateral plate mesoderm and present

with mostly right isomerisms of the lungs (Pennekamp et al. 2002). Similarly, in *Pkd1l1*$^{-/-}$ embryos, PKD2 fails to localise to nodal cilia, and would be unable to act as a mechanosensitive channel. However, the phenotype in *Pkd1l1*$^{-/-}$ embryos is the opposite of *Pkd2*$^{-/-}$ embryos; with embryos displaying bilateral expression of nodal in the left and right lateral plate mesoderm and mostly left isomerism of the lungs (Grimes et al. 2016). Understanding the mechanisms leading to these two distinct phenotypes in *Pkd1l1*$^{-/-}$ and *Pkd2*$^{-/-}$ embryos, would provide great insight into the role of the polycystins in left-right pattern determination.

It remains to determine the localisation of PKD2 in *Pkd1l1*$^{rks/rks}$ embryos and PKD1L1 in *Pkd2*$^{lrm4/lrm4}$ embryos, which would provide further insight into the co-dependent relationship between PKD1L1 and PKD2. Both *Pkd1l1*$^{rks/rks}$ and *Pkd2*$^{lrm4/lrm4}$ embryos show absent nodal expression in the lateral plate mesoderm and mostly right isomerism of the lungs – the same phenotype as *Pkd2*$^{-/-}$ embryos (Ermakov et al. 2009; Field et al. 2011; Grimes et al. 2016). The localisation of PKD1L1^{rks} protein is also undetermined, due to the lack of a specific PKD1L1 antibody. Considering that the PKD1L1^{rks} point mutation is located in a PKD domain of the extracellular N-terminal tail, it seems most likely that its localisation will not be affected. As I have not been able to verify the specificity of PKD1L1 antibodies, this could be investigated by introducing a fluorescent tag into the *Pkd1l1*^{rks} allele. Due to the uncertainty of alternative transcripts in *Pkd1l1*$^{-/-}$, it would be intriguing to examine a tagged allele of *Pkd1l1*$^{-/-}$ to ascertain whether any protein is expressed from this sequence. This could be performed in *Pkd1l1*$^{-/-}$ cell lines using CRISPR/Cas9 mediated insertion of a tag , a small FLAG or HIS tag would enable immunofluorescent staining, western blots and immunoprecipitations to be performed using an anti-His or anti-FLAG antibody.

In hindsight, my decision to tag *Pkd1l1* with mTFP1 was not optimal. The mTFP1 fluorescence was weak, however it is difficult to know whether this is due to the tag, or to the expression of PKD1L1; we expect PKD1L1 to form a heterotetrameric complex in a 3:1 ratio of PKD2:PKD1L1, suggesting that three times less PKD1L1 that PKD2 is present in nodal cilia. The main problem I encountered with the mTFP1 tag, is the lack of an antibody against it, which could be used to enhance the fluorescent signal as well as for western blots and immunoprecipitation. For any generation of tagged alleles of *Pkd1l1*, *Pkd1l1*$^{-/-}$ or *Pkd1l1*$^{rks/rks}$ in the future, I would suggest the use of a different tag. In contrast, the mNeonGreen tag showed good fluorescence and has options available for antibodies and affinity resins for immunoprecipitation; however, a new tag would have to be chosen for *Pkd2* alleles if further investigation involving co-localisation is sought after.

Recent work by Hiroshi Hamada's lab has revealed asymmetric expression of PKD2 within nodal cilia. Using 3D STED imaging they showed PKD2 preferentially localised to the dorsal side of cilia on both right and left sides of the node (Katoh et al. 2022). This work was performed using the *NDE2-hsp-Pkd2-Venus* transgene, previously described in Yoshiba et al., which overexpresses PKD2 in crown cell cilia at the edge of the node (Katoh et al. 2022; Yoshiba et al. 2012). It would be intriguing to examine the localisation of our PKD2^{mNG} in nodal cilia using super resolution fluorescence microscopy, to ascertain whether the same findings are observed with endogenous expression. Super resolution imaging would also provide further insight into the specifics of *Pkd2*^{mNG} and *Pkd1l1*^{mTFP1} co-localisation.

6. Discussion

The work in this thesis has examined the polycystins (PKD1L1 and PKD2) using a variety of molecular, cellular and in vivo experiments, in order to further our understanding of these polycystins in left-right pattern determination.

6.1. Summary of findings

6.1.1. *Pkd1l1* contains an additional seven 5' exons to the Ensembl annotated sequence

In Chapter 2, I presented my work in predicting and confirming additional 5' exons of *Pkd1l1*. Initially, I predicted the presence of an additional 6 exons, which I confirmed using RT-PCR. However, when I performed 5' RACE in order to ascertain the full extent of the 5' UTR, I identified a second distinct 5' transcript. The second transcript (5' long) contains an addition exon at the 5' end which splices into the 5' UTR of the 5' short transcript.

By analysing RNA-Seq data from 8 d.p.c. B6J embryos, and performing qPCR on cDNA synthesised from wild type B6J and C3H, I determined that the long 5' is the predominant transcript present during left-right patterning. I also demonstrated that these additional 5' exons are strongly expressed in the embryonic node and notochord of 8 d.p.c. embryos.

Further investigation into the localisation of the distinct 5' transcripts could answer questions about the roles of these two transcripts. It seems likely that there could be an N-terminal signalling motif that may lead to trafficking into different compartments, perhaps one of the proteins will show stronger ciliary expression than the other.

6.1.2. A lower ~85 kDa isoform of PKD2 is present in multiple tissues and cell lines

At the start of my project, I developed new rabbit polyclonal antibodies for PKD2 in collaboration with Covalab. When using these antibodies for immunoprecipitation, I observed the presence of a band below the expected sized band of PKD2. In immunoprecipitations using mouse embryonic fibroblasts, the lower band appeared to decrease in intensity in *Pkd2*$^{+/-}$ and *Pkd2*$^{-/-}$ MEFs along with the expected sized PKD2 band. I performed immunoprecipitations in multiple tissues and cell lines and observed different ratios of the expected 110 kDa and lower ~85 kDa bands in the western blots. Mass spectrometry analysis, revealed the presence of PKD2 in the ~85 kDa band in both kidney and lung immunoprecipitation samples.

Mapping of the peptides identified in the mass spec analysis, suggests that the N-terminal region of PKD2 may be missing in the lower isoform. Whether this is due to transcriptional changes or post-translational modification, is yet to be determined. The lower isoform was particularly abundant in the kidney samples, which may prove to have significant functional relevance; it would be highly intriguing to investigate this further.

6.1.3. Mass spectrometry analysis of *Pkd2*$^{lrm4/lrm4}$ kidney and lung samples identified candidate interacting partners for ciliary localisation

To understand the mechanism leading to the mislocalisation of PKD2^{lrm4}, which accumulates in a ring like formation at the ciliary base, I performed immunoprecipitations using kidneys and lungs from *Pkd2*$^{+/+}$, *Pkd2*$^{+/-}$ and *Pkd2*$^{lrm4/lrm4}$ 14.5 d.p.c. embryos. Samples were sent for mass spec analysis to

identify candidate interacting partners. This highlighted four proteins present in *Pkd2*$^{+/+}$ samples that were missing in *Pkd2*$^{lrm4/lrm4}$ samples (CHMP4B, HIP1, RAB26, and CCT5), and two proteins that were detected in *Pkd2*$^{lrm4/lrm4}$ samples but not in *Pkd2*$^{+/+}$ samples (SNX9, and SEPT2).

Any of these proteins could play a role in the ciliary localisation of PKD2, due to their roles in ciliogenesis; however, the most striking candidate is SEPT2. Localisation of SEPT2 shows a ring-like appearance at the ciliary base, similar to that seen for PDK2^{lrm4}. Further evidence for this interaction through co-immunoprecipitation and co-localisation could prove valuable in understanding the mislocalisation of PKD2^{lrm4}, and in turn the mechanisms of PKD2 ciliary entry.

6.1.4. *Pkd2*^{mNG} and *Pkd1l1*^{mTFP1} are homozygous viable

With the help of the transgenics team at Harwell, we developed C-terminal endogenous tagged alleles of *Pkd2* and *Pkd1l1*. Homozygous mice carrying the tagged alleles, *Pkd2*$^{mNG/mNG}$ and *Pkd1l1*$^{mTFP1/mTFP1}$ show no gross abnormalities, and are fully viable. These mice are indistinguishable from wild type mice, and are capable of breeding without any complications. Through crosses and intercrosses, we were able to generate double homozygous embryos and a few double homozygous mice. Again, *Pkd2*$^{mNG/mNG}$;*Pkd1l1*$^{mTFP1/mTFP1}$ embryos and mice show no indication of situs defects or other abnormality; consistent with the alleles producing fully functional tagged proteins.

6.1.5. PKD2^{mNG} and PKD1L1^{mTFP1} co-localise within nodal cilia

Fluorescent imaging of the node in 8 d.p.c. embryos, revealed that both PKD2^{mNG} and PKD1L1^{mTFP1} localised to nodal cilia, and they co-localised in cilia at the periphery and anterior edge of the node. This provided the first direct evidence of PKD1L1 in mammalian nodal cilia, previously this had only been shown in medakafish. This finding is important in understanding the role of the polycystins in left-right pattern determination, as it verifies that PKD1L1 could be acting as a mechanosensor within nodal cilia in the detection of nodal flow.

6.1.6. PKD2 and PKD1L1 are co-dependent for ciliary localisation in the embryonic node

Analysis of fluorescent imaging of PKD2^{mNG} in *Pkd1l1*$^{-/-}$ embryonic nodes and the contrary, PKD1L1^{mTFP1} in *Pkd2*$^{-/-}$ embryonic nodes, revealed a complete loss of ciliary localisation in the absence of either PKD2 or PKD1L1. Previous staining and imaging of PKD2 in *Pkd1l1*$^{-/-}$ embryonic nodes, suggested only a partial loss of PKD2. However, my experiments are consistent with a complete loss of ciliary localisation of one polycystin in the absence of the other. The Airyscan mode on the Zeiss LSM 710 confocal microscope, provides good resolution and detail when imaging nodal cilia, but further super resolution imaging could provide more detail into the precise localisation of the polycystins in the absence of one or another; it would be intriguing to investigate whether they can be observed at the ciliary base, as seen for PKD2^{lrm4}.

6.7. Future work

6.7.1. Implications of additional *Pkd1l1* 5' exons

The identification of seven additional exons at the 5' end of *Pkd1l1*, and two distinct 5' variants, leads to questions about the implications of the variants on *Pkd1l1* function. This variation could be tissue specific, in which case identifying the predominant variant in different tissues and cell types may better our understanding of their functional implications. To investigate this, RT-qPCR could be performed, with the same or similar primers to my experimental data, using different tissue samples. Supporting data for this could also be obtained through mining RNA-Seq databases and examining the read coverage of the first and second exons (as performed in section 3.2.4).

In my experiments, I examined the expression of the newly identified exons using whole mount in-situ hybridisation (section 3.2.5). This highlighted expression within the embryonic node in 8 d.p.c embryos, however I did not investigate differences in expression of the two 5' variants of *Pkd1l1*. Follow up experiments could be performed using fluorescence in-situ hybridisation with probes designed specifically for the 5' long and 5' short variants. This method would allow for increased sensitivity and enhanced resolution using fluorescence microscopy, such as confocal or Airyscan imaging; making it possible to identify specific regions of expression within the embryonic node. It would also be possible to examine both variants in the same sample to assess relative levels and differences in expression.

To assess whether the two variants localise to different cellular compartments, each variant could be cloned into an expression vector with a tag for fluorescent imaging or immunofluorescent staining and imaging. These could be transfected

into various cell lines, both ciliated and non-ciliated cells, stained and imaged to examine localisation of each variant. Using the same constructs, it could be possible to test for differences in channel activity and mechanosensation using a flow chamber and calcium dyes.

6.7.2. Further investigation into the smaller ~85 kDa PKD2 isoform

Similar to additional 5' *Pkd1l1* exons, the smaller isoform of PKD2 identified could play a significant role in protein function and expression. Peptide mapping, from the mass spectrometry peptide sequencing, is indicative of a missing region at the n-terminus, however the remaining sequence is not fully covered by the peptide mapping. For further investigation into functions of the smaller isoform, it is important to ascertain the true protein sequence. Additional samples could be sent for mass spectrometry, both to determine the exact molecular weight of the lower isoform and for further peptide sequencing to improve the read coverage. However, it is possible that specific regions of the protein will be difficult to detect using peptide sequencing due to the trypsin digestion and chromatography separation. Alternatively, the sequence could be determined through *De Novo* protein sequencing. Once the protein sequence has been ascertained, it would be possible to generate constructs to investigate localisation and channel activity.

It is also intriguing as to how the smaller isoform is produced, whether it is through post translational modification and protein cleavage or if there is transcriptional variation as seen for *Pkd1l1*. There is no published information for PKD2 cleavage, therefor further investigation into potential cleavage sites within PKD2 may help specify regions of interest. To test for transcriptional variants of PKD2, 5' and 3' RACE could be performed with a variety of gene specific primers

throughout the sequence. If multiple bands are observed using any of the primers, this could indicate the presence of an alternate transcript.

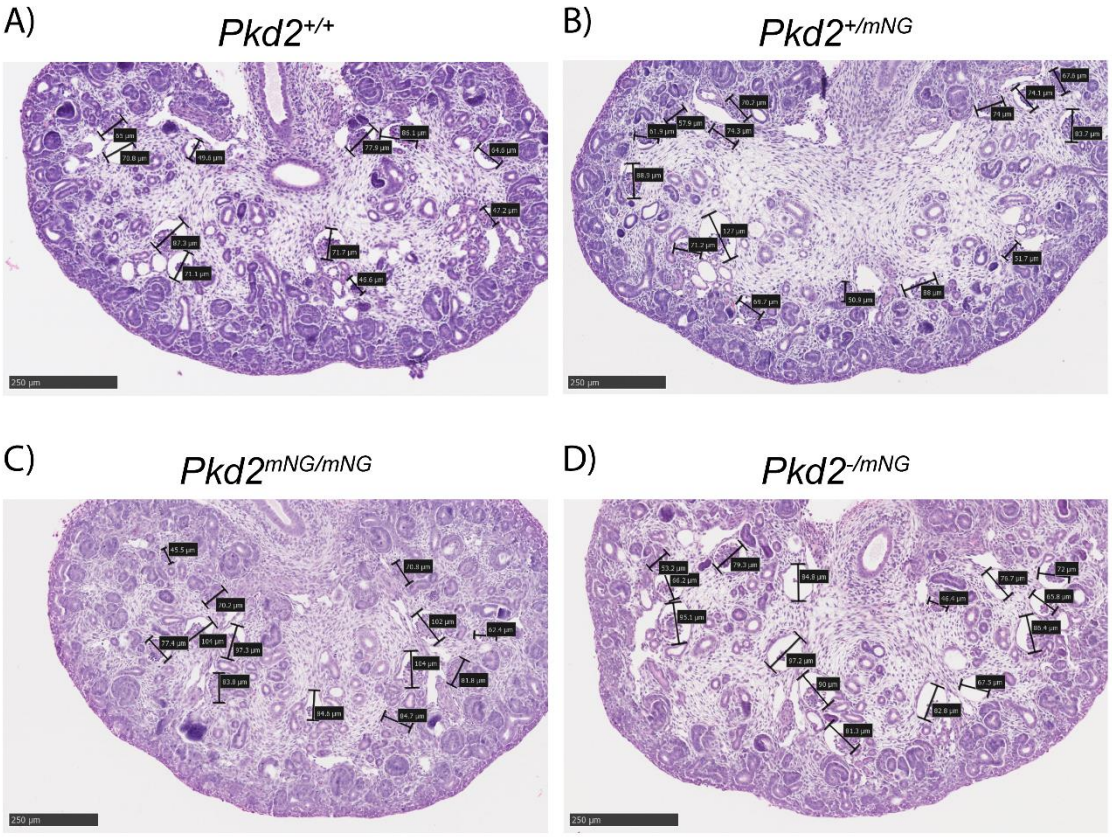
6.7.3. *Pkd2^{mNG}* and *Pkd1l1^{mTFP1}*

The *Pkd2^{mNG}* and *Pkd1l1^{mTFP}* alleles provided valuable insight into the expression of PKD1L1 in nodal cilia and the co-dependent relationship for correct ciliary localisation. In my experiments, I observed a complete loss of ciliary localisation of PKD2 in *Pkd1l1$^{-/-}$* embryos and vice versa for PKD1L1 in *Pkd2$^{-/-}$* embryos; this contradicts previous data that showed a reduction of PKD2 in *Pkd1l1$^{-/-}$* and *Pkd1l1$^{rks/rks}$* embryos rather than a loss. This could be due to difference in experimental design, antibody staining vs endogenously tagged protein, or due to the sensitivity of these methods with the imaging techniques used. It would be good to perform super resolution imaging, such as SIM, to further assess the loss of PKD2^{mNG} or PKD1L1^{mTFP1} in *Pkd1l1$^{-/-}$* or *Pkd2$^{-/-}$* embryos respectively. Further crosses with *Pkd2^{lrm4}* and *Pkd1l1^{rks}* mice could also provide a deeper understanding into the co-dependent relationship.

When performing my experiments, the *Pkd1l1^{rks}* mouse line was unavailable and would have needed re-deriving from the archive. However, due to the opposing phenotype in *Pkd1l1$^{rks/rks}$* and *Pkd1l1$^{-/-}$* embryos, re-deriving this line may help to answer some of the remaining questions about the role of PKD2 and PKD1L1 in left-right pattern determination. Ideally, it would be useful to examine the localisation of PKD1L1^{rks}, as currently it is unknown where this mutant localises correctly to nodal cilia. To do this, additional tagged alleles could be developed for *Pkd1l1^{rks}* and also *Pkd2^{lrm4}*, which could be used to study co-dependent relationships and dynamics in the presence of these mutations.

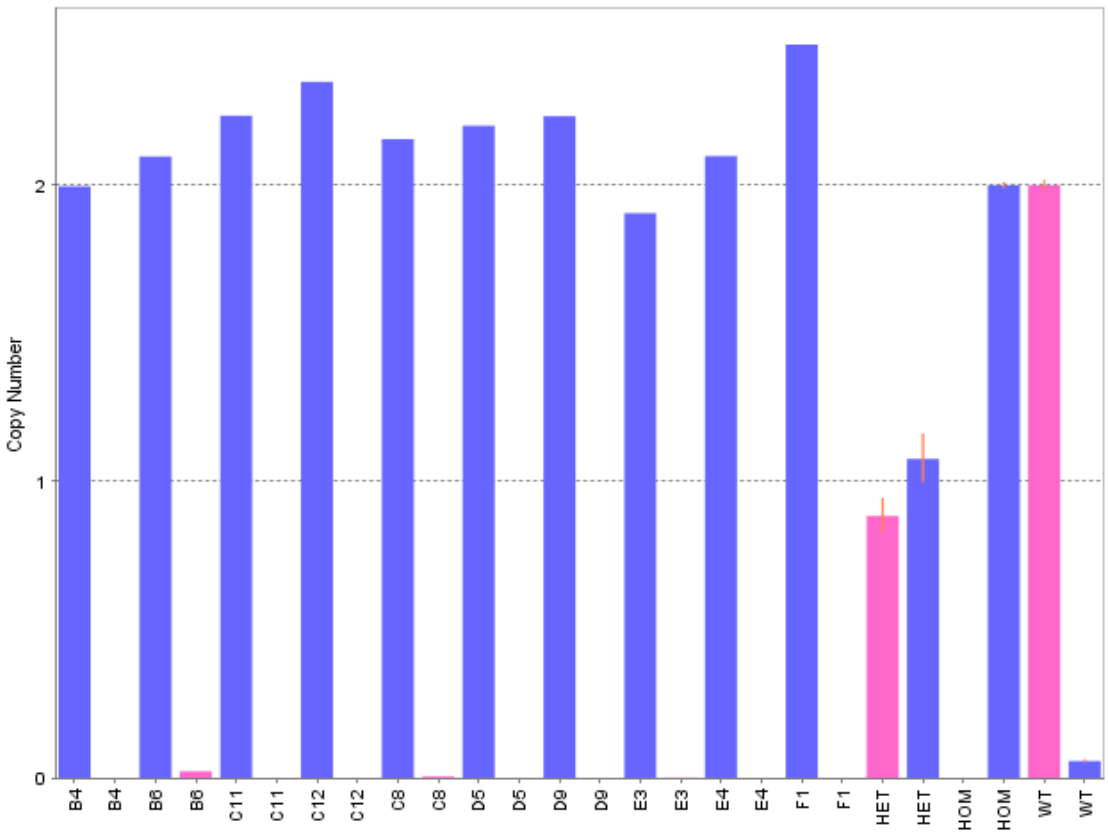
7. Appendix

7.1 Supplementary Figures



Supplementary Figure 7.1 Glomerular dilation measurements in 14.5 d.p.c. kidney sections

Kidney sections from *Pkd2*$^{+/+}$ (A), *Pkd2*$^{+/mNG}$ (B), *Pkd2*$^{mNG/mNG}$ (C) and *Pkd2*$^{-/mNG}$ (D) 14.5 d.p.c. embryos, showing the glomerular measurements annotated in the Hamamatsu NDP.view2 software. Glomerular dilations were measured in the software across the longest diameter of the dilation, only glomerular dilations >50 µm were recorded for further analysis. Scale bars represent 250 µm.



Supplementary Figure 7.2 CopyCaller analysis of *Pkd1l1*$^{-/-}$ genotyping

Exported graph from CopyCaller, showing the results of the *Pkd1l1*$^{-/-}$ qPCR genotyping assay performed on 8 d.p.c. embryos from *Pkd1l1*$^{+/-}$;*Pkd2*$^{+/mNG}$ intercrosses. The embryo exhibiting ciliary expression of PKD2^{mNG} was B6, which shows a very small bar of WT DNA in the CopyCaller analysis. Purple bars = HOM, Pink bars = WT.

7.2 Mass Spectrometry data tables

Table 7.1 – Adult Kidney IP 1 (~150-250 kDa)

Accession	Description	Coverage [%]	# PSMs	# Unique Peptides
Q8VDD5	Myosin-9 GN=Myh9	66	635	135
O08638	Myosin-11 GN=Myh11	56	295	95
Q68FD5	Clathrin heavy chain 1 GN=Cltc	69	287	96
Q61879	Myosin-10 GN=Myh10	55	231	83
P16546	Spectrin alpha chain, non-erythrocytic 1 GN=Sptan1	58	215	123
Q62261	Spectrin beta chain, non-erythrocytic 1 GN=Sptbn1	56	199	107
Q64331	Unconventional myosin-VI GN=Myo6	40	94	46
Q6URW6	Myosin-14 GN=Myh14	33	76	43
P21271	Unconventional myosin-Vb GN=Myo5b	36	68	47
Q9JMH9	Unconventional myosin-XVIIIa GN=Myo18a	32	57	50
Q9JKF1	Ras GTPase-activating-like protein IQGAP1 GN=Iqgap1	32	45	39
Q99MZ6	Unconventional myosin-VIIb GN=Myo7b	14	28	24
P15508	Spectrin beta chain, erythrocytic GN=Sptb	6	17	8
O35245	Polycystin-2 GN=Pkd2	17	13	12
Q80X90	Filamin-B GN=Flnb	6	13	13
Q9JJ28	Protein flightless-1 homolog GN=Flii	11	11	11
Q8BTM8	Filamin-A GN=Flna	5	10	10
P08032	Spectrin alpha chain, erythrocytic 1 GN=Spta1	5	10	9
Q99104	Unconventional myosin-Va GN=Myo5a	4	7	2
Q9WTI7	Unconventional myosin-Ic GN=Myo1c	7	7	7
P97479	Unconventional myosin-VIIa GN=Myo7a	3	6	4
Q62468	Villin-1 GN=Vil1	8	6	6
Q05793	Basement membrane-specific heparan sulfate proteoglycan core protein GN=Hspg2	2	5	5
P57110	A disintegrin and metalloproteinase with thrombospondin motifs 8 GN=Adamts8	4	5	1
O35969	Guanidinoacetate N-methyltransferase GN=Gamt	18	5	1
Q3UQ44	Ras GTPase-activating-like protein IQGAP2 GN=Iqgap2	2	5	1
Q8CJ40	Rootletin GN=Crocc	3	5	5
Q9QXS1	Plectin GN=Plec	1	4	4
Q9Z1N2	Origin recognition complex subunit 1 GN=Orc1	2	4	1
P60710	Actin, cytoplasmic 1 GN=Actb	14	4	4
Q8R1A4	Dedicator of cytokinesis protein 7 GN=Dock7	1	3	1
Q8VBS7	Vomeronasal type-1 receptor 42 GN=Vmn1r42	4	2	1
Q8R3F5	Malonyl-CoA-acyl carrier protein transacylase, mitochondrial GN=Mcat	8	2	1
P62983	Ubiquitin-40S ribosomal protein S27a GN=Rps27a	16	2	2

Q922B9	Protein ITPRID2 GN=Itprid2	2	2	2
Q8VDN2	Sodium/potassium-transporting ATPase subunit alpha-1 GN=Atp1a1	3	2	2
Q8BI84	Transport and Golgi organization protein 1 homolog GN=Mia3	1	2	1
Q8BFZ2	Phospholipid phosphatase-related protein type 1 GN=Plppr1	3	2	1
P02535	Keratin, type I cytoskeletal 10 GN=Krt10	2	1	1
P11881	Inositol 1,4,5-trisphosphate receptor type 1 GN=Itpr1	0	1	1
A7L9Z8	Calcium-transporting ATPase type 2C member 2 GN=Atp2c2	1	1	1
Q02788	Collagen alpha-2(VI) chain GN=Col6a2	2	1	1
Q8CIE6	Coatomer subunit alpha GN=Copa	1	1	1
Q3V132	ADP/ATP translocase 4 GN=Slc25a31	3	1	1
Q61194	Phosphatidylinositol 4-phosphate 3-kinase C2 domain-containing subunit alpha GN=Pik3c2a	1	1	1
Q7TT50	Serine/threonine-protein kinase MRCK beta GN=Cdc42bpb	1	1	1
Q8VDJ3	Vigilin GN=Hdlbp	1	1	1
Q8CB62	Centrobin GN=Cntrob	2	1	1
Q3USF0	Acetylgalactosaminyl-O-glycosyl-glycoprotein beta-1,3-N-acetylglucosaminyltransferase GN=B3gnt6	2	1	1
Q9QXN0	Protein Shroom3 GN=Shroom3	2	1	1
P04104	Keratin, type II cytoskeletal 1 GN=Krt1	2	1	1
Q05D44	Eukaryotic translation initiation factor 5B GN=Eif5b	1	1	1
Q91XI1	tRNA-dihydrouridine(47) synthase [NAD(P)(+)]-like GN=Dus3l	1	1	1
Q5SQX6	Cytoplasmic FMR1-interacting protein 2 GN=Cyfip2	1	1	1
Q9CYK1	Tryptophan--tRNA ligase, mitochondrial GN=Wars2	4	1	1
O54774	AP-3 complex subunit delta-1 GN=Ap3d1	1	1	1
P55014	Solute carrier family 12 member 1 GN=Slc12a1	1	1	1
Q3UV17	Keratin, type II cytoskeletal 2 oral GN=Krt76	2	1	1
P97449	Aminopeptidase N GN=Anpep	1	1	1
O88712	C-terminal-binding protein 1 GN=Ctbp1	6	1	1

Table 7.2 – Adult Kidney IgG 1 (~150-250 kDa)

Accession	Description	Coverage [%]	# PSMs	# Unique Peptides
Q8VDD5	Myosin-9 GN=Myh9	15	27	19
O08638	Myosin-11 GN=Myh11	4	9	2
Q61879	Myosin-10 GN=Myh10	4	8	1
Q62261	Spectrin beta chain, non-erythrocytic 1 GN=Sptbn1	3	6	6
P02535	Keratin, type I cytoskeletal 10 GN=Krt10	8	6	5
Q922U2	Keratin, type II cytoskeletal 5 GN=Krt5	8	6	3
Q68FD5	Clathrin heavy chain 1 GN=Cltc	4	5	5
P04104	Keratin, type II cytoskeletal 1 GN=Krt1	5	5	2
Q6IFX2	Keratin, type I cytoskeletal 42 GN=Krt42	10	4	2
Q3TTY5	Keratin, type II cytoskeletal 2 epidermal GN=Krt2	4	3	2
Q61781	Keratin, type I cytoskeletal 14 GN=Krt14	6	3	1
Q8VED5	Keratin, type II cytoskeletal 79 GN=Krt79	5	3	1
P16546	Spectrin alpha chain, non-erythrocytic 1 GN=Sptan1	1	3	3
P60710	Actin, cytoplasmic 1 GN=Actb	9	3	3
Q3UV17	Keratin, type II cytoskeletal 2 oral GN=Krt76	3	2	1
Q6P5H2	Nestin GN=Nes	0	1	1
Q8BFU3	RING finger protein 214 GN=Rnf214	1	1	1
Q1H9T6	Telomere zinc finger-associated protein GN=Zbtb48	3	1	1
P01027	Complement C3 GN=C3	0	1	1
O08852	Polycystin-1 GN=Pkd1	0	1	1

Table 7.3 – Adult Kidney IP 2 (~100-130 kDa)

Accession	Description	Coverage [%]	# PSMs	# Unique Peptides
Q9WTI7	Unconventional myosin-Ic GN=Myo1c	45	92	44
Q5SYD0	Unconventional myosin-Id GN=Myo1d	46	56	44
Q64331	Unconventional myosin-VI GN=Myo6	27	52	31
P46735	Unconventional myosin-Ib GN=Myo1b	30	39	33
Q62468	Villin-1 GN=Vil1	38	38	31
E9Q634	Unconventional myosin-Ie GN=Myo1e	21	27	25
O35245	Polycystin-2 GN=Pkd2	24	24	19
Q8VDD5	Myosin-9 GN=Myh9	12	24	22
Q9Z1T1	AP-3 complex subunit beta-1 GN=Ap3b1	18	20	20
Q05920	Pyruvate carboxylase, mitochondrial GN=Pc	16	18	17
Q922D8	C-1-tetrahydrofolate synthase, cytoplasmic GN=Mthfd1	17	17	16
Q9DBG3	AP-2 complex subunit beta GN=Ap2b1	15	14	13
Q6ZQ38	Cullin-associated NEDD8-dissociated protein 1 GN=Cand1	11	13	13
P21271	Unconventional myosin-Vb GN=Myo5b	7	13	13
Q8VDN2	Sodium/potassium-transporting ATPase subunit alpha-1 GN=Atp1a1	12	11	11
P28660	Nck-associated protein 1 GN=Nckap1	8	11	10
Q6P542	ATP-binding cassette sub-family F member 1 GN=Abcf1	11	10	8
Q04857	Collagen alpha-1(VI) chain GN=Col6a1	10	10	9
P17710	Hexokinase-1 GN=Hk1	11	10	10
P97479	Unconventional myosin-VIIa GN=Myo7a	4	10	9
P57780	Alpha-actinin-4 GN=Actn4	11	10	8
P60710	Actin, cytoplasmic 1 GN=Actb	29	10	9
Q5SV80	Unconventional myosin-XIX GN=Myo19	10	9	8
Q3U1J4	DNA damage-binding protein 1 GN=Ddb1	8	9	9
Q78PY7	Staphylococcal nuclease domain-containing protein 1 GN=Snd1	8	8	8
O88343	Electrogenic sodium bicarbonate cotransporter 1 GN=Slc4a4	7	8	8
Q68FD5	Clathrin heavy chain 1 GN=Cltc	4	7	6
P55014	Solute carrier family 12 member 1 GN=Slc12a1	6	7	7
P02535	Keratin, type I cytoskeletal 10 GN=Krt10	9	6	5
Q60597	2-oxoglutarate dehydrogenase, mitochondrial GN=Ogdh	4	5	5
Q9ESJ0	Exportin-4 GN=Xpo4	4	5	5
Q9JKY5	Huntingtin-interacting protein 1-related protein GN=Hip1r	4	5	5
Q8K2V1	Serine/threonine-protein phosphatase 4 regulatory subunit 1 GN=Ppp4r1	7	5	5
P97434	Myosin phosphatase Rho-interacting protein GN=Mprip	5	5	5
Q7TQG1	Pleckstrin homology domain-containing family A member 6 GN=Plekha6	5	5	5
P04104	Keratin, type II cytoskeletal 1 GN=Krt1	5	4	3
Q68FH0	Plakophilin-4 GN=Pkp4	4	4	4
Q99MR6	Serrate RNA effector molecule homolog GN=Srrt	5	4	4
E9QAT4	Protein transport protein Sec16A GN=Sec16a	2	4	4
Q8BZ60	Stonin-2 GN=Ston2	6	4	4

P19001	Keratin, type I cytoskeletal 19 GN=Krt19	9	4	2
Q8CC88	von Willebrand factor A domain-containing protein 8 GN=Vwa8	2	3	3
Q8VD75	Huntingtin-interacting protein 1 GN=Hip1	2	3	3
Q924C1	Exportin-5 GN=Xpo5	2	3	3
B2RY56	RNA-binding protein 25 GN=Rbm25	5	3	3
Q80U95	Ubiquitin-protein ligase E3C GN=Ube3c	3	3	3
O35382	Exocyst complex component 4 GN=Exoc4	4	3	3
P28843	Dipeptidyl peptidase 4 GN=Dpp4	4	3	3
Q6NV83	U2 snRNP-associated SURP motif-containing protein GN=U2surp	3	3	3
P09803	Cadherin-1 GN=Cdh1	4	3	3
P42567	Epidermal growth factor receptor substrate 15 GN=Eps15	3	3	3
Q6IFX2	Keratin, type I cytoskeletal 42 GN=Krt42	6	3	1
Q3UV17	Keratin, type II cytoskeletal 2 oral GN=Krt76	3	2	1
Q6PDG5	SWI/SNF complex subunit SMARCC2 GN=Smarcc2	1	2	2
Q69ZB8	Zinc finger CCHC domain-containing protein 2 GN=Zcchc2	3	2	1
O08810	116 kDa U5 small nuclear ribonucleoprotein component GN=Eftud2	2	2	2
Q91X17	Uromodulin GN=Umod	3	2	2
P62983	Ubiquitin-40S ribosomal protein S27a GN=Rps27a	16	2	2
P24547	Inosine-5'-monophosphate dehydrogenase 2 GN=Impdh2	4	2	2
P17426	AP-2 complex subunit alpha-1 GN=Ap2a1	2	2	2
Q3TTY5	Keratin, type II cytoskeletal 2 epidermal GN=Krt2	3	2	1
Q61768	Kinesin-1 heavy chain GN=Kif5b	2	2	2
Q569Z5	Probable ATP-dependent RNA helicase DDX46 GN=Ddx46	2	2	2
Q922U2	Keratin, type II cytoskeletal 5 GN=Krt5	3	2	1
F8VPU2	FERM, ARHGEF and pleckstrin domain-containing protein 1 GN=Farp1	2	2	2
Q8CGK3	Lon protease homolog, mitochondrial GN=Lonp1	2	2	2
Q99MZ6	Unconventional myosin-VIIb GN=Myo7b	1	2	1
Q61559	IgG receptor FcRn large subunit p51 GN=Fcgrt	8	2	1
Q5U3K5	Rab-like protein 6 GN=Rabl6	2	2	2
Q05D44	Eukaryotic translation initiation factor 5B GN=Eif5b	1	2	2
Q7TMC8	L-fucose kinase GN=Fcsk	2	2	2
P16546	Spectrin alpha chain, non-erythrocytic 1 GN=Sptan1	1	2	2
Q922B9	Protein ITPRID2 GN=Itprid2	2	2	2
Q6A4J8	Ubiquitin carboxyl-terminal hydrolase 7 GN=Usp7	1	1	1
Q8R1A4	Dedicator of cytokinesis protein 7 GN=Dock7	0	1	1
Q8K382	DENN domain-containing protein 1A GN=Dennd1a	1	1	1
Q8R307	Vacuolar protein sorting-associated protein 18 homolog GN=Vps18	1	1	1
Q9JMH9	Unconventional myosin-XVIIIa GN=Myo18a	0	1	1
Q9R1C7	Pre-mRNA-processing factor 40 homolog A GN=Prpf40a	1	1	1
P97290	Plasma protease C1 inhibitor GN=Serping1	2	1	1
P05213	Tubulin alpha-1B chain GN=Tuba1b	2	1	1
Q3V132	ADP/ATP translocase 4 GN=Slc25a31	3	1	1

Q8BYF6	Sodium-coupled monocarboxylate transporter 1 GN=Slc5a8	2	1	1
Q62266	Cornifin-A GN=Sprr1a	17	1	1
Q8CG16	Complement C1r-A subcomponent GN=C1ra	2	1	1
Q9EP71	Ankycorbin GN=Rai14	1	1	1
Q5F2E8	Serine/threonine-protein kinase TAO1 GN=Taok1	1	1	1
Q91WL5	Cytochrome P450 4A12A GN=Cyp4a12a	2	1	1
Q62261	Spectrin beta chain, non-erythrocytic 1 GN=Sptbn1	0	1	1
Q8CGZ0	Calcium homeostasis endoplasmic reticulum protein GN=Cherp	1	1	1
Q8R1B4	Eukaryotic translation initiation factor 3 subunit C GN=Eif3c	1	1	1
P30999	Catenin delta-1 GN=Ctnnd1	1	1	1
P97326	Cadherin-6 GN=Cdh6	2	1	1
Q3UM83	Killer cell lectin-like receptor subfamily G member 2 GN=Klrg2	6	1	1
Q9CZU3	Exosome RNA helicase MTR4 GN=Mtrex	1	1	1
O55143	Sarcoplasmic/endoplasmic reticulum calcium ATPase 2 GN=Atp2a2	1	1	1
P59158	Solute carrier family 12 member 3 GN=Slc12a3	1	1	1
Q8R5F7	Interferon-induced helicase C domain-containing protein 1 GN=Ifih1	1	1	1
Q01149	Collagen alpha-2(I) chain GN=Col1a2	1	1	1
Q91ZW3	SWI/SNF-related matrix-associated actin-dependent regulator of chromatin subfamily A member 5 GN=Smarca5	1	1	1
Q9EPK7	Exportin-7 GN=Xpo7	1	1	1
E0CYV9	Uncharacterized protein C4orf54 homolog	1	1	1

Table 7.4 – Adult Kidney IgG 2 (~100-130 kDa)

Accession	Description	Coverage [%]	# PSMs	# Unique Peptides
P02535	Keratin, type I cytoskeletal 10 GN=Krt10	12	10	7
Q922U2	Keratin, type II cytoskeletal 5 GN=Krt5	14	8	4
Q62468	Villin-1 GN=Vil1	7	5	5
P04104	Keratin, type II cytoskeletal 1 GN=Krt1	5	5	2
Q9WTI7	Unconventional myosin-Ic GN=Myo1c	3	4	4
Q3UV17	Keratin, type II cytoskeletal 2 oral GN=Krt76	6	4	1
Q9QWL7	Keratin, type I cytoskeletal 17 GN=Krt17	8	4	2
Q6IFX2	Keratin, type I cytoskeletal 42 GN=Krt42	8	4	2
Q6NXH9	Keratin, type II cytoskeletal 73 GN=Krt73	7	4	1
Q3TTY5	Keratin, type II cytoskeletal 2 epidermal GN=Krt2	5	4	2
P08883	Granzyme F GN=Gzmf	8	3	1
P97290	Plasma protease C1 inhibitor GN=Serping1	6	3	3
P60710	Actin, cytoplasmic 1 GN=Actb	9	3	3
P13020	Gelsolin GN=Gsn	3	3	3
Q8VED5	Keratin, type II cytoskeletal 79 GN=Krt79	5	3	1
P01029	Complement C4-B GN=C4b	1	2	2
Q9D3R6	Katanin p60 ATPase-containing subunit A-like 2 GN=Katnal2	4	1	1
Q9QYX7	Protein piccolo GN=Pclo	0	1	1
P17897	Lysozyme C-1 GN=Lyz1	8	1	1
P07724	Serum albumin GN=Alb	2	1	1
P01027	Complement C3 GN=C3	0	1	1

Table 7.5 – Adult Kidney IP 3 (~75-90 kDa)

Accession	Description	Coverage [%]	# PSMs	# Unique Peptides
Q62468	Villin-1 GN=Vil1	61	131	46
O35245	Polycystin-2 GN=Pkd2	38	72	35
P13020	Gelsolin GN=Gsn	43	62	25
Q8VDN2	Sodium/potassium-transporting ATPase subunit alpha-1 GN=Atp1a1	39	57	23
P57780	Alpha-actinin-4 GN=Actn4	59	46	26
Q60604	Adseverin GN=Scin	52	38	29
Q5SYD0	Unconventional myosin-Id GN=Myo1d	34	37	30
P17427	AP-2 complex subunit alpha-2 GN=Ap2a2	36	33	20
Q9DBG3	AP-2 complex subunit beta GN=Ap2b1	36	32	28
P17426	AP-2 complex subunit alpha-1 GN=Ap2a1	36	30	20
Q9WTI7	Unconventional myosin-Ic GN=Myo1c	30	28	27
P11499	Heat shock protein HSP 90-beta GN=Hsp90ab1	32	28	13
Q920R6	V-type proton ATPase 116 kDa subunit a isoform 4 GN=Atp6v0a4	27	27	20
Q7TPR4	Alpha-actinin-1 GN=Actn1	30	27	9
Q6PIE5	Sodium/potassium-transporting ATPase subunit alpha-2 GN=Atp1a2	17	24	1
O55143	Sarcoplasmic/endoplasmic reticulum calcium ATPase 2 GN=Atp2a2	26	24	22
Q8CAQ8	MICOS complex subunit Mic60 GN=Immt	32	23	18
Q8CG16	Complement C1r-A subcomponent GN=C1ra	31	20	16
Q99MZ6	Unconventional myosin-VIIb GN=Myo7b	8	19	16
P26231	Catenin alpha-1 GN=Ctnna1	25	18	18
Q8CG14	Complement C1s-A subcomponent GN=C1sa	30	17	17
P07901	Heat shock protein HSP 90-alpha GN=Hsp90aa1	20	17	4
Q02248	Catenin beta-1 GN=Ctnnb1	25	16	15
Q68FD5	Clathrin heavy chain 1 GN=Cltc	11	16	15
Q8VDD5	Myosin-9 GN=Myh9	9	15	14
Q91YD6	Villin-like protein GN=Vill	21	14	14
P60710	Actin, cytoplasmic 1 GN=Actb	35	14	5
Q9QXS6	Drebrin GN=Dbn1	20	14	12
P17710	Hexokinase-1 GN=Hk1	16	14	14
P58252	Elongation factor 2 GN=Eef2	16	13	12
P58281	Dynamin-like 120 kDa protein, mitochondrial GN=Opa1	14	13	12
O55029	Coatomer subunit beta' GN=Copb2	16	12	12
Q7TPW1	Nexilin GN=Nexn	15	11	11
Q9ERG0	LIM domain and actin-binding protein 1 GN=Lima1	19	10	10
O88343	Electrogenic sodium bicarbonate cotransporter 1 GN=Slc4a4	9	9	9
Q99KI0	Aconitate hydratase, mitochondrial GN=Aco2	14	9	8
P09405	Nucleolin GN=Ncl	12	9	9
P68033	Actin, alpha cardiac muscle 1 GN=Actc1	22	8	1
Q68FH0	Plakophilin-4 GN=Pkp4	8	8	8
Q64331	Unconventional myosin-VI GN=Myo6	6	8	8
Q9QZE5	Coatomer subunit gamma-1 GN=Copg1	10	8	6

P30999	Catenin delta-1 GN=Ctnnd1	9	7	7
P28825	Meprin A subunit alpha GN=Mep1a	10	7	6
P98078	Disabled homolog 2 GN=Dab2	12	7	7
Q8R0Y6	Cytosolic 10-formyltetrahydrofolate dehydrogenase GN=Aldh1l1	8	7	7
P47857	ATP-dependent 6-phosphofructokinase, muscle type GN=Pfkm	10	7	7
E9Q634	Unconventional myosin-Ie GN=Myo1e	6	6	6
Q80XL6	Acyl-CoA dehydrogenase family member 11 GN=Acad11	8	6	6
Q3UQN2	F-BAR domain only protein 2 GN=Fcho2	10	6	6
P04919	Band 3 anion transport protein GN=Slc4a1	7	6	6
Q9ERK4	Exportin-2 GN=Cse1l	6	6	6
Q99KC8	von Willebrand factor A domain-containing protein 5A GN=Vwa5a	7	6	5
O88338	Cadherin-16 GN=Cdh16	11	6	6
Q8BMS1	Trifunctional enzyme subunit alpha, mitochondrial GN=Hadha	8	6	6
Q811U4	Mitofusin-1 GN=Mfn1	7	5	5
Q9JIF7	Coatomer subunit beta GN=Copb1	7	5	5
Q9QYC0	Alpha-adducin GN=Add1	9	5	5
P39054	Dynamin-2 GN=Dnm2	5	5	5
Q9QXK3	Coatomer subunit gamma-2 GN=Copg2	5	4	3
P05784	Keratin, type I cytoskeletal 18 GN=Krt18	9	4	3
Q8VDM4	26S proteasome non-ATPase regulatory subunit 2 GN=Psmd2	6	4	4
P21271	Unconventional myosin-Vb GN=Myo5b	2	4	4
Q9EQK5	Major vault protein GN=Mvp	5	4	4
P02535	Keratin, type I cytoskeletal 10 GN=Krt10	7	4	3
Q6P2B1	Transportin-3 GN=Tnpo3	4	4	4
Q9Z1T1	AP-3 complex subunit beta-1 GN=Ap3b1	3	4	4
P04104	Keratin, type II cytoskeletal 1 GN=Krt1	5	4	3
P08113	Endoplasmin GN=Hsp90b1	5	4	3
Q9EP71	Ankycorbin GN=Rai14	4	3	3
P48962	ADP/ATP translocase 1 GN=Slc25a4	9	3	3
Q8JZQ9	Eukaryotic translation initiation factor 3 subunit B GN=Eif3b	4	3	3
Q9WUA3	ATP-dependent 6-phosphofructokinase, platelet type GN=Pfkp	3	3	3
Q91X17	Uromodulin GN=Umod	4	3	3
Q91VR5	ATP-dependent RNA helicase DDX1 GN=Ddx1	4	3	3
P55014	Solute carrier family 12 member 1 GN=Slc12a1	1	2	2
Q91XT6	Tandem C2 domains nuclear protein GN=Tc2n	5	2	1
Q8BML9	Glutamine--tRNA ligase GN=Qars	2	2	2
P70168	Importin subunit beta-1 GN=Kpnb1	2	2	2
Q8R1U1	Conserved oligomeric Golgi complex subunit 4 GN=Cog4	3	2	2
Q3TL44	NLR family member X1 GN=Nlrx1	2	2	2
Q8CI94	Glycogen phosphorylase, brain form GN=Pygb	2	2	2
Q9Z1G4	V-type proton ATPase 116 kDa subunit a isoform 1 GN=Atp6v0a1	2	2	1
Q8R313	Exocyst complex component 6 GN=Exoc6	2	2	2

B1AVD1	Xaa-Pro aminopeptidase 2 GN=Xpnpep2	3	2	2
Q62172	RalA-binding protein 1 GN=Ralbp1	3	2	2
Q8BTM8	Filamin-A GN=Flna	1	2	2
Q922U2	Keratin, type II cytoskeletal 5 GN=Krt5	3	2	1
Q8CGK3	Lon protease homolog, mitochondrial GN=Lonp1	2	2	2
Q9QYB5	Gamma-adducin GN=Add3	3	2	2
P01872	Immunoglobulin heavy constant mu GN=Ighm	4	2	2
Q8CIE6	Coatomer subunit alpha GN=Copa	2	2	2
Q61847	Meprin A subunit beta GN=Mep1b	3	2	2
P26039	Talin-1 GN=Tln1	1	1	1
Q5SV80	Unconventional myosin-XIX GN=Myo19	1	1	1
Q9ES07	Solute carrier family 15 member 2 GN=Slc15a2	1	1	1
Q8VHE0	Translocation protein SEC63 homolog GN=Sec63	1	1	1
Q99MQ1	Protein bicaudal C homolog 1 GN=Bicc1	2	1	1
P62046	Leucine-rich repeat and calponin homology domain-containing protein 1 GN=Lrch1	2	1	1
Q68FL6	Methionine--tRNA ligase, cytoplasmic GN=Mars	1	1	1
P16858	Glyceraldehyde-3-phosphate dehydrogenase GN=Gapdh	5	1	1
P60330	Separin GN=Espl1	0	1	1
G5E8K5	Ankyrin-3 GN=Ank3	1	1	1
Q9QY23	Plakophilin-3 GN=Pkp3	5	1	1
B2RY56	RNA-binding protein 25 GN=Rbm25	2	1	1
P10852	4F2 cell-surface antigen heavy chain GN=Slc3a2	2	1	1
Q8JZQ2	AFG3-like protein 2 GN=Afg3l2	1	1	1
Q7TQG1	Pleckstrin homology domain-containing family A member 6 GN=Plekha6	1	1	1
Q922B9	Protein ITPRID2 GN=Itprid2	1	1	1
P16460	Argininosuccinate synthase GN=Ass1	2	1	1
O54781	SRSF protein kinase 2 GN=Srpk2	1	1	1
Q8BZI0	Actin filament-associated protein 1-like 1 GN=Afap1l1	1	1	1
Q6KAR6	Exocyst complex component 3 GN=Exoc3	1	1	1
P62983	Ubiquitin-40S ribosomal protein S27a GN=Rps27a	6	1	1
Q8CGU1	Calcium-binding and coiled-coil domain-containing protein 1 GN=Calcoco1	2	1	1
P11438	Lysosome-associated membrane glycoprotein 1 GN=Lamp1	3	1	1
Q8BG67	Protein EFR3 homolog A GN=Efr3a	1	1	1
Q91WV7	Neutral and basic amino acid transport protein rBAT GN=Slc3a1	2	1	1
Q8CCJ3	E3 UFM1-protein ligase 1 GN=Ufl1	1	1	1
P05213	Tubulin alpha-1B chain GN=Tuba1b	2	1	1
Q99PL5	Ribosome-binding protein 1 GN=Rrbp1	1	1	1
Q9JLF6	Protein-glutamine gamma-glutamyltransferase K GN=Tgm1	1	1	1
Q61584	Fragile X mental retardation syndrome-related protein 1 GN=Fxr1	1	1	1

Table 7.6 – Adult Kidney IgG 3 (~75-90 kDa)

Accession	Description	Coverage [%]	# PSMs	# Unique Peptides
P60710	Actin, cytoplasmic 1 GN=Actb	57	42	1
P63260	Actin, cytoplasmic 2 GN=Actg1	57	42	1
P62737	Actin, aortic smooth muscle GN=Acta2	36	26	5
Q8CG16	Complement C1r-A subcomponent GN=C1ra	29	19	14
Q8CG14	Complement C1s-A subcomponent GN=C1sa	31	17	16
Q8BFZ3	Beta-actin-like protein 2 GN=Actbl2	23	14	2
P05064	Fructose-bisphosphate aldolase A GN=Aldoa	17	8	7
P07310	Creatine kinase M-type GN=Ckm	20	7	6
Q8CHW4	Translation initiation factor eIF-2B subunit epsilon GN=Eif2b5	10	6	6
P01872	Immunoglobulin heavy constant mu GN=Ighm	13	6	6
Q62468	Villin-1 GN=Vil1	8	6	6
P21550	Beta-enolase GN=Eno3	14	5	5
Q3TTY5	Keratin, type II cytoskeletal 2 epidermal GN=Krt2	5	4	2
Q922U2	Keratin, type II cytoskeletal 5 GN=Krt5	6	4	1
P07724	Serum albumin GN=Alb	6	4	3
P16858	Glyceraldehyde-3-phosphate dehydrogenase GN=Gapdh	17	4	4
Q6IFZ6	Keratin, type II cytoskeletal 1b GN=Krt77	7	4	1
P02535	Keratin, type I cytoskeletal 10 GN=Krt10	5	3	3
P52480	Pyruvate kinase PKM GN=Pkm	6	3	3
Q9JHJ0	Tropomodulin-3 GN=Tmod3	11	3	3
P04104	Keratin, type II cytoskeletal 1 GN=Krt1	5	3	1
P06151	L-lactate dehydrogenase A chain GN=Ldha	7	2	2
P13020	Gelsolin GN=Gsn	2	2	2
P17751	Triosephosphate isomerase GN=Tpi1	9	2	2
P58771	Tropomyosin alpha-1 chain GN=Tpm1	7	2	2
O70250	Phosphoglycerate mutase 2 GN=Pgam2	8	2	2
Q8VDN2	Sodium/potassium-transporting ATPase subunit alpha-1 GN=Atp1a1	2	2	2
P01787	Ig heavy chain V regions TEPC 15/S107/HPCM1/HPCM2/HPCM3	9	1	1
Q01149	Collagen alpha-2(I) chain GN=Col1a2	1	1	1
P11087	Collagen alpha-1(I) chain GN=Col1a1	2	1	1
Q9ET01	Glycogen phosphorylase, liver form GN=Pygl	1	1	1
P16015	Carbonic anhydrase 3 GN=Ca3	3	1	1

Table 7.7 – Adult Kidney IP 4 (~37-42 kDa)

Accession	Description	Coverage [%]	# PSMs	# Unique Peptides
P60710	Actin, cytoplasmic 1 GN=Actb	77	122	1
P63260	Actin, cytoplasmic 2 GN=Actg1	77	121	1
P62737	Actin, aortic smooth muscle GN=Acta2	55	47	7
Q8BFZ3	Beta-actin-like protein 2 GN=Actbl2	30	30	5
Q9JHJ0	Tropomodulin-3 GN=Tmod3	39	18	11
P19001	Keratin, type I cytoskeletal 19 GN=Krt19	35	16	12
P61161	Actin-related protein 2 GN=Actr2	27	10	9
Q8BFZ9	Erlin-2 GN=Erlin2	16	5	5
Q9Z2I9	Succinate--CoA ligase [ADP-forming] subunit beta, mitochondrial GN=Sucla2	11	5	5
P30275	Creatine kinase U-type, mitochondrial GN=Ckmt1	19	5	5
P45952	Medium-chain specific acyl-CoA dehydrogenase, mitochondrial GN=Acadm	11	4	4
P05784	Keratin, type I cytoskeletal 18 GN=Krt18	10	4	3
O55028	[3-methyl-2-oxobutanoate dehydrogenase [lipoamide]] kinase, mitochondrial GN=Bckdk	3	3	1
P27659	60S ribosomal protein L3 GN=Rpl3	8	3	3
Q9QXS6	Drebrin GN=Dbn1	7	3	3
Q9R0N0	Galactokinase GN=Galk1	6	2	2
Q9DB77	Cytochrome b-c1 complex subunit 2, mitochondrial GN=Uqcrc2	7	2	2
Q9R112	Sulfide:quinone oxidoreductase, mitochondrial GN=Sqor	6	2	2
Q9DCV7	Keratin, type II cytoskeletal 7 GN=Krt7	4	2	2
P11679	Keratin, type II cytoskeletal 8 GN=Krt8	4	2	2
P16460	Argininosuccinate synthase GN=Ass1	4	2	2
Q99N23	Carbonic anhydrase 15 GN=Ca15	7	2	2
P61620	Protein transport protein Sec61 subunit alpha isoform 1 GN=Sec61a1	4	2	2
O88986	2-amino-3-ketobutyrate coenzyme A ligase, mitochondrial GN=Gcat	6	2	2
P20152	Vimentin GN=Vim	2	1	1
P04104	Keratin, type II cytoskeletal 1 GN=Krt1	2	1	1
Q91Y97	Fructose-bisphosphate aldolase B GN=Aldob	2	1	1
P02535	Keratin, type I cytoskeletal 10 GN=Krt10	2	1	1
P68372	Tubulin beta-4B chain GN=Tubb4b	2	1	1
P55302	Alpha-2-macroglobulin receptor-associated protein GN=Lrpap1	4	1	1
P51174	Long-chain specific acyl-CoA dehydrogenase, mitochondrial GN=Acadl	3	1	1
Q9Z1G3	V-type proton ATPase subunit C 1 GN=Atp6v1c1	3	1	1
Q3V132	ADP/ATP translocase 4 GN=Slc25a31	3	1	1
P58771	Tropomyosin alpha-1 chain GN=Tpm1	5	1	1
Q99M87	DnaJ homolog subfamily A member 3, mitochondrial GN=Dnaja3	3	1	1
P15105	Glutamine synthetase GN=Glul	2	1	1

Table 7.8 – Adult Kidney IgG 4 (~37-42 kDa)

Accession	Description	Coverage [%]	# PSMs	# Unique Peptides
P63260	Actin, cytoplasmic 2 GN=Actg1	62	36	8
P68033	Actin, alpha cardiac muscle 1 GN=Actc1	38	23	4
Q99LD9	Translation initiation factor eIF-2B subunit beta GN=Eif2b2	15	7	6
P02535	Keratin, type I cytoskeletal 10 GN=Krt10	9	6	5
Q922U2	Keratin, type II cytoskeletal 5 GN=Krt5	10	6	3
P04104	Keratin, type II cytoskeletal 1 GN=Krt1	5	4	2
Q3TTY5	Keratin, type II cytoskeletal 2 epidermal GN=Krt2	5	4	2
P51881	ADP/ATP translocase 2 GN=Slc25a5	13	4	4
Q6NXH9	Keratin, type II cytoskeletal 73 GN=Krt73	7	4	1
P08883	Granzyme F GN=Gzmf	8	3	1
Q8VED5	Keratin, type II cytoskeletal 79 GN=Krt79	5	3	1
Q3UPF5	Zinc finger CCCH-type antiviral protein 1 GN=Zc3hav1	3	2	1
Q61781	Keratin, type I cytoskeletal 14 GN=Krt14	4	2	1
P14106	Complement C1q subcomponent subunit B GN=C1qb	10	2	2
Q02105	Complement C1q subcomponent subunit C GN=C1qc	7	1	1
P98086	Complement C1q subcomponent subunit A GN=C1qa	5	1	1
P21107	Tropomyosin alpha-3 chain GN=Tpm3	4	1	1
Q80YF9	Rho GTPase-activating protein 33 GN=Arhgap33	1	1	1
Q91WE6	Threonylcarbamoyladenosine tRNA methylthiotransferase GN=Cdkal1	3	1	1
O54988	STE20-like serine/threonine-protein kinase GN=Slk	1	1	1
Q9D0F6	Replication factor C subunit 5 GN=Rfc5	6	1	1
Q6P5H2	Nestin GN=Nes	0	1	1
P01027	Complement C3 GN=C3	0	1	1
Q9D6Z1	Nucleolar protein 56 GN=Nop56	3	1	1
Q61502	Transcription factor E2F5 GN=E2f5	12	1	1

Table 7.9 – Adult Kidney IP 5 (~26-30 kDa)

Accession	Description	Coverage [%]	# PSMs	# Unique Peptides
P48962	ADP/ATP translocase 1 GN=Slc25a4	47	26	7
P51881	ADP/ATP translocase 2 GN=Slc25a5	45	25	6
P21107	Tropomyosin alpha-3 chain GN=Tpm3	24	20	5
Q6IRU2	Tropomyosin alpha-4 chain GN=Tpm4	42	16	13
Q9QZD8	Mitochondrial dicarboxylate carrier GN=Slc25a10	38	14	10
P58771	Tropomyosin alpha-1 chain GN=Tpm1	19	14	2
Q8VEM8	Phosphate carrier protein, mitochondrial GN=Slc25a3	27	12	8
Q9CR62	Mitochondrial 2-oxoglutarate/malate carrier protein GN=Slc25a11	36	10	8
P50518	V-type proton ATPase subunit E 1 GN=Atp6v1e1	35	9	7
P60710	Actin, cytoplasmic 1 GN=Actb	32	9	8
Q60931	Voltage-dependent anion-selective channel protein 3 GN=Vdac3	38	8	6
P67778	Prohibitin GN=Phb	26	7	7
Q02105	Complement C1q subcomponent subunit C GN=C1qc	22	7	4
P62908	40S ribosomal protein S3 GN=Rps3	40	7	7
Q91VR2	ATP synthase subunit gamma, mitochondrial GN=Atp5f1c	20	7	6
Q60605	Myosin light polypeptide 6 GN=Myl6	48	6	6
P48758	Carbonyl reductase [NADPH] 1 GN=Cbr1	26	6	6
P14106	Complement C1q subcomponent subunit B GN=C1qb	19	6	4
P12970	60S ribosomal protein L7a GN=Rpl7a	22	6	6
P98086	Complement C1q subcomponent subunit A GN=C1qa	17	6	3
P42125	Enoyl-CoA delta isomerase 1, mitochondrial GN=Eci1	24	5	5
Q9CY27	Very-long-chain enoyl-CoA reductase GN=Tecr	14	5	4
Q60930	Voltage-dependent anion-selective channel protein 2 GN=Vdac2	25	5	5
Q9WVD5	Mitochondrial ornithine transporter 1 GN=Slc25a15	18	5	5
Q8JZU2	Tricarboxylate transport protein, mitochondrial GN=Slc25a1	14	4	4
Q9DCW4	Electron transfer flavoprotein subunit beta GN=Etfb	21	4	4
P10126	Elongation factor 1-alpha 1 GN=Eef1a1	8	4	4
O08585	Clathrin light chain A GN=Clta	11	4	3
P12242	Mitochondrial brown fat uncoupling protein 1 GN=Ucp1	15	4	4
P57746	V-type proton ATPase subunit D GN=Atp6v1d	18	3	3
P14869	60S acidic ribosomal protein P0 GN=Rplp0	10	3	3
Q6IRU5	Clathrin light chain B GN=Cltb	12	3	3
P24369	Peptidyl-prolyl cis-trans isomerase B GN=Ppib	14	3	3
Q9Z1Q5	Chloride intracellular channel protein 1 GN=Clic1	12	3	3
P04104	Keratin, type II cytoskeletal 1 GN=Krt1	4	3	3
Q791V5	Mitochondrial carrier homolog 2 GN=Mtch2	14	3	3
P62754	40S ribosomal protein S6 GN=Rps6	13	3	3
P62702	40S ribosomal protein S4, X isoform GN=Rps4x	8	3	3
P63038	60 kDa heat shock protein, mitochondrial GN=Hspd1	5	2	2
Q922U2	Keratin, type II cytoskeletal 5 GN=Krt5	4	2	2
P02535	Keratin, type I cytoskeletal 10 GN=Krt10	4	2	2

Q9D4J1	EF-hand domain-containing protein D1 GN=Efhd1	9	2	2
P62259	14-3-3 protein epsilon GN=Ywhae	9	2	2
P16858	Glyceraldehyde-3-phosphate dehydrogenase GN=Gapdh	9	2	2
Q3TTY5	Keratin, type II cytoskeletal 2 epidermal GN=Krt2	3	2	2
Q60932	Voltage-dependent anion-selective channel protein 1 GN=Vdac1	7	2	1
P62918	60S ribosomal protein L8 GN=Rpl8	11	2	2
P63158	High mobility group protein B1 GN=Hmgb1	13	2	2
Q9D0M3	Cytochrome c1, heme protein, mitochondrial GN=Cyc1	8	2	2
Q9Z2Z6	Mitochondrial carnitine/acylcarnitine carrier protein GN=Slc25a20	7	2	2
P97351	40S ribosomal protein S3a GN=Rps3a	6	2	2
Q91UZ4	Egl nine homolog 3 GN=Egln3	5	1	1
P47757	F-actin-capping protein subunit beta GN=Capzb	5	1	1
E9PV24	Fibrinogen alpha chain GN=Fga	1	1	1
P63101	14-3-3 protein zeta/delta GN=Ywhaz	6	1	1
P68254	14-3-3 protein theta GN=Ywhaq	6	1	1
Q8CFJ7	Solute carrier family 25 member 45 GN=Slc25a45	3	1	1
Q91W52	Transmembrane protein 19 GN=Tmem19	4	1	1
Q9CX56	26S proteasome non-ATPase regulatory subunit 8 GN=Psmd8	3	1	1
O09172	Glutamate--cysteine ligase regulatory subunit GN=Gclm	5	1	1
P47758	Signal recognition particle receptor subunit beta GN=Srprb	3	1	1
O35682	Myeloid-associated differentiation marker GN=Myadm	5	1	1
Q8BI08	Protein MAL2 GN=Mal2	6	1	1
P61982	14-3-3 protein gamma GN=Ywhag	4	1	1
O70503	Very-long-chain 3-oxoacyl-CoA reductase GN=Hsd17b12	3	1	1
Q78KK3	Solute carrier family 22 member 18 GN=Slc22a18	3	1	1
P25444	40S ribosomal protein S2 GN=Rps2	4	1	1
P70122	Ribosome maturation protein SBDS GN=Sbds	3	1	1
O70433	Four and a half LIM domains protein 2 GN=Fhl2	4	1	1
Q9CXI0	2-methoxy-6-polyprenyl-1,4-benzoquinol methylase, mitochondrial GN=Coq5	4	1	1
Q6TCG2	Membrane progesterone receptor epsilon GN=Paqr9	3	1	1
Q3UV17	Keratin, type II cytoskeletal 2 oral GN=Krt76	2	1	1
Q5SWT3	Solute carrier family 25 member 35 GN=Slc25a35	3	1	1
P01867	Ig gamma-2B chain C region GN=Igh-3	2	1	1

Table 7.10 – Adult Kidney IgG 5 (~26-30 kDa)

Accession	Description	Coverage [%]	# PSMs	# Unique Peptides
P98086	Complement C1q subcomponent subunit A GN=C1qa	22	8	4
P14106	Complement C1q subcomponent subunit B GN=C1qb	19	6	4
Q922U2	Keratin, type II cytoskeletal 5 GN=Krt5	7	5	3
Q02105	Complement C1q subcomponent subunit C GN=C1qc	20	5	4
P04104	Keratin, type II cytoskeletal 1 GN=Krt1	6	4	2
P51881	ADP/ATP translocase 2 GN=Slc25a5	12	4	4
P39038	Cadherin-4 GN=Cdh4	4	4	1
Q3THE2	Myosin regulatory light chain 12B GN=Myl12b	18	3	3
Q61414	Keratin, type I cytoskeletal 15 GN=Krt15	5	3	1
P02535	Keratin, type I cytoskeletal 10 GN=Krt10	4	3	1
Q61781	Keratin, type I cytoskeletal 14 GN=Krt14	6	3	1
Q3TTY5	Keratin, type II cytoskeletal 2 epidermal GN=Krt2	4	3	1
A6BLY7	Keratin, type I cytoskeletal 28 GN=Krt28	3	2	1
P03987	Ig gamma-3 chain C region	2	1	1
Q80U57	Regulating synaptic membrane exocytosis protein 3 GN=Rims3	7	1	1
P70174	Histamine H1 receptor GN=Hrh1	8	1	1
P21107	Tropomyosin alpha-3 chain GN=Tpm3	2	1	1
Q6TDP3	Kelch-like protein 17 GN=Klhl17	5	1	1
P01864	Ig gamma-2A chain C region secreted form	2	1	1

Table 7.11 – Adult Kidney IP 6 (~17-20 kDa)

Accession	Description	Coverage [%]	# PSMs	# Unique Peptides
Q3THE2	Myosin regulatory light chain 12B GN=Myl12b	51	41	3
Q9CQ19	Myosin regulatory light polypeptide 9 GN=Myl9	63	38	4
P0DP27	Calmodulin-2 GN=Calm2	52	11	7
P24369	Peptidyl-prolyl cis-trans isomerase B GN=Ppib	37	10	8
P59999	Actin-related protein 2/3 complex subunit 4 GN=Arpc4	23	9	4
P62281	40S ribosomal protein S11 GN=Rps11	45	9	9
Q60605	Myosin light polypeptide 6 GN=Myl6	38	8	6
P35700	Peroxiredoxin-1 GN=Prdx1	32	7	7
P02535	Keratin, type I cytoskeletal 10 GN=Krt10	12	7	6
P41105	60S ribosomal protein L28 GN=Rpl28	32	5	5
Q6IRU5	Clathrin light chain B GN=Cltb	19	5	5
P61205	ADP-ribosylation factor 3 GN=Arf3	24	5	2
P18760	Cofilin-1 GN=Cfl1	34	5	4
P84084	ADP-ribosylation factor 5 GN=Arf5	21	5	2
O35245	Polycystin-2 GN=Pkd2	6	4	4
P04104	Keratin, type II cytoskeletal 1 GN=Krt1	5	4	3
P14115	60S ribosomal protein L27a GN=Rpl27a	28	4	4
P35979	60S ribosomal protein L12 GN=Rpl12	24	4	3
Q9D898	Actin-related protein 2/3 complex subunit 5-like protein GN=Arpc5l	22	4	3
Q922U2	Keratin, type II cytoskeletal 5 GN=Krt5	7	4	3
Q9R0P5	Destrin GN=Dstn	27	4	4
Q9JIZ0	Probable N-acetyltransferase CML1 GN=Cml1	14	4	4
Q9JM76	Actin-related protein 2/3 complex subunit 3 GN=Arpc3	17	3	3
P16858	Glyceraldehyde-3-phosphate dehydrogenase GN=Gapdh	8	3	2
O08585	Clathrin light chain A GN=Clta	10	3	3
O70325	Phospholipid hydroperoxide glutathione peroxidase GN=Gpx4	14	3	3
P61750	ADP-ribosylation factor 4 GN=Arf4	16	3	2
P62911	60S ribosomal protein L32 GN=Rpl32	15	3	2
Q9DCJ5	NADH dehydrogenase [ubiquinone] 1 alpha subcomplex subunit 8 GN=Ndufa8	12	3	2
Q9QWL7	Keratin, type I cytoskeletal 17 GN=Krt17	6	3	2
Q920A5	Retinoid-inducible serine carboxypeptidase GN=Scpep1	4	2	2
Q62159	Rho-related GTP-binding protein RhoC GN=Rhoc	10	2	2
Q9CXW4	60S ribosomal protein L11 GN=Rpl11	12	2	2
P60335	Poly(rC)-binding protein 1 GN=Pcbp1	6	2	2
Q3UV17	Keratin, type II cytoskeletal 2 oral GN=Krt76	3	2	1
P61255	60S ribosomal protein L26 GN=Rpl26	10	2	2
P61358	60S ribosomal protein L27 GN=Rpl27	13	2	2
P60710	Actin, cytoplasmic 1 GN=Actb	6	2	2
P62270	40S ribosomal protein S18 GN=Rps18	13	2	2
P12815	Programmed cell death protein 6 GN=Pdcd6	8	2	2
Q9CXZ1	NADH dehydrogenase [ubiquinone] iron-sulfur protein 4, mitochondrial GN=Ndufs4	11	2	2

P45591	Cofilin-2 GN=Cfl2	11	2	1
P42925	Peroxisomal membrane protein 2 GN=Pxmp2	8	2	2
Q3TTY5	Keratin, type II cytoskeletal 2 epidermal GN=Krt2	3	2	1
Q6IFX2	Keratin, type I cytoskeletal 42 GN=Krt42	4	2	1
Q9EQX4	Allograft inflammatory factor 1-like GN=Aif1l	7	1	1
P62751	60S ribosomal protein L23a GN=Rpl23a	8	1	1
P62835	Ras-related protein Rap-1A GN=Rap1a	6	1	1
Q8BSZ2	AP-3 complex subunit sigma-2 GN=Ap3s2	6	1	1
P05213	Tubulin alpha-1B chain GN=Tuba1b	2	1	1
Q6P069	Sorcin GN=Sri	4	1	1
Q9CYL5	Golgi-associated plant pathogenesis-related protein 1 GN=Glipr2	8	1	1
Q6URW6	Myosin-14 GN=Myh14	0	1	1
Q9DCR2	AP-3 complex subunit sigma-1 GN=Ap3s1	6	1	1
P00416	Cytochrome c oxidase subunit 3 GN=mt-Co3	5	1	1
P61211	ADP-ribosylation factor-like protein 1 GN=Arl1	6	1	1
Q9R0Q9	Mannose-P-dolichol utilization defect 1 protein GN=Mpdu1	4	1	1
P63325	40S ribosomal protein S10 GN=Rps10	8	1	1
P62301	40S ribosomal protein S13 GN=Rps13	5	1	1
Q9WVL0	Maleylacetoacetate isomerase GN=Gstz1	5	1	1
Q9QZB9	Dynactin subunit 5 GN=Dctn5	6	1	1
Q99MS3	Mpv17-like protein GN=Mpv17l	4	1	1
Q9JHJ0	Tropomodulin-3 GN=Tmod3	2	1	1
P51881	ADP/ATP translocase 2 GN=Slc25a5	4	1	1
P62631	Elongation factor 1-alpha 2 GN=Eef1a2	2	1	1
Q8VEA4	Mitochondrial intermembrane space import and assembly protein 40 GN=Chchd4	6	1	1
P60764	Ras-related C3 botulinum toxin substrate 3 GN=Rac3	5	1	1
Q9ES97	Reticulon-3 GN=Rtn3	1	1	1
Q8BK08	Transmembrane protein 11, mitochondrial GN=Tmem11	5	1	1
Q61555	Fibrillin-2 GN=Fbn2	0	1	1
Q9WTX5	S-phase kinase-associated protein 1 GN=Skp1	7	1	1
P55258	Ras-related protein Rab-8A GN=Rab8a	3	1	1
Q9CQX2	Cytochrome b5 type B GN=Cyb5b	5	1	1
P62743	AP-2 complex subunit sigma GN=Ap2s1	5	1	1

Table 7.12 – Adult Kidney IgG 6 (~17-20 kDa)

Accession	Description	Coverage [%]	# PSMs	# Unique Peptides
Q60605	Myosin light polypeptide 6 GN=Myl6	64	14	9
Q3THE2	Myosin regulatory light chain 12B GN=Myl12b	45	7	2
Q9CQ19	Myosin regulatory light polypeptide 9 GN=Myl9	38	6	1
P02535	Keratin, type I cytoskeletal 10 GN=Krt10	3	2	2
Q3TTY5	Keratin, type II cytoskeletal 2 epidermal GN=Krt2	2	1	1
P04104	Keratin, type II cytoskeletal 1 GN=Krt1	2	1	1
P01942	Hemoglobin subunit alpha GN=Hba	11	1	1
Q3UV17	Keratin, type II cytoskeletal 2 oral GN=Krt76	2	1	1
Q62425	Cytochrome c oxidase subunit NDUFA4 GN=Ndufa4	12	1	1
O35972	39S ribosomal protein L23, mitochondrial GN=Mrpl23	14	1	1
Q9EQX4	Allograft inflammatory factor 1-like GN=Aif1l	7	1	1
P07724	Serum albumin GN=Alb	2	1	1
P10639	Thioredoxin GN=Txn	12	1	1
Q922U2	Keratin, type II cytoskeletal 5 GN=Krt5	2	1	1
Q3U0Y2	Transmembrane protein 35B GN=Tmem35b	5	1	1

Table 7.13 – Adult Kidney IP 7 (~13-16 kDa)

Accession	Description	Coverage [%]	# PSMs	# Unique Peptides
Q60605	Myosin light polypeptide 6 GN=Myl6	67	54	8
P09542	Myosin light chain 3 GN=Myl3	15	18	1
P16858	Glyceraldehyde-3-phosphate dehydrogenase GN=Gapdh	28	14	9
P19783	Cytochrome c oxidase subunit 4 isoform 1, mitochondrial GN=Cox4i1	50	14	9
P60710	Actin, cytoplasmic 1 GN=Actb	26	10	8
Q9EQX4	Allograft inflammatory factor 1-like GN=Aif1l	49	10	8
P62889	60S ribosomal protein L30 GN=Rpl30	58	10	5
P01942	Hemoglobin subunit alpha GN=Hba	43	9	6
P02088	Hemoglobin subunit beta-1 GN=Hbb-b1	65	9	8
Q9D023	Mitochondrial pyruvate carrier 2 GN=Mpc2	33	8	6
P10639	Thioredoxin GN=Txn	41	8	4
O35245	Polycystin-2 GN=Pkd2	5	8	5
Q9CQZ5	NADH dehydrogenase [ubiquinone] 1 alpha subcomplex subunit 6 GN=Ndufa6	54	8	7
P14131	40S ribosomal protein S16 GN=Rps16	40	8	7
P02535	Keratin, type I cytoskeletal 10 GN=Krt10	12	7	6
Q6IRU5	Clathrin light chain B GN=Cltb	23	7	7
Q9CZX8	40S ribosomal protein S19 GN=Rps19	34	7	7
Q9ERS2	NADH dehydrogenase [ubiquinone] 1 alpha subcomplex subunit 13 GN=Ndufa13	44	7	6
Q9CPW4	Actin-related protein 2/3 complex subunit 5 GN=Arpc5	58	6	5
Q8BG73	SH3 domain-binding glutamic acid-rich-like protein 2 GN=Sh3bgrl2	59	6	4
P99029	Peroxiredoxin-5, mitochondrial GN=Prdx5	32	6	6
P12787	Cytochrome c oxidase subunit 5A, mitochondrial GN=Cox5a	27	6	5
P56395	Cytochrome b5 GN=Cyb5a	48	6	5
P61358	60S ribosomal protein L27 GN=Rpl27	43	6	5
Q91WS0	CDGSH iron-sulfur domain-containing protein 1 GN=Cisd1	44	5	5
Q62425	Cytochrome c oxidase subunit NDUFA4 GN=Ndufa4	46	5	4
Q9CQ54	NADH dehydrogenase [ubiquinone] 1 subunit C2 GN=Ndufc2	26	5	4
Q9CPP6	NADH dehydrogenase [ubiquinone] 1 alpha subcomplex subunit 5 GN=Ndufa5	28	5	4
P19536	Cytochrome c oxidase subunit 5B, mitochondrial GN=Cox5b	25	5	4
P62830	60S ribosomal protein L23 GN=Rpl23	44	5	5
Q3THE2	Myosin regulatory light chain 12B GN=Myl12b	34	5	2
P62743	AP-2 complex subunit sigma GN=Ap2s1	30	5	4
P62270	40S ribosomal protein S18 GN=Rps18	24	5	5
P56391	Cytochrome c oxidase subunit 6B1 GN=Cox6b1	60	5	5
Q9CQ19	Myosin regulatory light polypeptide 9 GN=Myl9	34	5	2
P43024	Cytochrome c oxidase subunit 6A1, mitochondrial GN=Cox6a1	16	5	2
P0C0S6	Histone H2A.Z GN=H2afz	31	5	2
P48962	ADP/ATP translocase 1 GN=Slc25a4	11	4	4
Q922U2	Keratin, type II cytoskeletal 5 GN=Krt5	6	4	2

Q9CQC7	NADH dehydrogenase [ubiquinone] 1 beta subcomplex subunit 4 GN=Ndufb4	46	4	4
Q9D855	Cytochrome b-c1 complex subunit 7 GN=Uqcrb	25	4	3
P60867	40S ribosomal protein S20 GN=Rps20	29	4	4
P62806	Histone H4 GN=H4c1	29	4	3
O55142	60S ribosomal protein L35a GN=Rpl35a	27	4	4
P38575	Uroplakin-2 GN=Upk2	29	4	4
O08585	Clathrin light chain A GN=Clta	14	4	4
P99027	60S acidic ribosomal protein P2 GN=Rplp2	60	4	4
P62264	40S ribosomal protein S14 GN=Rps14	24	4	4
P62852	40S ribosomal protein S25 GN=Rps25	30	4	4
C0HKE4	Histone H2A type 1-E GN=Hist1h2ae	27	4	1
Q9CPQ1	Cytochrome c oxidase subunit 6C GN=Cox6c	29	4	3
Q3UV17	Keratin, type II cytoskeletal 2 oral GN=Krt76	4	3	1
Q9CR51	V-type proton ATPase subunit G 1 GN=Atp6v1g1	37	3	3
P62245	40S ribosomal protein S15a GN=Rps15a	13	3	2
Q6ZWY3	40S ribosomal protein S27-like GN=Rps27l	38	3	3
Q9CZB0	Succinate dehydrogenase cytochrome b560 subunit, mitochondrial GN=Sdhc	14	3	2
Q9CQH3	NADH dehydrogenase [ubiquinone] 1 beta subcomplex subunit 5, mitochondrial GN=Ndufb5	17	3	3
P62855	40S ribosomal protein S26 GN=Rps26	31	3	3
Q7TMF3	NADH dehydrogenase [ubiquinone] 1 alpha subcomplex subunit 12 GN=Ndufa12	14	3	2
Q8C2Q3	RNA-binding protein 14 GN=Rbm14	5	3	3
Q9CPU4	Microsomal glutathione S-transferase 3 GN=Mgst3	18	3	3
P63323	40S ribosomal protein S12 GN=Rps12	23	3	3
Q3TTY5	Keratin, type II cytoskeletal 2 epidermal GN=Krt2	4	3	1
P10853	Histone H2B type 1-F/J/L GN=Hist1h2bf	15	3	3
Q01768	Nucleoside diphosphate kinase B GN=Nme2	20	3	2
Q6P9L6	Kinesin-like protein KIF15 GN=Kif15	1	3	1
P62900	60S ribosomal protein L31 GN=Rpl31	25	3	3
P67984	60S ribosomal protein L22 GN=Rpl22	23	3	3
Q99LY9	NADH dehydrogenase [ubiquinone] iron-sulfur protein 5 GN=Ndufs5	30	3	3
Q9D8B4	NADH dehydrogenase [ubiquinone] 1 alpha subcomplex subunit 11 GN=Ndufa11	19	3	2
P63030	Mitochondrial pyruvate carrier 1 GN=Mpc1	15	3	2
P62317	Small nuclear ribonucleoprotein Sm D2 GN=Snrpd2	25	3	3
P04104	Keratin, type II cytoskeletal 1 GN=Krt1	5	3	2
Q9Z1P6	NADH dehydrogenase [ubiquinone] 1 alpha subcomplex subunit 7 GN=Ndufa7	18	2	2
P62267	40S ribosomal protein S23 GN=Rps23	16	2	2
Q6ZWV7	60S ribosomal protein L35 GN=Rpl35	15	2	2
Q9D1R9	60S ribosomal protein L34 GN=Rpl34	13	2	2
P61079	Ubiquitin-conjugating enzyme E2 D3 GN=Ube2d3	12	2	2
Q9D3D9	ATP synthase subunit delta, mitochondrial GN=Atp5f1d	12	2	2
P62315	Small nuclear ribonucleoprotein Sm D1 GN=Snrpd1	20	2	2
P63325	40S ribosomal protein S10 GN=Rps10	9	2	2
Q9D1K2	V-type proton ATPase subunit F GN=Atp6v1f	18	2	2

Q7TME2	Sperm-associated antigen 5 GN=Spag5	2	2	1
B1AR13	CDGSH iron-sulfur domain-containing protein 3, mitochondrial GN=Cisd3	15	2	2
Q9D0F9	Phosphoglucomutase-1 GN=Pgm1	4	2	1
Q8R404	MICOS complex subunit MIC13 GN=Micos13	12	2	2
Q91VW3	SH3 domain-binding glutamic acid-rich-like protein 3 GN=Sh3bgrl3	31	2	2
Q9CQ75	NADH dehydrogenase [ubiquinone] 1 alpha subcomplex subunit 2 GN=Ndufa2	21	2	2
P56389	Cytidine deaminase GN=Cda	21	2	2
P02301	Histone H3.3C GN=H3f3c	10	2	2
Q3UIU2	NADH dehydrogenase [ubiquinone] 1 beta subcomplex subunit 6 GN=Ndufb6	11	2	2
Q9CQZ6	NADH dehydrogenase [ubiquinone] 1 beta subcomplex subunit 3 GN=Ndufb3	17	2	2
P62320	Small nuclear ribonucleoprotein Sm D3 GN=Snrpd3	25	2	2
P63168	Dynein light chain 1, cytoplasmic GN=Dynll1	25	2	2
P84089	Enhancer of rudimentary homolog GN=Erh	22	2	2
P08730	Keratin, type I cytoskeletal 13 GN=Krt13	4	2	1
Q9CQ69	Cytochrome b-c1 complex subunit 8 GN=Uqcrq	18	2	2
P61514	60S ribosomal protein L37a GN=Rpl37a	28	2	2
O70325	Phospholipid hydroperoxide glutathione peroxidase GN=Gpx4	6	1	1
Q64331	Unconventional myosin-VI GN=Myo6	1	1	1
Q9CR61	NADH dehydrogenase [ubiquinone] 1 beta subcomplex subunit 7 GN=Ndufb7	7	1	1
Q9CQS8	Protein transport protein Sec61 subunit beta GN=Sec61b	10	1	1
Q9D7J4	Cytochrome c oxidase assembly protein COX20, mitochondrial GN=Cox20	10	1	1
Q62186	Translocon-associated protein subunit delta GN=Ssr4	6	1	1
P56382	ATP synthase subunit epsilon, mitochondrial GN=Atp5f1e	15	1	1
Q8VIM4	Barttin GN=Bsnd	4	1	1
Q9CQR4	Acyl-coenzyme A thioesterase 13 GN=Acot13	7	1	1
P47955	60S acidic ribosomal protein P1 GN=Rplp1	14	1	1
Q9DAS9	Guanine nucleotide-binding protein G(I)/G(S)/G(O) subunit gamma-12 GN=Gng12	10	1	1
P0CW02	Lymphocyte antigen 6C1 GN=Ly6c1	14	1	1
P18760	Cofilin-1 GN=Cfl1	5	1	1
Q9CXV1	Succinate dehydrogenase [ubiquinone] cytochrome b small subunit, mitochondrial GN=Sdhd	6	1	1
P63082	V-type proton ATPase 16 kDa proteolipid subunit GN=Atp6v0c	12	1	1
Q8BMC1	V-type proton ATPase subunit G 3 GN=Atp6v1g3	9	1	1
P63163	Small nuclear ribonucleoprotein-associated protein N GN=Snrpn	3	1	1
P83882	60S ribosomal protein L36a GN=Rpl36a	8	1	1
Q61878	Bone marrow proteoglycan GN=Prg2	5	1	1
Q9D6U8	Protein FAM162A GN=Fam162a	8	1	1
Q9CX13	Protein cornichon homolog 4 GN=Cnih4	14	1	1
P62631	Elongation factor 1-alpha 2 GN=Eef1a2	2	1	1
Q78XF5	Oligosaccharyltransferase complex subunit OSTC GN=Ostc	8	1	1
Q9JJV2	Profilin-2 GN=Pfn2	10	1	1

Q9CQ00	Distal membrane-arm assembly complex protein 1 GN=Dmac1	13	1	1
Q8VCH0	3-ketoacyl-CoA thiolase B, peroxisomal GN=Acaa1b	2	1	1
P07091	Protein S100-A4 GN=S100a4	8	1	1
P47964	60S ribosomal protein L36 GN=Rpl36	10	1	1
Q8CAQ8	MICOS complex subunit Mic60 GN=Immt	2	1	1
P19258	Protein Mpv17 GN=Mpv17	6	1	1
P50543	Protein S100-A11 GN=S100a11	7	1	1
Q9JM51	Prostaglandin E synthase GN=Ptges	5	1	1
O09111	NADH dehydrogenase [ubiquinone] 1 beta subcomplex subunit 11, mitochondrial GN=Ndufb11	7	1	1
P52503	NADH dehydrogenase [ubiquinone] iron-sulfur protein 6, mitochondrial GN=Ndufs6	13	1	1
Q04646	Sodium/potassium-transporting ATPase subunit gamma GN=Fxyd2	20	1	1
P48771	Cytochrome c oxidase subunit 7A2, mitochondrial GN=Cox7a2	12	1	1
P62897	Cytochrome c, somatic GN=Cycs	10	1	1
Q91WE6	Threonylcarbamoyladenosine tRNA methylthiotransferase GN=Cdkal1	3	1	1
Q99PL5	Ribosome-binding protein 1 GN=Rrbp1	1	1	1
P62869	Elongin-B GN=Elob	7	1	1
Q9CQI6	Coactosin-like protein GN=Cotl1	6	1	1
P17665	Cytochrome c oxidase subunit 7C, mitochondrial GN=Cox7c	14	1	1
Q91VS7	Microsomal glutathione S-transferase 1 GN=Mgst1	8	1	1
Q9CZT4	DNA-directed RNA polymerase III subunit RPC5 GN=Polr3e	2	1	1
Q9CRC0	Vitamin K epoxide reductase complex subunit 1 GN=Vkorc1	8	1	1
Q8C5W0	Calmin GN=Clmn	1	1	1
P11031	Activated RNA polymerase II transcriptional coactivator p15 GN=Sub1	9	1	1
Q9CPQ8	ATP synthase subunit g, mitochondrial GN=Atp5mg	9	1	1
Q06185	ATP synthase subunit e, mitochondrial GN=Atp5me	17	1	1
Q6ZQ06	Centrosomal protein of 162 kDa GN=Cep162	1	1	1
P47226	Testin GN=Tes	2	1	1
P03899	NADH-ubiquinone oxidoreductase chain 3 GN=Mtnd3	13	1	1
P62878	E3 ubiquitin-protein ligase RBX1 GN=Rbx1	7	1	1
P56135	ATP synthase subunit f, mitochondrial GN=Atp5mf	14	1	1

Table 7.14 – Adult Kidney IgG 7 (~13-16kDa)

Accession	Description	Coverage [%]	# PSMs	# Unique Peptides
Q8BI17	SH2 domain-containing protein 7 GN=Sh2d7	5	5	1
P02535	Keratin, type I cytoskeletal 10 GN=Krt10	5	3	2
P04104	Keratin, type II cytoskeletal 1 GN=Krt1	4	2	2
P01942	Hemoglobin subunit alpha GN=Hba	15	2	2
Q60605	Myosin light polypeptide 6 GN=Myl6	14	2	2
Q61414	Keratin, type I cytoskeletal 15 GN=Krt15	3	2	1
Q922U2	Keratin, type II cytoskeletal 5 GN=Krt5	4	2	2
Q3TTY5	Keratin, type II cytoskeletal 2 epidermal GN=Krt2	2	1	1
P97499	Telomerase protein component 1 GN=Tep1	1	1	1
Q3UV17	Keratin, type II cytoskeletal 2 oral GN=Krt76	2	1	1
P62737	Actin, aortic smooth muscle GN=Acta2	3	1	1
P07724	Serum albumin GN=Alb	2	1	1

Table 7.15 – Adult Lung IP 1 (~100-130 kDa)

Accession	Description	Coverage [%]	# PSMs	# Unique Peptides
Q9WTI7	Unconventional myosin-Ic GN=Myo1c	58	130	53
Q5SYD0	Unconventional myosin-Id GN=Myo1d	55	80	52
O35245	Polycystin-2 GN=Pkd2	36	42	29
P46735	Unconventional myosin-Ib GN=Myo1b	35	40	34
O54931	A-kinase anchor protein 2 GN=Akap2	30	37	23
P57780	Alpha-actinin-4 GN=Actn4	40	34	19
Q9EP71	Ankycorbin GN=Rai14	30	26	24
Q3UH68	LIM and calponin homology domains-containing protein 1 GN=Limch1	26	23	22
Q7TPR4	Alpha-actinin-1 GN=Actn1	26	21	7
Q5SUA5	Unconventional myosin-Ig GN=Myo1g	23	20	17
Q61768	Kinesin-1 heavy chain GN=Kif5b	16	14	14
Q6P542	ATP-binding cassette sub-family F member 1 GN=Abcf1	14	13	11
Q3U0S6	Ras-interacting protein 1 GN=Rasip1	18	13	12
E9Q634	Unconventional myosin-Ie GN=Myo1e	13	12	11
Q8VEK3	Heterogeneous nuclear ribonucleoprotein U GN=Hnrnpu	12	10	8
Q5FWH6	Rho guanine nucleotide exchange factor 15 GN=Arhgef15	14	10	10
Q8BX02	KN motif and ankyrin repeat domain-containing protein 2 GN=Kank2	15	10	10
O55143	Sarcoplasmic/endoplasmic reticulum calcium ATPase 2 GN=Atp2a2	10	9	7
Q9EPK7	Exportin-7 GN=Xpo7	7	8	8
Q8K2V1	Serine/threonine-protein phosphatase 4 regulatory subunit 1 GN=Ppp4r1	10	8	8
Q9ERG0	LIM domain and actin-binding protein 1 GN=Lima1	12	8	8
Q8VDD5	Myosin-9 GN=Myh9	4	7	7
Q9JI91	Alpha-actinin-2 GN=Actn2	9	7	1
Q8BYC6	Serine/threonine-protein kinase TAO3 GN=Taok3	8	7	7
P30999	Catenin delta-1 GN=Ctnnd1	8	7	7
Q922D8	C-1-tetrahydrofolate synthase, cytoplasmic GN=Mthfd1	7	7	7
Q60875	Rho guanine nucleotide exchange factor 2 GN=Arhgef2	8	7	7
Q64518	Sarcoplasmic/endoplasmic reticulum calcium ATPase 3 GN=Atp2a3	7	6	4
Q6R891	Neurabin-2 GN=Ppp1r9b	9	6	6
P28843	Dipeptidyl peptidase 4 GN=Dpp4	6	5	5
Q9QXS6	Drebrin GN=Dbn1	8	4	4
O70318	Band 4.1-like protein 2 GN=Epb41l2	4	4	4
O08810	116 kDa U5 small nuclear ribonucleoprotein component GN=Eftud2	5	4	4
Q9DBG3	AP-2 complex subunit beta GN=Ap2b1	5	4	4
P60710	Actin, cytoplasmic 1 GN=Actb	15	4	4
Q921U8	Smoothelin GN=Smtn	4	4	4
Q9JIK5	Nucleolar RNA helicase 2 GN=Ddx21	5	4	4
Q99MR6	Serrate RNA effector molecule homolog GN=Srrt	4	4	4
A2AJI0	MAP7 domain-containing protein 1 GN=Map7d1	5	4	4
B2RY56	RNA-binding protein 25 GN=Rbm25	4	3	3

P01027	Complement C3 GN=C3	2	3	3
Q69ZB8	Zinc finger CCHC domain-containing protein 2 GN=Zcchc2	3	3	1
Q80U95	Ubiquitin-protein ligase E3C GN=Ube3c	3	3	3
Q62261	Spectrin beta chain, non-erythrocytic 1 GN=Sptbn1	1	3	3
Q64331	Unconventional myosin-VI GN=Myo6	2	3	3
Q8CG16	Complement C1r-A subcomponent GN=C1ra	4	3	3
Q8BHL4	Retinoic acid-induced protein 3 GN=Gprc5a	13	3	3
Q9Z0J1	Reversion-inducing cysteine-rich protein with Kazal motifs GN=Reck	3	3	3
Q8R307	Vacuolar protein sorting-associated protein 18 homolog GN=Vps18	2	2	2
Q8BYM7	Radial spoke head protein 4 homolog A GN=Rsph4a	3	2	2
Q9D071	MMS19 nucleotide excision repair protein homolog GN=Mms19	2	2	2
P34152	Focal adhesion kinase 1 GN=Ptk2	2	2	2
P02535	Keratin, type I cytoskeletal 10 GN=Krt10	3	2	1
Q61414	Keratin, type I cytoskeletal 15 GN=Krt15	3	2	1
P28660	Nck-associated protein 1 GN=Nckap1	2	2	2
Q5U3K5	Rab-like protein 6 GN=Rabl6	2	2	2
Q3U1J4	DNA damage-binding protein 1 GN=Ddb1	1	2	2
B2RQE8	Rho GTPase-activating protein 42 GN=Arhgap42	2	2	2
P04104	Keratin, type II cytoskeletal 1 GN=Krt1	4	2	2
Q9ESJ0	Exportin-4 GN=Xpo4	2	2	2
Q9CSN1	SNW domain-containing protein 1 GN=Snw1	3	2	1
P62983	Ubiquitin-40S ribosomal protein S27a GN=Rps27a	16	2	2
P86044	Anoctamin-9 GN=Ano9	5	2	1
Q7TMC8	L-fucose kinase GN=Fcsk	1	1	1
Q8VCC9	Spondin-1 GN=Spon1	1	1	1
Q922U2	Keratin, type II cytoskeletal 5 GN=Krt5	2	1	1
Q9ERK4	Exportin-2 GN=Cse1l	1	1	1
P70218	Mitogen-activated protein kinase kinase kinase kinase 1 GN=Map4k1	1	1	1
Q811D0	Disks large homolog 1 GN=Dlg1	1	1	1
Q9D2F7	Nuclear pore membrane glycoprotein 210-like GN=Nup210l	0	1	1
Q8K2V6	Importin-11 GN=Ipo11	1	1	1
P09055	Integrin beta-1 GN=Itgb1	1	1	1
Q5SSZ5	Tensin-3 GN=Tns3	1	1	1
Q6Q899	Probable ATP-dependent RNA helicase DDX58 GN=Ddx58	1	1	1
P61087	Ubiquitin-conjugating enzyme E2 K GN=Ube2k	4	1	1
Q8K4L3	Supervillin GN=Svil	1	1	1
P25799	Nuclear factor NF-kappa-B p105 subunit GN=Nfkb1	1	1	1
Q6P5F9	Exportin-1 GN=Xpo1	1	1	1
Q78PY7	Staphylococcal nuclease domain-containing protein 1 GN=Snd1	1	1	1
P55284	Cadherin-5 GN=Cdh5	2	1	1
P31001	Desmin GN=Des	2	1	1
O35382	Exocyst complex component 4 GN=Exoc4	1	1	1
Q7M757	Lys-63-specific deubiquitinase BRCC36-like GN=C6.1al	3	1	1

Q3UV17	Keratin, type II cytoskeletal 2 oral GN=Krt76	2	1	1
Q8BHL3	TBC1 domain family member 10B GN=Tbc1d10b	2	1	1
Q1H9T6	Telomere zinc finger-associated protein GN=Zbtb48	3	1	1
Q9QXL8	Nucleoside diphosphate kinase 7 GN=Nme7	4	1	1
P48193	Protein 4.1 GN=Epb41	1	1	1
Q80V31	Centrosomal protein of 104 kDa GN=Cep104	1	1	1

Table 7.16 – Adult Lung IgG 1 (~100-130 kDa)

Accession	Description	Coverage [%]	# PSMs	# Unique Peptides
Q3UKC1	Tax1-binding protein 1 homolog GN=Tax1bp1	14	11	10
P02535	Keratin, type I cytoskeletal 10 GN=Krt10	9	7	5
Q922U2	Keratin, type II cytoskeletal 5 GN=Krt5	12	7	4
P60710	Actin, cytoplasmic 1 GN=Actb	18	5	5
Q61781	Keratin, type I cytoskeletal 14 GN=Krt14	9	5	2
Q3TTY5	Keratin, type II cytoskeletal 2 epidermal GN=Krt2	5	4	2
Q6NXH9	Keratin, type II cytoskeletal 73 GN=Krt73	7	4	1
Q6IFX2	Keratin, type I cytoskeletal 42 GN=Krt42	8	4	1
Q3UV17	Keratin, type II cytoskeletal 2 oral GN=Krt76	6	4	1
P04104	Keratin, type II cytoskeletal 1 GN=Krt1	5	3	1
Q8VED5	Keratin, type II cytoskeletal 79 GN=Krt79	4	3	1
P97290	Plasma protease C1 inhibitor GN=Serping1	6	3	3
P07724	Serum albumin GN=Alb	4	3	2

Table 7.17 – Adult Lung IP 2 (~75-90 kDa)

Accession	Description	Coverage [%]	# PSMs	# Unique Peptides
P13020	Gelsolin GN=Gsn	47	116	28
Q7TPW1	Nexilin GN=Nexn	33	33	21
Q9ERG0	LIM domain and actin-binding protein 1 GN=Lima1	31	29	17
P11499	Heat shock protein HSP 90-beta GN=Hsp90ab1	35	27	12
P97434	Myosin phosphatase Rho-interacting protein GN=Mprip	32	26	24
Q99KC8	von Willebrand factor A domain-containing protein 5A GN=Vwa5a	34	25	20
Q8CAQ8	MICOS complex subunit Mic60 GN=Immt	31	21	18
Q8CG16	Complement C1r-A subcomponent GN=C1ra	31	21	15
Q5SYD0	Unconventional myosin-Id GN=Myo1d	20	20	17
Q8CG14	Complement C1s-A subcomponent GN=C1sa	32	19	16
Q3UH68	LIM and calponin homology domains-containing protein 1 GN=Limch1	20	19	17
P60710	Actin, cytoplasmic 1 GN=Actb	44	17	6
P07901	Heat shock protein HSP 90-alpha GN=Hsp90aa1	19	16	4
Q91VR5	ATP-dependent RNA helicase DDX1 GN=Ddx1	22	13	13
Q9WTI7	Unconventional myosin-Ic GN=Myo1c	14	13	13
P68033	Actin, alpha cardiac muscle 1 GN=Actc1	34	13	4
Q02257	Junction plakoglobin GN=Jup	21	13	13
P04919	Band 3 anion transport protein GN=Slc4a1	17	12	12
P62046	Leucine-rich repeat and calponin homology domain-containing protein 1 GN=Lrch1	15	10	9
Q8CIB5	Fermitin family homolog 2 GN=Fermt2	15	10	9
P30999	Catenin delta-1 GN=Ctnnd1	12	9	9
O54931	A-kinase anchor protein 2 GN=Akap2	11	8	6
Q08857	Platelet glycoprotein 4 GN=Cd36	24	8	8
Q8VDD5	Myosin-9 GN=Myh9	5	8	8
P26041	Moesin GN=Msn	11	8	3
P18654	Ribosomal protein S6 kinase alpha-3 GN=Rps6ka3	10	8	2
Q811U4	Mitofusin-1 GN=Mfn1	12	8	8
P26043	Radixin GN=Rdx	10	7	2
Q9QXS6	Drebrin GN=Dbn1	13	7	6
Q8BVA4	Leiomodin-1 GN=Lmod1	14	7	7
Q8VHE0	Translocation protein SEC63 homolog GN=Sec63	10	6	6
P18653	Ribosomal protein S6 kinase alpha-1 GN=Rps6ka1	9	6	1
Q9R1Z8	Vinexin GN=Sorbs3	9	6	5
Q60604	Adseverin GN=Scin	10	6	6
Q8BJS4	SUN domain-containing protein 2 GN=Sun2	11	6	6
P01872	Immunoglobulin heavy constant mu GN=Ighm	17	6	6
Q9QYB5	Gamma-adducin GN=Add3	12	6	6
O35245	Polycystin-2 GN=Pkd2	5	5	4
Q8BMS1	Trifunctional enzyme subunit alpha, mitochondrial GN=Hadha	8	5	5
P50427	Steryl-sulfatase GN=Sts	9	5	5
Q9D0R2	Threonine--tRNA ligase 1, cytoplasmic GN=Tars1	7	5	5
Q8BHL4	Retinoic acid-induced protein 3 GN=Gprc5a	22	5	4

Q9ES28	Rho guanine nucleotide exchange factor 7 GN=Arhgef7	5	5	4
P26040	Ezrin GN=Ezr	6	5	1
Q9DBP0	Sodium-dependent phosphate transport protein 2B GN=Slc34a2	7	5	4
Q05512	Serine/threonine-protein kinase MARK2 GN=Mark2	9	5	4
Q9Z2B9	Ribosomal protein S6 kinase alpha-4 GN=Rps6ka4	6	4	4
Q62009	Periostin GN=Postn	6	4	4
Q9QXK3	Coatomer subunit gamma-2 GN=Copg2	4	4	4
Q6DIA2	Exocyst complex component 3-like protein 4 GN=Exoc3l4	5	4	4
P12382	ATP-dependent 6-phosphofructokinase, liver type GN=Pfkl	5	4	3
Q8R1U1	Conserved oligomeric Golgi complex subunit 4 GN=Cog4	6	4	4
P42227	Signal transducer and activator of transcription 3 GN=Stat3	8	4	4
Q6KAR6	Exocyst complex component 3 GN=Exoc3	5	3	3
P62983	Ubiquitin-40S ribosomal protein S27a GN=Rps27a	22	3	3
P02535	Keratin, type I cytoskeletal 10 GN=Krt10	6	3	3
P04104	Keratin, type II cytoskeletal 1 GN=Krt1	4	3	3
Q9ET54	Palladin GN=Palld	3	3	3
P28740	Kinesin-like protein KIF2A GN=Kif2a	4	3	3
Q8CHW4	Translation initiation factor eIF-2B subunit epsilon GN=Eif2b5	5	3	3
Q8K4L3	Supervillin GN=Svil	1	3	3
P58069	Ras GTPase-activating protein 2 GN=Rasa2	3	3	1
Q3UV17	Keratin, type II cytoskeletal 2 oral GN=Krt76	3	2	1
Q9D279	Mitotic interactor and substrate of PLK1 GN=Misp	3	2	2
Q501J6	Probable ATP-dependent RNA helicase DDX17 GN=Ddx17	4	2	2
P54103	DnaJ homolog subfamily C member 2 GN=Dnajc2	3	2	2
P27659	60S ribosomal protein L3 GN=Rpl3	5	2	2
P26450	Phosphatidylinositol 3-kinase regulatory subunit alpha GN=Pik3r1	3	2	2
Q03141	MAP/microtubule affinity-regulating kinase 3 GN=Mark3	3	2	1
P46735	Unconventional myosin-Ib GN=Myo1b	2	2	2
Q8R370	Usher syndrome type-1C protein-binding protein 1 GN=Ushbp1	3	2	2
P58281	Dynamin-like 120 kDa protein, mitochondrial GN=Opa1	2	2	2
Q922U2	Keratin, type II cytoskeletal 5 GN=Krt5	3	2	1
P01787	Ig heavy chain V regions TEPC 15/S107/HPCM1/HPCM2/HPCM3	20	2	2
Q8K4G5	Actin-binding LIM protein 1 GN=Ablim1	3	2	2
Q9JLV5	Cullin-3 GN=Cul3	3	2	2
Q62172	RalA-binding protein 1 GN=Ralbp1	3	2	2
Q9EQH3	Vacuolar protein sorting-associated protein 35 GN=Vps35	3	2	2
Q9WTX6	Cullin-1 GN=Cul1	2	2	2
P42225	Signal transducer and activator of transcription 1 GN=Stat1	3	2	2
Q80WQ2	Protein VAC14 homolog GN=Vac14	3	2	2
A2A5Z6	E3 ubiquitin-protein ligase SMURF2 GN=Smurf2	4	2	2
Q05BC3	Echinoderm microtubule-associated protein-like 1 GN=Eml1	2	1	1

P20444	Protein kinase C alpha type GN=Prkca	1	1	1
O35682	Myeloid-associated differentiation marker GN=Myadm	5	1	1
O54781	SRSF protein kinase 2 GN=Srpk2	1	1	1
Q9QYC7	Vitamin K-dependent gamma-carboxylase GN=Ggcx	1	1	1
Q8BQ30	Phostensin GN=Ppp1r18	2	1	1
Q8C754	Vacuolar protein sorting-associated protein 52 homolog GN=Vps52	2	1	1
Q9JKF1	Ras GTPase-activating-like protein IQGAP1 GN=Iqgap1	1	1	1
Q99MJ9	ATP-dependent RNA helicase DDX50 GN=Ddx50	1	1	1
P48962	ADP/ATP translocase 1 GN=Slc25a4	3	1	1
P10852	4F2 cell-surface antigen heavy chain GN=Slc3a2	2	1	1
Q9QUR8	Semaphorin-7A GN=Sema7a	2	1	1
P13597	Intercellular adhesion molecule 1 GN=Icam1	2	1	1
Q8JZQ2	AFG3-like protein 2 GN=Afg3l2	1	1	1
Q8BJ71	Nuclear pore complex protein Nup93 GN=Nup93	1	1	1
Q9CZJ2	Heat shock 70 kDa protein 12B GN=Hspa12b	2	1	1
Q9JLV1	BAG family molecular chaperone regulator 3 GN=Bag3	2	1	1
Q61033	Lamina-associated polypeptide 2, isoforms alpha/zeta GN=Tmpo	1	1	1
Q8VBZ3	Cleft lip and palate transmembrane protein 1 homolog GN=Clptm1	2	1	1
Q9WTV7	E3 ubiquitin-protein ligase RLIM GN=Rlim	2	1	1
Q68FF6	ARF GTPase-activating protein GIT1 GN=Git1	1	1	1
Q8VED5	Keratin, type II cytoskeletal 79 GN=Krt79	2	1	1
P15306	Thrombomodulin GN=Thbd	1	1	1
P16546	Spectrin alpha chain, non-erythrocytic 1 GN=Sptan1	0	1	1
Q01405	Protein transport protein Sec23A GN=Sec23a	2	1	1
Q921L5	Conserved oligomeric Golgi complex subunit 2 GN=Cog2	2	1	1
Q61584	Fragile X mental retardation syndrome-related protein 1 GN=Fxr1	1	1	1

Table 7.18 – Adult Lung IgG 2 (~75-90 kDa)

Accession	Description	Coverage [%]	# PSMs	# Unique Peptides
P01872	Immunoglobulin heavy constant mu GN=Ighm	48	37	23
Q8CG16	Complement C1r-A subcomponent GN=C1ra	26	21	16
Q8CG14	Complement C1s-A subcomponent GN=C1sa	22	15	14
P01801	Ig heavy chain V-III region J606	49	11	7
P13020	Gelsolin GN=Gsn	15	11	10
P60710	Actin, cytoplasmic 1 GN=Actb	24	8	7
P04104	Keratin, type II cytoskeletal 1 GN=Krt1	5	7	3
P50446	Keratin, type II cytoskeletal 6A GN=Krt6a	7	6	2
Q3TTY5	Keratin, type II cytoskeletal 2 epidermal GN=Krt2	6	6	2
P02535	Keratin, type I cytoskeletal 10 GN=Krt10	7	5	3
P01787	Ig heavy chain V regions TEPC 15/S107/HPCM1/HPCM2/HPCM3	33	5	4
Q8CHW4	Translation initiation factor eIF-2B subunit epsilon GN=Eif2b5	7	4	4
Q8VED5	Keratin, type II cytoskeletal 79 GN=Krt79	4	4	1
P08730	Keratin, type I cytoskeletal 13 GN=Krt13	5	3	1
Q99M74	Keratin, type II cuticular Hb2 GN=Krt82	2	3	2
P01786	Ig heavy chain V region MOPC 47A	17	2	2
Q4KWH5	1-phosphatidylinositol 4,5-bisphosphate phosphodiesterase eta-1 GN=Plch1	1	2	1
P63017	Heat shock cognate 71 kDa protein GN=Hspa8	4	2	2
P97290	Plasma protease C1 inhibitor GN=Serping1	5	2	2
P01029	Complement C4-B GN=C4b	1	1	1
Q02105	Complement C1q subcomponent subunit C GN=C1qc	4	1	1
Q6IFX2	Keratin, type I cytoskeletal 42 GN=Krt42	3	1	1
P11499	Heat shock protein HSP 90-beta GN=Hsp90ab1	1	1	1
Q9WVP1	AP-1 complex subunit mu-2 GN=Ap1m2	8	1	1
Q6ZQ06	Centrosomal protein of 162 kDa GN=Cep162	1	1	1
Q9ERG0	LIM domain and actin-binding protein 1 GN=Lima1	2	1	1

Table 7.19 – 14.5 d.p.c. *Pkd2*$^{+/+}$ Kidney IPs

Accession	Description
Q3U9N8	Inosine-5'-monophosphate dehydrogenase GN=Impdh2
P62806	Histone H4 GN=H4c1
Q3U4U6	T-complex protein 1 subunit gamma GN=Cct3
Q921L4	Histone H2B GN=LOC665622
Q3TFD9	IF rod domain-containing protein GN=Vim
P43275	Histone H1.1 GN=H1-1
P43277	Histone H1.3 GN=H1-3
P15864	Histone H1.2 GN=H1-2
P43274	Histone H1.4 GN=H1-4
Q3U6P5	RRM domain-containing protein GN=Hnrnpc
A0A1Y7VJN6	Immunoglobulin heavy constant gamma 3 (Fragment) GN=Ighg3
A0A2I3BRL8	Predicted gene 7324 GN=Gm7324
B2RRX1	Actin, beta GN=Actb
Q1WWK3	Hist1h1b protein (Fragment) GN=H1f5
E9PZ16	Basement membrane-specific heparan sulfate proteoglycan core protein GN=Hspg2
P61358	60S ribosomal protein L27 GN=Rpl27
A2AB79	Histone H2A GN=H2aw
Q6GSS7	Histone H2A type 2-A GN=Hist2h2aa1
P47911	60S ribosomal protein L6 GN=Rpl6
Q3UZG3	Uncharacterized protein GN=Hnrnpa3
Q80UT7	Rpl7a protein (Fragment) GN=Rpl7a
O35245	Polycystin-2 GN=Pkd2
P05213	Tubulin alpha-1B chain GN=Tuba1b
P19324	Serpin H1 GN=Serpinh1
Q3U944	L-type lectin-like domain-containing protein GN=Lman1
P29341	Polyadenylate-binding protein 1 GN=Pabpc1
Q8VIJ6	Splicing factor, proline- and glutamine-rich GN=Sfpq
O88569	Heterogeneous nuclear ribonucleoproteins A2/B1 GN=Hnrnpa2b1
P63017	Heat shock cognate 71 kDa protein GN=Hspa8
Q3UK83	Uncharacterized protein GN=Hnrnpa1
Q4FZH2	MCG50660, isoform CRA_a GN=Rpl26
P53395	Lipoamide acyltransferase component of branched-chain alpha-keto acid dehydrogenase complex, mitochondrial GN=Dbt
P62751	60S ribosomal protein L23a GN=Rpl23a
A0A3B0INZ4	Adiponectin b GN=Adib
Q3UW40	TRASH domain-containing protein GN=Rpl24
Q58EW0	MCG132477, isoform CRA_a GN=Rpl18
O35129	Prohibitin-2 GN=Phb2
P14148	60S ribosomal protein L7 GN=Rpl7
P62911	60S ribosomal protein L32 GN=Rpl32
P56959	RNA-binding protein FUS GN=Fus
P10126	Elongation factor 1-alpha 1 GN=Eef1a1
P0C0S6	Histone H2A.Z GN=H2az1
P63038	60 kDa heat shock protein, mitochondrial GN=Hspd1

Q03265	ATP synthase subunit alpha, mitochondrial GN=Atp5f1a
Q5XFY8	Uncharacterized protein
A0A1Y7VKY1	MCG116671 GN=Rps18-ps5
P27661	Histone H2AX GN=H2afx
P97351	40S ribosomal protein S3a GN=Rps3a
Q3TF40	Uncharacterized protein (Fragment) GN=Nono
Q9CQK2	40S ribosomal protein S24 GN=Rps24
Q545A2	MCG11560 GN=Slc25a5
A8DUK2	Beta-globin GN=Hbbt1
Q925S1	MRP5 (Fragment) GN=Ighv9-4
A0A0B4J1I1	Immunoglobulin kappa variable 16-104 (Fragment) GN=Igkv16-104
Q60668	Heterogeneous nuclear ribonucleoprotein D0 GN=Hnrnpd
O70569	Ribosomal protein S14 GN=rps14
A0A1W2P768	H3 clustered histone 14 GN=H3c14
Q6ZWV7	60S ribosomal protein L35 GN=Rpl35
I6L978	Igk protein GN=Igk
O08583	THO complex subunit 4 GN=Alyref
P68040	Receptor of activated protein C kinase 1 GN=Rack1
P63325	40S ribosomal protein S10 GN=Rps10
Q9CWK0	Ribosomal_L14e domain-containing protein GN=Rpl14
Q5BLJ7	MCG10205 GN=Rps13
P68372	Tubulin beta-4B chain GN=Tubb4b
A0A0A6YX26	60S ribosomal protein L31 GN=Rpl31
Q5RJV5	Polypyrimidine tract binding protein 1 GN=Ptbp1
P63163	Small nuclear ribonucleoprotein-associated protein N GN=Snrpn
P62702	40S ribosomal protein S4, X isoform GN=Rps4x
Q58DZ3	MCG20799 GN=Rpl30
Q3TL71	Uncharacterized protein GN=Hnrnpk
P62852	40S ribosomal protein S25 GN=Rps25
Q91V99	40S ribosomal protein S30 (Fragment) GN=fau
Q5CZY9	Rps16 protein GN=Rps16
P31001	Desmin GN=Des
P27659	60S ribosomal protein L3 GN=Rpl3
Q4FZE6	40S ribosomal protein S7 GN=Rps7
Q20BD0	Heterogeneous nuclear ribonucleoprotein A/B GN=Hnrnpab
A0A0G2JE47	Immunoglobulin kappa variable 8-28 (Fragment) GN=Igkv8-28
P62242	40S ribosomal protein S8 GN=Rps8
P62830	60S ribosomal protein L23 GN=Rpl23
Q3TL53	40S ribosomal protein S6
Q3V0Z8	Uncharacterized protein (Fragment) GN=Ddx5
P62317	Small nuclear ribonucleoprotein Sm D2 GN=Snrpd2
A0A0A0MQF6	Glyceraldehyde-3-phosphate dehydrogenase GN=Gapdh
P62320	Small nuclear ribonucleoprotein Sm D3 GN=Snrpd3
O55142	60S ribosomal protein L35a GN=Rpl35a
Q5M9L1	60S ribosomal protein L36 GN=Rpl36
P20029	Endoplasmic reticulum chaperone BiP GN=Hspa5

P62918	60S ribosomal protein L8 GN=Rpl8
A2J1C8	McAB 0.1C3 mmunoglobulin heavy chain (Fragment)
A0A2I3BPG9	MCG113838 GN=Rpl36a-ps1
P01027	Complement C3 GN=C3
P10922	Histone H1.0 GN=H1-0
Q3U850	Ribosomal_L18_c domain-containing protein GN=Rpl5
Q8C2Q7	Heterogeneous nuclear ribonucleoprotein H GN=Hnrnph1
Q3TVV6	Uncharacterized protein GN=Hnrnpu
Q6ZWN5	40S ribosomal protein S9 GN=Rps9
Q8R3H6	Ighg protein GN=Ighg
Q3U8M3	Uncharacterized protein GN=Rpl37a
G5E924	Heterogeneous nuclear ribonucleoprotein L (Fragment) GN=Hnrnpl
A0A075B5L7	Immunoglobulin kappa variable 4-80 (Fragment) GN=Igkv4-80
P47963	60S ribosomal protein L13 GN=Rpl13
Q9JJI8	60S ribosomal protein L38 GN=Rpl38
P62315	Small nuclear ribonucleoprotein Sm D1 GN=Snrpd1
D3Z722	40S ribosomal protein S19 GN=Rps19
Q80ZM5	H1 histone family, member X GN=H1f10
P47915	60S ribosomal protein L29 GN=Rpl29
P02301	Histone H3.3C GN=H3f3c
P68433	Histone H3.1 GN=H3c1
A0A0B4J1J7	Immunoglobulin heavy variable 1-82 GN=Ighv1-82
Q5M9J8	MCG13936 GN=Rpl28
Q9D995	Cyclin N-terminal domain-containing protein 1 GN=Cntd1
Q9D1R9	60S ribosomal protein L34 GN=Rpl34
A0A1L1STE4	Interleukin enhancer-binding factor 3 GN=Ilf3
P84089	Enhancer of rudimentary homolog GN=Erh
P24369	Peptidyl-prolyl cis-trans isomerase B GN=Ppib
A0A0A6YWI9	Immunoglobulin heavy variable V1-11 (Fragment) GN=Ighv1-11
P09405	Nucleolin GN=Ncl
A0A0G2JG88	T cell receptor alpha joining 48 (Fragment) GN=Traj48
Q64012	RNA-binding protein Raly GN=Raly
A0A140T8N8	Immunoglobulin kappa variable 9-123 (Fragment) GN=Igkv9-123
Q9CX86	Heterogeneous nuclear ribonucleoprotein A0 GN=Hnrnpa0
Q9Z2X1	Heterogeneous nuclear ribonucleoprotein F GN=Hnrnpf
A0A1D5RM85	60S ribosomal protein L18a (Fragment) GN=Rpl18a
Q3TJ94	Prothrombin GN=F2
P52480	Pyruvate kinase PKM GN=Pkm
Q810A4	RNA helicase (Fragment) GN=Ddx55
Q3THA0	Eukaryotic translation initiation factor 3 subunit G GN=Eif3g
Q8C2Q3	RNA-binding protein 14 GN=Rbm14
A0A1S6GWJ8	Uncharacterized protein GN=Hnrnpm
Q3U7D2	Ribosomal protein L15 GN=Rpl15
Q3U536	Uncharacterized protein GN=Npm1
B2CY77	Laminin receptor (Fragment) GN=Rpsa
P60867	40S ribosomal protein S20 GN=Rps20

Q99NF2	NMDA receptor synaptonuclear signaling and neuronal migration factor GN=Nsmf
P62858	40S ribosomal protein S28 GN=Rps28
P06684	Complement C5 GN=C5
Q6NSP9	High mobility group protein HMGI-C GN=Hmga2
O09167	60S ribosomal protein L21 GN=Rpl21
Q3U8W9	Uncharacterized protein GN=Hnrnpr
P14733	Lamin-B1 GN=Lmnb1
H3BLG3	Ras-related protein Rab-26 GN=Rab26
P35550	rRNA 2'-O-methyltransferase fibrillarin GN=Fbl
P25444	40S ribosomal protein S2 GN=Rps2
Q5I0T8	Ribosomal protein L19 GN=Rpl19
P04104	Keratin, type II cytoskeletal 1 GN=Krt1
Q6ZWU9	40S ribosomal protein S27 GN=Rps27
Q8VD75	Huntingtin-interacting protein 1 GN=Hip1
A8DUV3	Alpha-globin GN=Hbat1
Q3T9Y8	Eukaryotic translation initiation factor 3 subunit I GN=Eif3i
A0A0G2JDG9	Immunoglobulin kappa variable 8-16 (Fragment) GN=Igkv8-16
Q71LX8	Heat shock protein 84b GN=Hsp90ab1
Q9DB79	Ribosomal_S17_N domain-containing protein GN=Rps11
P19253	60S ribosomal protein L13a GN=Rpl13a
O35074	Prostacyclin synthase GN=Ptgis
P56480	ATP synthase subunit beta, mitochondrial GN=Atp5f1b
A0A0R4IZX2	Na(+)/H(+) exchange regulatory cofactor NHE-RF GN=Slc9a3r2
Q569X3	U1 small nuclear ribonucleoprotein C GN=Snrpc
Q3TF25	Uncharacterized protein GN=Atp5o
Q8CAQ8	MICOS complex subunit Mic60 GN=Immt
E9Q6D8	Complement component 6 GN=C6
Q62425	Cytochrome c oxidase subunit NDUFA4 GN=Ndufa4
P35979	60S ribosomal protein L12 GN=Rpl12
Q9CQ69	Cytochrome b-c1 complex subunit 8 GN=Uqcrq
P14115	60S ribosomal protein L27a GN=Rpl27a
A0A3B0ITG8	Adiponectin a GN=Adia
P62843	40S ribosomal protein S15 GN=Rps15
Q3UCL7	KH type-2 domain-containing protein GN=Rps3
P53026	60S ribosomal protein L10a GN=Rpl10a
Q8BXX2	Zinc finger and BTB domain-containing protein 49 GN=Zbtb49
Q9QWL7	Keratin, type I cytoskeletal 17 GN=Krt17
Q3U7N1	KOW domain-containing protein
A0A0B4J1I9	Immunoglobulin kappa variable 4-55 (Fragment) GN=Igkv4-55
A0A4E9FT70	IgG3 (Fragment) GN=IGHG3
Q32P04	Keratin 5 GN=Krt5
Q6NXH9	Keratin, type II cytoskeletal 73 GN=Krt73
Q9D4E6	Polyadenylate-binding protein GN=Pabpc6
Q9Z1R9	MCG124046 GN=Prss1
A0A075B6A0	Immunoglobulin heavy constant mu (Fragment) GN=Ighm
A0A075B5V1	Immunoglobulin heavy variable 1-31 GN=Ighv1-31

P62983	Ubiquitin-40S ribosomal protein S27a GN=Rps27a
Q8BH35	Complement component C8 beta chain GN=C8b
Q3URY2	Geminin coiled-coil domain-containing protein 1 GN=Gmnc
A0A140T8M1	Immunoglobulin kappa variable 10-96 (Fragment) GN=Igkv10-96
A2IXM7	Anti-CD30 moab Ki-4 scFv (Fragment)
Q3V0D3	Uncharacterized protein GN=Gm10827
E9Q0B5	Fc fragment of IgG-binding protein GN=Fcgbp
Q8BN87	Uncharacterized protein (Fragment) GN=Mdk
D3YXF5	Complement component 7 GN=C7
Q9D8B3	Charged multivesicular body protein 4b GN=Chmp4b
A8DUV1	Alpha-globin GN=Hbat1
P01655	Ig kappa chain V-III region PC 7132
A0A075B5N5	Immunoglobulin kappa variable 8-26 (Fragment) GN=Igkv8-26
Q3UXI9	Uncharacterized protein GN=Ilf2
P10639	Thioredoxin GN=Txn

Table 7.20 – 14.5 d.p.c. *Pkd2*$^{-/-}$ Kidney IP

Accession	Description
Q3U9N8	Inosine-5'-monophosphate dehydrogenase GN=Impdh2
P62806	Histone H4 GN=H4c1
Q3U4U6	T-complex protein 1 subunit gamma GN=Cct3
Q921L4	Histone H2B GN=LOC665622
Q3TFD9	IF rod domain-containing protein GN=Vim
P43275	Histone H1.1 GN=H1-1
P43277	Histone H1.3 GN=H1-3
P15864	Histone H1.2 GN=H1-2
P43274	Histone H1.4 GN=H1-4
Q3U6P5	RRM domain-containing protein GN=Hnrnpc
A0A1Y7VJN6	Immunoglobulin heavy constant gamma 3 (Fragment) GN=Ighg3
A0A2I3BRL8	Predicted gene 7324 GN=Gm7324
B2RRX1	Actin, beta GN=Actb
Q1WWK3	Hist1h1b protein (Fragment) GN=H1f5
E9PZ16	Basement membrane-specific heparan sulfate proteoglycan core protein GN=Hspg2
P61358	60S ribosomal protein L27 GN=Rpl27
P47911	60S ribosomal protein L6 GN=Rpl6
Q3UZG3	Uncharacterized protein GN=Hnrnpa3
Q80UT7	Rpl7a protein (Fragment) GN=Rpl7a
P05213	Tubulin alpha-1B chain GN=Tuba1b
P19324	Serpin H1 GN=Serpinh1
Q3U944	L-type lectin-like domain-containing protein GN=Lman1
P29341	Polyadenylate-binding protein 1 GN=Pabpc1
Q8VIJ6	Splicing factor, proline- and glutamine-rich GN=Sfpq
O88569	Heterogeneous nuclear ribonucleoproteins A2/B1 GN=Hnrnpa2b1
P63017	Heat shock cognate 71 kDa protein GN=Hspa8
Q4FZH2	MCG50660, isoform CRA_a GN=Rpl26
P53395	Lipoamide acyltransferase component of branched-chain alpha-keto acid dehydrogenase complex, mitochondrial GN=Dbt
P62751	60S ribosomal protein L23a GN=Rpl23a
A0A3B0INZ4	Adiponectin b GN=Adib
Q3UW40	TRASH domain-containing protein GN=Rpl24
Q58EW0	MCG132477, isoform CRA_a GN=Rpl18
O35129	Prohibitin-2 GN=Phb2
P14148	60S ribosomal protein L7 GN=Rpl7
P62911	60S ribosomal protein L32 GN=Rpl32
P56959	RNA-binding protein FUS GN=Fus
P10126	Elongation factor 1-alpha 1 GN=Eef1a1
P63038	60 kDa heat shock protein, mitochondrial GN=Hspd1
Q5XFY8	Uncharacterized protein
A8DUK2	Beta-globin GN=Hbbt1
Q925S1	MRP5 (Fragment) GN=Ighv9-4
A0A0B4J1I1	Immunoglobulin kappa variable 16-104 (Fragment) GN=Igkv16-104
Q60668	Heterogeneous nuclear ribonucleoprotein D0 GN=Hnrnpd

O70569	Ribosomal protein S14 GN=rps14
Q6ZWV7	60S ribosomal protein L35 GN=Rpl35
P48962	ADP/ATP translocase 1 GN=Slc25a4
O08583	THO complex subunit 4 GN=Alyref
Q80ZQ9	Protein Abitram GN=Abitram
P68040	Receptor of activated protein C kinase 1 GN=Rack1
P68372	Tubulin beta-4B chain GN=Tubb4b
A0A0A6YX26	60S ribosomal protein L31 GN=Rpl31
P63163	Small nuclear ribonucleoprotein-associated protein N GN=Snrpn
Q91V99	40S ribosomal protein S30 (Fragment) GN=fau
Q5CZY9	Rps16 protein GN=Rps16
Q4FZE6	40S ribosomal protein S7 GN=Rps7
A0A0G2JE47	Immunoglobulin kappa variable 8-28 (Fragment) GN=Igkv8-28
P62242	40S ribosomal protein S8 GN=Rps8
P62830	60S ribosomal protein L23 GN=Rpl23
Q3TL53	40S ribosomal protein S6
Q3V0Z8	Uncharacterized protein (Fragment) GN=Ddx5
O55142	60S ribosomal protein L35a GN=Rpl35a
Q5M9L1	60S ribosomal protein L36 GN=Rpl36
P62918	60S ribosomal protein L8 GN=Rpl8
A2J1C8	McAB 0.1C3 mmunoglobulin heavy chain (Fragment)
A0A2I3BPG9	MCG113838 GN=Rpl36a-ps1
P01027	Complement C3 GN=C3
P10922	Histone H1.0 GN=H1-0
A0A075B5L7	Immunoglobulin kappa variable 4-80 (Fragment) GN=Igkv4-80
P47963	60S ribosomal protein L13 GN=Rpl13
Q9JJI8	60S ribosomal protein L38 GN=Rpl38
P62315	Small nuclear ribonucleoprotein Sm D1 GN=Snrpd1
Q9Z1R9	MCG124046 GN=Prss1
Q9D1R9	60S ribosomal protein L34 GN=Rpl34
P84089	Enhancer of rudimentary homolog GN=Erh
A0A0A6YWI9	Immunoglobulin heavy variable V1-11 (Fragment) GN=Ighv1-11
A0A0G2JG88	T cell receptor alpha joining 48 (Fragment) GN=Traj48
A0A140T8N8	Immunoglobulin kappa variable 9-123 (Fragment) GN=Igkv9-123
A0A4E9FU10	IgG4 (Fragment) GN=IGHG4
P19137	Laminin subunit alpha-1 GN=Lama1
A0A075B6A0	Immunoglobulin heavy constant mu (Fragment) GN=Ighm
A0A571BEV2	Predicted gene 8251 GN=Gm8251
P10639	Thioredoxin GN=Txn
Q9D3E0	Uncharacterized protein GN=5830453K13Rik
Q99NE5	Regulating synaptic membrane exocytosis protein 1 GN=Rims1

Table 7.21 – 14.5 d.p.c. *Pkd2*$^{lrm4/lrm4}$ Kidney IP

Accession	Description
Q3U4U6	T-complex protein 1 subunit gamma GN=Cct3
P62806	Histone H4 GN=H4c1
Q921L4	Histone H2B GN=LOC665622
O35245	Polycystin-2 GN=Pkd2
Q3U9N8	Inosine-5'-monophosphate dehydrogenase GN=Impdh2
B2RRX1	Actin, beta GN=Actb
P43275	Histone H1.1 GN=H1-1
A0A1Y7VJN6	Immunoglobulin heavy constant gamma 3 (Fragment) GN=Ighg3
P43274	Histone H1.4 GN=H1-4
Q3U6P5	RRM domain-containing protein GN=Hnrnpc
Q1WWK3	Hist1h1b protein (Fragment) GN=H1f5
E9PZ16	Basement membrane-specific heparan sulfate proteoglycan core protein GN=Hspg2
P61358	60S ribosomal protein L27 GN=Rpl27
A0A3B0INZ4	Adiponectin b GN=Adib
A0A2I3BRM6	Heterogeneous nuclear ribonucleoproteins C1/C2 (Fragment) GN=Hnrnpc
Q3U944	L-type lectin-like domain-containing protein GN=Lman1
P53395	Lipoamide acyltransferase component of branched-chain alpha-keto acid dehydrogenase complex, mitochondrial GN=Dbt
P05213	Tubulin alpha-1B chain GN=Tuba1b
Q9CQK2	40S ribosomal protein S24 GN=Rps24
P56959	RNA-binding protein FUS GN=Fus
P01027	Complement C3 GN=C3
P63038	60 kDa heat shock protein, mitochondrial GN=Hspd1
Q9DB79	Ribosomal_S17_N domain-containing protein GN=Rps11
Q9CWK0	Ribosomal_L14e domain-containing protein GN=Rpl14
A0A0A6YX26	60S ribosomal protein L31 GN=Rpl31
P63163	Small nuclear ribonucleoprotein-associated protein N GN=Snrpn
P62918	60S ribosomal protein L8 GN=Rpl8
A0A0B4J1I1	Immunoglobulin kappa variable 16-104 (Fragment) GN=Igkv16-104
Q925S1	MRP5 (Fragment) GN=Ighv9-4
A0A4E9FT70	IgG3 (Fragment) GN=IGHG3
Q9Z1R9	MCG124046 GN=Prss1
A0A075B6A0	Immunoglobulin heavy constant mu (Fragment) GN=Ighm
A0A0G2JG88	T cell receptor alpha joining 48 (Fragment) GN=Traj48
A0A075B5L7	Immunoglobulin kappa variable 4-80 (Fragment) GN=Igkv4-80
V9GWY0	40S ribosomal protein S4 GN=Gm15013
A2BDX3	Adenylyltransferase and sulfurtransferase MOCS3 GN=Mocs3
O55142	60S ribosomal protein L35a GN=Rpl35a
Q3TJ94	Prothrombin GN=F2

Table 7.22 – 14.5 d.p.c. *Pkd2*$^{+/+}$ Lung IPs

Accession	Description
Q5FWJ3	Vimentin GN=Vim
Q921L4	Histone H2B GN=LOC665622
P62806	Histone H4 GN=H4c1
Q64524	Histone H2B type 2-E GN=Hist2h2be
P43275	Histone H1.1 GN=H1-1
P47911	60S ribosomal protein L6 GN=Rpl6
Q80UT7	Rpl7a protein (Fragment) GN=Rpl7a
Q8VIJ6	Splicing factor, proline- and glutamine-rich GN=Sfpq
Q3U9N8	Inosine-5'-monophosphate dehydrogenase GN=Impdh2
P15864	Histone H1.2 GN=H1-2
Q1WWK3	Hist1h1b protein (Fragment) GN=H1f5
Q6GSS7	Histone H2A type 2-A GN=Hist2h2aa1
A2AB79	Histone H2A GN=H2aw
P43274	Histone H1.4 GN=H1-4
P43277	Histone H1.3 GN=H1-3
P29341	Polyadenylate-binding protein 1 GN=Pabpc1
O88569	Heterogeneous nuclear ribonucleoproteins A2/B1 GN=Hnrnpa2b1
Q3UZG3	Uncharacterized protein GN=Hnrnpa3
Q3UK83	Uncharacterized protein GN=Hnrnpa1
P63017	Heat shock cognate 71 kDa protein GN=Hspa8
P56959	RNA-binding protein FUS GN=Fus
A0A2I3BRL8	Predicted gene 7324 GN=Gm7324
Q9WV02	RNA-binding motif protein, X chromosome GN=Rbmx
P43276	Histone H1.5 GN=H1-5
P19324	Serpin H1 GN=Serpinh1
Q0VG47	Heterogeneous nuclear ribonucleoprotein A3 GN=Hnrnpa3
Q03265	ATP synthase subunit alpha, mitochondrial GN=Atp5f1a
Q5FWJ5	Hnrpk protein GN=Hnrnpk
B2RRX1	Actin, beta GN=Actb
Q3V0Z8	Uncharacterized protein (Fragment) GN=Ddx5
A0A1Y7VJN6	Immunoglobulin heavy constant gamma 3 (Fragment) GN=Ighg3
P61358	60S ribosomal protein L27 GN=Rpl27
Q3UW40	TRASH domain-containing protein GN=Rpl24
A0A1W2P768	H3 clustered histone 14 GN=H3c14
P24369	Peptidyl-prolyl cis-trans isomerase B GN=Ppib
Q4FZH2	MCG50660, isoform CRA_a GN=Rpl26
Q3U4U6	T-complex protein 1 subunit gamma GN=Cct3
O08583	THO complex subunit 4 GN=Alyref
Q3U6P5	RRM domain-containing protein GN=Hnrnpc
P10126	Elongation factor 1-alpha 1 GN=Eef1a1
P62751	60S ribosomal protein L23a GN=Rpl23a
Q9D8E6	60S ribosomal protein L4 GN=Rpl4
P20029	Endoplasmic reticulum chaperone BiP GN=Hspa5
O35129	Prohibitin-2 GN=Phb2

P62242	40S ribosomal protein S8 GN=Rps8
O70499	Small nuclear ribonucleoprotein-associated protein GN=Snrpn
O70569	Ribosomal protein S14 GN=rps14
A0A0A6YX26	60S ribosomal protein L31 GN=Rpl31
P62702	40S ribosomal protein S4, X isoform GN=Rps4x
P27659	60S ribosomal protein L3 GN=Rpl3
Q58EU8	Igk protein GN=Igk
Q58DZ3	MCG20799 GN=Rpl30
Q5RJV5	Polypyrimidine tract binding protein 1 GN=Ptbp1
P05784	Keratin, type I cytoskeletal 18 GN=Krt18
P68372	Tubulin beta-4B chain GN=Tubb4b
Q64522	Histone H2A type 2-B GN=Hist2h2ab
A0A1L1STE4	Interleukin enhancer-binding factor 3 GN=Ilf3
Q9CX86	Heterogeneous nuclear ribonucleoprotein A0 GN=Hnrnpa0
P05213	Tubulin alpha-1B chain GN=Tuba1b
E9QNN1	ATP-dependent RNA helicase A GN=Dhx9
Q9DCV7	Keratin, type II cytoskeletal 7 GN=Krt7
Q3UCL7	KH type-2 domain-containing protein GN=Rps3
P62911	60S ribosomal protein L32 GN=Rpl32
P31001	Desmin GN=Des
P97351	40S ribosomal protein S3a GN=Rps3a
P62320	Small nuclear ribonucleoprotein Sm D3 GN=Snrpd3
Q60668	Heterogeneous nuclear ribonucleoprotein D0 GN=Hnrnpd
P0C0S6	Histone H2A.Z GN=H2az1
G5E924	Heterogeneous nuclear ribonucleoprotein L (Fragment) GN=Hnrnpl
P14733	Lamin-B1 GN=Lmnb1
P14148	60S ribosomal protein L7 GN=Rpl7
Q58EW0	MCG132477, isoform CRA_a GN=Rpl18
Q3U741	DEAD (Asp-Glu-Ala-Asp) box polypeptide 17, isoform CRA_a GN=Ddx17
Q9CQK2	40S ribosomal protein S24 GN=Rps24
Q9DB79	Ribosomal_S17_N domain-containing protein GN=Rps11
P62918	60S ribosomal protein L8 GN=Rpl8
A8DUK4	Beta-globin GN=Hbb-bs
Q4FZE6	40S ribosomal protein S7 GN=Rps7
Q64012	RNA-binding protein Raly GN=Raly
A0A0A0MQF6	Glyceraldehyde-3-phosphate dehydrogenase GN=Gapdh
Q9CWK0	Ribosomal_L14e domain-containing protein GN=Rpl14
Q3TF40	Uncharacterized protein (Fragment) GN=Nono
P62317	Small nuclear ribonucleoprotein Sm D2 GN=Snrpd2
P63325	40S ribosomal protein S10 GN=Rps10
Q3TVV6	Uncharacterized protein GN=Hnrnpu
Q8BN87	Uncharacterized protein (Fragment) GN=Mdk
Q8C2Q3	RNA-binding protein 14 GN=Rbm14
A8DUV3	Alpha-globin GN=Hbat1
Q20BD0	Heterogeneous nuclear ribonucleoprotein A/B GN=Hnrnpab
Q8C2Q7	Heterogeneous nuclear ribonucleoprotein H GN=Hnrnph1

A0A3B0INZ4	Adiponectin b GN=Adib
P47963	60S ribosomal protein L13 GN=Rpl13
P35550	rRNA 2'-O-methyltransferase fibrillarin GN=Fbl
Q5SQB7	MCG68069 GN=Npm1
Q60932	Voltage-dependent anion-selective channel protein 1 GN=Vdac1
Q3THG0	Uncharacterized protein GN=Atp5o
P47915	60S ribosomal protein L29 GN=Rpl29
Q5M9J8	MCG13936 GN=Rpl28
P25444	40S ribosomal protein S2 GN=Rps2
A0A1Y7VKY1	MCG116671 GN=Rps18-ps5
Q3U8M3	Uncharacterized protein GN=Rpl37a
F8WGL3	Cofilin-1 GN=Cfl1
Q8BTM8	Filamin-A GN=Flna
Q80V08	Rpl17 protein (Fragment) GN=Rpl17
Q9CY58	Plasminogen activator inhibitor 1 RNA-binding protein GN=Serbp1
Q9JJI8	60S ribosomal protein L38 GN=Rpl38
P62315	Small nuclear ribonucleoprotein Sm D1 GN=Snrpd1
P70372	ELAV-like protein 1 GN=Elavl1
Q5BLJ7	MCG10205 GN=Rps13
P68040	Receptor of activated protein C kinase 1 GN=Rack1
Q5M9L1	60S ribosomal protein L36 GN=Rpl36
P62983	Ubiquitin-40S ribosomal protein S27a GN=Rps27a
P68433	Histone H3.1 GN=H3c1
Q6ZWV7	60S ribosomal protein L35 GN=Rpl35
P60867	40S ribosomal protein S20 GN=Rps20
A0A0B4J1J7	Immunoglobulin heavy variable 1-82 GN=Ighv1-82
Q58E56	Igh protein GN=Igh
Q3U7F6	Uncharacterized protein GN=Zfp422
A0A0F7QZE4	MAb 110 heavy chain GN=HC
A0A3B0ITG8	Adiponectin a GN=Adia
Q3U561	Ribosomal protein GN=Rpl10a
H7BX95	Serine/arginine-rich-splicing factor 1 GN=Srsf1
O35245	Polycystin-2 GN=Pkd2
Q91V99	40S ribosomal protein S30 (Fragment) GN=fau
Q9CY57	Chromatin target of PRMT1 protein GN=Chtop
P62852	40S ribosomal protein S25 GN=Rps25
Q80ZM5	H1 histone family, member X GN=H1f10
P57776	Elongation factor 1-delta GN=Eef1d
A0A338P6F6	High mobility group protein HMG-I/HMG-Y GN=Hmga1
Q5BLK1	40S ribosomal protein S6 GN=Rps6
Q8BQ46	TAF15 RNA polymerase II, TATA box binding protein (TBP)-associated factor GN=Taf15
Q8CAQ8	MICOS complex subunit Mic60 GN=Immt
P62843	40S ribosomal protein S15 GN=Rps15
O09167	60S ribosomal protein L21 GN=Rpl21
Q3UBK2	Uncharacterized protein
Q6ZWN5	40S ribosomal protein S9 GN=Rps9

Q62189	U1 small nuclear ribonucleoprotein A GN=Snrpa
Q3U7B3	Uncharacterized protein GN=Tmpo
Q7TMK9	Heterogeneous nuclear ribonucleoprotein Q GN=Syncrip
Q3U850	Ribosomal_L18_c domain-containing protein GN=Rpl5
P30681	High mobility group protein B2 GN=Hmgb2
Q8JZX4	Splicing factor 45 GN=Rbm17
Q3THU7	Clathrin light chain GN=Clta
P60335	Poly(rC)-binding protein 1 GN=Pcbp1
P63168	Dynein light chain 1, cytoplasmic GN=Dynll1
Q80U76	Ribosome biogenesis regulatory protein (Fragment) GN=Rrs1
P70670	Nascent polypeptide-associated complex subunit alpha, muscle-specific form GN=Naca
P19253	60S ribosomal protein L13a GN=Rpl13a
Q3U7D2	Ribosomal protein L15 GN=Rpl15
Q497N1	40S ribosomal protein S26 GN=Rps26
P84089	Enhancer of rudimentary homolog GN=Erh
A0A0B4J1I9	Immunoglobulin kappa variable 4-55 (Fragment) GN=Igkv4-55
O88477	Insulin-like growth factor 2 mRNA-binding protein 1 GN=Igf2bp1
Q3TJ01	tRNA-splicing ligase RtcB homolog GN=Rtcb
Q9D0E1	Heterogeneous nuclear ribonucleoprotein M GN=Hnrnpm
P62830	60S ribosomal protein L23 GN=Rpl23
Q9CR49	Globin b1 GN=Hbb-y
Q9D8B3	Charged multivesicular body protein 4b GN=Chmp4b
Q60749	KH domain-containing, RNA-binding, signal transduction-associated protein 1 GN=Khdrbs1
P14115	60S ribosomal protein L27a GN=Rpl27a
O55142	60S ribosomal protein L35a GN=Rpl35a
E9PZ16	Basement membrane-specific heparan sulfate proteoglycan core protein GN=Hspg2
P06330	Ig heavy chain V region AC38 205.12
Q8BT90	Uncharacterized protein (Fragment) GN=Rps17
Q6NSP9	High mobility group protein HMGI-C GN=Hmga2
Q9D1R9	60S ribosomal protein L34 GN=Rpl34
Q99JF8	PC4 and SFRS1-interacting protein GN=Psip1
Q569X3	U1 small nuclear ribonucleoprotein C GN=Snrpc
Q3TVP0	MCG120563, isoform CRA_a GN=mCG_120563
Q5SUS9	RNA-binding protein EWS GN=Ewsr1
P02301	Histone H3.3C GN=H3f3c
Q3TFG3	Uncharacterized protein GN=Eif4a1
Q3UXI9	Uncharacterized protein GN=Ilf2
P09405	Nucleolin GN=Ncl
Q3TKG5	H/ACA ribonucleoprotein complex subunit GN=Gar1
P10922	Histone H1.0 GN=H1-0
P35979	60S ribosomal protein L12 GN=Rpl12
Q3THA0	Eukaryotic translation initiation factor 3 subunit G GN=Eif3g
Q6ZQ61	MCG121979, isoform CRA_c (Fragment) GN=Matr3
Q3UEB3	Poly(U)-binding-splicing factor PUF60 GN=Puf60
A0A1W2P7Q9	Myosin light polypeptide 6 GN=Myl6
Q62425	Cytochrome c oxidase subunit NDUFA4 GN=Ndufa4

Q9CQ69	Cytochrome b-c1 complex subunit 8 GN=Uqcrq
Q925S1	MRP5 (Fragment) GN=Ighv9-4
Q9CXW4	60S ribosomal protein L11 GN=Rpl11
Q5EBP9	Tripartite motif-containing 28 GN=Trim28
F6W687	Non-histone chromosomal protein HMG-17 (Fragment) GN=Hmgn2
A0A1D5RM85	60S ribosomal protein L18a (Fragment) GN=Rpl18a
Q6ZWU9	40S ribosomal protein S27 GN=Rps27
A0A075B5R5	Immunoglobulin heavy variable 4-1 (Fragment) GN=Ighv4-1
O70251	Elongation factor 1-beta GN=Eef1b
A2IXM7	Anti-CD30 moab Ki-4 scFv (Fragment)
Q3TLH4	Protein PRRC2C GN=Prrc2c
Q9CQS2	H/ACA ribonucleoprotein complex subunit 3 GN=Nop10
B1ASA5	Zinc finger protein 362 GN=Zfp362
P57784	U2 small nuclear ribonucleoprotein A' GN=Snrpa1
Q5SF07	Insulin-like growth factor 2 mRNA-binding protein 2 GN=Igf2bp2
Q5I0T8	Ribosomal protein L19 GN=Rpl19
A0A075B5L7	Immunoglobulin kappa variable 4-80 (Fragment) GN=Igkv4-80
E9Q317	Histone deacetylase complex subunit SAP18 GN=Sap18
A0A2I3BPG9	MCG113838 GN=Rpl36a-ps1
A2AM97	Ribosomal protein 10 GN=RP23-436K3.4-001
A0A075B5S2	Immunoglobulin heavy variable 7-1 (Fragment) GN=Ighv7-1
Q99JY0	Trifunctional enzyme subunit beta, mitochondrial GN=Hadhb
P62858	40S ribosomal protein S28 GN=Rps28
Q3TW77	Uncharacterized protein GN=Grn
Q06477	IFN-response element binding factor 2 (Fragment) GN=Srsf2
Q9D2G2	Dihydrolipoyllysine-residue succinyltransferase component of 2-oxoglutarate dehydrogenase complex, mitochondrial GN=Dlst
P63038	60 kDa heat shock protein, mitochondrial GN=Hspd1
P35700	Peroxiredoxin-1 GN=Prdx1
Q9CZI5	Uncharacterized protein GN=Rps23
A0A0B4J1I1	Immunoglobulin kappa variable 16-104 (Fragment) GN=Igkv16-104
Q571G8	MKIAA1649 protein (Fragment) GN=Poldip3
A0A0B4J1E2	SNW domain-containing protein 1 GN=Snw1
P11031	Activated RNA polymerase II transcriptional coactivator p15 GN=Sub1
Q9CQN7	39S ribosomal protein L41, mitochondrial GN=Mrpl41
P48962	ADP/ATP translocase 1 GN=Slc25a4
Q505A8	MCG17585 GN=Rpl39
S4R1M2	Scaffold attachment factor B1 GN=Safb
Q3U944	L-type lectin-like domain-containing protein GN=Lman1
P52480	Pyruvate kinase PKM GN=Pkm
F6T4M4	Serine/arginine repetitive matrix protein 1 (Fragment) GN=Srrm1
Q9DB77	Cytochrome b-c1 complex subunit 2, mitochondrial GN=Uqcrc2
Q7TPV4	Myb-binding protein 1A GN=Mybbp1a
P62259	14-3-3 protein epsilon GN=Ywhae
Q71LX8	Heat shock protein 84b GN=Hsp90ab1
P80315	T-complex protein 1 subunit delta GN=Cct4
P27773	Protein disulfide-isomerase A3 GN=Pdia3

P01027	Complement C3 GN=C3
P01662	Ig kappa chain V-III region ABPC 22/PC 9245
A0A0G2JGE7	Immunoglobulin kappa variable 4-86 (Fragment) GN=Igkv4-86
Q3UKH3	Uncharacterized protein GN=Acaa2
E9Q7G0	Nuclear mitotic apparatus protein 1 GN=Numa1
Q99JB2	Stomatin-like protein 2, mitochondrial GN=Stoml2
Q3TUQ5	Pinin GN=Pnn
P62305	Small nuclear ribonucleoprotein E GN=Snrpe
A0A1W2P7A1	40S ribosomal protein S12 GN=Rps12
Q9DB15	39S ribosomal protein L12, mitochondrial GN=Mrpl12
A0A0G2JDG9	Immunoglobulin kappa variable 8-16 (Fragment) GN=Igkv8-16
Q9D937	Uncharacterized protein C11orf98 homolog
P48771	Cytochrome c oxidase subunit 7A2, mitochondrial GN=Cox7a2
P53996	Cellular nucleic acid-binding protein GN=Cnbp
Q00899	Transcriptional repressor protein YY1 GN=Yy1
Q8VDG6	Mitogen-activated protein kinase kinase kinase 21 GN=Map3k21
Q8BG13	RNA-binding protein 3 GN=Rbm3
A2AKX3	Probable helicase senataxin GN=Setx
Q3TL71	Uncharacterized protein GN=Hnrnpk
I6L958	Igk protein GN=Igk
P63163	Small nuclear ribonucleoprotein-associated protein N GN=Snrpn
Q3U5I2	Uncharacterized protein GN=Ptbp1
P68033	Actin, alpha cardiac muscle 1 GN=Actc1
A0A2I3BRM6	Heterogeneous nuclear ribonucleoproteins C1/C2 (Fragment) GN=Hnrnpc
P11679	Keratin, type II cytoskeletal 8 GN=Krt8
P56480	ATP synthase subunit beta, mitochondrial GN=Atp5f1b
Q571F9	MKIAA4115 protein (Fragment) GN=G3bp1
Q545A2	MCG11560 GN=Slc25a5
P04104	Keratin, type II cytoskeletal 1 GN=Krt1
Q3U536	Uncharacterized protein GN=Npm1
P24270	Catalase GN=Cat
Q32P04	Keratin 5 GN=Krt5
P19001	Keratin, type I cytoskeletal 19 GN=Krt19
P38647	Stress-70 protein, mitochondrial GN=Hspa9
D3YTQ3	Heterogeneous nuclear ribonucleoprotein D-like GN=Hnrnpdl
Q6IFZ6	Keratin, type II cytoskeletal 1b GN=Krt77
P53395	Lipoamide acyltransferase component of branched-chain alpha-keto acid dehydrogenase complex, mitochondrial GN=Dbt
Q6PDG5	SWI/SNF complex subunit SMARCC2 GN=Smarcc2
Q3T9Y8	Eukaryotic translation initiation factor 3 subunit I GN=Eif3i
Q3TF25	Uncharacterized protein GN=Atp5o
Q5CZY9	Rps16 protein GN=Rps16
P98086	Complement C1q subcomponent subunit A GN=C1qa
Q6PFA2	Clathrin light chain GN=Clta
Q9Z2X1	Heterogeneous nuclear ribonucleoprotein F GN=Hnrnpf
Q80U89	MKIAA0034 protein (Fragment) GN=mKIAA0034
Q9CQF3	Cleavage and polyadenylation specificity factor subunit 5 GN=Nudt21

P62245	40S ribosomal protein S15a GN=Rps15a
Q3U8W9	Uncharacterized protein GN=Hnrnpr
P59708	Splicing factor 3B subunit 6 GN=Sf3b6
Q8BX10	Serine/threonine-protein phosphatase PGAM5, mitochondrial GN=Pgam5
F7DEU6	Inosine-5'-monophosphate dehydrogenase GN=Impdh1
B2RUC7	Serine/threonine kinase receptor associated protein GN=Strap
Q9CQE8	RNA transcription, translation and transport factor protein GN=RTRAF
A0A075B5V1	Immunoglobulin heavy variable 1-31 GN=Ighv1-31
Q7TNV0	Protein DEK GN=Dek
P17751	Triosephosphate isomerase GN=Tpi1
Q922V4	Pleiotropic regulator 1 GN=Plrg1
D3Z420	Family with sequence similarity 186, member B GN=Fam186b
P62274	40S ribosomal protein S29 GN=Rps29
B2CY77	Laminin receptor (Fragment) GN=Rpsa
Q3UV17	Keratin, type II cytoskeletal 2 oral GN=Krt76
Q8CCK0	Core histone macro-H2A.2 GN=H2afy2
Q99PL5	Ribosome-binding protein 1 GN=Rrbp1
Q3UIJ2	Tr-type G domain-containing protein GN=Eif2s3x
Q99KP6	Pre-mRNA-processing factor 19 GN=Prpf19
Q3UAD6	Heat shock protein 90kDa beta (Grp94), member 1 GN=Hsp90b1
P83882	60S ribosomal protein L36a GN=Rpl36a
Q3THE2	Myosin regulatory light chain 12B GN=Myl12b
A0A0G2JE47	Immunoglobulin kappa variable 8-28 (Fragment) GN=Igkv8-28
O54941	SWI/SNF-related matrix-associated actin-dependent regulator of chromatin subfamily E member 1 GN=Smarce1
P01675	Ig kappa chain V-VI region XRPC 44
Q3THH1	Uncharacterized protein GN=Pdia6
I6L9I7	Cbx3 protein GN=Cbx3
Q9Z1R9	MCG124046 GN=Prss1
Q4VAG4	MCG12304 GN=Rpl22
Q0VBA4	MCG16976, isoform CRA_c GN=Rpl22l1
P01655	Ig kappa chain V-III region PC 7132
Q3TVM2	Aldedh domain-containing protein GN=Aldh2
Q8C671	RRM domain-containing protein GN=Srsf2
Q6P5H2	Nestin GN=Nes
Q6PE01	U5 small nuclear ribonucleoprotein 40 kDa protein GN=Snrnp40
Q3U900	Dolichyl-diphosphooligosaccharide--protein glycosyltransferase subunit 1 GN=Rpn1
Q91VN4	MICOS complex subunit Mic25 GN=Chchd6
E9Q6D8	Complement component 6 GN=C6
Q3U6B1	Uncharacterized protein (Fragment) GN=G3bp2
A0A0M4KPD8	B2 12-1 anti-human butyrylcholinesterase (BChE) light chain variable region (Fragment)
A0A1S6GWH2	Uncharacterized protein GN=Ddx39b
A0A1B0GSX0	L-lactate dehydrogenase GN=Ldha
P10639	Thioredoxin GN=Txn
P18608	Non-histone chromosomal protein HMG-14 GN=Hmgn1
Q03958	Prefoldin subunit 6 GN=Pfdn6
H3BLG3	Ras-related protein Rab-26 GN=Rab26

Q80VD1	Protein FAM98B GN=Fam98b
P67778	Prohibitin GN=Phb
Q5FWB6	60S acidic ribosomal protein P0 GN=Rplp0
A0A0A1HAM8	80K protein GN=Marcks
Q3TAH3	Nucleoplasmin domain-containing protein GN=Npm3
Q3V1M8	Uncharacterized protein GN=Hdlbp
P61965	WD repeat-containing protein 5 GN=Wdr5
Q99MP8	BRCA1-associated protein GN=Brap
A0A0R4J008	Histone deacetylase 2 GN=Hdac2
Q8VEA0	Igh protein GN=Igh
Q08288	Cell growth-regulating nucleolar protein GN=Lyar
O70591	Prefoldin subunit 2 GN=Pfdn2
Q3UL54	Uncharacterized protein GN=Rsl1d1
Q6A0D0	MKIAA0106 protein (Fragment) GN=Prdx6
E9Q0F0	Keratin 78 GN=Krt78
P80313	T-complex protein 1 subunit eta GN=Cct7
A6ZI44	Fructose-bisphosphate aldolase GN=Aldoa
Q8C817	Transmembrane protein 200A GN=Tmem200a
Q60865	Caprin-1 GN=Caprin1
Q3THB0	RRM domain-containing protein GN=Eif4b
Q8VDP4	Cell cycle and apoptosis regulator protein 2 GN=Ccar2
A2RS68	Small nuclear ribonucleoprotein 70 (U1) GN=Snrnp70
Q810A4	RNA helicase (Fragment) GN=Ddx55
A0A087WSB8	High mobility group nucleosome-binding domain-containing protein 3 GN=Hmgn3
J3QNK8	Abl interactor 1 GN=Abi1
Q9CQZ5	NADH dehydrogenase [ubiquinone] 1 alpha subcomplex subunit 6 GN=Ndufa6
Q8R2K3	Single-stranded DNA binding protein 1 GN=Ssbp1
Q3TQP7	Uncharacterized protein GN=Acat1
Q6A0C9	MKIAA0109 protein (Fragment) GN=Ap2m1
Q99N92	39S ribosomal protein L27, mitochondrial GN=Mrpl27
P39447	Tight junction protein ZO-1 GN=Tjp1
B2RXS4	Plexin-B2 GN=Plxnb2
Q8BL97	Serine/arginine-rich splicing factor 7 GN=Srsf7
Q9JKB3	Y-box-binding protein 3 GN=Ybx3
Q8R1S0	Ubiquinone biosynthesis monooxygenase COQ6, mitochondrial GN=Coq6
Q80ZI7	Igh protein GN=Igh
Q3TG93	Uncharacterized protein GN=Ssb
A0A0G2JFH2	Microtubule-associated protein (Fragment) GN=Map4
A6H622	GTP-binding nuclear protein Ran GN=Rasl2-9
Q01730	Ras suppressor protein 1 GN=Rsu1
Q9Z1A1	TFG protein GN=Tfg
Q9CRB9	MICOS complex subunit Mic19 GN=Chchd3
Q3TEA8	Heterochromatin protein 1-binding protein 3 GN=Hp1bp3
P48678	Prelamin-A/C GN=Lmna
A0A0R4J170	Transcription activator BRG1 GN=Smarca4
Q6R0H7	Guanine nucleotide-binding protein G(s) subunit alpha isoforms XLas GN=Gnas

Q9CPQ1	Cytochrome c oxidase subunit 6C GN=Cox6c
Q9D411	Testis-specific serine/threonine-protein kinase 4 GN=Tssk4
P0DP27	Calmodulin-2 GN=Calm2
Q8QZY9	Splicing factor 3B subunit 4 GN=Sf3b4
Q91X78	Erlin-1 GN=Erlin1
P26516	26S proteasome non-ATPase regulatory subunit 7 GN=Psmd7
Q9Z0X1	Apoptosis-inducing factor 1, mitochondrial GN=Aifm1
E9PVX6	Proliferation marker protein Ki-67 GN=Mki67
Q8R4R6	Nucleoporin NUP35 GN=Nup35
P57722	Poly(rC)-binding protein 3 GN=Pcbp3
Q8BH95	Enoyl-CoA hydratase, mitochondrial GN=Echs1
P11983	T-complex protein 1 subunit alpha GN=Tcp1
Q3UD06	ATP synthase subunit gamma GN=Atp5c1
Q9CZD6	Proliferating cell nuclear antigen GN=Pcna
Q8BFR5	Elongation factor Tu, mitochondrial GN=Tufm
Q99M87	DnaJ homolog subfamily A member 3, mitochondrial GN=Dnaja3
P62897	Cytochrome c, somatic GN=Cycs
Q8BTW3	Exosome complex component MTR3 GN=Exosc6
Q3TQX5	Uncharacterized protein GN=Ddx3x
D3Z2H9	Tropomyosin 3, related sequence 7 GN=Tpm3-rs7
P80316	T-complex protein 1 subunit epsilon GN=Cct5
Q5SQX6	Cytoplasmic FMR1-interacting protein 2 GN=Cyfip2
Q3TJ21	Pyrroline-5-carboxylate reductase GN=Pycr2

Table 7.23 – 14.5 d.p.c. *Pkd2*$^{-/-}$ Lung IP

Accession	Description
Q5FWJ3	Vimentin GN=Vim
Q921L4	Histone H2B GN=LOC665622
P62806	Histone H4 GN=H4c1
Q64524	Histone H2B type 2-E GN=Hist2h2be
P43275	Histone H1.1 GN=H1-1
P47911	60S ribosomal protein L6 GN=Rpl6
Q80UT7	Rpl7a protein (Fragment) GN=Rpl7a
Q8VIJ6	Splicing factor, proline- and glutamine-rich GN=Sfpq
Q3U9N8	Inosine-5'-monophosphate dehydrogenase GN=Impdh2
P15864	Histone H1.2 GN=H1-2
Q1WWK3	Hist1h1b protein (Fragment) GN=H1f5
Q6GSS7	Histone H2A type 2-A GN=Hist2h2aa1
A2AB79	Histone H2A GN=H2aw
P43274	Histone H1.4 GN=H1-4
P43277	Histone H1.3 GN=H1-3
P29341	Polyadenylate-binding protein 1 GN=Pabpc1
O88569	Heterogeneous nuclear ribonucleoproteins A2/B1 GN=Hnrnpa2b1
Q3UZG3	Uncharacterized protein GN=Hnrnpa3
Q3UK83	Uncharacterized protein GN=Hnrnpa1
P63017	Heat shock cognate 71 kDa protein GN=Hspa8
P56959	RNA-binding protein FUS GN=Fus
A0A2I3BRL8	Predicted gene 7324 GN=Gm7324
Q9WV02	RNA-binding motif protein, X chromosome GN=Rbmx
P43276	Histone H1.5 GN=H1-5
P19324	Serpin H1 GN=Serpinh1
Q03265	ATP synthase subunit alpha, mitochondrial GN=Atp5f1a
Q5FWJ5	Hnrpk protein GN=Hnrnpk
B2RRX1	Actin, beta GN=Actb
Q3V0Z8	Uncharacterized protein (Fragment) GN=Ddx5
A0A1Y7VJN6	Immunoglobulin heavy constant gamma 3 (Fragment) GN=Ighg3
P61358	60S ribosomal protein L27 GN=Rpl27
Q3UW40	TRASH domain-containing protein GN=Rpl24
A0A1W2P768	H3 clustered histone 14 GN=H3c14
P24369	Peptidyl-prolyl cis-trans isomerase B GN=Ppib
Q4FZH2	MCG50660, isoform CRA_a GN=Rpl26
Q3U4U6	T-complex protein 1 subunit gamma GN=Cct3
O08583	THO complex subunit 4 GN=Alyref
Q3U6P5	RRM domain-containing protein GN=Hnrnpc
P10126	Elongation factor 1-alpha 1 GN=Eef1a1
P62751	60S ribosomal protein L23a GN=Rpl23a
Q9D8E6	60S ribosomal protein L4 GN=Rpl4
P20029	Endoplasmic reticulum chaperone BiP GN=Hspa5
O35129	Prohibitin-2 GN=Phb2
P62242	40S ribosomal protein S8 GN=Rps8

O70499	Small nuclear ribonucleoprotein-associated protein GN=Snrpn
O70569	Ribosomal protein S14 GN=rps14
A0A0A6YX26	60S ribosomal protein L31 GN=Rpl31
P62702	40S ribosomal protein S4, X isoform GN=Rps4x
P27659	60S ribosomal protein L3 GN=Rpl3
Q58EU8	Igk protein GN=Igk
Q58DZ3	MCG20799 GN=Rpl30
Q5RJV5	Polypyrimidine tract binding protein 1 GN=Ptbp1
P05784	Keratin, type I cytoskeletal 18 GN=Krt18
P68372	Tubulin beta-4B chain GN=Tubb4b
Q64522	Histone H2A type 2-B GN=Hist2h2ab
A0A1L1STE4	Interleukin enhancer-binding factor 3 GN=Ilf3
Q9CX86	Heterogeneous nuclear ribonucleoprotein A0 GN=Hnrnpa0
P05213	Tubulin alpha-1B chain GN=Tuba1b
E9QNN1	ATP-dependent RNA helicase A GN=Dhx9
Q9DCV7	Keratin, type II cytoskeletal 7 GN=Krt7
P68033	Actin, alpha cardiac muscle 1 GN=Actc1
Q3UCL7	KH type-2 domain-containing protein GN=Rps3
Q32P04	Keratin 5 GN=Krt5
P62911	60S ribosomal protein L32 GN=Rpl32
P31001	Desmin GN=Des
P97351	40S ribosomal protein S3a GN=Rps3a
P62320	Small nuclear ribonucleoprotein Sm D3 GN=Snrpd3
Q60668	Heterogeneous nuclear ribonucleoprotein D0 GN=Hnrnpd
P0C0S6	Histone H2A.Z GN=H2az1
G5E924	Heterogeneous nuclear ribonucleoprotein L (Fragment) GN=Hnrnpl
P14733	Lamin-B1 GN=Lmnb1
P14148	60S ribosomal protein L7 GN=Rpl7
Q58EW0	MCG132477, isoform CRA_a GN=Rpl18
Q3U741	DEAD (Asp-Glu-Ala-Asp) box polypeptide 17, isoform CRA_a GN=Ddx17
A0A2I3BRM6	Heterogeneous nuclear ribonucleoproteins C1/C2 (Fragment) GN=Hnrnpc
Q9CQK2	40S ribosomal protein S24 GN=Rps24
Q9DB79	Ribosomal_S17_N domain-containing protein GN=Rps11
P62918	60S ribosomal protein L8 GN=Rpl8
A8DUK4	Beta-globin GN=Hbb-bs
P11679	Keratin, type II cytoskeletal 8 GN=Krt8
Q4FZE6	40S ribosomal protein S7 GN=Rps7
Q64012	RNA-binding protein Raly GN=Raly
A0A0A0MQF6	Glyceraldehyde-3-phosphate dehydrogenase GN=Gapdh
Q9CWK0	Ribosomal_L14e domain-containing protein GN=Rpl14
Q3TF40	Uncharacterized protein (Fragment) GN=Nono
P62317	Small nuclear ribonucleoprotein Sm D2 GN=Snrpd2
P63325	40S ribosomal protein S10 GN=Rps10
Q3TVV6	Uncharacterized protein GN=Hnrnpu
Q8BN87	Uncharacterized protein (Fragment) GN=Mdk
Q8C2Q3	RNA-binding protein 14 GN=Rbm14

A8DUV3	Alpha-globin GN=Hbat1
Q20BD0	Heterogeneous nuclear ribonucleoprotein A/B GN=Hnrnpab
Q8C2Q7	Heterogeneous nuclear ribonucleoprotein H GN=Hnrnph1
A0A3B0INZ4	Adiponectin b GN=Adib
P47963	60S ribosomal protein L13 GN=Rpl13
P50446	Keratin, type II cytoskeletal 6A GN=Krt6a
P35550	rRNA 2'-O-methyltransferase fibrillarin GN=Fbl
Q5SQB7	MCG68069 GN=Npm1
Q60932	Voltage-dependent anion-selective channel protein 1 GN=Vdac1
Q3THG0	Uncharacterized protein GN=Atp5o
P47915	60S ribosomal protein L29 GN=Rpl29
Q5M9J8	MCG13936 GN=Rpl28
P25444	40S ribosomal protein S2 GN=Rps2
A0A1Y7VKY1	MCG116671 GN=Rps18-ps5
Q3U8M3	Uncharacterized protein GN=Rpl37a
F8WGL3	Cofilin-1 GN=Cfl1
P19001	Keratin, type I cytoskeletal 19 GN=Krt19
P04104	Keratin, type II cytoskeletal 1 GN=Krt1
Q8BTM8	Filamin-A GN=Flna
Q80V08	Rpl17 protein (Fragment) GN=Rpl17
Q9CY58	Plasminogen activator inhibitor 1 RNA-binding protein GN=Serbp1
Q9JJI8	60S ribosomal protein L38 GN=Rpl38
P62315	Small nuclear ribonucleoprotein Sm D1 GN=Snrpd1
P70372	ELAV-like protein 1 GN=Elavl1
Q5BLJ7	MCG10205 GN=Rps13
P68040	Receptor of activated protein C kinase 1 GN=Rack1
Q5M9L1	60S ribosomal protein L36 GN=Rpl36
P62983	Ubiquitin-40S ribosomal protein S27a GN=Rps27a
Q9QWL7	Keratin, type I cytoskeletal 17 GN=Krt17
P68433	Histone H3.1 GN=H3c1
Q6ZWV7	60S ribosomal protein L35 GN=Rpl35
P60867	40S ribosomal protein S20 GN=Rps20
Q6IFX2	Keratin, type I cytoskeletal 42 GN=Krt42
A0A0B4J1J7	Immunoglobulin heavy variable 1-82 GN=Ighv1-82
Q58E56	Igh protein GN=Igh
Q3U7F6	Uncharacterized protein GN=Zfp422
A0A0F7QZE4	MAb 110 heavy chain GN=HC
A0A3B0ITG8	Adiponectin a GN=Adia
Q3U561	Ribosomal protein GN=Rpl10a
H7BX95	Serine/arginine-rich-splicing factor 1 GN=Srsf1
Q91V99	40S ribosomal protein S30 (Fragment) GN=fau
Q9CY57	Chromatin target of PRMT1 protein GN=Chtop
Q6IFZ6	Keratin, type II cytoskeletal 1b GN=Krt77
P62852	40S ribosomal protein S25 GN=Rps25
Q80ZM5	H1 histone family, member X GN=H1f10
E9Q0F0	Keratin 78 GN=Krt78

Q8VDD5	Myosin-9 GN=Myh9
P57776	Elongation factor 1-delta GN=Eef1d
A0A338P6F6	High mobility group protein HMG-I/HMG-Y GN=Hmga1
Q8VED5	Keratin, type II cytoskeletal 79 GN=Krt79
Q5CZY9	Rps16 protein GN=Rps16
Q5BLK1	40S ribosomal protein S6 GN=Rps6
Q3UH59	Myosin-10 GN=Myh10
Q8CAQ8	MICOS complex subunit Mic60 GN=Immt
P62843	40S ribosomal protein S15 GN=Rps15
O09167	60S ribosomal protein L21 GN=Rpl21
Q3UBK2	Uncharacterized protein
Q6ZWN5	40S ribosomal protein S9 GN=Rps9
Q62189	U1 small nuclear ribonucleoprotein A GN=Snrpa
Q3U7B3	Uncharacterized protein GN=Tmpo
Q7TMK9	Heterogeneous nuclear ribonucleoprotein Q GN=Syncrip
Q3U850	Ribosomal_L18_c domain-containing protein GN=Rpl5
P30681	High mobility group protein B2 GN=Hmgb2
P56480	ATP synthase subunit beta, mitochondrial GN=Atp5f1b
Q8JZX4	Splicing factor 45 GN=Rbm17
Q3THU7	Clathrin light chain GN=Clta
P53395	Lipoamide acyltransferase component of branched-chain alpha-keto acid dehydrogenase complex, mitochondrial GN=Dbt
P60335	Poly(rC)-binding protein 1 GN=Pcbp1
P63168	Dynein light chain 1, cytoplasmic GN=Dynll1
Q80U76	Ribosome biogenesis regulatory protein (Fragment) GN=Rrs1
P70670	Nascent polypeptide-associated complex subunit alpha, muscle-specific form GN=Naca
P19253	60S ribosomal protein L13a GN=Rpl13a
Q3U7D2	Ribosomal protein L15 GN=Rpl15
Q497N1	40S ribosomal protein S26 GN=Rps26
P84089	Enhancer of rudimentary homolog GN=Erh
A0A0B4J1I9	Immunoglobulin kappa variable 4-55 (Fragment) GN=Igkv4-55
Q3TJ01	tRNA-splicing ligase RtcB homolog GN=Rtcb
Q9D0E1	Heterogeneous nuclear ribonucleoprotein M GN=Hnrnpm
P62830	60S ribosomal protein L23 GN=Rpl23
Q9Z2X1	Heterogeneous nuclear ribonucleoprotein F GN=Hnrnpf
Q9CR49	Globin b1 GN=Hbb-y
Q9D8B3	Charged multivesicular body protein 4b GN=Chmp4b
Q60749	KH domain-containing, RNA-binding, signal transduction-associated protein 1 GN=Khdrbs1
P14115	60S ribosomal protein L27a GN=Rpl27a
O55142	60S ribosomal protein L35a GN=Rpl35a
E9PZ16	Basement membrane-specific heparan sulfate proteoglycan core protein GN=Hspg2
P06330	Ig heavy chain V region AC38 205.12
Q8BT90	Uncharacterized protein (Fragment) GN=Rps17
Q6NSP9	High mobility group protein HMGI-C GN=Hmga2
P38647	Stress-70 protein, mitochondrial GN=Hspa9
Q9D1R9	60S ribosomal protein L34 GN=Rpl34
Q569X3	U1 small nuclear ribonucleoprotein C GN=Snrpc

Q3TVP0	MCG120563, isoform CRA_a GN=mCG_120563
P02301	Histone H3.3C GN=H3f3c
Q3TFG3	Uncharacterized protein GN=Eif4a1
Q3UXI9	Uncharacterized protein GN=Ilf2
P09405	Nucleolin GN=Ncl
Q3TKG5	H/ACA ribonucleoprotein complex subunit GN=Gar1
P10922	Histone H1.0 GN=H1-0
B2RTP7	Krt2 protein GN=Krt2
P35979	60S ribosomal protein L12 GN=Rpl12
Q3THA0	Eukaryotic translation initiation factor 3 subunit G GN=Eif3g
Q6ZQ61	MCG121979, isoform CRA_c (Fragment) GN=Matr3
Q3UEB3	Poly(U)-binding-splicing factor PUF60 GN=Puf60
A0A1W2P7Q9	Myosin light polypeptide 6 GN=Myl6
P02535	Keratin, type I cytoskeletal 10 GN=Krt10
Q62425	Cytochrome c oxidase subunit NDUFA4 GN=Ndufa4
Q9CQ69	Cytochrome b-c1 complex subunit 8 GN=Uqcrq
Q925S1	MRP5 (Fragment) GN=Ighv9-4
Q9CXW4	60S ribosomal protein L11 GN=Rpl11
Q5EBP9	Tripartite motif-containing 28 GN=Trim28
F6W687	Non-histone chromosomal protein HMG-17 (Fragment) GN=Hmgn2
A0A1D5RM85	60S ribosomal protein L18a (Fragment) GN=Rpl18a
Q6ZWU9	40S ribosomal protein S27 GN=Rps27
Q02257	Junction plakoglobin GN=Jup
A0A075B5R5	Immunoglobulin heavy variable 4-1 (Fragment) GN=Ighv4-1
O70251	Elongation factor 1-beta GN=Eef1b
Q3THH1	Uncharacterized protein GN=Pdia6
A2IXM7	Anti-CD30 moab Ki-4 scFv (Fragment)
P59708	Splicing factor 3B subunit 6 GN=Sf3b6
Q544R5	MCG16669, isoform CRA_b GN=Tardbp
Q3TLH4	Protein PRRC2C GN=Prrc2c
Q9CQS2	H/ACA ribonucleoprotein complex subunit 3 GN=Nop10
Q9WUM5	Succinate--CoA ligase [ADP/GDP-forming] subunit alpha, mitochondrial GN=Suclg1
B1ASA5	Zinc finger protein 362 GN=Zfp362
Q9CQF3	Cleavage and polyadenylation specificity factor subunit 5 GN=Nudt21
Q3T9Y8	Eukaryotic translation initiation factor 3 subunit I GN=Eif3i
P57784	U2 small nuclear ribonucleoprotein A' GN=Snrpa1
Q5SF07	Insulin-like growth factor 2 mRNA-binding protein 2 GN=Igf2bp2
Q5I0T8	Ribosomal protein L19 GN=Rpl19
Q3UL54	Uncharacterized protein GN=Rsl1d1
A0A075B5L7	Immunoglobulin kappa variable 4-80 (Fragment) GN=Igkv4-80
E9Q317	Histone deacetylase complex subunit SAP18 GN=Sap18
A0A2I3BPG9	MCG113838 GN=Rpl36a-ps1
Q571F9	MKIAA4115 protein (Fragment) GN=G3bp1
Q9EQD6	Keratin intermediate filament 16a GN=K16
Q8BX10	Serine/threonine-protein phosphatase PGAM5, mitochondrial GN=Pgam5
Q99JY0	Trifunctional enzyme subunit beta, mitochondrial GN=Hadhb

P62858	40S ribosomal protein S28 GN=Rps28
O54941	SWI/SNF-related matrix-associated actin-dependent regulator of chromatin subfamily E member 1 GN=Smarce1
P39447	Tight junction protein ZO-1 GN=Tjp1
Q06477	IFN-response element binding factor 2 (Fragment) GN=Srsf2
Q9D2G2	Dihydrolipoyllysine-residue succinyltransferase component of 2-oxoglutarate dehydrogenase complex, mitochondrial GN=Dlst
P63038	60 kDa heat shock protein, mitochondrial GN=Hspd1
P24270	Catalase GN=Cat
P35700	Peroxiredoxin-1 GN=Prdx1
Q9CZI5	Uncharacterized protein GN=Rps23
A0A0G2JE47	Immunoglobulin kappa variable 8-28 (Fragment) GN=Igkv8-28
Q3TQX5	Uncharacterized protein GN=Ddx3x
Q9Z1R9	MCG124046 GN=Prss1
P11031	Activated RNA polymerase II transcriptional coactivator p15 GN=Sub1
Q9CQE8	RNA transcription, translation and transport factor protein GN=RTRAF
Q9CQN7	39S ribosomal protein L41, mitochondrial GN=Mrpl41
P48962	ADP/ATP translocase 1 GN=Slc25a4
Q3U944	L-type lectin-like domain-containing protein GN=Lman1
Q8BL97	Serine/arginine-rich splicing factor 7 GN=Srsf7
Q9CRB2	H/ACA ribonucleoprotein complex subunit 2 GN=Nhp2
Q9CYR0	Single-stranded DNA-binding protein, mitochondrial GN=Ssbp1
Q58E35	MCG10168 GN=Rplp1
Q3V0D3	Uncharacterized protein GN=Gm10827
A0A0R4J275	NADH dehydrogenase [ubiquinone] 1 alpha subcomplex subunit 12 GN=Ndufa12
Q08288	Cell growth-regulating nucleolar protein GN=Lyar
P62245	40S ribosomal protein S15a GN=Rps15a
E9PWD2	Thrombospondin type-1 domain-containing protein 7A GN=Thsd7a
B2CY77	Laminin receptor (Fragment) GN=Rpsa
P18608	Non-histone chromosomal protein HMG-14 GN=Hmgn1
I6L9I7	Cbx3 protein GN=Cbx3
D4AFX7	DnaJ heat shock protein family (Hsp40) member C13 GN=Dnajc13
Q3TF62	Uncharacterized protein GN=Actl6a
P29391	Ferritin light chain 1 GN=Ftl1
A0A0G2JG88	T cell receptor alpha joining 48 (Fragment) GN=Traj48
Q5FWB6	60S acidic ribosomal protein P0 GN=Rplp0
Q3THE2	Myosin regulatory light chain 12B GN=Myl12b
P98086	Complement C1q subcomponent subunit A GN=C1qa
O89079	Coatomer subunit epsilon GN=Cope
Q4VAG4	MCG12304 GN=Rpl22
D3Z722	40S ribosomal protein S19 GN=Rps19
A0A0R4J008	Histone deacetylase 2 GN=Hdac2
A0A087WSB8	High mobility group nucleosome-binding domain-containing protein 3 GN=Hmgn3
Q6A0C9	MKIAA0109 protein (Fragment) GN=Ap2m1
P67778	Prohibitin GN=Phb
P61965	WD repeat-containing protein 5 GN=Wdr5
Q6A0F1	MKIAA0002 protein (Fragment) GN=Cct8

P10639	Thioredoxin GN=Txn
Q5FWH6	Rho guanine nucleotide exchange factor 15 GN=Arhgef15
Q6PE01	U5 small nuclear ribonucleoprotein 40 kDa protein GN=Snrnp40
E9PVX6	Proliferation marker protein Ki-67 GN=Mki67
Q99KP6	Pre-mRNA-processing factor 19 GN=Prpf19
Q5M9N9	Prdx2 protein GN=Prdx2
Q91VN4	MICOS complex subunit Mic25 GN=Chchd6
Q8QZY9	Splicing factor 3B subunit 4 GN=Sf3b4
P62960	Y-box-binding protein 1 GN=Ybx1
A0A140T8N8	Immunoglobulin kappa variable 9-123 (Fragment) GN=Igkv9-123
P11276	Fibronectin GN=Fn1
A0A2S0DFG2	Anti-HIV fusion peptide monocolonal anitbody heavy chain vFP6.01 (Fragment)
Q9D1I6	39S ribosomal protein L14, mitochondrial GN=Mrpl14
Q9DCT2	NADH dehydrogenase [ubiquinone] iron-sulfur protein 3, mitochondrial GN=Ndufs3
P11983	T-complex protein 1 subunit alpha GN=Tcp1
P62274	40S ribosomal protein S29 GN=Rps29
P58252	Elongation factor 2 GN=Eef2
Q0VBA4	MCG16976, isoform CRA_c GN=Rpl22l1
Q8VEA0	Igh protein GN=Igh
P42208	Septin-2 GN=Septin2
A0A140T8T4	Ribosomal protein L9, pseudogene 6 GN=Rpl9-ps6
Q6A068	Cell division cycle 5-like protein GN=Cdc5l

Table 7.24 – 14.5 d.p.c. *Pkd2*$^{lrm4/lrm4}$ Lung IP

Accession	Description
Q5FWJ3	Vimentin GN=Vim
P62806	Histone H4 GN=H4c1
Q921L4	Histone H2B GN=LOC665622
Q3U9N8	Inosine-5'-monophosphate dehydrogenase GN=Impdh2
Q64524	Histone H2B type 2-E GN=Hist2h2be
P43275	Histone H1.1 GN=H1-1
P19324	Serpin H1 GN=Serpinh1
Q3UZG3	Uncharacterized protein GN=Hnrnpa3
P15864	Histone H1.2 GN=H1-2
O88569	Heterogeneous nuclear ribonucleoproteins A2/B1 GN=Hnrnpa2b1
P43274	Histone H1.4 GN=H1-4
P63017	Heat shock cognate 71 kDa protein GN=Hspa8
P43277	Histone H1.3 GN=H1-3
P29341	Polyadenylate-binding protein 1 GN=Pabpc1
Q80UT7	Rpl7a protein (Fragment) GN=Rpl7a
Q8VIJ6	Splicing factor, proline- and glutamine-rich GN=Sfpq
Q0VG47	Heterogeneous nuclear ribonucleoprotein A3 GN=Hnrnpa3
P47911	60S ribosomal protein L6 GN=Rpl6
Q3UK83	Uncharacterized protein GN=Hnrnpa1
A2AB79	Histone H2A GN=H2aw
A0A1W2P768	H3 clustered histone 14 GN=H3c14
A0A1Y7VJN6	Immunoglobulin heavy constant gamma 3 (Fragment) GN=Ighg3
Q6GSS7	Histone H2A type 2-A GN=Hist2h2aa1
B2RRX1	Actin, beta GN=Actb
Q9WV02	RNA-binding motif protein, X chromosome GN=Rbmx
A0A2I3BRL8	Predicted gene 7324 GN=Gm7324
P24369	Peptidyl-prolyl cis-trans isomerase B GN=Ppib
Q1WWK3	Hist1h1b protein (Fragment) GN=H1f5
Q3TL71	Uncharacterized protein GN=Hnrnpk
O35245	Polycystin-2 GN=Pkd2
Q3V0Z8	Uncharacterized protein (Fragment) GN=Ddx5
Q3U4U6	T-complex protein 1 subunit gamma GN=Cct3
Q4FZH2	MCG50660, isoform CRA_a GN=Rpl26
Q03265	ATP synthase subunit alpha, mitochondrial GN=Atp5f1a
P56959	RNA-binding protein FUS GN=Fus
Q3U6P5	RRM domain-containing protein GN=Hnrnpc
Q9DCV7	Keratin, type II cytoskeletal 7 GN=Krt7
P10126	Elongation factor 1-alpha 1 GN=Eef1a1
O35129	Prohibitin-2 GN=Phb2
P61358	60S ribosomal protein L27 GN=Rpl27
P62702	40S ribosomal protein S4, X isoform GN=Rps4x
Q3TVV6	Uncharacterized protein GN=Hnrnpu
P14148	60S ribosomal protein L7 GN=Rpl7
P43276	Histone H1.5 GN=H1-5

Q9CQK2	40S ribosomal protein S24 GN=Rps24
A0A1L1STE4	Interleukin enhancer-binding factor 3 GN=Ilf3
P68040	Receptor of activated protein C kinase 1 GN=Rack1
P27659	60S ribosomal protein L3 GN=Rpl3
P62751	60S ribosomal protein L23a GN=Rpl23a
P20029	Endoplasmic reticulum chaperone BiP GN=Hspa5
Q58DZ3	MCG20799 GN=Rpl30
Q58EU8	Igk protein GN=Igk
E9QNN1	ATP-dependent RNA helicase A GN=Dhx9
Q8BTM8	Filamin-A GN=Flna
P62911	60S ribosomal protein L32 GN=Rpl32
P05784	Keratin, type I cytoskeletal 18 GN=Krt18
P63163	Small nuclear ribonucleoprotein-associated protein N GN=Snrpn
O70569	Ribosomal protein S14 GN=rps14
Q3U5I2	Uncharacterized protein GN=Ptbp1
P68372	Tubulin beta-4B chain GN=Tubb4b
A0A0A6YX26	60S ribosomal protein L31 GN=Rpl31
P62918	60S ribosomal protein L8 GN=Rpl8
P62242	40S ribosomal protein S8 GN=Rps8
Q64522	Histone H2A type 2-B GN=Hist2h2ab
P05213	Tubulin alpha-1B chain GN=Tuba1b
A0A0A0MQF6	Glyceraldehyde-3-phosphate dehydrogenase GN=Gapdh
O08583	THO complex subunit 4 GN=Alyref
Q3UW40	TRASH domain-containing protein GN=Rpl24
P62317	Small nuclear ribonucleoprotein Sm D2 GN=Snrpd2
P97351	40S ribosomal protein S3a GN=Rps3a
P14733	Lamin-B1 GN=Lmnb1
Q4FZE6	40S ribosomal protein S7 GN=Rps7
Q3U741	DEAD (Asp-Glu-Ala-Asp) box polypeptide 17, isoform CRA_a GN=Ddx17
Q3TF40	Uncharacterized protein (Fragment) GN=Nono
Q9CX86	Heterogeneous nuclear ribonucleoprotein A0 GN=Hnrnpa0
Q9D8E6	60S ribosomal protein L4 GN=Rpl4
P68033	Actin, alpha cardiac muscle 1 GN=Actc1
P0C0S6	Histone H2A.Z GN=H2az1
Q9CWK0	Ribosomal_L14e domain-containing protein GN=Rpl14
P35550	rRNA 2'-O-methyltransferase fibrillarin GN=Fbl
A0A2I3BRM6	Heterogeneous nuclear ribonucleoproteins C1/C2 (Fragment) GN=Hnrnpc
Q3UCL7	KH type-2 domain-containing protein GN=Rps3
Q8C2Q3	RNA-binding protein 14 GN=Rbm14
P63325	40S ribosomal protein S10 GN=Rps10
P62320	Small nuclear ribonucleoprotein Sm D3 GN=Snrpd3
A8DUV3	Alpha-globin GN=Hbat1
Q5M9L1	60S ribosomal protein L36 GN=Rpl36
Q5BLJ7	MCG10205 GN=Rps13
P11679	Keratin, type II cytoskeletal 8 GN=Krt8
Q8BQ46	TAF15 RNA polymerase II, TATA box binding protein (TBP)-associated factor GN=Taf15

Q58EW0	MCG132477, isoform CRA_a GN=Rpl18
Q8C2Q7	Heterogeneous nuclear ribonucleoprotein H GN=Hnrnph1
P56480	ATP synthase subunit beta, mitochondrial GN=Atp5f1b
Q571F9	MKIAA4115 protein (Fragment) GN=G3bp1
P25444	40S ribosomal protein S2 GN=Rps2
G5E924	Heterogeneous nuclear ribonucleoprotein L (Fragment) GN=Hnrnpl
A8DUK4	Beta-globin GN=Hbb-bs
Q3U561	Ribosomal protein GN=Rpl10a
Q64012	RNA-binding protein Raly GN=Raly
Q9JJI8	60S ribosomal protein L38 GN=Rpl38
P31001	Desmin GN=Des
Q8BN87	Uncharacterized protein (Fragment) GN=Mdk
Q9DB79	Ribosomal_S17_N domain-containing protein GN=Rps11
Q3U7D2	Ribosomal protein L15 GN=Rpl15
Q6ZWN5	40S ribosomal protein S9 GN=Rps9
P47963	60S ribosomal protein L13 GN=Rpl13
Q91V99	40S ribosomal protein S30 (Fragment) GN=fau
Q545A2	MCG11560 GN=Slc25a5
Q20BD0	Heterogeneous nuclear ribonucleoprotein A/B GN=Hnrnpab
A0A338P6F6	High mobility group protein HMG-I/HMG-Y GN=Hmga1
Q3U850	Ribosomal_L18_c domain-containing protein GN=Rpl5
P48962	ADP/ATP translocase 1 GN=Slc25a4
Q5M9J8	MCG13936 GN=Rpl28
A0A1Y7VKY1	MCG116671 GN=Rps18-ps5
P04104	Keratin, type II cytoskeletal 1 GN=Krt1
A0A3B0INZ4	Adiponectin b GN=Adib
Q80V08	Rpl17 protein (Fragment) GN=Rpl17
Q60932	Voltage-dependent anion-selective channel protein 1 GN=Vdac1
Q3U536	Uncharacterized protein GN=Npm1
E9PZ16	Basement membrane-specific heparan sulfate proteoglycan core protein GN=Hspg2
Q3UEB3	Poly(U)-binding-splicing factor PUF60 GN=Puf60
P68433	Histone H3.1 GN=H3c1
Q3U8M3	Uncharacterized protein GN=Rpl37a
Q9CR49	Globin b1 GN=Hbb-y
P47915	60S ribosomal protein L29 GN=Rpl29
Q60668	Heterogeneous nuclear ribonucleoprotein D0 GN=Hnrnpd
Q8CAQ8	MICOS complex subunit Mic60 GN=Immt
Q58E56	Igh protein GN=Igh
P24270	Catalase GN=Cat
P02301	Histone H3.3C GN=H3f3c
Q3UBK2	Uncharacterized protein
Q6ZWV7	60S ribosomal protein L35 GN=Rpl35
P09405	Nucleolin GN=Ncl
Q32P04	Keratin 5 GN=Krt5
P60867	40S ribosomal protein S20 GN=Rps20
P19001	Keratin, type I cytoskeletal 19 GN=Krt19

P38647	Stress-70 protein, mitochondrial GN=Hspa9
P62983	Ubiquitin-40S ribosomal protein S27a GN=Rps27a
P62852	40S ribosomal protein S25 GN=Rps25
Q80ZM5	H1 histone family, member X GN=H1f10
D3YTQ3	Heterogeneous nuclear ribonucleoprotein D-like GN=Hnrnpdl
Q497N1	40S ribosomal protein S26 GN=Rps26
Q6IFZ6	Keratin, type II cytoskeletal 1b GN=Krt77
P30681	High mobility group protein B2 GN=Hmgb2
P53395	Lipoamide acyltransferase component of branched-chain alpha-keto acid dehydrogenase complex, mitochondrial GN=Dbt
Q62425	Cytochrome c oxidase subunit NDUFA4 GN=Ndufa4
Q6PDG5	SWI/SNF complex subunit SMARCC2 GN=Smarcc2
Q3T9Y8	Eukaryotic translation initiation factor 3 subunit I GN=Eif3i
A0A3B0ITG8	Adiponectin a GN=Adia
Q3TF25	Uncharacterized protein GN=Atp5o
P57776	Elongation factor 1-delta GN=Eef1d
Q5CZY9	Rps16 protein GN=Rps16
Q62189	U1 small nuclear ribonucleoprotein A GN=Snrpa
P98086	Complement C1q subcomponent subunit A GN=C1qa
Q6PFA2	Clathrin light chain GN=Clta
Q80U76	Ribosome biogenesis regulatory protein (Fragment) GN=Rrs1
P62315	Small nuclear ribonucleoprotein Sm D1 GN=Snrpd1
Q9Z2X1	Heterogeneous nuclear ribonucleoprotein F GN=Hnrnpf
Q9CY57	Chromatin target of PRMT1 protein GN=Chtop
P62830	60S ribosomal protein L23 GN=Rpl23
F6W687	Non-histone chromosomal protein HMG-17 (Fragment) GN=Hmgn2
Q80U89	MKIAA0034 protein (Fragment) GN=mKIAA0034
P63038	60 kDa heat shock protein, mitochondrial GN=Hspd1
O09167	60S ribosomal protein L21 GN=Rpl21
F8WGL3	Cofilin-1 GN=Cfl1
Q9CQF3	Cleavage and polyadenylation specificity factor subunit 5 GN=Nudt21
P62245	40S ribosomal protein S15a GN=Rps15a
Q5BLK1	40S ribosomal protein S6 GN=Rps6
Q6NSP9	High mobility group protein HMGI-C GN=Hmga2
Q9CQN7	39S ribosomal protein L41, mitochondrial GN=Mrpl41
O70251	Elongation factor 1-beta GN=Eef1b
A0A0F7QZE4	MAb 110 heavy chain GN=HC
Q505A8	MCG17585 GN=Rpl39
Q9D2G2	Dihydrolipoyllysine-residue succinyltransferase component of 2-oxoglutarate dehydrogenase complex, mitochondrial GN=Dlst
P59708	Splicing factor 3B subunit 6 GN=Sf3b6
P10922	Histone H1.0 GN=H1-0
P84089	Enhancer of rudimentary homolog GN=Erh
A1A4A7	Pgam5 protein (Fragment) GN=Pgam5
O55142	60S ribosomal protein L35a GN=Rpl35a
P14115	60S ribosomal protein L27a GN=Rpl27a
Q5SUS9	RNA-binding protein EWS GN=Ewsr1

P62843	40S ribosomal protein S15 GN=Rps15
P70670	Nascent polypeptide-associated complex subunit alpha, muscle-specific form GN=Naca
Q6ZWU9	40S ribosomal protein S27 GN=Rps27
Q9D0E1	Heterogeneous nuclear ribonucleoprotein M GN=Hnrnpm
Q3UXI9	Uncharacterized protein GN=Ilf2
F7DEU6	Inosine-5'-monophosphate dehydrogenase GN=Impdh1
Q3TKG5	H/ACA ribonucleoprotein complex subunit GN=Gar1
Q9CZI5	Uncharacterized protein GN=Rps23
Q569X3	U1 small nuclear ribonucleoprotein C GN=Snrpc
Q8BT90	Uncharacterized protein (Fragment) GN=Rps17
P19253	60S ribosomal protein L13a GN=Rpl13a
H7BX95	Serine/arginine-rich-splicing factor 1 GN=Srsf1
Q3U7F6	Uncharacterized protein GN=Zfp422
A0A0B4J1I1	Immunoglobulin kappa variable 16-104 (Fragment) GN=Igkv16-104
B2RUC7	Serine/threonine kinase receptor associated protein GN=Strap
Q9CQE8	RNA transcription, translation and transport factor protein GN=RTRAF
E9Q317	Histone deacetylase complex subunit SAP18 GN=Sap18
A0A0B4J1I9	Immunoglobulin kappa variable 4-55 (Fragment) GN=Igkv4-55
Q99JF8	PC4 and SFRS1-interacting protein GN=Psip1
A0A075B5V1	Immunoglobulin heavy variable 1-31 GN=Ighv1-31
Q99JY0	Trifunctional enzyme subunit beta, mitochondrial GN=Hadhb
A0A0B4J1J7	Immunoglobulin heavy variable 1-82 GN=Ighv1-82
A0A1D5RM85	60S ribosomal protein L18a (Fragment) GN=Rpl18a
Q7TNV0	Protein DEK GN=Dek
P17751	Triosephosphate isomerase GN=Tpi1
Q922V4	Pleiotropic regulator 1 GN=Plrg1
D3Z420	Family with sequence similarity 186, member B GN=Fam186b
Q9DB77	Cytochrome b-c1 complex subunit 2, mitochondrial GN=Uqcrc2
P62274	40S ribosomal protein S29 GN=Rps29
B2CY77	Laminin receptor (Fragment) GN=Rpsa
B2RTP7	Krt2 protein GN=Krt2
P52480	Pyruvate kinase PKM GN=Pkm
G8JL55	Chitinase domain-containing protein 1 (Fragment) GN=Chid1
Q8VDD5	Myosin-9 GN=Myh9
Q3U7B3	Uncharacterized protein GN=Tmpo
Q8CCK0	Core histone macro-H2A.2 GN=H2afy2
Q3UH59	Myosin-10 GN=Myh10
Q99KP6	Pre-mRNA-processing factor 19 GN=Prpf19
Q3TJ01	tRNA-splicing ligase RtcB homolog GN=Rtcb
Q60749	KH domain-containing, RNA-binding, signal transduction-associated protein 1 GN=Khdrbs1
Q3UAD6	Heat shock protein 90kDa beta (Grp94), member 1 GN=Hsp90b1
P83882	60S ribosomal protein L36a GN=Rpl36a
Q3THE2	Myosin regulatory light chain 12B GN=Myl12b
A0A0G2JE47	Immunoglobulin kappa variable 8-28 (Fragment) GN=Igkv8-28
A0A075B5R5	Immunoglobulin heavy variable 4-1 (Fragment) GN=Ighv4-1
O54941	SWI/SNF-related matrix-associated actin-dependent regulator of chromatin subfamily E member 1 GN=Smarce1

P01675	Ig kappa chain V-VI region XRPC 44
Q3THH1	Uncharacterized protein GN=Pdia6
I6L9I7	Cbx3 protein GN=Cbx3
P01662	Ig kappa chain V-III region ABPC 22/PC 9245
Q9Z1R9	MCG124046 GN=Prss1
Q8VED5	Keratin, type II cytoskeletal 79 GN=Krt79
P80315	T-complex protein 1 subunit delta GN=Cct4
Q4VAG4	MCG12304 GN=Rpl22
Q9CY58	Plasminogen activator inhibitor 1 RNA-binding protein GN=Serbp1
A0A1W2P7Q9	Myosin light polypeptide 6 GN=Myl6
Q8JZX4	Splicing factor 45 GN=Rbm17
Q0VBA4	MCG16976, isoform CRA_c GN=Rpl22l1
P01655	Ig kappa chain V-III region PC 7132
P63168	Dynein light chain 1, cytoplasmic GN=Dynll1
Q3TVM2	Aldedh domain-containing protein GN=Aldh2
Q8C671	RRM domain-containing protein GN=Srsf2
Q6P5H2	Nestin GN=Nes
Q9D1R9	60S ribosomal protein L34 GN=Rpl34
P35979	60S ribosomal protein L12 GN=Rpl12
Q91VN4	MICOS complex subunit Mic25 GN=Chchd6
E9Q6D8	Complement component 6 GN=C6
Q3U6B1	Uncharacterized protein (Fragment) GN=G3bp2
Q9CQ69	Cytochrome b-c1 complex subunit 8 GN=Uqcrq
Q9CQS2	H/ACA ribonucleoprotein complex subunit 3 GN=Nop10
A0A1S6GWH2	Uncharacterized protein GN=Ddx39b
Q9D937	Uncharacterized protein C11orf98 homolog
Q3TFG3	Uncharacterized protein GN=Eif4a1
A0A1B0GSX0	L-lactate dehydrogenase GN=Ldha
P10639	Thioredoxin GN=Txn
Q78PA4	Globin e1 GN=Hba-x
P18608	Non-histone chromosomal protein HMG-14 GN=Hmgn1
P02535	Keratin, type I cytoskeletal 10 GN=Krt10
A2AKX3	Probable helicase senataxin GN=Setx
P62259	14-3-3 protein epsilon GN=Ywhae
H3BLG3	Ras-related protein Rab-26 GN=Rab26
P57784	U2 small nuclear ribonucleoprotein A' GN=Snrpa1
Q9CXW4	60S ribosomal protein L11 GN=Rpl11
Q9D8B3	Charged multivesicular body protein 4b GN=Chmp4b
Q6ZQ61	MCG121979, isoform CRA_c (Fragment) GN=Matr3
A0A0A1HAM8	80K protein GN=Marcks
Q3TAH3	Nucleoplasmin domain-containing protein GN=Npm3
Q3V1M8	Uncharacterized protein GN=Hdlbp
P61965	WD repeat-containing protein 5 GN=Wdr5
Q99JB2	Stomatin-like protein 2, mitochondrial GN=Stoml2
S4R1M2	Scaffold attachment factor B1 GN=Safb
A0A0R4J008	Histone deacetylase 2 GN=Hdac2

Q925S1	MRP5 (Fragment) GN=Ighv9-4
Q3TUQ5	Pinin GN=Pnn
Q8VEA0	Igh protein GN=Igh
Q3TW77	Uncharacterized protein GN=Grn
P27773	Protein disulfide-isomerase A3 GN=Pdia3
P62305	Small nuclear ribonucleoprotein E GN=Snrpe
F6T4M4	Serine/arginine repetitive matrix protein 1 (Fragment) GN=Srrm1
Q58E35	MCG10168 GN=Rplp1
A0A571BEV2	Predicted gene 8251 GN=Gm8251
P11087	Collagen alpha-1(I) chain GN=Col1a1
A0A4E9FT70	IgG3 (Fragment) GN=IGHG3
G3UY42	Polyadenylate-binding protein 2 GN=Pabpn1
O54962	Barrier-to-autointegration factor GN=Banf1
P62858	40S ribosomal protein S28 GN=Rps28
D3Z722	40S ribosomal protein S19 GN=Rps19
P0DP43	Cation channel sperm-associated protein subunit epsilon GN=Catspere
P62309	Small nuclear ribonucleoprotein G GN=Snrpg
Q3TZU7	Sorting nexin GN=Snx9
P01027	Complement C3 GN=C3
Q9JMD0	BUB3-interacting and GLEBS motif-containing protein ZNF207 GN=Znf207
Q9CQR2	40S ribosomal protein S21 GN=Rps21
Q8R1I1	Cytochrome b-c1 complex subunit 9 GN=Uqcr10
A0A140T8T4	Ribosomal protein L9, pseudogene 6 GN=Rpl9-ps6
Q9D8N0	Elongation factor 1-gamma GN=Eef1g
Q5FWH6	Rho guanine nucleotide exchange factor 15 GN=Arhgef15
Q3U9G9	Delta(14)-sterol reductase LBR GN=Lbr
A0A140T8N8	Immunoglobulin kappa variable 9-123 (Fragment) GN=Igkv9-123
Q01149	Collagen alpha-2(I) chain GN=Col1a2
P62307	Small nuclear ribonucleoprotein F GN=Snrpf
Q544R5	MCG16669, isoform CRA_b GN=Tardbp
Q566I6	Complement component 1, r subcomponent GN=C1ra
P54071	Isocitrate dehydrogenase [NADP], mitochondrial GN=Idh2
A0A0G2JG88	T cell receptor alpha joining 48 (Fragment) GN=Traj48
Q6A0F1	MKIAA0002 protein (Fragment) GN=Cct8
P42208	Septin-2 GN=Septin2

Bibliography

Afzelius, B. A. 1976. A human syndrome caused by immotile cilia. *Science* 193(4250), p. 317.

Arakel, E. C. and Schwappach, B. 2018. Formation of COPI-coated vesicles at a glance. *Journal of Cell Science* 131(5), p. jcs209890.

Baillie, M. 1788. An Account of a Remarkable Transposition of the Viscera. By Matthew Baillie, M. D. In a Letter to John Hunter, Esq. F. R. S. *Philosophical Transactions of the Royal Society of London* 78, pp. 350-363.

Beddington, R. S. and Robertson, E. J. 1999. Axis development and early asymmetry in mammals. *Cell* 96(2), pp. 195-209.

Blacque, O. E. et al. 2018. Rab GTPases in cilium formation and function. *Small GTPases* 9(1-2), pp. 76-94.

Blum, M. et al. 2007. Ciliation and gene expression distinguish between node and posterior notochord in the mammalian embryo. *Differentiation* 75(2), pp. 133-146.

Blum, M. et al. 2014. The evolution and conservation of left-right patterning mechanisms. *Development* 141(8), pp. 1603-1613.

Brown, N. A. and Wolpert, L. 1990. The development of handedness in left/right asymmetry. *Development* 109(1), pp. 1-9.

Brücker, L. et al. 2020. The entangled relationship between cilia and actin. *The international journal of biochemistry & cell biology* 129.

Bukowy-Bieryllo, Z. et al. 2022. Perspectives for Primary Ciliary Dyskinesia. *International Journal of Molecular Sciences* [Online] 23(8). Available at.

Béthune, J. and Wieland, F. T. 2018. Assembly of COPI and COPII Vesicular Coat Proteins on Membranes. *Annual Review of Biophysics* 47(1), pp. 63-83.

Cai, Y. et al. 2014. Altered trafficking and stability of polycystins underlie polycystic kidney disease. *The Journal of Clinical Investigation* 124(12), pp. 5129-5144.

Cai, Y. et al. 1999. Identification and characterization of polycystin-2, the PKD2 gene product. *J Biol Chem* 274(40), pp. 28557-28565.

Cantero, María del R. and Cantiello, Horacio F. 2015. Polycystin-2 (TRPP2) Regulation by Ca2+ Is Effected and Diversified by Actin-Binding Proteins. *Biophysical Journal* 108(9), pp. 2191-2200.

Cartwright, J. H. et al. 2004. Fluid-dynamical basis of the embryonic development of left-right asymmetry in vertebrates. *Proc Natl Acad Sci U S A* 101(19), pp. 7234-7239.

Cartwright, J. H. E. et al. 2020. Chemosensing versus mechanosensing in nodal and Kupffer's vesicle cilia and in other left-right organizer organs. *Philos Trans R Soc Lond B Biol Sci* 375(1792), p. 20190566.

Charron, A. J. et al. 2000. ADPKD: A Human Disease Altering Golgi Function and Basolateral Exocytosis in Renal Epithelia. *Traffic* 1(8), pp. 675-686.

Chun, J. et al. 2008. Characterization of Class I and II ADP-Ribosylation Factors (Arfs) in Live Cells: GDP-bound Class II Arfs Associate with the ER-Golgi Intermediate Compartment Independently of GBF1. *Molecular Biology of the Cell* 19(8), pp. 3488-3500.

Cleveland, M. 1926. SITUS INVERSUS VISCERUM: AN ANATOMIC STUDY. *Archives of Surgery* 13(3), pp. 343-368.

Collignon, J. et al. 1996. Relationship between asymmetric nodal expression and the direction of embryonic turning. *Nature* 381(6578), pp. 155-158.

Copeland, J. 2020. Actin-based regulation of ciliogenesis - The long and the short of it. *Seminars in cell & developmental biology* 102.

Cornec-Le Gall, E. et al. 2018. Genetic Complexity of Autosomal Dominant Polycystic Kidney and Liver Diseases. *Journal of the American Society of Nephrology* 29(1).

Cosens, D. J. and Manning, A. 1969. Abnormal Electroretinogram from a Drosophila Mutant. *Nature* 224(5216), pp. 285-287.

Costa, S. et al. 2014. Fusion tags for protein solubility, purification and immunogenicity in Escherichia coli: the novel Fh8 system. *Frontiers in Microbiology* 0.

Cranfill, P. J. et al. 2016. Quantitative assessment of fluorescent proteins. *Nature Methods* 13(7), pp. 557-562.

Dalagiorgou, G. et al. 2010. Polycystin-1: Function as a mechanosensor. *The International Journal of Biochemistry & Cell Biology* 42(10), pp. 1610-1613.

Davila, S. et al. 2004. Mutations in SEC63 cause autosomal dominant polycystic liver disease. *Nature Genetics* 36(6), pp. 575-577.

Dejgaard, S. Y. and Presley, J. F. 2020. Class II Arfs require a brefeldin-A-sensitive factor for Golgi association. *Biochemical and Biophysical Research Communications* 530(1), pp. 301-306.

Deretic, D. et al. 1995. rab8 in retinal photoreceptors may participate in rhodopsin transport and in rod outer segment disk morphogenesis. *Journal of Cell Science* 108(1), pp. 215-224.

Douguet, D. et al. 2019. Structure and function of polycystins: insights into polycystic kidney disease. *Nature Reviews Nephrology* 15(7), pp. 412-422.

Dyer, L. et al. 2022. Lightsheet Microscopy. *Current Protocols* 2(7), p. e448.

El Alaoui, F. et al. 2022. Structural organization and dynamics of FCHo2 docking on membranes. *eLife* 11, p. e73156.

Ermakov, A. et al. 2009. Mouse mutagenesis identifies novel roles for left-right patterning genes in pulmonary, craniofacial, ocular, and limb development. *Dev Dyn* 238(3), pp. 581-594.

Fedeles, S. V. et al. 2015. Sec63 and Xbp1 regulate IRE1α activity and polycystic disease severity. *The Journal of Clinical Investigation* 125(5), pp. 1955-1967.

Fedeles, S. V. et al. 2011. A genetic interaction network of five genes for human polycystic kidney and liver diseases defines polycystin-1 as the central determinant of cyst formation. *Nature Genetics* 43(7), pp. 639-647.

Field, S. 2009. The role of *Pkd1l1* in the establishment of the mammalian left right axis (PhD Thesis).University of Oxford.

Field, S. et al. 2011. Pkd1l1 establishes left-right asymmetry and physically interacts with Pkd2. *Development* 138(6), pp. 1131-1142.

Gainullin, V. G. et al. 2015. Polycystin-1 maturation requires polycystin-2 in a dose-dependent manner. *The Journal of Clinical Investigation* 125(2), pp. 607-620.

Gallagher, A. R. et al. 2000. The polycystic kidney disease protein PKD2 interacts with Hax-1, a protein associated with the actin cytoskeleton. *Proceedings of the National Academy of Sciences* 97(8), pp. 4017-4022.

Garcia-Gonzalez, M. A. et al. 2010. Pkd1 and Pkd2 Are Required for Normal Placental Development. *PLOS ONE* 5(9), p. e12821.

Ge, R. et al. 2022. Cytoskeletal networks in primary cilia: Current knowledge and perspectives. *Journal of cellular physiology* 237(11).

Geng, L. et al. 2006. Polycystin-2 traffics to cilia independently of polycystin-1 by using an N-terminal RVxP motif. *J Cell Sci* 119(Pt 7), pp. 1383-1395.

Grande, C. and Patel, N. H. 2009. Nodal signalling is involved in left–right asymmetry in snails. *Nature* 457(7232), pp. 1007-1011.

Grieben, M. et al. 2017. Structure of the polycystic kidney disease TRP channel Polycystin-2 (PC2). *Nature Structural & Molecular Biology* 24(2), pp. 114-122.

Grimes, D. T. and Burdine, R. D. 2017. Left–Right Patterning: Breaking Symmetry to Asymmetric Morphogenesis. *Trends in Genetics* 33(9), pp. 616-628.

Grimes, D. T. et al. 2016. Genetic Analysis Reveals a Hierarchy of Interactions between Polycystin-Encoding Genes and Genes Controlling Cilia Function during Left-Right Determination. *PLoS Genet* 12(6), p. e1006070.

Guénet, J. L. 2005. The mouse genome. *Genome Research* 15(12), pp. 1729-1740.

Hanaoka, K. et al. 2000. Co-assembly of polycystin-1 and -2 produces unique cation-permeable currents. *Nature* 408(6815), pp. 990-994.

Hardy, E. and Tsiokas, L. 2020. Polycystins as components of large multiprotein complexes of polycystin interactors. *Cellular Signalling* 72, p. 109640.

Hoffman, H. and Prekeris, R. 2022. Roles of the actin cytoskeleton in ciliogenesis. *Journal of cell science* 135(10).

Hoffmeister, H. et al. 2011. Polycystin-2 takes different routes to the somatic and ciliary plasma membrane. *Journal of Cell Biology* 192(4), pp. 631-645.

Hofherr, A. and Köttgen, M. 2011. TRPP Channels and Polycystins. In: Islam, M.S. ed. *Transient Receptor Potential Channels*. Dordrecht: Springer Netherlands, pp. 287-313.

Hoso, M. et al. 2010. A speciation gene for left-right reversal in snails results in anti-predator adaptation. *Nature communications* 1, pp. 133-133.

Houde, C. et al. 2006. Hippi is essential for node cilia assembly and Sonic hedgehog signaling. *Developmental Biology* 300(2), pp. 523-533.

Hu, Q. et al. 2010. A Septin Diffusion Barrier at the Base of the Primary Cilium Maintains Ciliary Membrane Protein Distribution. *Science* 329(5990), pp. 436-439.

Huan, Y. and van Adelsberg, J. 1999. Polycystin-1, the PKD1 gene product, is in a complex containing E-cadherin and the catenins. *The Journal of Clinical Investigation* 104(10), pp. 1459-1468.

Hughes, J. et al. 1995. The polycystic kidney disease 1 (PKD1) gene encodes a novel protein with multiple cell recognition domains. *Nature Genetics* 10(2), pp. 151-160.

Ishimoto, Y. et al. 2017. Mitochondrial Abnormality Facilitates Cyst Formation in Autosomal Dominant Polycystic Kidney Disease. *Molecular and Cellular Biology* 37(24), pp. e00337-00317.

Jin, H. et al. 2010. The conserved Bardet-Biedl syndrome proteins assemble a coat that traffics membrane proteins to cilia. *Cell* 141(7), pp. 1208-1219.

Jung, E. et al. 2020. ESCRT subunit CHMP4B localizes to primary cilia and is required for the structural integrity of the ciliary membrane. *The FASEB Journal* 34(1), pp. 1331-1344.

Jung, S.-j. et al. 2019. Proper insertion and topogenesis of membrane proteins in the ER depend on Sec63. *Biochimica et Biophysica Acta (BBA) - General Subjects* 1863(9), pp. 1371-1380.

Jung, S.-j. and Kim, H. 2021. Emerging View on the Molecular Functions of Sec62 and Sec63 in Protein Translocation. *International Journal of Molecular Sciences* [Online] 22(23). Available at.

Kahn, R. A. et al. 2005. Arf family GTPases: roles in membrane traffic and microtubule dynamics. *Biochemical Society Transactions* 33(6), pp. 1269-1272.

Kamura, K. et al. 2011. Pkd1l1 complexes with Pkd2 on motile cilia and functions to establish the left-right axis. *Development* 138(6), pp. 1121-1129.

Karcher, C. et al. 2005. Lack of a laterality phenotype in Pkd1 knock-out embryos correlates with absence of polycystin-1 in nodal cilia. *Differentiation* 73(8), pp. 425-432.

Kartagener, M. 1933. Zur Pathogenese der Bronchiektasien. *Beiträge zur Klinik der Tuberkulose und spezifischen Tuberkulose-Forschung* 83(4), pp. 489-501.

Katoh, T. A. et al. 2022. Immotile cilia of the mouse node sense a fluid flow–induced mechanical force for left-right symmetry breaking. *bioRxiv*, p. 2022.2004.2011.487968.

Keryer, G. et al. 2011. Ciliogenesis is regulated by a huntingtin-HAP1-PCM1 pathway and is altered in Huntington disease. *J Clin Invest* 121(11), pp. 4372-4382.

Kim, H. et al. 2014. Ciliary membrane proteins traffic through the Golgi via a Rabep1/GGA1/Arl3-dependent mechanism. *Nature Communications* 5(1), p. 5482.

Kim, J. et al. 2015. Actin remodelling factors control ciliogenesis by regulating YAP/TAZ activity and vesicle trafficking. *Nat Commun* 6, p. 6781.

Kim, J. et al. 2010. Functional genomic screen for modulators of ciliogenesis and cilium length. *Nature* 464(7291).

Kohli, P. et al. 2017. The ciliary membrane-associated proteome reveals actin-binding proteins as key components of cilia. *EMBO reports* 18(9).

Kondo, Y. et al. 2012. ARF1 and ARF3 Are Required for the Integrity of Recycling Endosomes and the Recycling Pathway. *Cell Structure and Function* 37(2), pp. 141-154.

Kotsis, F. et al. 2007. Ciliary calcium signaling is modulated by kidney injury molecule-1 (Kim1). *Pflügers Archiv - European Journal of Physiology* 453(6), pp. 819-829.

Kuo, I. Y. et al. 2019. Polycystin 2 regulates mitochondrial Ca2+ signaling, bioenergetics, and dynamics through mitofusin 2. *Science Signaling* 12(580), p. eaat7397.

Lakshmipathi, J. et al. 2020. Nephron-Specific Disruption of Polycystin-1 Induces Cyclooxygenase-2–Mediated Blood Pressure Reduction Independent of Cystogenesis. *Journal of the American Society of Nephrology* 31(6).

LaVallie, E. R. et al. 1993. A Thioredoxin Gene Fusion Expression System That Circumvents Inclusion Body Formation in the E. coli Cytoplasm. *Bio/Technology* 11(2), pp. 187-193.

Legendre-Guillemin, V. et al. 2002. HIP1 and HIP12 Display Differential Binding to F-actin, AP2, and Clathrin: IDENTIFICATION OF A NOVEL INTERACTION WITH CLATHRIN LIGHT CHAIN*. *Journal of Biological Chemistry* 277(22), pp. 19897-19904.

Leikola, A. 1976. Hensen's node — The 'Organizer' of the amniote embryo. *Experientia* 32(3), pp. 269-277.

Levin, M. et al. 1995. A molecular pathway determining left-right asymmetry in chick embryogenesis. *Cell* 82(5), pp. 803-814.

Li, Q. et al. 2003. Polycystin-2 Associates with Tropomyosin-1, an Actin Microfilament Component. *Journal of Molecular Biology* 325(5), pp. 949-962.

Li, Q. et al. 2005. Alpha-actinin associates with polycystin-2 and regulates its channel activity. *Human Molecular Genetics* 14(12), pp. 1587-1603.

Little, R. B. and Norris, D. P. 2021. Right, left and cilia: How asymmetry is established. *Seminars in Cell & Developmental Biology* 110, pp. 11-18.

Liu, X. et al. 2018. Polycystin-2 is an essential ion channel subunit in the primary cilium of the renal collecting duct epithelium. *eLife* 7, p. e33183.

Lowe, L. A. et al. 1996. Conserved left–right asymmetry of nodal expression and alterations in murine situs inversus. *Nature* 381(6578), pp. 158-161.

Lundmark, R. and Carlsson, S. R. 2003. Sorting Nexin 9 Participates in Clathrin-mediated Endocytosis through Interactions with the Core Components*. *Journal of Biological Chemistry* 278(47), pp. 46772-46781.

Ma, L. et al. 2009. Naturally occurring mutations alter the stability of polycystin-1 polycystic kidney disease (PKD) domains. *J Biol Chem* 284(47), pp. 32942-32949.

Marques, S. et al. 2004. The activity of the Nodal antagonist Cerl-2 in the mouse node is required for correct L/R body axis. *Genes Dev* 18(19), pp. 2342-2347.

Mazelova, J. et al. 2009. Ciliary targeting motif VxPx directs assembly of a trafficking module through Arf4. *The EMBO Journal* 28(3), pp. 183-192.

McGrath, J. et al. 2003. Two populations of node monocilia initiate left-right asymmetry in the mouse. *Cell* 114(1), pp. 61-73.

McMahon, H. T. and Boucrot, E. 2011. Molecular mechanism and physiological functions of clathrin-mediated endocytosis. *Nature Reviews Molecular Cell Biology* 12(8), pp. 517-533.

Meno, C. et al. 1996. Left–right asymmetric expression of the TGFβ-family member lefty in mouse embryos. *Nature* 381(6578), pp. 151-155.

Mettlen, M. et al. 2018. Regulation of Clathrin-Mediated Endocytosis. *Annual Review of Biochemistry* 87(1), pp. 871-896.

Minegishi, K. et al. 2021. Fluid flow-induced left-right asymmetric decay of Dand5 mRNA in the mouse embryo requires a Bicc1-Ccr4 RNA degradation complex. *Nature Communications* 12(1), p. 4071.

Mishra, S. K. et al. 2002. Disabled-2 exhibits the properties of a cargo-selective endocytic clathrin adaptor. *The EMBO Journal* 21(18), pp. 4915-4926.

Mochizuki, T. et al. 1996. PKD2, a Gene for Polycystic Kidney Disease That Encodes an Integral Membrane Protein. *Science* 272(5266), pp. 1339-1342.

Molla-Herman, A. et al. 2010. The ciliary pocket: an endocytic membrane domain at the base of primary and motile cilia. *Journal of cell science* 123(Pt 10).

Nager, A. R. et al. 2017. An Actin Network Dispatches Ciliary GPCRs into Extracellular Vesicles to Modulate Signaling. *Cell* 168(1-2), pp. 252-263 e214.

Nakai, W. et al. 2013. ARF1 and ARF4 regulate recycling endosomal morphology and retrograde transport from endosomes to the Golgi apparatus. *Molecular Biology of the Cell* 24(16), pp. 2570-2581.

Nakamura, T. et al. 2006. Generation of robust left-right asymmetry in the mouse embryo requires a self-enhancement and lateral-inhibition system. *Dev Cell* 11(4), pp. 495-504.

Nakamura, T. et al. 2012. Fluid flow and interlinked feedback loops establish left-right asymmetric decay of Cerl2 mRNA. *Nat Commun* 3, p. 1322.

Nauli, S. M. et al. 2003. Polycystins 1 and 2 mediate mechanosensation in the primary cilium of kidney cells. *Nat Genet* 33(2), pp. 129-137.

Newby, L. J. et al. 2002. Identification, Characterization, and Localization of a Novel Kidney Polycystin-1-Polycystin-2 Complex*. *Journal of Biological Chemistry* 277(23), pp. 20763-20773.

Nigro, E. A. and Boletta, A. 2021. Role of the polycystins as mechanosensors of extracellular stiffness. *American Journal of Physiology-Renal Physiology* 320(5), pp. F693-F705.

Nonaka, S. et al. 2002. Determination of left-right patterning of the mouse embryo by artificial nodal flow. *Nature* 418(6893), pp. 96-99.

Nonaka, S. et al. 1998. Randomization of left-right asymmetry due to loss of nodal cilia generating leftward flow of extraembryonic fluid in mice lacking KIF3B motor protein. *Cell* 95(6), pp. 829-837.

Nonaka, S. et al. 2005. De novo formation of left-right asymmetry by posterior tilt of nodal cilia. *PLoS Biol* 3(8), p. e268.

Norris, D. P. 2012. Cilia, calcium and the basis of left-right asymmetry. *BMC Biol* 10, p. 102.

Nweeia, M. T. et al. 2012. Vestigial Tooth Anatomy and Tusk Nomenclature for Monodon Monoceros. *The Anatomical Record* 295(6), pp. 1006-1016.

Okada, Y. et al. 1999. Abnormal nodal flow precedes situs inversus in iv and inv mice. *Mol Cell* 4(4), pp. 459-468.

Okada, Y. et al. 2005. Mechanism of nodal flow: a conserved symmetry breaking event in left-right axis determination. *Cell* 121(4), pp. 633-644.

Ong, A. C. M. and Harris, P. C. 2015. A polycystin-centric view of cyst formation and disease: the polycystins revisited. *Kidney International* 88(4), pp. 699-710.

Owen, D. J. et al. 2004. ADAPTORS FOR CLATHRIN COATS: Structure and Function. *Annual Review of Cell and Developmental Biology* 20(1), pp. 153-191.

Palander, O. et al. 2017. Uncovering the Roles of Septins in Cilia. *Frontiers in Cell and Developmental Biology* 5.

Park, Sang Y. and Guo, X. 2014. Adaptor protein complexes and intracellular transport. *Bioscience Reports* 34(4).

Pearce, J. J. et al. 1999. A mouse cerberus/Dan-related gene family. *Dev Biol* 209(1), pp. 98-110.

Pennekamp, P. et al. 2002. The ion channel polycystin-2 is required for left-right axis determination in mice. *Curr Biol* 12(11), pp. 938-943.

Pennekamp, P. et al. 2015. Situs inversus and ciliary abnormalities: 20 years later, what is the connection? *Cilia* 4(1), p. 1.

Phua, S. C. et al. 2017. Dynamic Remodeling of Membrane Composition Drives Cell Cycle through Primary Cilia Excision. *Cell* 168(1-2), pp. 264-279 e215.

Piao, H. et al. 2017. Sec16A is critical for both conventional and unconventional secretion of CFTR. *Scientific Reports* 7(1), p. 39887.

Pierce, R. 1979. Foods and feeding of the wrybill (Anarhynchus frontalis) on its riverbed breeding grounds. *Notornis* 26, pp. 1-21.

Popoff, V. et al. 2011. Several ADP-ribosylation Factor (Arf) Isoforms Support COPI Vesicle Formation*. *Journal of Biological Chemistry* 286(41), pp. 35634-35642.

Praetorius, H. A. and Spring, K. R. 2001. Bending the MDCK Cell Primary Cilium Increases Intracellular Calcium. *The Journal of Membrane Biology* 184(1), pp. 71-79.

Ramsey, I. S. et al. 2006. AN INTRODUCTION TO TRP CHANNELS. *Annual Review of Physiology* 68(1), pp. 619-647.

Reithmeier, R. A. F. et al. 2016. Band 3, the human red cell chloride/bicarbonate anion exchanger (AE1, SLC4A1), in a structural context. *Biochimica et Biophysica Acta (BBA) - Biomembranes* 1858(7, Part A), pp. 1507-1532.

Royle, S. J. 2006. The cellular functions of clathrin. *Cellular and Molecular Life Sciences CMLS* 63(16), pp. 1823-1832.

Sahlmüller, M. C. et al. 2011. Recombinant Heptameric Coatomer Complexes: Novel Tools to Study Isoform-Specific Functions. *Traffic* 12(6), pp. 682-692.

Samanta, A. et al. 2018. Transient Receptor Potential (TRP) Channels. In: Harris, J.R. and Boekema, E.J. eds. *Membrane Protein Complexes: Structure and Function*. Singapore: Springer Singapore, pp. 141-165.

Seixas, C. et al. 2003. Subunits of the chaperonin CCT are associated with Tetrahymena microtubule structures and are involved in cilia biogenesis. *Experimental Cell Research* 290(2), pp. 303-321.

Seo, S. et al. 2010. BBS6, BBS10, and BBS12 form a complex with CCT/TRiC family chaperonins and mediate BBSome assembly. *Proceedings of the National Academy of Sciences* 107(4), pp. 1488-1493.

Shen, P. S. et al. 2016. The Structure of the Polycystic Kidney Disease Channel PKD2 in Lipid Nanodiscs. *Cell* 167(3), pp. 763-773.e711.

Shiratori, H. et al. 2006. Conserved regulation and role of Pitx2 in situs-specific morphogenesis of visceral organs. *Development* 133(15), pp. 3015-3025.

Sleigh, M. A. 1981. PRIMARY CILIARY DYSKINESIA. *The Lancet* 318(8244), p. 476.

Smith, C. E. L. et al. 2020. Primary Cilia, Ciliogenesis and the Actin Cytoskeleton: A Little Less Resorption, A Little More Actin Please. *Frontiers in Cell and Developmental Biology* 8.

Smith, S. and Smith, C. 2022. Capturing the mechanics of clathrin-mediated endocytosis. *Current opinion in structural biology* 75.

Stehberger, P. A. et al. 2003. Localization and Regulation of the ATP6V0A4 (a4) Vacuolar H+-ATPase Subunit Defective in an Inherited Form of Distal Renal Tubular Acidosis. *Journal of the American Society of Nephrology* 14(12).

Streets, A. and Ong, A. 2020. Post-translational modifications of the polycystin proteins. *Cellular Signalling* 72, p. 109644.

Streets, A. J. et al. 2003. Functional Analysis of PKD1 Transgenic Lines Reveals a Direct Role for Polycystin-1 in Mediating Cell-Cell Adhesion. *Journal of the American Society of Nephrology* 14(7).

Su, Q. et al. 2018. Structure of the human PKD1-PKD2 complex. *Science* 361(6406), p. eaat9819.

Sulik, K. et al. 1994. Morphogenesis of the murine node and notochordal plate. *Developmental Dynamics* 201(3), pp. 260-278.

Supp, D. M. et al. 1997. Mutation of an axonemal dynein affects left-right asymmetry in inversus viscerum mice. *Nature* 389(6654), pp. 963-966.

Swanson, B. O. et al. 2013. Evolutionary variation in the mechanics of fiddler crab claws. *BMC Evolutionary Biology* 13(1), p. 137.

Tanaka, Y. et al. 2005. FGF-induced vesicular release of Sonic hedgehog and retinoic acid in leftward nodal flow is critical for left-right determination. *Nature* 435, pp. 172-177.

Tang, B. L. 2017. Sec16 in conventional and unconventional exocytosis: Working at the interface of membrane traffic and secretory autophagy? *Journal of Cellular Physiology* 232(12), pp. 3234-3243.

The European Polycystic Kidney Disease, C. 1994. The polycystic kidney disease 1 gene encodes a 14 kb transcript and lies within a duplicated region on chromosome 16. *Cell* 77(6), pp. 881-894.

Uezu, A. et al. 2011. Characterization of the EFC/F-BAR domain protein, FCHO2. *Genes to Cells* 16(8), pp. 868-878.

Venkatachalam, K. and Montell, C. 2007. TRP channels. *Annual review of biochemistry* 76, pp. 387-417.

Viebahn, C. 2001. Hensen's node. *genesis* 29(2), pp. 96-103.

Vogel, P. et al. 2010. Situs inversus in Dpcd/Poll-/-, Nme7-/- , and Pkd1l1-/- mice. *Vet Pathol* 47(1), pp. 120-131.

Walker, R. 2016. Investigating the role of ciliary localisation of the TRPP Channel, Polycystin2 (PKD2), on development and progression of polycystic kidney disease (PhD Thesis).

Walker, R. V. et al. 2019. Ciliary exclusion of Polycystin-2 promotes kidney cystogenesis in an autosomal dominant polycystic kidney disease model. *Nat Commun* 10(1), p. 4072.

Wallace, D. P. et al. 2008. Periostin induces proliferation of human autosomal dominant polycystic kidney cells through αV-integrin receptor. *American Journal of Physiology-Renal Physiology* 295(5), pp. F1463-F1471.

Wandelt, J. and Nagy, L. M. 2004. Left-Right Asymmetry: More Than One Way to Coil a Shell. *Current Biology* 14(16), pp. R654-R656.

Wang, G. et al. 2018. Role of Rab GTPases in the export trafficking of G protein-coupled receptors. *Small GTPases* 9(1-2), pp. 130-135.

Wang, Q. et al. 2012. Structural Interaction and Functional Regulation of Polycystin-2 by Filamin. *PLOS ONE* 7(7), p. e40448.

Wang, Q. et al. 2015. Filamin-A Increases the Stability and Plasma Membrane Expression of Polycystin-2. *PLOS ONE* 10(4), p. e0123018.

Wilhelmi, I. et al. 2016. Sec16 alternative splicing dynamically controls COPII transport efficiency. *Nature Communications* 7(1), p. 12347.

Witzgall, R. 2005. Polycystin-2—an intracellular or plasma membrane channel? *Naunyn-Schmiedeberg's Archives of Pharmacology* 371(4), pp. 342-347.

Wu, C. et al. 2018. Myosin-Va is required for preciliary vesicle transportation to the mother centriole during ciliogenesis. *Nature cell biology* 20(2).

Wu, G. et al. 1998. Somatic inactivation of Pkd2 results in polycystic kidney disease. *Cell* 93(2), pp. 177-188.

Xing, J. et al. 2019. Eye location, cranial asymmetry, and swimming behavior of different variants of Solea senegalensis. *Aquaculture and Fisheries*.

Yarar, D. et al. 2007. SNX9 Couples Actin Assembly to Phosphoinositide Signals and Is Required for Membrane Remodeling during Endocytosis. *Developmental Cell* 13(1), pp. 43-56.

Yoshiba, S. et al. 2012. Cilia at the node of mouse embryos sense fluid flow for left-right determination via Pkd2. *Science* 338(6104), pp. 226-231.

Yoshimura, S.-i. et al. 2007. Functional dissection of Rab GTPases involved in primary cilium formation. *Journal of Cell Biology* 178(3), pp. 363-369.

Yu, Y. et al. 2009. Structural and molecular basis of the assembly of the TRPP2/PKD1 complex. *Proc Natl Acad Sci U S A*.

Yuasa, T. et al. 2002. The sequence, expression, and chromosomal localization of a novel polycystic kidney disease 1-like gene, PKD1L1, in human. *Genomics* 79(3), pp. 376-386.

Zhang, Y.-C. et al. 2021. CEP55 promotes cilia disassembly through stabilizing Aurora A kinase. *Journal of Cell Biology* 220(2), p. e202003149.